Physik Department

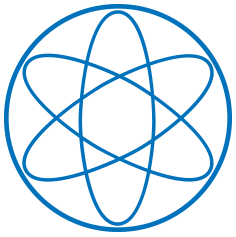

Single Polymer Friction
Desorption Stick Meets Geometrical Interlock

Dissertation
von

Bizan Nicolas Anosarwan Balzer

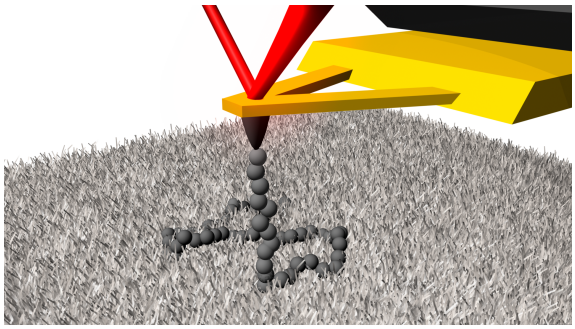

Technische Universität München

Technische Universität München

Physik Department
Lehrstuhl für Biophysik E22
und
Institut für Medizintechnik

Single Polymer Friction
Desorption Stick Meets Geometrical Interlock

Bizan Nicolas Anosarwan Balzer

Vollständiger Abdruck der von der Fakultät für Physik der Technischen Universität München zur Erlangung des akademischen Grades eines

Doktors der Naturwissenschaften (Dr. rer. nat.)

genehmigten Dissertation.

Vorsitzender:

Univ.-Prof. Dr. Martin Zacharias

Prüfer der Dissertation:

1. Univ.-Prof. Dr. Thorsten Hugel
2. Univ.-Prof. Dr. Peter Müller-Buschbaum

Die Dissertation wurde am 28.11.2013 bei der Technischen Universität eingereicht und durch die Fakultät für Physik am 13.12.2013 angenommen.

Der Glaube an eine einzige Wahrheit und deren Besitzer zu sein,
ist die tiefste Wurzel allen Übels auf der Welt.
Max Born (1882-1970)

Summary

Energy dissipation by friction is a major obstacle in the construction of energy efficient and wear resistant devices. This is of basic interest for both solid substrates and polymer coated surfaces, which are frequently utilized to modify and control substrate properties. As polymers serve both as lubricants and as substrate coatings, they have a tremendous impact on tribological applications. Therefore, a profound understanding is required, in particular at the nanoscale. This thesis presents a novel atomic force microscope (AFM)-based single molecule method, which reveals friction motifs on solid substrates and polymer coated substrates with unmatched force and spacial resolution. A single polymer, covalently attached to an AFM cantilever tip (molecular force sensor), is vertically and laterally pulled in order to determine both adhesion and friction properties at the solid-liquid interface and in thin polymer film boundary layers.

Single polymer friction is determined by pulling a partly adsorbed molecular force sensor laterally over a substrate. Unexpectedly, two motifs of stick mechanisms are discovered besides slipping:
First, a novel mechanism is found, which is called desorption stick (DS). This mechanism is independent of normal force, velocity and adsorbed polymer length. At the same time, DS is dominated by a combination of surface chemistry, solvent quality and collapsed structure of the polymer, leading to confinement in two dimensions. While the polymer part adsorbed to the substrate cannot follow the cantilever tip motion, the polymer chain desorbs into solution with low internal friction. This interpretation is based on measurements with various polymers, such as polypeptides and polystyrene (PS)-based polymers on topographically and chemically nanostructured surfaces. Although DS contrasts with several tribological models, such as Amontons' law or the Rouse model, DS-slip events are similar to macroscopic stick-slip.
Second, cooperative stick (CS) based on strong directional bonds like hydrogen bonds is experienced. CS is preferentially probed on hydrophilic substrates with hydrophilic molecular force sensors.

Polyelectrolyte multilayers (PEMs) consisting of poly(sodium 4-styrene sulfonate) (PSS) and poly(diallyl dimethyl ammonium chloride) (PDADMAC) provide a well defined model system for polymer coated substrates. The swelling behavior of PEMs under varying humidity is determined by AFM imaging. A transition from interphase to bulk-like behavior is detected after four double layers of PSS/PDADMAC. Furthermore, the spatially resolved adhesion properties of the PEM interphase are measured by desorbing a molecular force sensor from those PEMs. The adhesion

properties of the first few layers (up to three double layers) are dominated by the surface potential of the substrate, where previously described equilibrium desorption similar to solid substrate desorption is observed. In that case, a plateau of constant force in the force-extension curve is characteristic. Thicker PEMs are controlled by non-equilibrium desorption with a non-linear force-extension behavior, which is a measure of bulk-like behavior. This finding is generalized by utilizing oligoelectrolyte multilayers (OEMs) and molecular force sensors, consisting of hydrophilic and hydrophobic polymers.

Besides hydrophilic PEMs other types of polymer films are investigated, which are hydrophobic. These comprise spin coated polystyrene films (scPSs) and covalently surface-attached polystyrene films (saPSs). Annealed scPSs only show adsorption of molecular force sensors, when the scPSs dewet. For both dewetted scPSs and saPSs two different desorption mechanisms are found: equilibrium desorption (plateaus) and non-equilibrium desorption (non-linear force-extension). Non-equilibrium desorption is even observed below the glass transition temperature of PS, where a glassy polymer film is expected, and is promoted by good solvent conditions.

A mechanism for non-equilibrium single polymer desorption on polymer films is proposed, called geometrical interlock. This interlock model is based on slow relaxation of the molecular force sensor entangled into the polymer film boundary region. Furthermore, geometrical interlock is responsible for the high occurrence of CS in the complex stick-slip friction patterns of the observed thin polymer films.

The results of this thesis open new ways to characterize and to gain a profound understanding of adhesion and friction at the nanoscale.

Contents

Chapter 1

Introduction

Friction and lubrication have been present in our everyday life for centuries. The oldest evidence goes back to 3500 BC, where large stone building blocks or monuments were transported by sleds with water-based or animal fat lubricants. Although friction is a long known phenomenon, its scientific description has been developed between the 15th and the 19th century by Leonardo da Vinci, Guillaume Amontons, Leonard Euler, Charles Augustin Coulomb and Jules Arthur-Morin. Their studies led to the phenomenological equation for the friction force F_R: $F_R = \mu F_N$ with the normal force F_N and the friction coefficient μ. This relation is only valid within certain limits and describes the dry friction between solid bodies only. It neglects the role of surface asperities (surface roughness and real area of contact) and the surface softness. Furthermore, friction can be divided into static friction and dynamic friction (e.g. sliding and rolling friction). In the 19th century industrialization led to a deeper scientific understanding of friction, in particular the hydrodynamic lubrication based on developments in the petroleum industry [1].
It was 1966 when Peter Jost first introduced the notion of tribology. This term comes from the greek word for rubbing, *tribos*. It describes the science and technology of two surfaces acting on each other in relative motion. Tribology includes friction, wear and lubrication of solids, liquids and gases [1]. Tribology is an interdisciplinary field covering engineering, physics, chemistry and in parts biology and medicine.
Examples of productive friction and wear include writing with a pencil, polishing of surfaces or the use of brakes or wheels on trains and automobiles. At the same time, unproductive friction and wear lead to energy dissipation and material loss, which are responsible for a loss of about 8 % of Germany's GDP or 200 billion Euro [2]. Therefore, low maintenance costs for technical components and reduction of material- as well as energy-loss are an important motivation for tribological research. Here, economic reasons, such as high service life, functionality and safety demands meet environmental objectives and sustainability. Tribologically optimized components have a great field of industrial applications, ranging from automotive, manufacturing technology and aerospace to medical technology.
Polymers are used to reduce friction in lubricants, such as in engine oils, and in surface coatings, including nanocomposites being reinforced with different additives [3, 4]. Still, basic knowledge and understanding are sparse.
The tribological properties at the nanoscale (nanotribology) are becoming more and more important due to the miniaturization of devices with a high surface-volume

ratio. Famous examples are magnetic storage devices and micro-electro-mechanical systems (MEMS) [5, 6]. Here, sample mass and load become less important, but interfacial phenomena are of particular interest for many applications. The tribological behavior of a sample is often linked to the adhesive behavior [7, 8]. The automotive and computer industry require appropriate low friction (superlubricity) surface coatings, where diamond-like carbon (DLC) [9, 10, 11] or polymer coatings play a great role [12]. The description of molecular friction mechanisms in biological systems, such as stick-slip friction in articular cartilage [13], cells sticking to blood vessels [14, 15], internal friction of proteins [16] or the motion of molecular motors [17] are likewise of tremendous interest. In all tribological systems friction causes kinetic energy to be dissipated mainly as heat or to a lesser extent as sound emission or wear.
Polymer films are important for stabilizing colloidal dispersions and for changing surface properties, e.g. to make them biocompatible, antibacterial or non-fouling. They can be designed to be sensitive to external stimuli. In addition to many possible commercial applications for microelectronics, sensors or medical devices, such films can serve as lubricating coatings [18].
New methods to understand nanotribology and adhesion on the nanoscale have been found thanks to the development of the surface force apparatus (SFA) and the atomic force microscope (AFM). While the SFA serves to detect the frictional behavior of molecularly thin liquid films between two contacting surfaces, the AFM can go beyond that and investigate the friction properties of polymer-surface interactions with single molecule force spectroscopy (SMFS). This method is capable of measuring forces in the piconewton (pN) range with a spatial resolution below a nanometer (nm). Single molecule techniques have the advantage of revealing effects that are usually masked in bulk experiments.

The thesis is structured as follows. After a theoretical overview and a methods section, introducing polymers, adhesion, friction and AFM-based SMFS, the thesis is divided into four sections. In Chapter 4 single polymer friction on solid substrates is investigated by lateral pulling, presenting the mechanisms of slip, desorption stick and cooperative stick. Furthermore, single polymer stick-slip is discussed. As friction and adhesion are often linked, Chapter 5 and Chapter 6 deal with polymer film adhesion. These chapters show a detailed film characterization and SMFS experiments of polyelectrolyte multilayer (PEM), with an emphasis on the interphase, and of PS-based thin polymer films. Both chapters describe the mechanism of geometrical interlock between polymers. Finally, the role of geometrical interlock is further elaborated for polymer dynamics within thin polymer films in Chapter 7. Here, lateral pulling is used in order to determine the dynamics in the horizontal direction. Detailed protocols for polymer and substrate synthesis, polymer coupling chemistry as well as a fluorescence microscopy-based approach to single polymer friction are presented in the Appendix.
This thesis serves to measure and to understand single polymer mechanisms on solid substrates and on thin polymer films. Using this knowledge, future substrate coatings can be designed to manipulate frictional and adhesive behavior and to connect science and engineering.

Chapter 2

Theoretical Framework

2.1 Polymers

2.1.1 Polymer Chains

The word polymer refers to molecules consisting of repeating elementary units, the monomers. The structure of a polymer is created by polymerization, where the monomers are covalently linked together. In the 19th century chemists began to polymerize synthetic macromolecules. For many years the assumption was that those molecules consisted of colloids forming large aggregates. In 1920 Hermann Staudinger realized that those molecules are built of covalently bonded elementary units and the concept of polymers arose. In the following, W.H. Carothers synthesized many polymers in the 1920ies [19].
The molar mass results from the product of monomer mass and degree of polymerization (number monomers). The molar mass distribution of a polymer defines its polydispersity. Here, the polydispersity index (PDI) represents the ratio of weight-average and number-average molar masses. Monodisperse samples have a PDI of 1. Apart from chemical identity, the microstructure (isomerism) is important to identify a polymer. Polymers containing only one type of monomers are called homopolymers, while those consisting of several types of monomers are known as heteropolymers or copolymers, which can be alternating, random, block or graft. Molecules with a small number of monomers are called oligomers. Furthermore, polymers can have different architectures: linear, ring, star-branched, H-branched, comb, ladder, dendrimer or randomly branched [19].
Flexible polymers are subject to Brownian motion in solution. Thus, polymer chains fluctuate between different conformations. The mean equilibrium conformation of such a polymer chain in solution can be derived by a statistical approach. The partition function of the specific system corresponds to the probability to take a certain conformation. On this basis, the end-to-end distance and the radius of gyration can be determined, which are both a measure for polymer size [20, 19].

2.1.2 Different Types of Bonds

Bonds and intermolecular forces can be divided into three categories: Coulombic, quantum mechanical and entropic. A short overview based on refs. [8, 21] is given in the following.

Covalent Bond Rupture

Covalent bonds or chemical bonds are highly specific, stochiometric, short-ranged and directional interatomic bonds of quantum mechanical nature. The bond energies range between 100 and 300 k_BT per bond [21], while covalent bond lengths are of the order of Å. The forces for covalent bond breakage are about 2 nN. Car-Parrinello molecular dynamics (MD) simulations, based on density functional theory to describe the electrons, lead to similar results [22]. There, the rupture force changes from 6.6 nN for a dimer to 5.2 nN for a trimer to 4.4 nN for a decamer (with a pulling velocity of 55 $\mathrm{m{\cdot}s^{-1}}$) of siloxanes.
Bond ruptures have been observed by AFM (single molecule force spectroscopy, SMFS) with velocities of the order of 1 $\mu\mathrm{m{\cdot}s^{-1}}$. A single polymer, covalently anchored between a solid substrate and an AFM tip, is stretched until rupture. A force of 1.4 nN has been reported for a S-Au bond [23, 24], 1.3 nN for a Si-O bond [25], and 2.1 nN for a Si-C bond [26].

Van-der-Waals Bond

Ionic bonds are long-ranged physical bonds based on the Coulomb interaction of charged groups and are classified to be weaker than covalent bonds [21]. Another type of physical bond, being independent of charges, is the Van-der-Waals interaction [21]. It is non-additive and spans a distance range from 0.2 nm to more than 10 nm. Van-der-Waals interaction is strongly dependent on distance and has a strength of several k_BT. Three contributions can be distinguished:

- Debye interaction which includes the interaction of a permanent and an induced dipole with α as the polarizability of a molecule, p as the permanent dipole moment, ϵ as the dielectric constant and r being the distance of the dipoles:

$$E_{Debye} = -\frac{p^2\alpha}{(4\pi\epsilon)^2 r^6} \tag{2.1}$$

- Keesom interaction which is the Boltzmann averaged interaction of two permanent freely rotating dipoles p_1 and p_2:

$$E_{Keesom} = -\frac{p_1^2 p_2^2}{3(4\pi\epsilon)^2 k_B T r^6} \tag{2.2}$$

- London or dispersion interaction which gives the interaction of two induced dipoles with the ionization frequencies ν_1 and ν_2. This contribution is present between any atoms and molecules and comprises the main contribution to the Van-der-Waals interaction.

$$E_{London} = -\frac{3}{2}\frac{\alpha_1\alpha_2 h\nu_1\nu_2}{(4\pi\epsilon)^2 r^6(\nu_1+\nu_2)} \tag{2.3}$$

For distances in the Å range a repulsive forces dominates, which is caused by the overlap of the atomic orbitals of two different molecules. The Pauli exclusion principle forbids two electrons to occupy the same state. This results in a repulsive force, which is described by a r^{-n} potential. Both the attractive and repulsive interaction define the interaction between a pair of neutral atoms, which is often described by the Lennard-Jones potential with $n = 12$ [21].
For distances larger than 5-10 nm between two molecules, a retardation of Van-der-Waals interaction is observed showing a r^{-7} dependence. For macroscopic objects, the distance behavior of Van-der-Waals interaction is dependent on the geometry of the objects. The Van-der-Waals interaction between different materials is proportional to the Hamaker constant A_H, which depends on the dielectric properties [27, 28, 8, 21]. Based on the Lifschitz theory, assuming an object as a continuum, and due to experimental data, this constant can be described using the Van-der-Waals energy coefficient $C_{1,2}$ and the body densities ρ_1 and ρ_2:

$$A_H = \pi^2 C_{1,2} \rho_1 \rho_2 \tag{2.4}$$

This leads to the Van-der-Waals force between a sphere or a molecule of radius R and a flat surface:

$$F = -\frac{dE}{dr} = -\frac{A_H R}{6r^2} \tag{2.5}$$

Dejarguin, Landau, Verwey and Overbeek developed a theory (DLVO) that explains the aggregation of aqueous dispersions [29, 30] by the interplay of the Van-der-Waals force and repulsive electrostatic double-layer forces. While the Van-der-Waals force leads to coagulation, the double-layer forces promote the stabilization of a dispersion. At small separations continuum theories often break down. Here, the discrete nature of interacting interfaces and specific interactions, such as the hydrophobic effect, have to be considered. These complex interactions are summarized by the notion non-DLVO forces [21].

Hydrogen Bond

A hydrogen bond (HB) is strong and directional. It can be formed between electronegative atoms such as O, N, F or Cl and a H atom, which is covalently bound to similar electronegative atoms. Hence, HBs constitute a H-mediated bond between two electronegative atoms. The strength of HBs is 5-10 k_BT per bond. They can act inter- as well as intramolecularly and even in non-polar environment [21].

Hydrophobic Effect

The hydrophobic effect (HE) describes the low affinity for H_2O and low solubility of non-polar groups in H_2O [31, 32]. Although the notion hydrophobic means H_2O-fearing, the interaction between a hydrophobic molecule and H_2O is attractive due to dispersive interaction. Still, the H_2O-H_2O interaction is much higher than the hydrophobic solute-H_2O interaction [21]. Therefore, two hydrophobic molecules tend to aggregate in aqueous solvent, leading to a decrease of solute-H_2O contact area and reduction of the total Gibbs free energy:

$$\Delta G = \Delta H - T\Delta S \tag{2.6}$$

with the enthalpy, H, the temperature, T, and the entropy, S.
The term "hydrophobic bond" was introduced by Kauzmann [33] to describe the adhesion between non-polar groups of proteins in aqueous solution and underlines the relevance for the folding structure of native proteins. As the attraction between non-polar groups lacks any of the characteristic features that distinguish chemical bonds from Van-der-Waals interaction, the term "bond" seemed inappropriate. The role of H_2O molecules, regarding the attraction between non-polar groups, turned out to be larger than expected from the classic Lifshitz theory of Van-der-Waals forces between these groups [34].
For the prediction of protein structure and function, the magnitude and nature of the hydrophobic attraction acting between peptide segments is a central issue that has not been fully resolved. It is not clear, weather the HE has to be considered as a solvation force due to H_2O structure, as a long-range electrostatic interaction, as a Van-der-Waals interaction or as capillary bridges of nanoscopic gas bubbles.
Frank and Evans [35] developed a detailed theory of the HE and described H_2O molecules that take a microscopic "iceberg" structure around a non-polar molecule. This phenomenon is called hydrophobic solvation. The precise shape and chemical structure of the solute molecules are of basic importance because the H_2O structure can be highly sensitive to local solute structure. Hence, such "iceberg" structures around small solute molecules are very distinct from those close to surfaces known as hydrophobic hydration layers [36, 37, 38, 21]. Since the H_2O structure is disrupted, this effect is of entropic origin and depends strongly on temperature [39, 40]. For large molecules, such as proteins, the H_2O molecules prefer an orientation enabling to built up as many HBs as possible. MD simulations as well as x-ray and neutron scattering show a H_2O depletion layer (reduced H_2O density in comparison to bulk) with a thickness range of Å adjacent to hydrophobic substrates [41, 8]. Then, a highly ordered hydration layer [42] with reduced dynamics is found [43].
Further manifestations of long-range HE are H_2O droplets with a large contact angle on hydrophobic substrates, protein folding or polymer collapse [44, 45], micellization, self-assembly of lipids, oil–H_2O demixing and any supermolecular aggregation in H_2O [34]. Much effort has been put in force measurements between well defined model systems, e.g. between coated mica surfaces using the SFA and AFM. Hence, the forces resulting from HE between two hydrophobic surfaces or molecular groups could be determined directly [34]. Even if complications such as air bubbles can be excluded, the very short-ranged hydrophobic interaction between surfaces proves to be challenging due to mechanical instabilities of the measuring device [34].
A further challenge for the description of the HE is to explain the interaction over the entire range of observed distances, solution conditions, methods of hydrophobization, surface roughness, fluidity and "hydrophobicity" of specific chemical groups. There has been much discussion about the two regimes of the forces between hydrophobic surfaces: a long-range attraction at separations > 200 Å that is related to indirectly hydrophobicity dependent effects, such as bridging nanobubbles, and a short-range attraction at separations smaller than 100 Å, which is rather known as the truly hydrophobic interaction. Further experiments indicate another regime to consider, which is smaller than 10 Å. Here, the force is stronger than the exponentially attractive forces at larger separations [34].

2.1.3 Real Polymer Chains

In ideal polymer chains non-neighboring polymer chains do not interact. The mean-square end-to-end distance with N freely jointed monomers and monomer or Kuhn length l leads to:

$$\left\langle R^2 \right\rangle = Nl^2 \tag{2.7}$$

The end-to-end length and the conformation of a real polymer chain is decisively influenced by the monomer-monomer as well as monomer-solvent molecule interaction. Segments of a real polymer chain cannot overlap. Therefore, the random walk model for ideal chains has to be extended to a self-avoiding random walk model. The excluded volume is the volume that cannot be occupied by polymer segments. In general, an interaction potential between two monomers consists of an attractive and a repulsive part (hard core potential) [19].
A net attraction between monomers has a negative excluded volume $V < 0$, while a net repulsion takes a value $V > 0$. The excluded volume is described as a cylinder of Kuhn length l and diameter d. On account of this, the polymer conformation is dependent on the quality of the solvent [19]:

- Athermal solution: for high temperatures the repulsive interaction dominates. Here, the excluded volume reaches l^2d and becomes independent of temperature.

- Good solvent: in a typical solvent the monomer-monomer interaction turns out to be stronger than the monomer-solvent interaction. The net attraction leads to an attractive potential minimum, which leads to: $0 < V < l^2d$. A decrease of temperature results in a smaller excluded volume.

- θ solvent: at the θ temperature the attractive potential and the repulsive hard core potential counterbalance each other. Now, the excluded volume is 0, which represents ideal polymer behavior.

- Poor solvent: a further decrease of temperature leads to a dominance of the attractive potential. The monomers approach so that the excluded volume becomes negative: $-l^2d < V < 0$.

- Non-solvent: The limiting case of a poor solvent is characterized by such a strong attraction that almost all solvent molecules are excluded from the volume within the polymer chain leading to: $V \approx -l^2d$.

The polymer conformation in good solvent is dependent on the balance between monomer repulsion and the entropy loss due to chain deformation. This balance is the central issue of the Flory Theory [46, 19]. The minimum free energy in Flory approximation leads to a universal power law for the dependence of polymer size on monomer number N:

$$R \propto N^{\nu} \tag{2.8}$$

Flory approximation for a swollen linear polymer leads to a scaling exponent of $\frac{3}{5}$ for good and athermal solvents and $\frac{1}{3}$ for poor and non-solvents instead of $\frac{1}{2}$ for ideal linear chains [19].

2.1.4 Charged Polymer Chains

A polymer bearing charged groups is called a polyelectrolyte (PE). The electrolyte groups dissociate in aqueous solutions, leading to charged polymers. PEs with both cationic and anionic repeat units are called polyampholytes. Examples of PEs appearing in nature are polypeptides, DNA and polysaccharides. Strong PEs dissociate completely in aqueous medium, while weak PEs dissociate only partly. The state of dissociation is dependent on the pH of the solution and counter ion concentration [47].
Apart from short ranged Van-der-Waals and steric interactions, long ranged electrostatic interactions between PE charges as well as PE charges and counter ions are most prominent obeying the Coulomb law.
The length scale of interaction is decisively dependent on the counter ion concentration around the PE and influences the chain conformation. Like PE charges lead to intrachain repulsion, which puts strongly charged chains into a more stretched state (higher persistence length) than less charged ones. By contrast, screening due to counter ions leads to a more collapsed conformation similar to uncharged chains. Electrostatic interactions of PEs in ionic solutions can be described by the Debye-Hückel theory [48]. The electrostatic charge of a PE is screened by the surrounding counter ions, which leads to a decay of the interaction with increasing distance characterized by the Debye screening length κ^{-1}:

$$\kappa^{-1} = (8\pi l_B \sum_i c_i q_i^2)^{-\frac{1}{2}} \tag{2.9}$$

with the Bjerrum length l_B (which is defined as the distance between charged, where the interaction energy equals k_BT) and the concentration c_i of charges q_i. The persistence length l_0 of an uncharged chain has to be modified for the self-repulsion of like PE charges using the OSF-theory, established independently by Odijk [49], Skolnick and Fixman [50]:

$$l_p = l_0 + \frac{\tau^2 l_B \kappa^{-2}}{4} \tag{2.10}$$

with $\tau = a^{-1}$ as line charge density using a as the monomer length [47]. Nevertheless, several experiments show that the OSF-theory is an oversimplified model not accounting for a charged polymer chain under stress [51, 52]. Weakly charged PEs are not fully stretched but can be assumed as elongated chains of Gaussian electrostatic blobs that scale according to:

$$\zeta_{el} \propto a \left(a\tau^2 l_B\right)^{-\frac{1}{3}} \tag{2.11}$$

The size of such a blob reflects an electrostatic interaction of k_BT inside the blob. At a certain salt concentration the screening length becomes smaller than the size of the chain. Thus, the chains start to bend [53].

2.1.5 Polyelectrolytes at Interfaces

PEs can adsorb onto substrates, when the PE-substrate interaction is more pronounced than the PE-solvent interaction. The attractive surface potential competes

with a repulsion of entropic origin. When polymers adsorb to a substrate, three different parts are distinguished: trains that contact the substrate, loops which represent unbound parts residing between trains and tails constituting unbound free ends of the polymer chains. A broad overview is given in refs. [54, 47, 19].
In short, the adsorption of PEs on a solid surface carrying an opposite charge per unit area $q\sigma$ is considered. Counter ions lead to screening of this field, which can be determined by the Poisson-Boltzmann equation with q as the ion valency, e the elementary charge, c_0 the salt concentration in solution and $\psi(r)$ the electrostatic potential of the substrate:

$$\Delta\phi(r) = -\frac{\rho(r)}{\epsilon} = \frac{c_0 eq}{\epsilon}\left(\exp(\frac{qe\psi(r)}{k_B T}) - \exp(-\frac{qe\psi(r)}{k_B T})\right) \tag{2.12}$$

The counter ions are captured close to the substrate with the characteristic Gouy-Chapman length:

$$\lambda = \frac{1}{2\pi\sigma l_B} \tag{2.13}$$

This equation has an analytical solution for a planar charged wall only. The asymptotic behavior of the potential with the Debye screening length κ^{-1} is [55]:

$$\frac{e\phi(r)}{k_B T} = \begin{cases} -\frac{2}{\lambda\kappa}\ \exp(-\kappa r), & for\ \lambda\kappa \gg 1\ or\ r \gg \kappa^{-1} \\ 2\ ln\left(\frac{\lambda\kappa}{2}\right) + 2\ ln\left(1+\frac{r}{\lambda}\right), & for\ \lambda\kappa \ll 1\ and\ r \ll \kappa^{-1} \end{cases} \tag{2.14}$$

The first limit represents the Debye-Hückel regime and follows from linearization of the Poisson-Boltzmann equation. Here, the screening length is so short that nonlinear effects can be neglected. The Debye-Hückel regime is characterized by the electrostatic potential acting on an elementary charge to be smaller than $k_B T$. In particular, this applies to surface potentials of roughly less than 25 mV. The Debye-Hückel approximation breaks down close to the charged surface, which is called Gouy-Chapman regime [21]. A detailed discussion of the limitations of the Poisson-Boltzmann theory (which is a continuum model based on electrostatics only) is given in refs. [8, 21]. For low ionic strength a PE chain is attracted by an oppositely charged surface and is confined within a distance δ from the surface. For $\delta < \lambda$ the chain feels the surface field and δ is given by:

$$\delta \propto \left(\frac{a}{\tau\sigma l_B}\right)^{\frac{1}{3}} \tag{2.15}$$

For higher ionic strength, where the screening length becomes smaller than the chain thickness δ, and in case of insufficient non-electrostatic interaction the chain possibly desorbs (de-adsorbs) from the surface [53]. Furthermore, the dissociation equilibrium of weak PE is affected by the substrate potential, which leads to charge regulation of the PE [56].

2.1.6 Grafted Polymer Films

Grafted polymer chains on particles are often used to stabilize dispersions from aggregation or to enhance adhesion or friction properties of substrates [47, 18, 8]. This stabilization effect is obtained by steric repulsion between the grafted chains, once the particles approach.

The chains can either be chemisorbed by means of the "grafting to" or the "grafting from" approach or physisorbed. The scaling behavior of the film thickness is given by a Flory-like mean-field theory, which is a simplified version of the original Alexander theory [57] for grafted polymer chains. Different theories by de Gennes [58, 59] as well as Milner, Witten and Cates [60, 61, 62] describe the behavior of grafted chains. The Alexander model assumes a flat, non-adsorbing surface to which monodisperse polymer chains are tethered. The polymer chains consist of N statistical segments. A homogenous distribution of grafted chains in the volume Lb^2 with grafting density $\Gamma = b^{-2}$ is assumed, where b gives the distance between grafting sites.
On the one hand, a low grafting density represents the mushroom regime and leads to separated polymer blobs with the size of the radius of gyration R_g (Figure 2.1 a). On the other hand, for a high Γ value, such as $\Gamma \gg R_g^{-2}$, the brush regime is obtained (Figure 2.1 b).

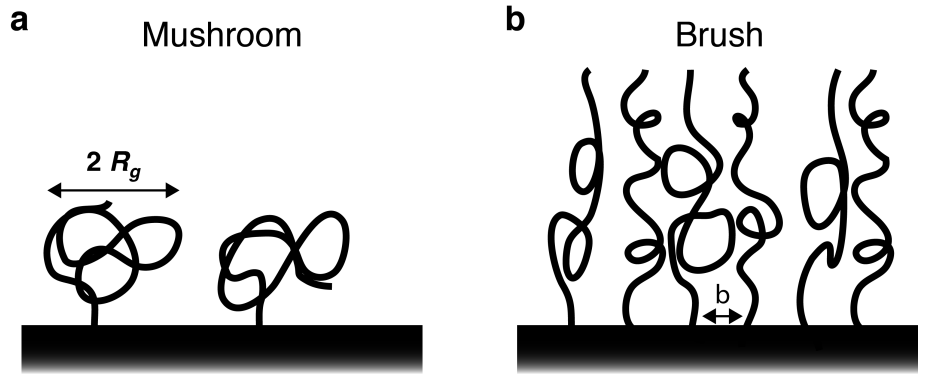

Figure 2.1: Grafted polymer films. (a) Low grafting density is characterized by the mushroom regime, while (b) high grafting density leads to brushes with chains taking an elongated conformation.

The thickness L of a undisturbed chain is dominated by the balance of two effects. While the repulsive interaction of the neighboring polymer segments causes the grafted polymers to stretch and to swell the film, the configurational entropy loss resists the stretching. In the brush regime, with the chains strongly interacting with their neighbors, the thickness of the brush L is related to the grafting density Γ:

$$L = N \left(\frac{\nu l^2 \Gamma}{6} \right)^{\frac{1}{3}} \tag{2.16}$$

with the segment number N, the excluded volume ν and the chain segment length l. The solvent quality alters the brush thickness due to the excluded volume (Section 2.1.3).
Milner, Witten and Cates rather assume a parabolic than a step profile for the grafted chain segment density. Thus, the thickness L is given by:

$$L = 1.07 \cdot N(\nu l^2 \Gamma)^{\frac{1}{3}} \tag{2.17}$$

De Gennes uses a self-consistent mean field theory with a step profile for the grafted chain density, leading to the following expression for L:

$$L = N l^{\frac{5}{3}} \Gamma^{\frac{1}{3}} \tag{2.18}$$

The reported expression $L \propto N\Gamma^{\frac{1}{3}}$ can be applied for good and theta solvents. In case of poor solvents, the experimentally confirmed [63] scaling law $L \propto N\Gamma$ is found for the collapsed film structures [64].

2.1.7 Polymer Elasticity Models

For an AFM-based SMFS experiment (Section 2.4.1) the ensemble constitutes a coupled cantilever-polymer system. This thermodynamically small system is prone to fluctuations. Different statistical ensembles can be used for its description, the Gibbs and the Helmholtz ensemble. While the first is based on length fluctuations (soft cantilever), the latter takes force fluctuations (stiff cantilever) into account [65]. Usual experimental conditions for SMFS are well approximated by the Gibbs ensemble. This serves as a basis for the stretching of single flexible polymer chains under an external force leading to the concept of entropic elasticity.
Molecular elasticity has two contributions: entropic and enthalpic. As the polymer is pulled and extended, the number of polymer chain conformations is reduced. This leads to a decrease in entropy. That is why work has to be done to reduce the polymer's entropy. Different polymer models have been proposed to account for that issue. The most common models are the freely jointed chain (FJC) [20] and the worm-like chain (WLC, or Kratky-Porod-model) [66, 67]. A broad review is given in refs. [68, 69].
The FJC [70] model describes a polymer as a chain of N rigid segments of equal length l. The segments are assumed to be orientationally independent or freely jointed. While the contour length of the polymer chain is given by $L = Nl$, the mean extension along the z-axis, z, is a function of the applied stretching force along the z-axis:

$$z(F) = L\left(coth(\frac{Fl}{k_BT}) - \frac{k_BT}{Fl}\right) = L\mathcal{L}\left(\frac{Fl}{k_BT}\right) \tag{2.19}$$

$\mathcal{L}(x) = (\coth(x) - x^{-1})$ is the Langevin function, while the fit parameters in this model are the segment length l, also known as the Kuhn length and the number of segments N. The $F(z)$ profile is given by the inverse function of $z(F)$.
The stretching force is a function of the chain's relative extension: $F \approx f(\frac{z}{L})$. When all force traces are scaled to the same contour length, those polymers originating from different chains but of identical structure will superimpose.
By contrast, the WLC model describes the polymer as a continuous flexible string of constant bending modulus, neglecting any discrete structure along the chain [66]. The characteristic length is represented by the persistence length l_p, which accounts for the flexibility of the polymer coil. l_p is defined as the decay length of the directional correlation along the polymer chain and given by the bending modulus B to $l_p = B(k_BT)^{-1}$. For flexible chains ($L \gg l_p$) and for small forces, the persistence length equals half of the Kuhn length l determined by the FJC model [67]. Although, the exact force–extension relation of a WLC can be given only numerically [71], an analytical approximation is widely used for the evaluation of experimental force-extension curves [72]:

$$F = \frac{k_BT}{l_p}\left(\frac{z}{L} + \frac{1}{4(1-\frac{z}{L})^2} - \frac{1}{4}\right) \tag{2.20}$$

Fit parameters are the contour length L as well as the persistence length l_p. For small and high forces, this approximation is very good, but it may differ from the exact solution by as much as 10 % leading to an overestimation of l_p by approximately 5 % [73].
At higher forces chemical bonds are extended and deformed. Then, the enthalpic contribution becomes important. This can be added to the entropic contribution by an additional linear stretching term. Besides the segment length l, the persistence length l_p and the polymer contour length L, a Hookean spring constant is added as additional fit parameter [74]. Here, one has to assume that the restoring force can be separated into an entropic and an enthalpic contribution.
Using the WLC or the FJC model, length changes like in the unfolding of titin [75] or transitions in polysaccharides [76], measured with Å precision, can be analyzed (Section 2.4.1).

2.1.8 Polymer Dynamics

Unentangled Polymer Dynamics

Polymers immersed in a solvent undergo a diffusive motion due to collisions with surrounding molecules. The three-dimensional mean-square displacement is given using the diffusion coefficient D:

$$\left\langle [\vec{r}(t) - \vec{r}(0)]^2 \right\rangle = 6Dt \tag{2.21}$$

A very successful model for polymer dynamics has been developed by Rouse [77]. There, the polymer chain is represented by a bead-spring model. When a constant force is applied to a Rouse chain, consisting of N beads in liquid, a motion of constant velocity v is obtained. The viscous friction force F_{Rouse} accounts to:

$$F_{Rouse} = N\mu v \tag{2.22}$$

The diffusion coefficient follows from the Einstein-Smoluchowski relation to:

$$D_{Rouse} = \frac{k_B T}{N\mu} \tag{2.23}$$

The Rouse chain diffuses a distance of its own size during the characteristic Rouse time τ_{Rouse} [19]:

$$\tau_{Rouse} \approx \frac{R^2}{D_R} \approx \frac{\mu N R^2}{k_B T} \approx \frac{\mu l^2}{k_B T} N^{1+2\nu} = \tau_0 N^{1+2\nu} \tag{2.24}$$

For times smaller than τ_{Rouse} the chain exhibits viscoelastic modes, while for times longer than τ_{Rouse} the chain motion is diffusive. Since polymers are self-similar objects, their viscoelastic time dependent properties can be described by a chain consisting of independent blobs. Therefore, the chain dynamics can be modeled by a wealth of relaxation modes similar to a vibrating string. The shortest mode corresponds to the relaxation time of a monomer τ_0. The Rouse model is applied particularly to a polymer system, where the hydrodynamic interaction is screened such as in unentangled (short chain) melts.
For dilute solutions, the Zimm model is used. This model considers that the solvent

within the pervaded volume is dragged with the polymer and leads to the following expression for the friction coefficient for a chain of size R and solvent viscosity $\eta_{solvent}$:

$$\zeta_{Zimm} \approx \eta_{solvent}\ R \tag{2.25}$$

The Zimm time τ_{Zimm} shows a lower dependence on polymer chain length than the Rouse time τ_{Rouse} (Equation 2.24). Thus, the polymer experiences a lower frictional drag in terms of the Zimm model in dilute solutions.
Single polymer dynamics near attractive surfaces scale differently with the monomer number N [78]:

- $D \propto N^{-\frac{3}{2}}$ for strongly-adsorbed, linear polymers on solid substrates in good solvents
- $D \propto N^{-1}$ for fluid substrates such as membranes, ring polymers or polymers commensurate with the substrate

Entangled Polymer Dynamics

The dynamics of single linear entangled chains can be described by the Edwards tube model [79, 80]. There, the polymer chains move by random walks (Brownian motion) within a tube-like primitive path, set by the topological constraints due to neighboring chains. The entanglements have a finite lifetime. The polymers disentangle either by a snake-like motion (reptation) [81] of a single chain in its tube or by the motion of the tube. These surrounding chains perform constraint release and local tube jump (Figure 2.2 a). Entanglement models can be applied to polymer gels, polymer melts and concentrated polymer solutions. A broad overview is given in ref. [19].
With the number of N_e monomers in the entanglement strand, the tube can be assumed as a chain of $\frac{N}{N_e}$ sections of size $a \approx l\sqrt{N_e}$ (for ideal chains in case of screened excluded volume interaction in a polymer melt). The average contour length of the primitive path is $\langle L \rangle \approx a\frac{N}{N_e}$. This is shorter than the chain length $L = lN$ for an unentangled strand. The relaxation time of a polymer melt is represented by the time it takes for a single polymer chain to reptate out of its original tube of average length $\langle L \rangle$. This time is called reptation time t_{rep} (Figure 2.2 b), which determines the three-dimensional diffusion coefficient D with the polymer mass M:

$$\tau_{rep} \propto M^3 \tag{2.26}$$

$$D \propto M^{-2} \tag{2.27}$$

Tube length fluctuations in time lead to a slight modification: $\tau_{rep} \propto M^{3.4}$ and $D \propto M^{-2.4}$ [84]. Entanglements are formed for long linear chains. A critical molar entanglement mass for PS is about 18.1 kDa [85].
In poyldisperse polymer melts two processes compete. These are the single chain p reptation in its confining tube consisting of chains n and the constraint release due to the Rouse motion of the tube chains n. The diffusion coefficient results from the sum of the respective diffusion coefficients:

$$D \approx \frac{R^2}{\tau_{rep}(p)} + \frac{R^2}{\tau_{tube}} \tag{2.28}$$

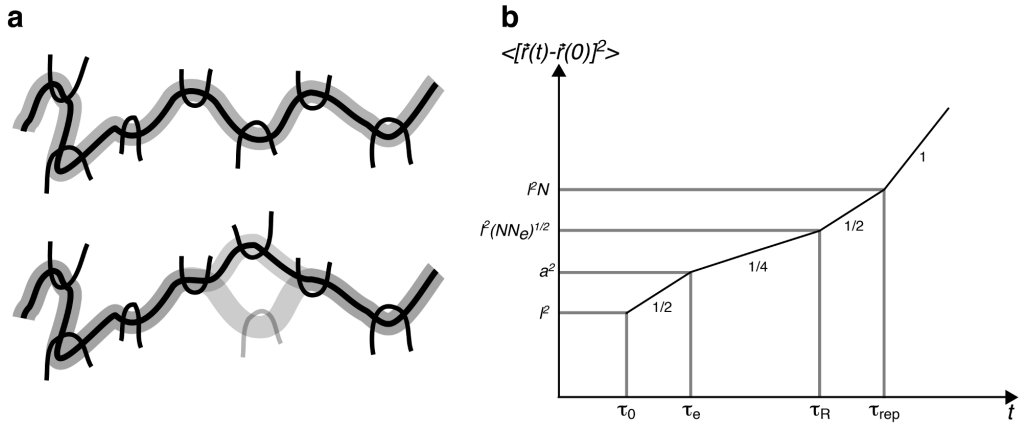

Figure 2.2: Reptation model. (a) Scheme of a polymer chain constrained in an entangled network. A chain performs a constrained movement within a virtual tube (light grey), defined by entanglements with neighboring polymers (constraints). The constraint release by Rouse-like motion of the confining tube is shown in the lower scheme. (b) Four different regimes of monomer displacement in melts of linear entangled polymers are theoretically predicted [19] and experimentally confirmed [82, 83]. On a timescale shorter than the relaxation time of an entanglement strand τ_e, the chain is not aware of the topological constraints. Below τ_e the sub-diffusive motion of the Rouse model is observed with $\langle[\vec{r}(t) - \vec{r}(0)]\rangle \propto t^{\frac{1}{2}}$. On longer timescales the polymer random walk is restricted by the confining tube. Here, the tube itself undergoes a random walk, which leads to $\langle[\vec{r}(t) - \vec{r}(0)]\rangle \propto t^{\frac{1}{4}}$. This regime is characteristic for entangled polymer motion. Once the Rouse time τ_R is reached, each monomer participates in a coherent Rouse motion of the whole chain, restricted by the tube. For times longer than τ_R the following scaling is obtained: $\langle[\vec{r}(t) - \vec{r}(0)]\rangle \propto t^{\frac{1}{2}}$. When τ_{rep} is reached, the whole chain has diffused through the tube. Now the polymer chain exhibits a simple diffusion (adapted from [19]).

The faster process dominates the resulting chain motion. For long chains p and short chains n the constraint release of chains n dominates, while short chains p and long chains n lead to a control by the reptation of the p chains.

2.2 Adhesion

Adhesion is a complex phenomenon and has a high relevance for science and technology, as well as everyday life. Adhesives are designed to show maximum adhesion, reversible removal, self-cleaning and self-healing ability [86, 87, 88]. Many new developments are related to examples from nature such as geckos [89, 90]. Adhesion science aims to understand the mechanical properties and to predict the long-term durability of adhesive joints.

2.2.1 Basic Adhesion Mechanisms

The adhesion force between two bodies in mechanical contact arises from the strength of attractive interaction, the contact area (including geometry and surface roughness) and the distance between those. Adhesion is composed of different contributions such as Van-der-Waals interaction, electrostatic interaction, hydrogen bonds, ionic bonds, metallic bonds, chemical bonds, donor-acceptor bonds, capillary bridges or steric interaction. Furthermore, the environmental conditions, such as humidity and temperature, play an important role [8, 91]. At the same time, the deformation of contacting bodies under force is decisive for the understanding of adhesion. Here, several contact models such as Hertz [92], JKR [93] and DMT [94] are usually used.

Although adhesion consists of a wealth of different effects, the following mechanisms are generally known [95, 91]:

- Materials can stick together by chemical reaction such as using coupling agents.
- Mechanical adhesion reaches high joint strengths for porous adherends by undergoing mechanical interlock.
- Electrostatic interaction is based on electrical double layer interaction between a pair of adherents.
- Diffusion theory [96] considers interdiffusion of polymers, including entanglement formation (Section 2.1.8), across the interface. This mechanism underlines that surface contact alone is not sufficient and is restricted to polymeric systems, in particular above glass transition temperature.
- Boundary layers determine the strength of adhesive joints as well as the mechanical properties of the materials (Section 2.2.3).

A broad variety of methods have been developed to quantify adhesive forces, such as peel tests, adhesive joints, centrifugal forces, wetting analysis due to contact angle measurements, SFA, AFM and optical methods or scanning electron microscopy (for contact area determination). A broad overview is given in refs. [8, 21].

2.2.2 Interfacial Energy

Adhesion is a phenomenon that is present in the macroscopic and the microscopic world as well. A basic concept that is valid on any length scale [21] is given by the work of adhesion W_{adh}, which has to be afforded to separate two objects A and B that are in contact. In case of two bodies consisting of two different materials, this work is denoted as work of adhesion W_{AB}, while objects consisting of the same material refer to the work of cohesion W_{AA}.
Separating these bodies A, B in vacuum requires a surface energy per unit area γ to create the new surfaces A and B. Thus, W_{AB} accounts to:

$$W_{AB} = \gamma_A + \gamma_B \tag{2.29}$$

In case of two bodies A, immersed into a solution B, the surface energy for the separation of the bodies A is given by two processes: First, two unit areas are created. Then, they are brought into contact. Both processes are summarized in the Dupré equation:

$$\gamma_{AB} = \gamma_A + \gamma_B - W_{AB} \tag{2.30}$$

A generalized form is given for two bodies A and B in a solution C:

$$W_{ABC} = W_{AB} + W_{CC} - W_{AC} - W_{BC} = \gamma_{AC} + \gamma_{BC} - \gamma_{AB} \tag{2.31}$$

The concept of work of adhesion W_{adh} and surface energy γ can be used to characterize the wetting of a macroscopic surface A in contact with a fluid medium B in an environment of a fluid or gaseous medium C (Figure 2.3). Once the system is in equilibrium, the surface energies of the system are minimal. The surface energies are directly linked to the interatomic and intermolecular forces. The contact angle

θ of the medium B is given by the surface energies and the work of adhesion per unit length ΔW_{ABC} by the Young and the Young-Dupré equation:

$$\gamma_{AB} + \gamma_{BC} \cos\theta = \gamma_{AC} \tag{2.32}$$

$$\gamma_{BC}(1 + \cos\theta) = \Delta W_{ABC} \tag{2.33}$$

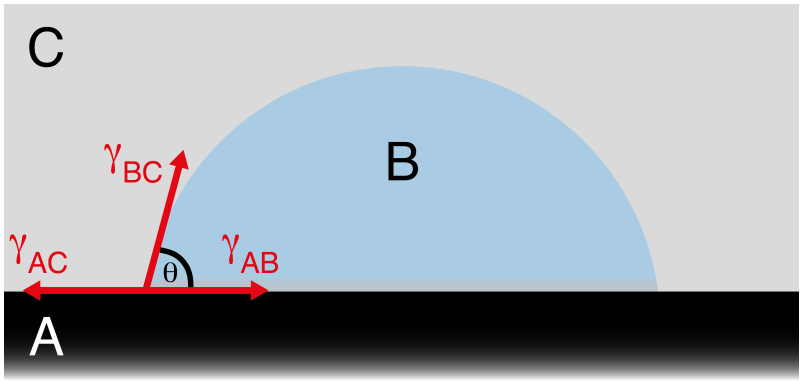

Figure 2.3: Contact angle determines wetting properties. Wetting of a solid substrate. A fluid B contacts the solid surface A in a fluid or gaseous medium C.

2.2.3 Interphase

A crucial question is whether the adhesive interaction occurs at a two dimension interface only, or weather a three dimensional interphase is involved. A broad overview is given in refs. [95, 97, 91, 98].
Adhesive systems have to be considered as multicomponent materials. They comprise two adherends and an adhesive, usually a compound or a polymer. Boundary layers between these different phases are known to have a great impact on adhesive strength. Such surface layers are also termed weak boundary layer [99].
The notion interphase for these weak boundary layer was first used in the 1960ies. Sharpe developed a concept for the interphase [95, 91]. It is defined as a region intermediate to two contacting solids that is distinct in structure and properties from either of the two contacting phases. As there are many interaction mechanisms involved, a generalization is difficult. However, the existence of the interphase is an accepted fact now [97].
The interphase depends on the combination of adherend and adhesive and on the process of contact formation as well. While some models assume homogeneous properties inside the layer, others consider a continuous change from one phase to the other. Many solids are themselves composite layer structures. The boundary layer is an integral part of a structure containing the solid in question. Thus, any analysis of mechanical behavior of adhesive joints has to pay regard to the possible presence and influence of a boundary layer. Due to its distinct structure, the interphase possesses properties that can be much different from the behavior of the bulk adhesive [100].
The interphase thickness is known to depend on the investigated property or structure, such as chemical composition, molecular orientation, cross-linking density or mechanical properties [98]. Possart et al. [101] showed that a chemical interphase

can have a thickness of several 100 nm, while a mechanical interphase can have a thickness in the μm range.
Methods that are able to determine the orientation and conformation of molecules on surfaces comprise sum-frequency generation (SFG), X-ray photoelectron spectroscopy (XPS), Auger electron spectroscopy (AES), mass spectrometry (ToF SIMS), near-edge x-ray absorption fine structure (NEXAFS), IR spectroscopy and vibrational circular dichroism (VCD) and molecular simulations [97, 98].
In summary, the interphase is considered as a region of an adhesive bond, which differs from the bulk in its equilibrium composition or conformation. In fact, the molecular composition and conformation influence greatly the adhesive behavior and macroscopic characteristics, such as mechanical, dielectrical, optical and transport properties.

2.3 Friction

Friction is defined as the force acting against the motion of two bodies sliding past each other. Although being highly important for technological applications and everyday life, friction and its related topics lubrication and wear remain still not fully understood. This is mainly due to its high complexity connecting different fields, such as physics, chemistry, biology, geology, biology and engineering. Tribology has evolved as a rather young field of scientific research, with mostly empirical approach. Here, a brief overview of friction, in particular nanoscopic friction, is given based on refs. [102, 103, 8, 21].

2.3.1 Basic Principles

The earliest empirical theories of friction between dry macroscopic solid bodies were developed by Leonardo da Vinci, Guillaume Amontons and Charles-Augustin de Coulomb between the 15th and the 19th century. They can be summarized as follows:

- **Amontons' First Law:** The force of friction is directly proportional to the applied load.
- **Amontons' Second Law:** The force of friction is independent of the apparent area of contact.
- **Coulomb's Law:** Kinetic friction is independent of the sliding velocity.

These laws lead to the famous linear relation between friction force F_R and normal force (which includes load and adhesion between contacting surfaces) F_N, known as Amontons' law:

$$F_R = \mu F_N \tag{2.34}$$

Here, μ depicts the friction coefficient. A tribological system consists of four elements: two base bodies, an interfacial medium (lubricant) and a surrounding medium. Hence, a friction coefficient describes a specific tribological system under environmental conditions, such as heat or relative humidity, instead of being a material parameter.
Amontons' law has been determined empirically. It turned out to be too simple to

describe the complexity of friction processes. For example, the true area of contact is just a fraction of the real contact area, which underlines the importance of surface roughness [104]. Bodies in sliding contact interact via microcontacts or asperities (Figure 2.4 a). The true area of contact is strongly dependent on the load and the plastic or elastic material properties. On the one hand, surface roughness leads to a reduced true area of contact, with a decrease of adhesion and thus normal force. On the other hand, surface roughness increases the friction force in case of interdigitating asperities (mechanical interlock), leading to material deformation, abrasion and finally wear.
In the 20th century it became more and more evident that friction is ultimately coupled to energy dissipation into heat, sound emission and wear, which causes material loss.

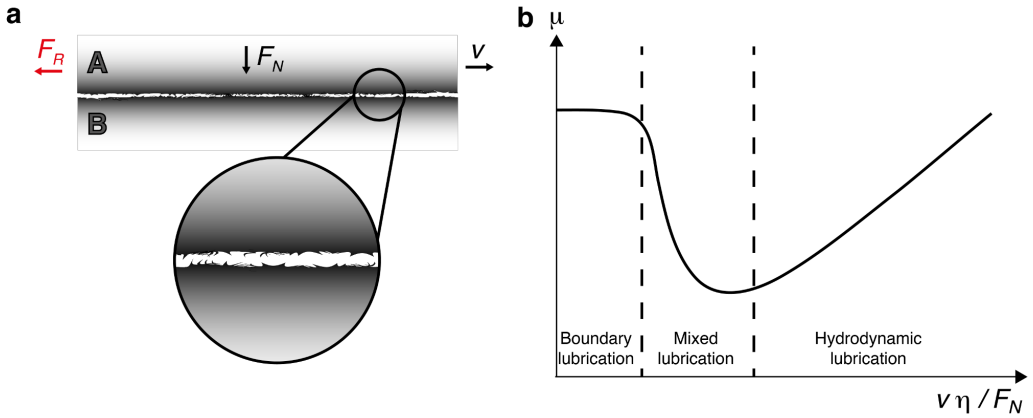

Figure 2.4: Macroscopic friction effects. (a) Scheme of two solid bodies undergoing dry friction. The zoom-in shows contacting microasperities. (b) Stribeck diagram for a lubricated friction contact, representing the dependence of the friction coefficient μ on the pulling velocity v, lubricant viscosity η and normal force F_N.

2.3.2 The Stribeck Curve

While the basic friction laws indicate that the friction force is independent on velocity, a more profound understanding of a tribo-system shows a much more complex situation. Here, the normal force (including load) F_N, the sliding velocity v and the viscosity of the lubricant fluid η (oil-based for technical applications or water-based in nature [5]) have to be considered [8]. The Stribeck curve summarizes the behavior of lubricated contacts (Figure 2.4 b).
For low viscosity, low velocity and high load the boundary regime dominates. As the load is mainly carried by the solid contacts, high friction force and wear are observable. Still, the thin lubricant film reduces the adhesion between the solid bodies and thus the friction force greatly compared to dry friction. This regime is highly important for starting and stopping of motion, where bodies in sliding contact are prone to wear.
Both, decreasing load or increasing velocity, lead to the mixed lubrication regime. Here, the load is mainly supported by the lubricant, while the surfaces do not contact directly.
When decreasing the load or increasing the velocity further, the fluid layer completely covers the surfaces, preventing solid contacts. Now, the hydrodynamic lu-

brication regime is reached, where the load is entirely carried by the fluid film. This reduces the friction force to a great extent. Finally, increasing the velocity leads to a linear increase in friction force with the velocity and the lubricant viscosity. Here, one way to reduce the friction force is to use low viscosity lubricants. However, the lubricant should assure that its film is thick enough to prevent the solid substrate asperities from coming into contact (boundary lubrication).
The temperature increase of the lubricant due to energy dissipation leads to a thinning of the lubricant film with $\eta = \eta_0 \exp\left(\frac{E_a}{k_B T}\right)$, which can reduce the friction force in the hydrodynamic lubrication regime. At the same time, reaching boundary lubrication has to be avoided. For non-Newtonian fluids shear thinning and thickening aspects, being dependent on shear rate or rather sliding velocity, have to be considered.
Additionally, the hydrodynamic lubrication includes a phase of elasto-hydrodynamic lubrication. The sliding surfaces entrain the lubricant. At high pressures, the lubricant viscosity increases with pressure or even undergoes a phase transition to a glassy state. This effect prevents wear under high loads.
Furthermore, the adhesion and wear of substrates can be reduced by polymer coatings or nanocomposites, implying solid lubricants such as PTFE, graphite or MoS_2 [4].

2.3.3 Stick-Slip Phenomenon

Leonhard Euler was the first to distinguish between static (sticking) and dynamic (sliding) friction [103]. In general, the static friction coefficient μ_{static} is at least as high as the dynamic friction coefficient $\mu_{kinetic}$. A descriptive explanation is that the static friction has to be overcome by an uphill motion along an asperity slope for a sliding motion to start.
Friction between two objects moving past each other can be caused by a transition between sticking and sliding [104]. This sawtooth motion is the most common type of non-uniform friction. Prominent examples are a glass harp, the squeaking sound of chalk on a blackboard, the sound from hydraulic cylinders, the music from bowed instruments, the motion of leukocytes along walls of endothelial cells and the motion of articular joints. Even the behavior of seismically active faults can be described by a stick-slip model with periods of rapid slip causing earthquakes [105, 106, 7, 5, 21, 13].
When a surface coupled to a spring is pulled with a constant velocity v over a second surface, stick-slip can be investigated: the spring is elongated until the static friction force is reached (stick phase). Then, the spring coupled block starts to move and is accelerated with a velocity greater than v, while the spring relaxes rapidly (slip phase). Now the force exerted by the spring decreases, which makes the surface stick again. General aspects are: stick-slip amplitudes decrease with increasing velocity, while the frequency of stick-slip events increases. After experiencing regular and chaotic stick-slip motion, pure sliding is reached at a critical velocity (Figure 2.5 a). Furthermore, the stick-slip amplitude increases with increasing difference between μ_{static} and $\mu_{kinetic}$. Therefore, a softer spring shows more significant stick-slip.
Stick-slip can be observed with polymer coated substrates using the SFA [7, 107, 21]. Here, a phase transition from solid-like to liquid-like state is used to describe the stick-slip behavior.

For earthquakes, the aging of contacts during stick phases is important, as this leads to an increase of static friction, which enhances the stick-slip effect [108].
Frenkel and Kontorova introduced a model for the plastic deformation of solids, which describes the stick-slip motion. The model assumes a polymer as a string of beads connected by harmonic springs, which is located in a one-dimensional harmonic potential. One of the particles is pulled by an external force (Figure 2.5 b) [109, 110, 111]. In the Frenkel-Kontorova model, the polymer or particle string is trapped in the potential minimum. The polymer motion is characterized by stick-slip behavior, where virtual bonds to the substrate due to trapping in potential minima, are broken and reformed. In case of zero velocity or vanishing external pulling force, the mobility is given by thermally activated diffusion processes. An increasing external force tilts the potential energy landscape and reduces the activation energy barriers. Therefore, the corrugation of the external potential becomes negligible and the mean mobility approaches intrinsic polymer mobility value $\langle \mu \rangle \approx \frac{\mu}{N}$. This exactly describes the transitions of stick-slip to a continuous and smooth motion.
The Frenkel-Kontorova model can be extended by the Tomlinson model, where independent oscillators are connected to a sliding surface in a fixed potential. This model has often been used to describe the friction of a tribo-system, consisting of two solid plates and a polymer in between [112].

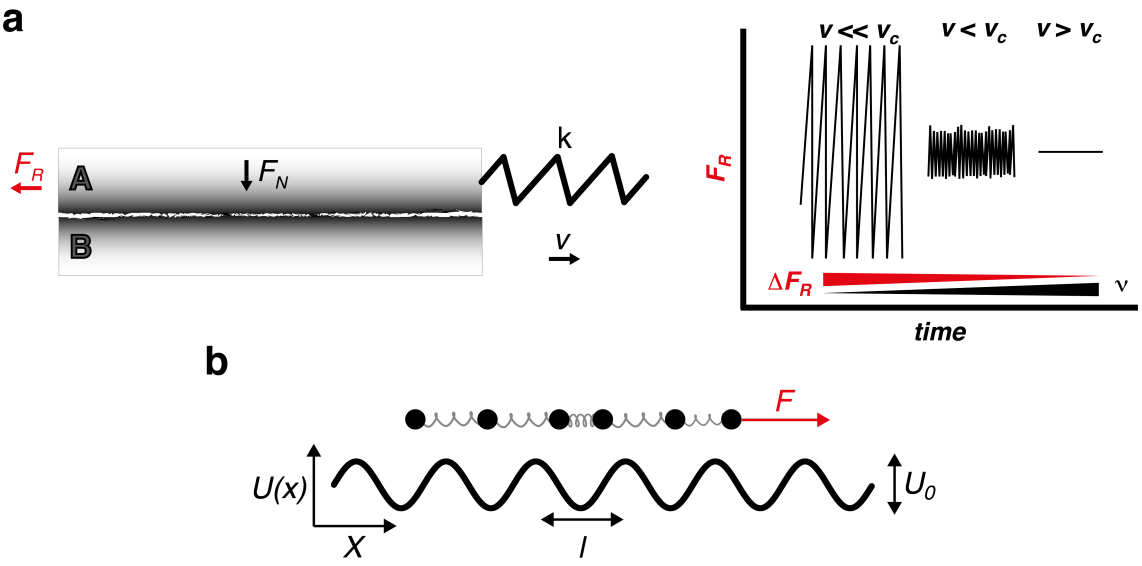

Figure 2.5: Stick-slip. (a) Stick-slip motion of a solid substrate A attached to a spring and moving over a second substrate B. Stick-slip with friction force amplitude ΔF_R and frequency ν at low sliding velocities transforms to smooth sliding above the critical velocity v_c such as given in refs. [113, 114]. (b) Theoretical model for stick-slip: the Frenkel-Kontorova model as used for the friction of a single polymer (bead connected via springs) on a one-dimensional corrugated surface. The sinusoidal potential energy landscape is described by a depth U_0 and a lattice constant l. An external force F acts on the first monomer (adapted from [111]).

2.3.4 Nanotribology

Many friction processes are related to microcontact formation. That is why, friction at the nanoscale has to be understood. As atomistic models do not seem directly scalable, one of the remaining challenges in tribology is to link the macro- to the nanoscale [115]. Several differences arise at the nanoscale: the ratio of real to ap-

parent contact area is close to 1. Additionally, the load has a rather small effect, while the influence of adhesion has a major effect due to the high surface to volume ration [5]. Atomic lattice vibrations (phonons) [116] as well as electron-hole pair generation (electronic friction) [117] contribute to energy dissipation. In order to reduce friction, contacting bodies are excited to oscillatory motion in vertical direction (dynamic superlubricity) [118]. So, the adhesion or in more general terms the normal force is decreased.
The development of the SFA [119], the quarz crystal microbalance [120], the AFM in friction force microscopy (FFM) mode [121] and MD simulations provide new means to study friction at the nanoscale. The dependence of friction force on load depends on single-asperity contacts, which leads to a non-linear friction force - load dependence. Here, the respective contact model plays a major role [122]. In particular, FFM is sensitive enough to detect friction anisotropy on e.g. graphene [123] or wear at the atomic scale [124].
Experiments directly addressing the friction of polymers at the liquid-solid interface are sparse. Accordingly, theories on polymer friction are mainly based on the Rouse model with linear dependence on velocity and chain length (Section 2.1.8). Such approaches and MD simulations claim chemical bonds, in particular HBs, as source of friction [125, 126, 127].
Recent developments of optical tweezers enable to measure the friction of a single kinesin molecule on a microtubule track [17]. The AFM-based SMFS has served to determine the frictional behavior of polymers such as DNA on solid substrates [128] and through carbon nanotubes [129].

2.4 Single Molecule Force Spectroscopy

In the last 50 years experimental techniques have been invented for direct detection of interaction forces between surfaces and small particles in the nanometer (nm) range. A major development has been the SFA, which reaches a force resolution 10 nN and a vertical resolution of 0.1 nm [130, 119]. So far, it has served to precisely determine the separation dependent forces and the frictional forces between two surfaces [131, 7, 13].
The properties and interactions of single polymer chains cannot be derived from conventional ensemble measurements. Techniques with very high spatial and force resolution, such as the AFM (5-10^3 pN), magnetic tweezers (10^{-3}-10^4 pN) and optical tweezers (10^{-1}-10 pN) are required to investigate inter- and intramolecular forces of single (bio)polymers [132, 133, 134, 135, 136].
Apart from imaging (contact, intermittent-contact or non-contact mode) [137], many different AFM applications can be covered nowadays with suitable cantilever resonance frequency, softness and coatings ranging from high speed imaging [138], FFM [121], magnetic force microscopy [139] to surface potential imaging [140] and chemical force microscopy [141]. A broad overview is given in [142]. As the AFM is applicable in aqueous environment, it has created the opportunity to image biological surfaces such as cells and protein layers at nm resolution under physiological conditions [143]. After spring constant determination (Section 3.1.3) molecular forces can be measured.

2.4.1 AFM-based Single Molecule Force Spectroscopy

The AFM enables to detect inter- and intramolecular forces in the pN range in ambient environment. Therefore, the AFM has become a prominent tool to investigate numerous biopolymer systems since the 1990ies. Single polymers can be tethered between cantilever tip and sample surface, either by unspecific attachment to tip and substrate or by covalent attachment to at least tip or substrate immersed in solution.
A covalent attachment, using a flexible linker system (Figure 3.1 b and Appendix A.2), allows long time measurements with one and the same individual polymer at various solid-liquid interfaces.
The measured vertical force F_z vs. vertical extension z curves lead to the detection of intramolecular stabilizing forces (Van-der-Waals, hydrophobic and electrostatic) [144, 145, 68, 146, 147], elasticity of a polymer chain [75], conformational transitions along the chain [76], mechanical stability of covalent bonds [23], structural energy barriers [148], co-solute binding to polymers [149], surface induced secondary structures of polypeptides [150] and temperature dependence of polymer desorption [147, 151]. Single molecule cut-and-paste, which allows the assembly of functional nanosystems [152, 153, 154] and the study of opto-mechanical energy transduction at the molecular level [155], represent a combination of AFM-based SMFS and total internal reflection fluorescence (TIRF) microscopy.

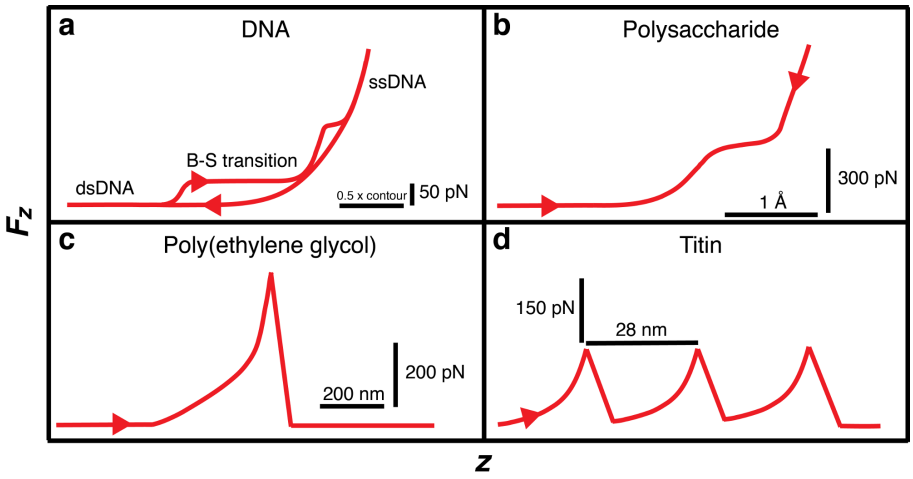

Figure 2.6: Scheme of molecular fingerprints. (a) Double-stranded DNA (dsDNA) shows a plateau of constant force at a force of 65 pN [156]. Different models are suggested: B–S transition, where DNA unwinds cooperatively with base pairing staying intact [157, 158]. Another model assumes breaking of base pairs leading to two single-stranded DNA (ssDNA), similar to a melting transition [159]. At higher forces (above 100 pN), a second transition has been reported, which is caused by melting of the dsDNA [160, 161]. Backward (relax) traces show the behavior of a ssDNA, which can be well described by the FJC model. During the relaxation, the DNA is able to reanneal. Then, the backward trace will follow the forward (extension) trace. (b) Polysaccharides are characterized by a kink at around 275 pN in H_2O. This is generally interpreted as chair–boat transition (conformational transition) in the pyran ring, with an extension of 0.5 Å per ring unit [23]. This transition is fully reversible, without hysteresis between the forward and backward traces. Therefore, the system is in thermodynamic equilibrium at any time. (c) Poly(ethylene glycol), PEG, behaves like an ideal entropic spring, which is well described by a FJC model. In H_2O, marked deviations are observed in the range of 20 to 200 pN. These result from the disruption of a suprastructure stabilized by HBs [162]. This fingerprint motif is reversible and thus in thermodynamic equilibrium. (d) Titin consists of many repeats of the Ig27 domain [75]. As each of the domains behaves like an ideal entropic spring after unfolding, both the WLC or FJC model (Section 2.1.7) can be used to describe the F_z-z behavior. The molecular fingerprint is represented by the unique repeat structure. Each Ig27 domain shows an equal spacing of around 28 nm [75]. This repeat structure serves as a well-known fingerprint and is often used to introduce artificially a repeat structure in a protein construct of unknown structure [148, 163]. Adapted from [69].

In SMFS a fingerprint, i.e. a specific feature in the force-extension or F_z-z trace, is required for correct identification of the probed molecule. Such features are deviations from the behavior of an ideal elastic polymer, such as configurational or conformational transitions. Several examples of molecular fingerprints are given in Figure 2.6.
The bond dissociation process has to be considered as a non-equilibrium dynamical process, where the bond strength is time and loading rate dependent. SMFS and theoretical models serve to link the unbinding forces at the molecular level to the binding potential and the energy landscape of molecular bonds [164, 165, 166].
At pulling rates much faster than the internal dynamics of the probed bonds, a saw-tooth pattern is observed, with each monomer-surface detachment corresponding to a peak. Lower pulling rates, comparable to the natural unbinding (and rebinding) rates (on/off rates), lead to consecutive dissociation events with individual peaks of low force. Those represent effectively a flat plateau of constant force at slow pulling rates.

2.4.2 Single Polymer Desorption

In the past 15 years the desorption of a single polymer, contacting a solid surface, has been directly measured using SMFS [144, 167, 145, 68]. Usually, the equilibrium desorption of a single polymer results in velocity independent plateaus of constant force (Figure 2.7 a) and leads to desorption force and free energy [168, 169]. While the height of the plateau describes the desorption force $F_{plateau}$, the location of the force drop to zero is defined as the detachment length z_{det} (Figure 2.7 a). The detachment length is reproducible. At the same time, the detachment length does not necessarily match the contour length of the detached polymer (including the linker system). Tough, establishing a relation between contour and detachment length, it can serve as a good fingerprint. Single polymer desorption has gained a great variety of applications, which will be summarized in the following.

Equilibrium Desorption

The notion equilibrium desorption refers to a velocity-independent plateau force. Stopping the pulling motion on the plateau or moving backward in z-direction does not change the force [170]. The polymer is pulled off the substrate in thermodynamic equilibrium to first approximation [171]. Hence, the detachment is assumed to be on a considerably faster timescale than the pulling. Therefore, plateaus of constant force $F_{plateau}$ on hydrophobic substrates are treated as an equilibrium desorption event [171]. Still, if a molecule is pulled quickly, compared to internal relaxation, non-equilibrium effects can be observed. A statistical mechanical model has been developed by Staple et al. [172].
There, the equilibrium detachment height $z_{eq} = z_{z,\max}(v_z = 0)$ is given by the condition that the free energy of the adsorbed polymer crosses the free energy of the free polymer. Here, non-equilibrium effects dominate at high vertical pulling velocity v_z. In order to account for non-equilibrium effects, the equilibrium model is extended within a master equation approach based on a two-state Markov process.
In this model, the detachment height $z_{z,\max}(v_z)$ is found to increase with pulling velocity v_z. For low pulling velocity v_z, the detachment height of the polymer converges to its equilibrium value. For intermediate v_z values, this dependence appears

logarithmic, when Bell-like models are used. In the limit of high v_z values, the detachment height approaches the contour length of the polymer. So, the detachment height varies in a sigmoidal fashion from its equilibrium value at zero pulling velocity to the contour length of the polymer at infinite pulling velocity.
Additionally, Staple et al. discovered that the dominant non-equilibrium effect is a broadening and an enhancement of the length fluctuations around z_{det}. Out of equilibrium, the molecule takes longer on average to detach from the surface and the z_{det} probability distribution becomes bimodal. Two peaks are observed in the probability distribution, corresponding to the two states of the model: either the molecule will be attached to the surface, with a smaller mean height, or it will be detached, with a Gaussian probability distribution around the cantilever position.
Such a velocity dependence, as predicted by the presented model, is not observed for various PS-based polymers in the range of pulling velocities used in this thesis. This has been reported for poly(lysine), PLL, as well [173]. That is why the plateaus of constant force, bearing velocity independent vertical desorption behavior, are assumed as equilibrium desorption plateaus throughout this thesis.

Electrostatic Contribution to Plateau Desorption Force

The measured $F_{plateau}$ constitutes the sum of a constant non-electrostatic contribution F_0, which includes the dispersion and the H_2O structural (for hydrophobic interaction see Section 2.1.2) forces and the electrostatic contribution F_{el} in case of charged polymers and charged surfaces in an electrolyte solution [68]. Due to the stretching of the polymer chain an entropic contribution F_{en} has to be added. Still, F_{en} is estimated to be around 6 pN for a Kuhn length of 1 nm, which makes up a small contribution of around 10% of the measured $F_{plateau}$ value [51, 68, 174]. F_{el} is of the order of several k_BT per monomer for a strongly adsorbed polymer. It can be described with an attractive linearized Debye–Hückel potential (Equation 2.14) [68]. Using the potential energy V_{el} for a charge in proximity of an oppositely charged surface, the force $F_{el}(z)$ is given by:

$$F_{el}(z) = \frac{dV_{el}(z)}{dz} = -4\pi l_B k_B T \sigma\tau \exp(-\kappa z) \tag{2.35}$$

where τ is the polymer line charge density, σ is the surface number charge density of the substrate, κ^{-1} is the Debye screening length and $l_B = e^2(4\pi\epsilon k_B T)^{-1}$ is the Bjerrum length.
The polymer is removed monomer by monomer from the substrate at $z = 0$ until eventually the end of the chain fully detaches from the substrate. Then, the plateau desorption force of the chain vanishes. Integration over z leads to the total electrostatic force F_{el} acting on a desorbing polymer chain:

$$F_{el} = 4\pi l_B k_B T \sigma\tau \int_{z=0}^{\infty} \exp(-\kappa z) dz = 4\pi l_B k_B T \sigma\tau \kappa^{-1} \tag{2.36}$$

The process, described by Equation 2.36, is equivalent to the transfer of one infinitesimal chain segment carrying the charge density τ from z = 0 to z = ∞ with the rest of the chain remaining at its position. An overview of the respective scaling laws is given in ref. [167]. The linear dependence of F_{el} on the polymer charge density and the Debye screening length by Equation 2.36 can be experimentally verified. The

analysis of $F_{plateau}$ with varying salt concentration (screening length) and polymer charge leads to the surface charge density [175, 176, 177, 178].

Effect of Interface

Single polymer desorption makes it possible to derive the plateau desorption force $F_{plateau}$ and free energy E_{des} as the area under the plateau in the F_z-z curve for various interfaces.
Surprisingly, $F_{plateau}$ does only change within 15% for varying substrate properties such as conductivity, wettability or surface potential [169, 181] (Figure 2.7 b). The measurements can be extended to other interfaces, such as liquid-liquid or liquid-air by chloroform or air bubbles caught on a hydrophobic solid substrate. Compared to the different interfacial energies the difference in $F_{plateau}$ is unexpectedly low [181] (Figure 2.7 c). At the same time, polymer properties like hydrophobicity and charge play a minor role [169].

Ion Specific Effects

In the 19th century Franz Hofmeister discovered that different ions have a different efficiency in precipitating hen-egg white proteins. Accordingly, he ordered the ions in a series, which is known as the Hofmeister series nowadays. This series is strongly coupled to the ion size and its ability to polarize the surrounding medium [182]. The Hofmeister series affects many properties, such as H_2O surface tension [183], protein precipitation [184] and peptide denaturation [185, 186]. The exact order of the Hofmeister series for ion adsorption at surfaces, depending on their surface charge and polarity, has been investigated by explicit solvent atomistic MD simulations [187, 188].
Experimentally, the effect of the Hofmeister series on $F_{plateau}$ has been measured by Pirzer et al. [189] (Figure 2.7 d). Here, $F_{plateau}$ increases linearly with ionic strength and follows the direct Hofmeister series in analogy to salting out or denaturation experiments [189]. Accordingly, kosmotropic anions as well as chaotropic cations show an increase in $F_{plateau}$. Still, the changes are within 30 % of the $F_{plateau}$ value. In particular, the effect for physiologically relevant salt concentrations below 1 M is less than 10%. These small changes are due to a compensation mechanism between dispersive and H_2O structural forces.

Solvent Impact

In order to reduce the interfacial energy and the interfacial hydration water, ethanol–H_2O mixtures are used. $F_{plateau}$ of poly(tyrosine), PT, on a CH_3-SAM decreases strongly with increasing ethanol concentration in H_2O [181, 146] (Figure 2.7 e). The presence of ethanol reduces the surface tension and the Van-der-Waals interaction because of the lower static dielectric constant of ethanol [21]. Furthermore, these experiments hint towards a desorption mechanism, where the desorbed molecule resides in the hydrophobic hydration layer, while the rest is in direct contact with the surface. The ethanol molecules reduce the Van-der-Waals interaction of the polypeptide in the depletion layer and take the place of the polypeptide at the surface. Both effects reduce $F_{plateau}$.

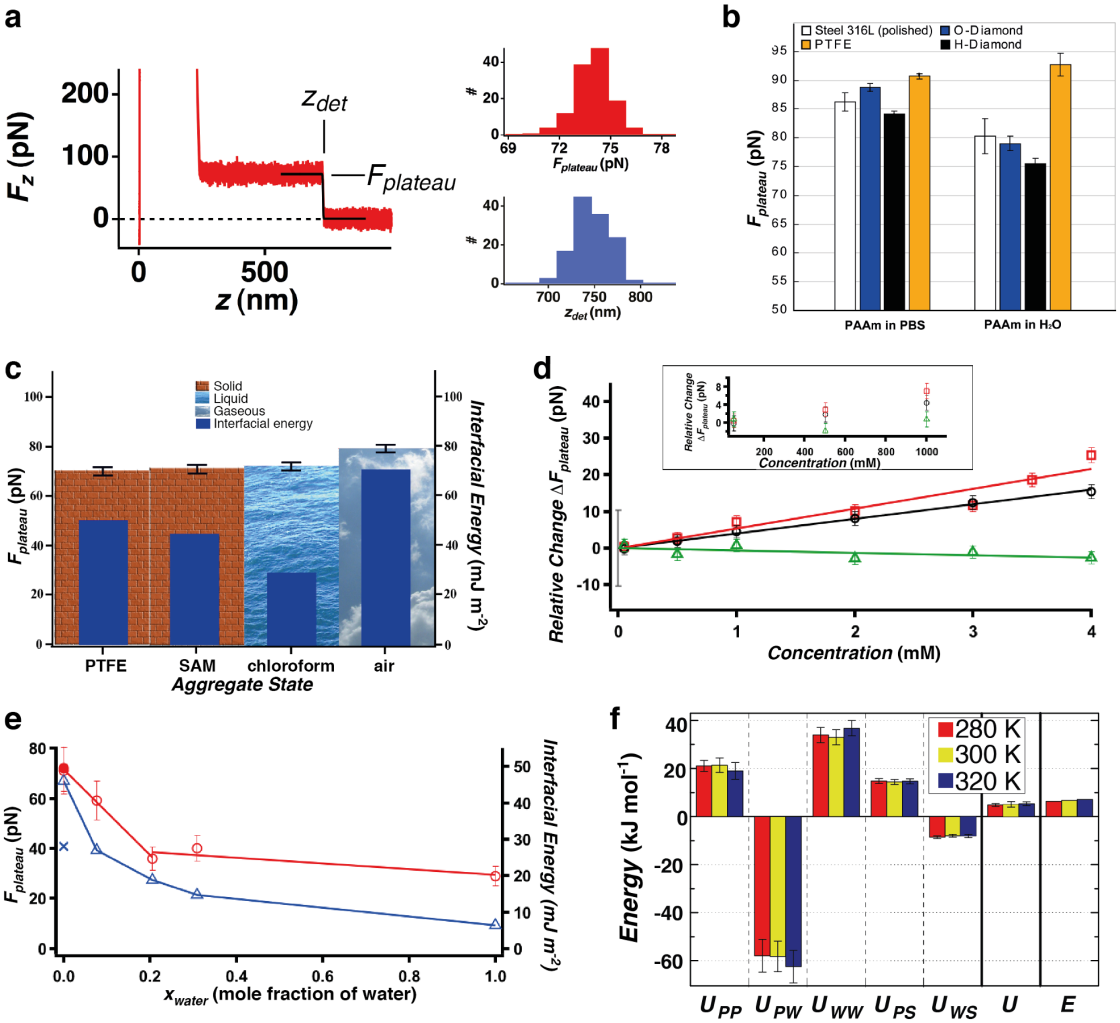

Figure 2.7: Plateau desorption force. (a) Example of a vertical force F_z vs. vertical extension z plot. The positive force axis represents attractive interaction. Close to the substrate, an unspecific adhesion peak stemming from tip–substrate interaction is observed. The following plateau shows a single polymer desorption event of a polystyrene-based block copolymer (PI-PS-PPS) on a self-assembled monolayer of CH_3-terminated alkanthiols on Au (CH_3-SAM) in H_2O. $F_{plateau}$ and z_{det} are taken from a sigmoidal fit (red) to the plateau end, leading to the depicted distributions (adapted from [69]). (b) $F_{plateau}$ for poly(allylamine), PAAm, in either phosphate buffered saline (PBS) or in H_2O on surfaces of varying conductivity, wettability and surface potential (adapted from [179]).(c) $F_{plateau}$ (left scale) for PT and interfacial energy (right scale) for different interfaces: PTFE (bricks)-H_2O, CH_3-SAM (bricks)-H_2O, chloroform (liquid)-H_2O and air (gas)-H_2O (adapted from [180]).(d) Relative $F_{plateau}$ values of (QAQ)8NR3 from a CH_3-SAM in different electrolyte solutions NaI (green), NaH_2PO_4 (red) and NaCl (black). $F_{plateau}$ presents a linear dependence on salt concentration. The inset zooms into the physiologically relevant range (adapted from [180]).(e) $F_{plateau}$ (left scale and open circles) and interfacial energy (right scale and open triangles) for PT from a CH_3-SAM in ethanol/H_2O mixtures are compared to the values from chloroform/H_2O interface taken from Figure (c) (solid circles for $F_{plateau}$ and solid triangles for interfacial energy). The lines represent a guide to the eye (adapted from [180]).(f) Decomposition of the total internal energy change per monomer U and comparison with the free energy E for three different temperatures: polymer–polymer (PP), polymer–water (PW), water–water (WW), polymer–substrate (PS), and water–substrate (WS) (adapted from [171]).

Compensation Mechanism

MD simulations can shed light into these unexpectedly low increase of $F_{plateau}$ with increasing salt concentration or increasing substrate hydrophobicity.
To that aim, the desorption of a single polymer from its surface adsorbed state into its stretched conformation has been investigated by MD simulations with explicit H_2O by Horinek et al. [171, 190] distinguishing between: polymer–polymer (PP), polymer–water (PW), water–water (WW), polymer–substrate (PS), and water–substrate (WS) interaction (Figure 2.7 f). The unexpected finding is that each individual energy contribution is large compared to the overall desorption energy U per peptide monomer, which can be described by:

$$U = U_{PP} + U_{PW} + U_{WW} + U_{PS} + U_{WS} \tag{2.37}$$

Furthermore, the MD simulation leads to the result that individual energy contributions cancel each other out. Therefore, the HE results from a balance of H_2O structural forces and the direct dispersion interaction between polymer and surface. Such inter- and intramolecular hydrophobic interactions are known to drive protein folding and adhesion [171].
A direct comparison of desorption forces from simulation and experiment is only justified if thermal equilibrium is achieved and dissipative effects are irrelevant in the pulling simulations. With different desorption rates and comparing dynamic with static simulations, Horinek et al. [171] underline that surface adsorbed polymers equilibrate very fast on hydrophobic surfaces within the time frame of the simulation. At the same time, theoretical and experimental data agree very well despite the differences in timescale (5 to 6 orders of magnitude higher velocity) and the shorter polypeptide length (1 to 2 orders of magnitude).
In conclusion, macroscopic adhesion of polymer coatings is much more dependent on cohesion effects between a great number of polymers rather than on the adsorption strength of a single polymer. An increase of $F_{plateau}$ with polymer chain number has already been observed in desorption measurements [191].

Adsorption Resistance of Hydrophilic Substrates

The work of adhesion and the wetting properties of surfaces can be macroscopically determined due to contact angle measurements (Section 2.2.2). Static H_2O contact angles can be related to $F_{plateau}$ of surfaces with varying surface hydrophobicity. A joint approach combining SMFS and MD simulations with explicit H_2O reveals the adsorption resistance of hydrophilic substrates.
Various homopolypeptides, which differ in their side chain hydrophobicity, are desorbed from SAMs. The latter are increasingly used for biofouling applications. They allow to control the surface energy, affecting the surface hydrophobicity, in a well defined and reproducible way using mixed self-assembled monolayers with alkanthiols on Au bearing various degrees of OH and CH_3 groups [192].
$F_{plateau}$ on hydrophobic surfaces is higher for hydrophobic amino acids and reduced for polar ones, as shown for PLL, poly(glutamic acid), PGA, and PT (Figure 2.8 a). While all polymers are driven energetically to the surface, the entropy leads to repulsion for hydrophilic residues and to attraction for the hydrophobic residues. This is in line with common expectations based on the HE. Additionally, $F_{plateau}$

decreases monotonically with the surface becoming more hydrophilic. Below a certain contact angle value (wetting coefficients between $k \approx 0.4$ and $k \approx 0.8$ or contact angles between $\theta = 65°$ and $\theta = 40°$) the adsorption turns into repulsion, depending only weakly on the peptide type. Then, single polymer desorption events cannot be observed any more (Figure 2.8 a).
The simulation data for polyalanine reveal an abrupt decrease of the $F_{plateau}$ at a wetting coefficient of about $k \approx 0.5$, corresponding to a contact angle of about 60° (Figure 2.8 b). Polar surfaces with OH-concentrations larger than 33%, lead to a vanishing $F_{plateau}$. The surface becomes resistant against adsorption of polyalanine. The only exception for adsorption on hydrophilic substrates are polymers with side-chain structures that are able to directly fit into the polar-surface hydrogen bonding pattern, but even for these cases (tyrosine and glutamic acid) the adsorption is weak. Apart from the surface contact angle another parameter is known to determine the protein adsorption: the type of HBs that a surface is able to form [193].

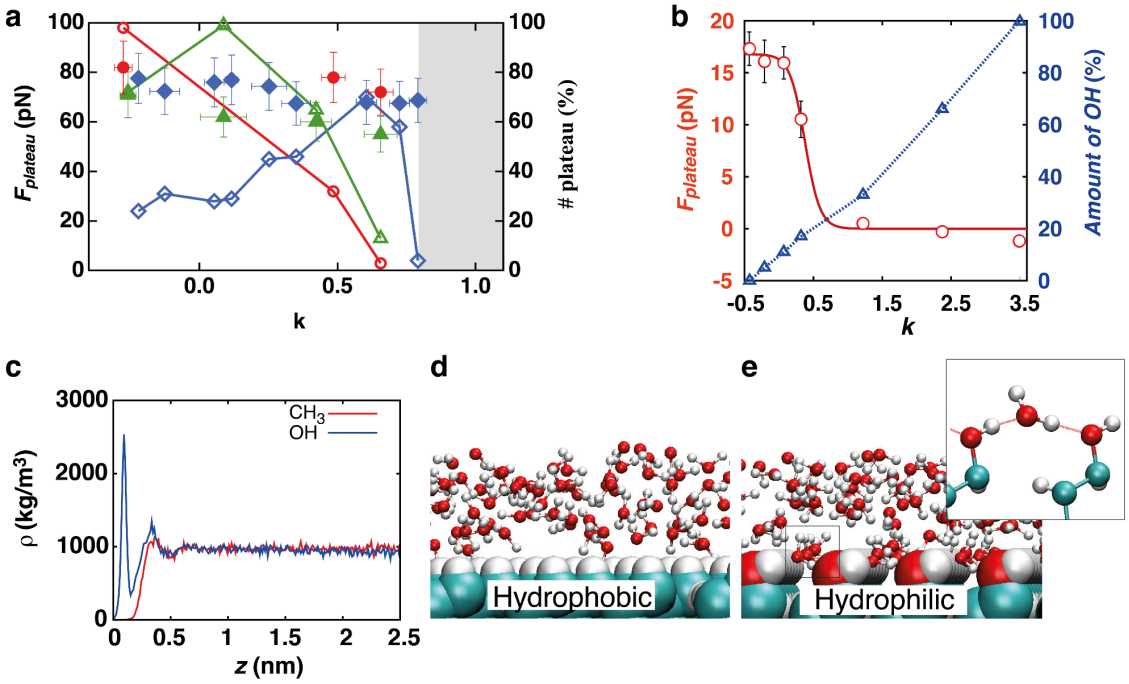

Figure 2.8: Dependence of plateau desorption force on polymer and surface hydrophobicity. (a) Experimentally measured $F_{plateau}$ (left axis) for PLL (filled green triangles), PT (filled red circles) and PGA (filled blue diamonds) from mixed OH-/CH_3-terminated SAMs in 1 M NaCl salt solution in dependence on the H_2O static contact angle. The wetting coefficient is given by $k = \cos\theta$ with e.g. $k = -0.13$ or static contact angle of $\theta = 98°$. As the surface becomes more polar (smaller contact angle), the amount of force traces that exhibit a plateau strongly decreases. The ratio of force measurements that exhibit a plateau curve (relative to the overall number of measured force extension curves, right axis) is shown as open symbols. Here, the gray area indicates the disappearance of plateau desorption events. The different salt concentrations in experiments and simulations only lead to small modifications of $F_{plateau}$ [171]. The solid curves are added to guide the eye. As the surface becomes more polar, the amount of plateau curves strongly decreases. (b) $F_{plateau}$ in dependence on the wetting coefficient $k = \cos\theta$, obtained by static simulations of polyalanine (red circles with fit function $\frac{a}{\exp(b(k-c))+1}$ with fit coefficients a, b, c). The dependence of the wetting coefficient k on the OH-surface concentration Φ is shown by blue triangles (dashed blue serves as a guide to the eye). (c) H_2O density profile at a hydrophobic (red) and at a hydrophilic surface (fully hydroxylated $\Phi = 100\%$, blue). (d,e) Simulation snapshot which presents H_2O at a hydrophobic and at a hydrophilic surface. The inset of (e) shows a zoom-in of HBs between a H_2O molecule and two OH-surface groups. Adapted from [192].

The reason for that resistance at hydrophilic surfaces is a strongly bound first hydration layer. This is represented by a high H_2O density close to the surface, in

contrast to the hydrophobic surface having a depletion layer with a thickness of 0.3 nm [194] (Figure 2.8 c,d). Simulation data show that a considerable fraction of H_2O molecules in the first hydration layer forms two HBs with the surface OH-groups of two neighboring alkane chains, as indicated in the inset of Figure 2.8 e. These H_2O molecules can only be displaced from the peptide-surface gap with a force of hundreds of pN (energetic repulsion of about 30 kJ·mol^{-1} per residue). Both entropy and enthalpy in the system favor this behavior. In particular, the enthalpy increases with the number of HBs between H_2O, peptide, and surface.
In summary, in case of peptide adsorbing surfaces the number of HBs and the total system entropy is maximized in the surface-adsorbed polypeptide configuration, while for peptide-resistant surfaces the number of HBs (in particular H_2O-H_2O HBs) is larger for polymers in bulk. The hydrophobicity region, where the transition from adsorption to repulsion occurs, corresponds to the so-called Berg-limit [195, 196]. This limit has major implications on protein and cell adsorption and the design of anti-fouling surfaces.

2.4.3 Single Polymer Friction

First, AFM-based studies have been performed by Kühner et al. [128], using angle dependent SMFS. A theoretical framework has been presented by Serr et al. [197, 111, 125] for lateral pulling of single polymers.
Figure 2.9 a depicts the scheme of a single polymer coupled to an AFM tip and adsorbed to a substrate. The polymer backbone and the normal to the substrate implicate an angle ϕ. The exact value of ϕ depends on the friction coefficient between polymer and substrate. For a physisorbed polymer with a high friction coefficient, the polymer can be peeled off the substrate with a steady increase in ϕ. This sticky case, which is quite different than the plateau desorption observed in Section 2.4.2, is characterized by a linear dependence of vertical force F_z on the vertical distance R_z, the initial vertical distance R_0 and the monomer adsorption energy ω:

$$\frac{F_z}{k_B T} = \omega \frac{R_z}{R_0} \tag{2.38}$$

By contrast, for small friction coefficients, the polymer can follow the AFM cantilever tip motion with a constant ϕ value. ϕ is dependent on the balance between friction and adhesion forces at the contact point between polymer and surface. For this slippery case, the polymer can slide on the surface due to either vertical or lateral pulling. The full contour length is given as $L = L_N + R$. The friction force F_R, acting against the lateral motion of the adsorbed polymer part L_N, follows with the sliding velocity in lateral direction $\dot{X}$ using the Rouse model (Section 2.1.8):

$$\frac{F_R}{k_B T} = \dot{X} L_N \mu = \dot{X} \frac{L^2 - X^2 - R_z^2}{2\,(L - X)} \mu \tag{2.39}$$

The monomer friction coefficient μ depends on monomer type, substrate properties as well as pH value and ionic strength of solution. The friction force caused by the solvent is negligible for the assumed velocity range. The tangential component of the adsorption force follows with the monomer adsorption energy ω and the total

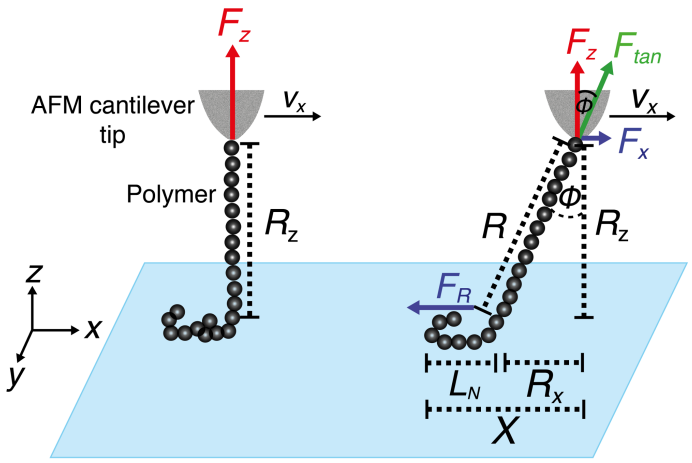

Figure 2.9: Scheme of lateral pulling. The angle ϕ between a tangent to the polymer and the normal to the substrate increases until the lateral force F_x equals the friction force F_R and the polymer slides. L_N denotes the adsorbed polymer length, v_x the lateral pulling velocity, R_z the fixed z-extension between AFM cantilever tip and substrate and F_{tan} the force acting along the polymer backbone.

free energy E:

$$\frac{F_x^{ads}}{k_BT} = -\left(\frac{\partial E}{\partial X}\right)_{R_z} = \frac{\omega}{2}\frac{L^2 + X^2 - 2LX - R_z^2}{(L-X)^2} = \omega\frac{R_x}{R_x - R} \tag{2.40}$$

Assuming F_R to balance F_x^{ads}, the following differential equation is obtained by rescaling all lengths with the total contour length L, the characteristic time scale $\tilde{t} = \frac{t}{L^3\mu}$, the adsorption energy $\tilde{\omega} = \omega L$ and the lateral cantilever velocity $\tilde{v}_x = v_x\mu L^2$:

$$\dot{\tilde{X}} = \tilde{\omega}\frac{1 + \tilde{X}^2 - 2\tilde{X} - \tilde{R}_z^2}{\left(1-\tilde{X}\right)\left(1-\tilde{X}^2-\tilde{R}_z^2\right)} + \tilde{v}_x \tag{2.41}$$

The vertical force F_z detected by the cantilever is given by:

$$\frac{F_z}{k_BT} = \left(\frac{\partial E}{\partial R_z}\right)_X = \omega\frac{\tilde{R}_z}{1-\tilde{X}} = \omega\frac{R_z}{R - R_x} = -\frac{R_z}{R_x}\frac{F_x}{k_BT} \tag{2.42}$$

Once a stationary state for horizontal pulling is reached, the geometry can be determined due to $\dot{\tilde{X}} = 0$. Thus, for a given R_z, the geometry of the adsorbed polymer and the force acting on the cantilever tip lead to:

$$F_R = F_x = \frac{R_x}{R_z}F_z \tag{2.43}$$

The polymer angle ϕ results from:

$$tan(\phi) = \frac{R_x}{R_z} \tag{2.44}$$

The F_z behavior with lateral extension x and tangential force F_{tan} acting along the polymer backbone can be given by:

$$F_z = F_{tan}\cos\left(\arctan\left(\frac{R_x}{R_z}\right)\right) \tag{2.45}$$

Chapter 3

Materials and Methods

3.1 Atomic Force Microscope

The AFM, developed by Binnig, Quate and Gerber [198], has opened new perspectives for the investigation of surfaces at high lateral and vertical resolution (Figure 3.1). The AFM consists of a cantilever with a sharp tip of about 10-30 nm tip radius at its free end. Cantilevers mostly consist of silicon (Si) or Si_3N_4 and are produced by photolithography and wet etching techniques [199].
The cantilever is moved along all three axes and positioned with nm accuracy relative to a sample surface with a piezoelectric actuator. The AFM can be used to contact a substrate surface and to exert a force on it. The most common way to detect the cantilever deflection is through the optical lever principle by means of a monochromatic light source and a position sensitive photodiode [200]. The light reflection is usually enhanced by Au or Ar as cantilever backside coating. As the diode is divided into four sectors, the respective combination of acquired voltage signals from each of the sectors can be used to determine the cantilever deflection in normal as well as in lateral direction. Finally, a feedback system consisting of a hardware- and software-based control unit is needed.
For soft cantilevers, the experimental noise is dominated by the thermal motion of the sensor rather than by detector noise. Then, the force resolution is limited by the thermal noise at temperature T as given by the Nyquist relation:

$$F_{min} = \sqrt{4k_B TRB} \tag{3.1}$$

with frequency bandwidth B and damping coefficient R. The force resolution can be increased by lowering R or by using smaller cantilevers [201].
All atomic force microscope (AFM) measurements are performed with a MFP3D-SA (Asylum Research, USA), using a closed fluid cell at room temperature. For temperature dependent measurements the Bioheater closed fluid cell is used in a temperature range of 25-65 °C. Each fluid cell is filled with a solution volume of 3-4 ml. After mounting the fluid cell an equilibration time of 20-30 minutes is used. The sampling rate is set to 5 kHz.

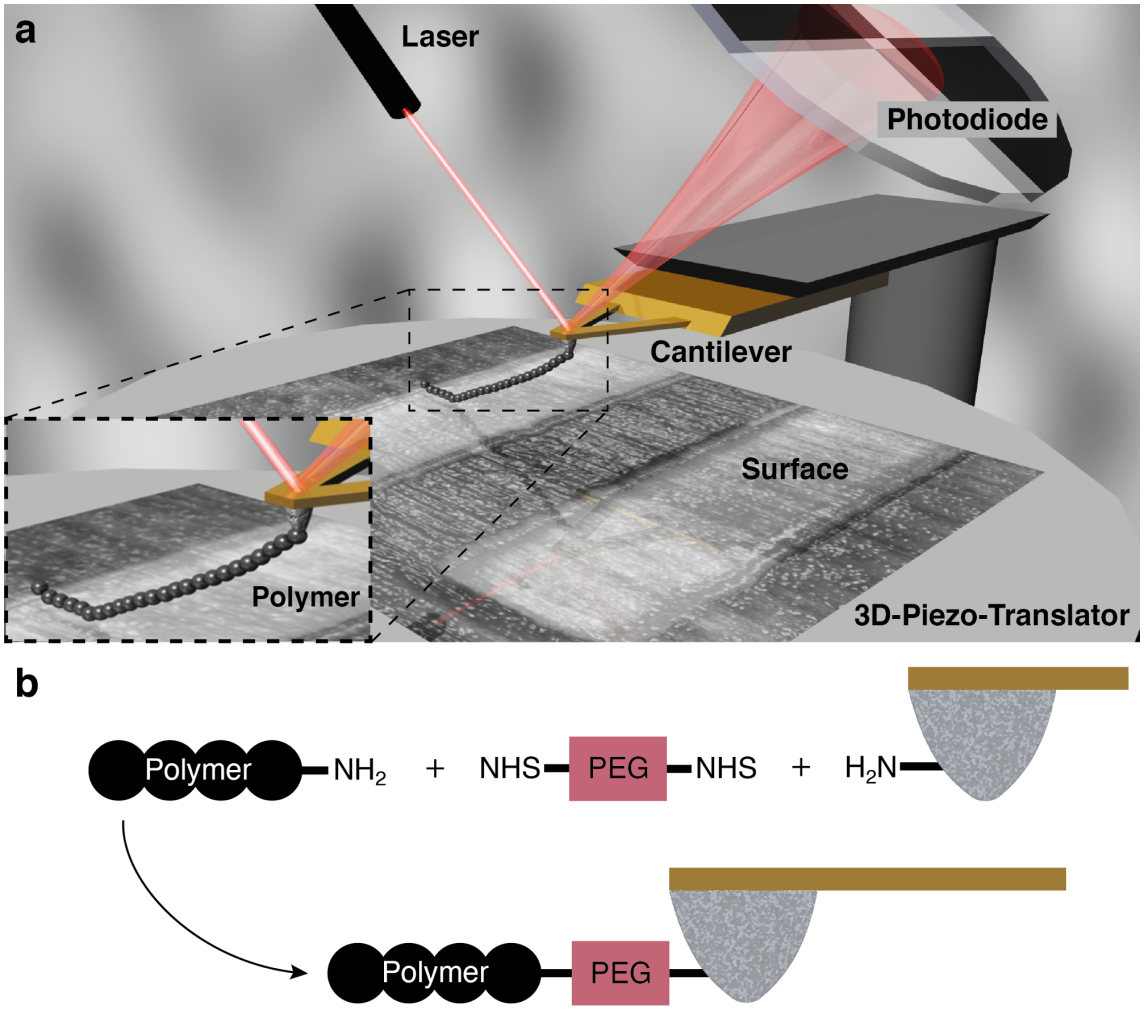

Figure 3.1: AFM setup. (a) Scheme of a SMFS setup with a cantilever deflection system using the light lever principle. (b) In order to couple covalently a single polymer to an AFM cantilever tip the Si_3N_4 substrate is modified with a linker system. For details see Appendix A.2. Adapted from [202].

3.1.1 Single Molecule Force Sensor

Charged Homopolymers

Poly-L-(glutamic acid) sodium salt (PGA, 50-100 kDa), poly-L-lysine hydrobromide (PLL, 150-300 kDa) and poly(allylamine) (PAAm, 20 wt. % in H_2O, 65 kDa) are purchased from Sigma Aldrich.

Polystyrene-Based Polymers

Besides poly (amino acids), polymers synthesized by living anionic polymerization are used, fulfilling several demands. These include a high contour length and a narrow mass distribution to provide a clear fingerprint. Furthermore, a specific binding site for successful covalent attachment to the AFM cantilever tip is needed. These polymers are summarized in Figure 3.2.

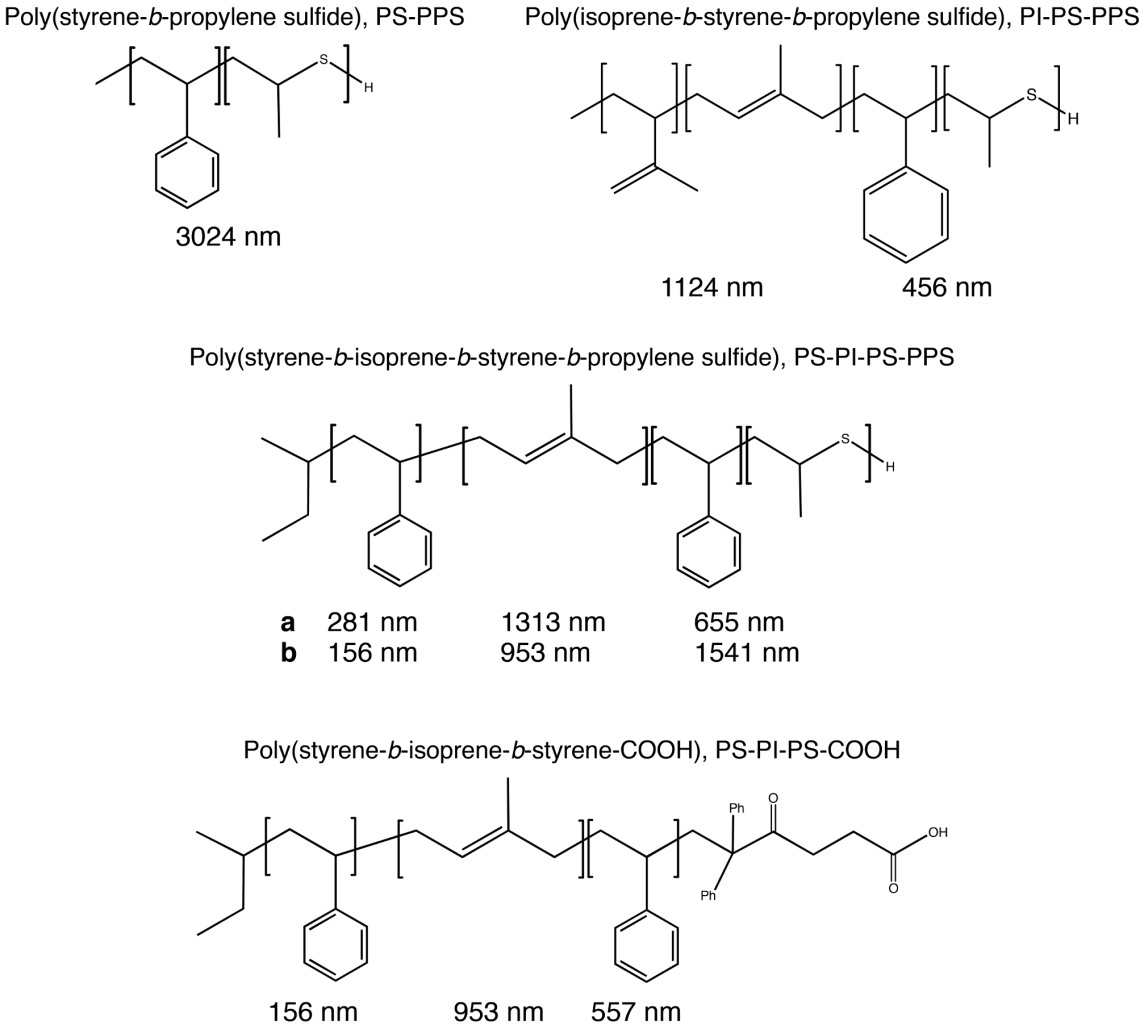

Figure 3.2: Overview of PS-based polymers. Structures and contour lengths of the polymer blocks based on monomer length values of 0.25 nm for styrene and 0.43 nm for isoprene (considering the high amount of 1,4-structure) [8]. These polymers are presented with the kind permission of Markus Gallei. Most of them are published in ref. [203]. The synthesis is given in Appendix A.1.

Molecular Force Sensors

The preparation of AFM tips and the attachment of single polymers as molecular sensors are performed with Si_3N_4 cantilevers (MLCT from Bruker AXS, USA).
Covalent attachment to the AFM tip via flexible linkers makes long measurements (several hours) possible with one and the same polymer on different substrates. The method used is capable of overcoming former limitations by means of a long, flexible PEG linker.
The functionalization quality is controlled before and after SMFS experiments. Solid substrates, such as PTFE, are used for that purpose. A good functionalization is expected to show a clear single polymer event (plateau of constant force) and a narrow detachment length distribution. The detailed protocol, described in Appendix A.2, is generally applicable to any biopolymer or a synthetic polymer with a respective attachment site, such as an amino, sulfhydryl or carboxyl group. The chemistry of various reactive groups is summarized in refs. [204, 205].

3.1.2 Substrates

Desorption and friction measurements are performed on solid substrates with different wettability and roughness. These comprise mica, hydrogen-terminated diamond (HD), self-assembled monolayer of CH_3-terminated alkanthiols on Au (CH_3-SAM) and poly(tetrafluorethylene) (PTFE). Structured surfaces, fabricated by electron beam lithography, such as structured gallium arsenide (GaAs) and oxygen/hydrogen-terminated diamond (OHD), are in particular designed for single polymer friction experiments.
Thin polymer films with different hydrophobicity and architecture are provided by polyelectrolyte multilayers (PEMs), spin coated polystyrene films (scPSs) and covalently surface-attached polystyrene films (saPSs). The detailed synthesis is given in Appendix B.

3.1.3 AFM Calibration

B, C and D cantilevers of MLCT (Bruder AXS, USA) are appropriate for force spectroscopy due to their low force constants of about 10-50 $mN \cdot m^{-1}$, leading to high force resolution. Force-extension traces are obtained from the deflection-piezopath signal [68, 69].
The MFP3D-SA uses the light lever principle to detect the cantilever deflection. Therefore, a focussed laser beam is reflected from the backside coating of a cantilever onto a segmented photodiode. The cantilever deflection is given by the signal change of the upper vs. lower segments of the photodiode. In order to convert the voltage signal of the photodiode to a deflection signal, the optical lever sensitivity (OLS) has to be obtained by recording the photodiode signal vs. driven piezo distance upon indentation of the cantilever into a solid substrate (Figure 3.3 a). The OLS is best determined symmetrically around the zero point of detection (Figure 3.3 b). The OLS determination should be performed very carefully, taking an average of at least 5 values at the beginning and the end of any experiment to minimize errors. Then, the photodiode voltage is converted into a cantilever deflection (Figure 3.3 c). The force is taken from the absolute deflection of the cantilever by means of the cantilever spring constant (Figure 3.3 d). In order to get the real z-extension, the

cantilever deflection amplitude has to be subtracted from the distance driven by the piezo. This distance is assigned by a linear variable differential transformer (LVDT) (Figure 3.3 e).

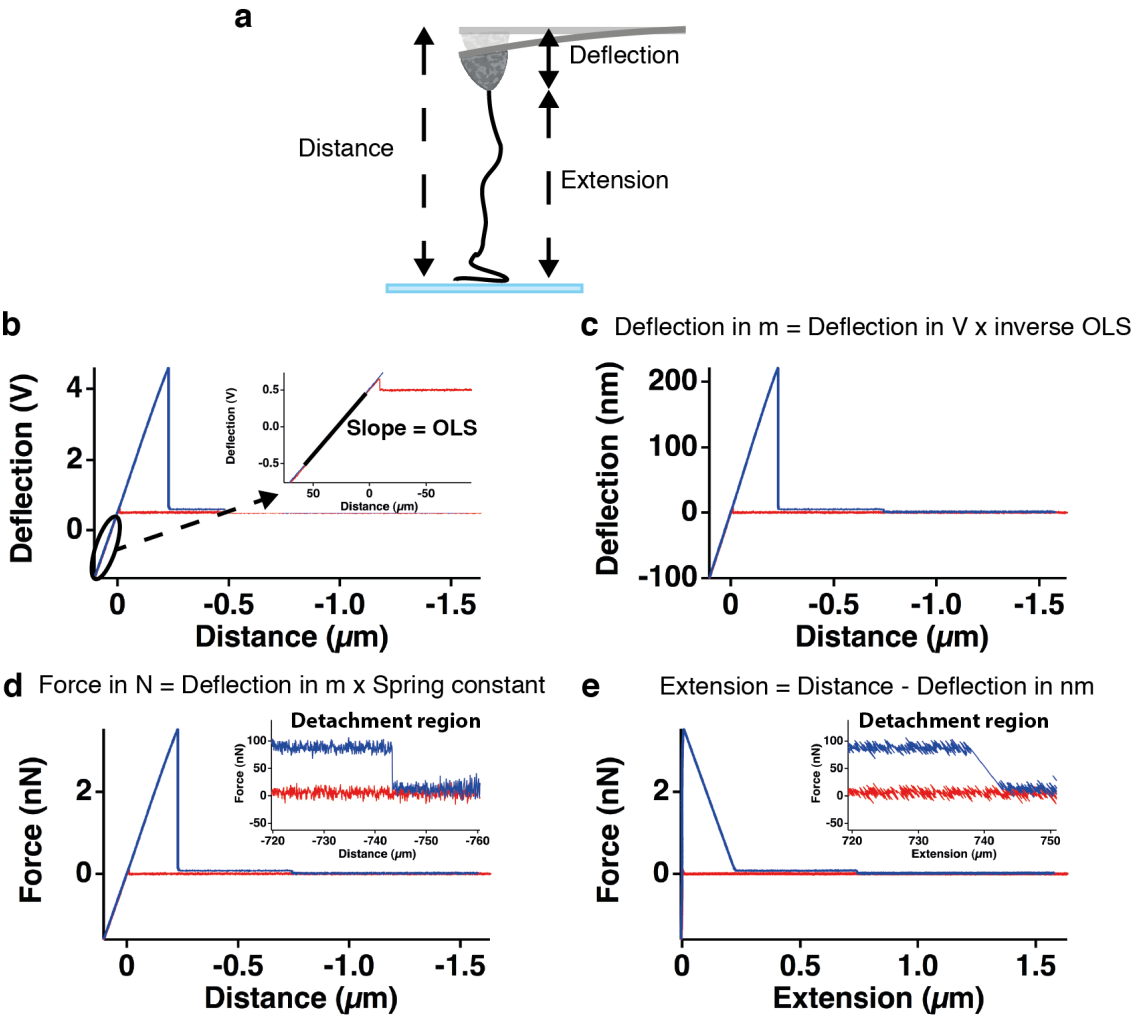

Figure 3.3: Acquisition of force-extension traces by AFM. (a) Scheme of the desorption experiment. (b) Deflection voltage signal vs. piezo distance. The inset shows the OLS determination. (c) The photodiode voltage is converted into a cantilever deflection using the inverse OLS (invOLS). (d) The force is obtained from the absolute deflection of the cantilever by means of the cantilever spring constant. (e) In order to get the real z-extension, the cantilever deflection amplitude has to be subtracted from the z-distance driven by the piezo. Adapted from [69].

Discussion and overview of calibration methods for cantilever spring constants are given in refs. [206, 207]. The most common ways to determine the cantilever spring constant are: the Cleveland method [208, 209], the Sader method [210, 209] and the thermal noise method [211, 212, 209]. In all experiments presented, the method of Pirzer et al. [213], based on the thermal noise method, is used for the spring constant calibration. Evaluation is done with the program Igor Pro (Wavemetrics). Several micrometers above the substrate the power spectral density (PSD) of the cantilever is taken. Using a fluid medium, the impact of its viscosity on the damping of the oscillatory motion of the cantilever has been reported by Bergaud et al. [214]. The effect of highly viscous mediums has been analyzed by Pirzer et al. [213]. The most widely used fit function for the PSD is a simple harmonic oscillator (SHO)

function with damping:

$$S_{SHO}(\omega) = A_{white}^2 + \frac{A^2\omega_R^4}{Q^2}\left[(\omega^2 - \omega_R^2)^2 + \frac{\omega^2\omega_R^2}{Q^2}\right]^{-1} \tag{3.2}$$

with ω as the frequency, ω_R the resonance frequency, Q the quality factor, A the amplitude noise at ω_R and A_{white} the amplitude background noise, which is approximated as white noise. Another very common function used to fit the PSD is the standard Lorentzian (sLor):

$$S_{sLor}(\omega) = A_{white}^2 + \frac{C_1}{(\omega - \omega_R)^2 + C_2} \tag{3.3}$$

with fitting parameters C_1 and C_2. The standard Lorentzian stems from a driven harmonic oscillator in a harmonic potential without damping. Taking $C_1 = \frac{A^2\omega_R^2}{4Q^2}$ and $C_2 = \frac{\omega_R^2}{4Q^2}$ this leads to a model such as used by Pirzer et al. [213] and describes well the PSD at low Q values:

$$S_{Lor}(\omega) = A_{white}^2 + \frac{A^2\omega_R^2}{4Q^2}\left[(\omega - \omega_R)^2 + \frac{\omega_R^2}{4Q^2}\right]^{-1}. \tag{3.4}$$

fitting Equation 3.4 to the thermal noise spectrum also gives the resonant frequency ω_R and quality factor Q. Equation 3.4 is found to describe the thermal noise spectrum better at low Q in comparison to Equation 3.2 [213]. The PSD is fit with Equation 3.4 from the lowest frequency possible to the minimum between the first and the second resonance peak. The given fitting parameters are then used to integrate the PSD analytically or numerically using Parseval's theorem [215]. Hence, the mean square displacement $\langle \Delta z^2(t) \rangle$ of the free end of the cantilever is gained.
The equipartition theorem states that in thermal equilibrium any degree of freedom (such as a component of the position or the velocity of a particle), which appears only quadratically in the energy, has an average energy of $\frac{1}{2}\ k_B T$. In case of the cantilever:

$$\frac{1}{2}k\langle \Delta z^2(t) \rangle = \frac{1}{2}k_B T \tag{3.5}$$

and

$$k = \chi\frac{k_B T}{\langle \Delta z^2(t) \rangle} \tag{3.6}$$

are used to determine the cantilever spring constant, denoted as k [211]. χ is a correction factor, taking the cantilever shape and the position and size of the laser spot into account [216, 217, 206, 218, 219].
Generally, an AFM cantilever has both a normal and lateral force constant. While the first results from deflection in normal direction, the latter follows from torsional deflection due to a torque exerted on the cantilever tip. Both force constants can be determined using either the Cleveland or the Sader method.
The lateral force constant $k_{lateral}$ for beam shaped cantilevers is given by [220]:

$$k_{lateral} = \frac{2L^2}{3(1+\nu)h^2}k_z \tag{3.7}$$

with the cantilever length L, the cantilever tip height h, the Poisson ratio ν (0.25 for Si_3N_4) and the normal force constant k_z. For the B cantilever of MLCT (Bruder AXS, USA) of with L = 210 μm, h = 2.5-8.0 μm and k_z = 30-40 pN·nm^{-1} the lateral force constant ranges to about $k_{lateral}$ = 30 nN·nm^{-1}. Thus, single polymer friction with forces of up to 100 pN cannot induce detectable lateral cantilever deflection. Triangular cantilevers tend to be even stiffer. The respective geometrical description can be found in refs. [221, 222]. Hence, the normal cantilever deflection is used for single polymer desorption and friction measurements throughout this thesis.
Within the velocity range of the presented experiments (1 nm·s^{-1}- 10 μm·s^{-1} in lateral and normal direction) the hydrodynamic drag on cantilever, scaling linearly with the pulling velocity, is rather small, in particular for lateral pulling experiments. A detailed discussion in given in refs. [223, 224, 225].

3.1.4 Evaluation of Desorption Plateaus

For desorption plateau evaluation at least 100 F_z-z curves at different positions on the sample are taken for each mean desorption force $F_{plateau}$ and detachment length z_{det}. Each plateau of constant force corresponds to the desorption process of a single polymer. The detachment process at the plateau end shows a finite detachment slope, which represents the cantilever spring constant, once the cantilever has a finite stiffness [172]. Evaluation is done with the program Igor Pro (Wavemetrics) and self programmed procedures. The desorption force and the detachment length for each F_z-z curve are determined from a sigmoidal function fitted to the plateau end (Figure 3.4 a). In case of multiplateaus, multiple polymers are desorbed, starting with the shortest and ending with the longest [191]. The longest plateau indicating the desorption of the last polymer is taken for evaluation (Figure 3.4 b). Force values of double plateaus (Figure 3.4 c) are not taken into account, as they might shift the force distribution and lead to wrong conclusions.
All the force and length values obtained from these plateaus are plotted in a histogram respectively. Finally, the average histogram values give $F_{plateau}$ and z_{det}, used throughout the thesis. Absolute plateau force values are subject to uncertainty in cantilever spring constant calibration. Therefore, the absolute force error ranges around 10 %, while the relative uncertainties are about 2 %, when one and the same cantilever is used, as argued by Pirzer et al. [189]. The detachment length error corresponds to the standard deviation.

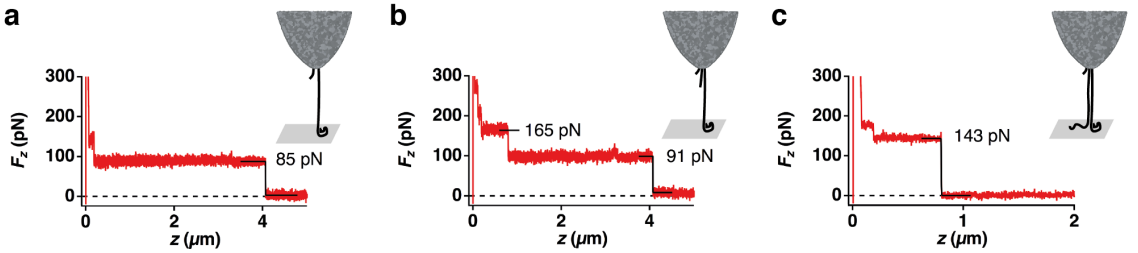

Figure 3.4: Evaluation of plateau desorption curves. (a) Desorption plateau evaluation: a sigmoidal function is fitted to the plateau of constant force. (b) Each plateau represents a single polymer desorption event. In order to gain well defined statistics for plateau desorption force and detachment length the last plateau should be evaluated only. (c) An event with possibly two polymers desorbing at the same time. The examples shown are taken with PS-PI-PS-PPS b on PTFE in H_2O at a vertical pulling velocity of 1 μm·s^{-1}.

3.1.5 Pulling Protocol for Single Polymer Friction Detection

As shown in Figure 3.5 a, an AFM cantilever tip, functionalized with a single polymer is approached to the substrate. Then, the polymer is allowed to adsorb onto the surface (Figure 3.5 b). While retracting the cantilever tip, the polymer successively desorbs from the surface (Figure 3.5 c). For measuring single polymer friction, the polymer is pulled up to a certain height (z-extension, z).
The cantilever deflection accounts to 0.2-10 nm in the relevant force range of 10-100 pN, which is negligible compared to the R_z- and R_x- extensions of more than 100 nm. Then, the partly adsorbed single polymer is pulled laterally over the substrate (Figure 3.5 d-f), keeping z fixed (creep and drift effects from the z-piezo are of the order of 5 nm·s^{-1}, which is much less than the relevant distances presented here), enabling frictional forces to be investigated. Finally, the polymer is pulled in z-direction until it desorbs completely from the substrate (Figure 3.5 g,h).
The blue and black traces in Figure 3.5 depict the forward and backward lateral motion, respectively. Here, the polymer follows the cantilever tip motion up to a lateral extension x of about 4 μm and back to the starting point. The vertical cantilever deflection is used to monitor the lateral force, because the lateral force constant is more than two orders of magnitude larger than the vertical one [220] (Section 3.1.3). Thus, single polymer friction cannot be detected by the lateral cantilever deflection. Lateral pulling is done perpendicular to the long cantilever axis in order to use symmetric coupling of the force exerted by the polymer on the cantilever for forward and backward lateral motion [226]. The magnitude of the friction force F_R (along the x-direction, equal to F_x) is detected by a change in cantilever deflection in the z-direction (F_z). A detailed description is given in Chapter 4. Prior to friction experiments, desorption data are taken to check the single molecule force sensor quality and to gain force and length distributions (Table 4.1).

3.1.6 AFM Imaging

AFM imaging is done with AC 240 TS cantilevers (Olympus, Japan) with a force constant of about 1.8 N·m^{-1} and a resonance frequency of 70 kHz at a scan rate of 0.5 Hz for intermittent-contact mode. CSC 37 cantilevers (0.3 N·m^{-1}, Micromasch, Estonia) are taken for contact mode imaging and FFM at a scan rate of 1 Hz.

3.1.7 Humidity Dependent AFM Imaging

AC 240 TS cantilevers (1.8 N·m^{-1} and 70 kHz, Olympus, Japan) are used at a scan rate of 0.5 Hz. The samples are mounted on a home-built fluid cell, having a relative humidity (r.h.) sensor, HIH-4000-002 (Honeywell, Germany), for measurements in air. The respective r.h. is achieved by:

- having a reservoir of dimethyl sulfoxide, DMSO (dry, max. 0.005 % H_2O, Merck, Germany), underneath the substrate, reaching a r.h. of 5–10 %
- taking room conditions (20–30 % r.h.)
- saturated NaCl solution in a reservoir underneath polyelectrolyte multilayer (PEM) samples (75–85 % r.h.)

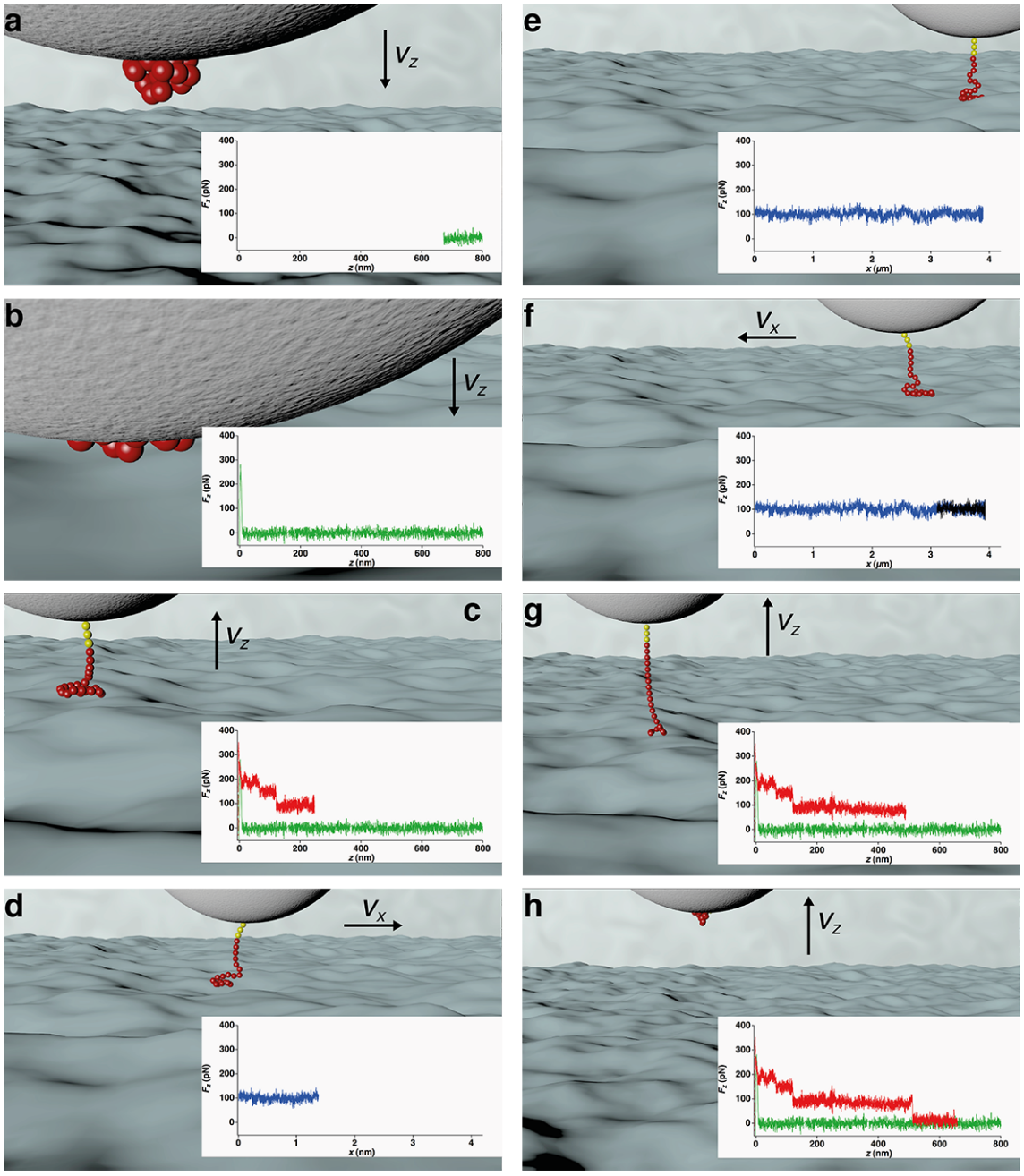

Figure 3.5: Protocol for a combined desorption and friction experiment. PGA on CH_3-SAM in 1 M NaCl. (a) Approach and (b) contact with substrate (dwell time on substrate: 1 s). (c) Desorption from substrate with a velocity of 1 $\mu m \cdot s^{-1}$. The final plateau (single polymer) starts at $z = 120$ nm. At $R_z = 240$ nm the desorption is stopped. (d-f) Then, the single polymer is pulled laterally, keeping the z-height fixed (blue and black part of the trace). (g,h) Finally, the polymer desorbs after retraction of the cantilever in z-direction. The cantilever tip bound polymer is indicated by red blobs, while the linker system is represented by yellow blobs. [Adapted from *Atomic Force Microscopy-based Single Polymer Friction*, animation film by Sylvia Kempe and Lukas Kappeler.]

The data points marked as 100 % r.h. are measured by immersing the sample in ultrapure H_2O (sterile, for HPLC use, Biochrom, Germany). Each time the sample is changed, the medium is given at least 30 minutes (60 minutes for measurements in H_2O) for equilibration.

3.2 Contact Angle Determination

For contact angle measurements, a home-built goniometer equipped with a charge-coupled device (CCD) camera is used. Using the *drop analysis* plugin [227, 228] for the Java-based program ImageJ, the contact-angles of a drop are determined by a polynomial fit to the edge of the droplet. Then, a tangent is fit to this polynomial at the triple points, where surface, liquid and gaseous medium meet, to obtain the enclosed angles (Figure 3.6). Static contact angles of H_2O (using a volume of 1.5 μl) are obtained at room temperature. They are taken at least five times at different positions of the sample. The errors correspond to the standard deviation.

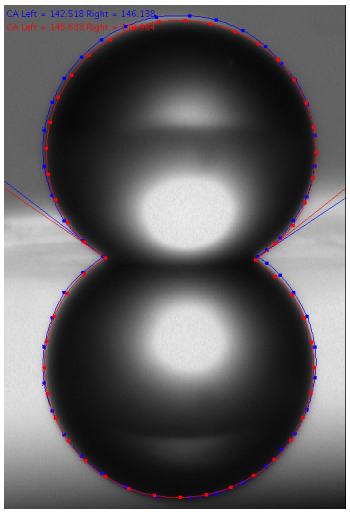

Figure 3.6: Static contact angle measurement. H_2O droplet on a saPS with TCS-DPE initiator (Appendix B.6). Using the Java-based program ImageJ with the plugin *drop analysis*, the contact angles can be determined.

Chapter 4

Single Polymer Friction at the Solid-Liquid Interface

For most technical applications, wear resistant low friction surfaces are desired, in particular for miniaturized moving components having a high surface to volume ratio. Hence, the understanding of the processes underlying nanoscale friction is essential for the construction of optimized nanoscopic components. Experiments directly addressing the friction of polymers at the liquid-solid interface are sparse. Here, this problem is addressed by pulling single polymers covalently bound to an AFM cantilever tip across chemically and topographically structured surfaces in a liquid environment, enabling frictional forces to be investigated. The presented combination of desorption in z-direction and lateral pulling allows to determine the friction behavior with respect to pulling velocity, adhesion force and adsorbed polymer length for a single polymer by decoupling friction [128, 203] and adhesion [68] in an AFM-based experiment (Section 2.4.3 and Section 3.1.5). This approach presents a broader view than experiments measuring the free diffusion of a (labeled) polymer [229] and utilizing the Einstein relation (Equation 2.23). Most parts of this chapter are published in refs. [203, 202].

4.1 Stick-Slip on Hydrophobic Substrates

The various force components and the polymer geometry for the laterally pulled single polymer are determined as depicted in Figure 4.1 a. Figure 4.1 b shows lateral pulling (F_z-x) for PGA, across a hydrophobic self-assembled monolayer of CH_3-terminated alkanthiols on Au (CH_3-SAM) in ultrapure H_2O with a velocity of $v_x = 0.42\ \mu\text{m}\cdot\text{s}^{-1}$ and a fixed z-extension of $R_z = 240$ nm. This demonstrates directly nanoscale stick-slip. First, the F_z-x plot exhibits a plateau of constant force. The polymer slides across the surface with undetectable F_x and therefore friction force F_R, until it reaches a point at about $x = 0.4\ \mu$m, where it sticks to the substrate and R_x becomes non-zero. During the following decrease in F_z, starting at 0.4 μm until 0.7 μm, the lateral force F_x increases (Figure 4.1 b, bottom). The static friction coefficient is high enough to favor desorption over sliding and is consequently called desorption stick (DS). While the polymer does not move laterally, it leaves the surface continuously with very low internal friction. This contrasts experiments with proteins, where a compact folded structure corresponds to high internal friction [230, 231, 16]. While F_z decreases, the polymer angle ϕ increases until the force

component F_x counterbalances F_R and the polymer starts to slide again. For simplicity the initial anchor point of the PGA molecule, which has a radius of gyration of about 4 nm (Table 4.1 and Appendix C.2) is assumed to lie perpendicularly under the AFM tip. Lateron, the initial polymer angle is estimated (Section 4.3).

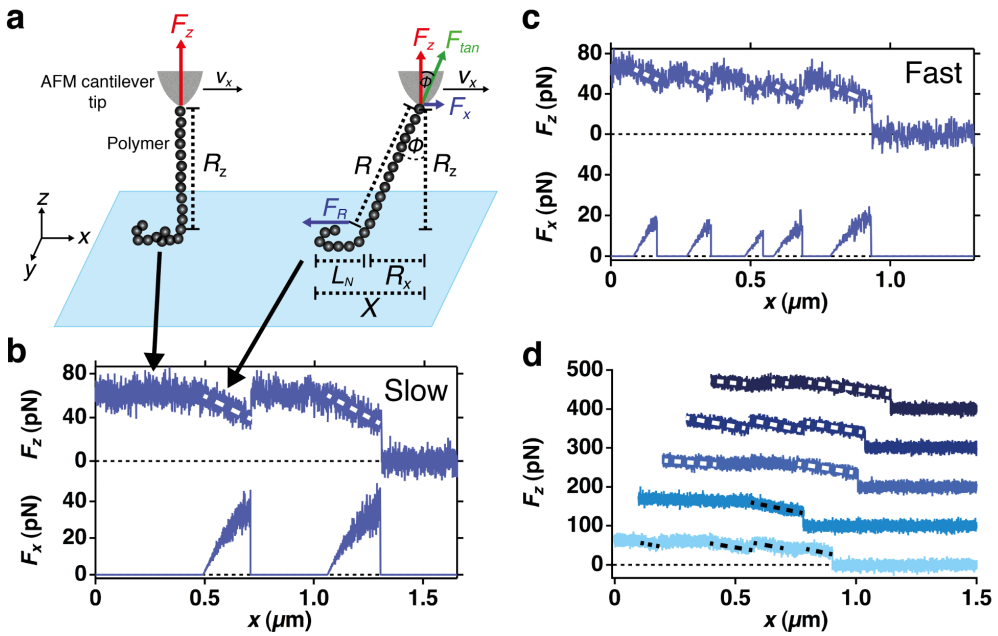

Figure 4.1: Single polymer stick-slip. (a) Schematics of the AFM experiment to monitor single polymer stick-slip friction. Upon stick the angle ϕ between a tangent to the polymer and the normal to the substrate and R_x increase, until the lateral force F_x equals the friction force F_R and the polymer slides. The F_x values are calculated from F_z using Equation 2.43. For slip events F_x is set to 0. (b) Vertical force F_z and lateral force F_x vs. lateral extension x for PGA on a CH_3-SAM in H_2O with $v_x = 0.42$ μm·s^{-1}. The slopes in the top part (dashed white lines) and the peaks in the bottom part show the sticking events. (c) F_z-x curve with ten times higher velocity compared to (b) demonstrating increasing spatial frequency and lower amplitude stick-slip, reminiscent of macroscopic stick-slip. (d) Consecutive F_z-x curves along the same line with a lateral velocity of 0.43 μm·s^{-1} (curves are vertically offset by 100 pN). As the piezo has to be operated in open loop, a shift in x-direction of around 50 nm in between two successive traces occurs. Therefore, each curve is laterally offset for another 50 nm in x-direction. There is no repeated pattern, each of the traces reveals a different stick-slip pattern, therefore the substrate pattern is not reflected by the stick-slip pattern. Dashed white and black lines indicate DS events. Adapted from [203].

The forces can easily be detected, if they exceed half of the noise, which results to a value of 10 pN. Assuming $R_x = 10$ nm and $R_z = 1$ μm, a value of 0.1 pN for F_R is obtained using Equation 2.43. An overview of the respective values is given in Table 4.1. At $x = 0.7$ μm F_z jumps back to its initial value, i.e. the polymer relaxes to a conformation with similar friction to the original one. This scenario is repeated in a periodic manner (here twice) until the polymer detaches from the surface (at around 1.3 μm).

A 10 times higher lateral pulling velocity (Figure 4.1 c) results in a higher frequency but lower amplitude (F_x) of the stick-slip motion. Such a behavior is a characteristic feature of stick-slip motion of two (macroscopic) solid bodies in contact [114] (Section 2.3.3). In the first example (Figure 4.1 b,c) F_R is about 43 pN for 0.42 μm·s^{-1} and 19 pN for 4.20 μm·s^{-1}, already rendering the Rouse model (Section 2.1.8) inappropriate.

Another important insight into DS-slip events is obtained from PGA on CH_3-SAM in H_2O. First, the spatial DS-slip frequency increases with velocity, although DS itself is not a velocity dependent process. Second, the amplitude of the friction force

decreases with velocity. Both observations are a characteristic feature of stick-slip motion of two (macroscopic) solid bodies in contact. Up to a critical pulling velocity the amplitude decreases, while the frequency increases. Above this critical velocity pure sliding is discovered (Figure 2.3.3). In these macroscopic experiments an inhomogeneous surface is required, which is either chemically or topographically structured (e.g. a violin bow or an earthquake vault).
On the single molecule level the DS-slip transition is explained as follows. Here, the polymer slides on the surface, until a two dimensional confinement occurs. Then, the polymer desorbs into solution, until the force component F_x of the desorbing polymer equals the friction force F_R for the adsorbed polymer part at a certain extension x. The spatial stick-slip frequency of PGA on CH_3-SAM does not resemble the CH_3-SAM structure, because the CH_3-SAM has a fixed (inhomogeneous) chemical and topographical structure. Different stick-slip patterns are observed for consecutive traces with one and the same polymer on the same surface along the same line (Figure 4.1 d). Therefore, it can be excluded that the periodicity of stick-slip directly reflects the surface pattern, consistent with macroscopic stick-slip. A significant difference compared to the macroscopic explanation for stick-slip is the origin of DS-slip. The common view for macroscopic bodies is that surface defects and asperities lead to interlock and cause stick [5].

4.2 Influence of Surface Topography on Stick-Slip

Next, the role of surface topography in single polymer friction is probed. To that aim, a triblock copolymer consisting of polystyrene (PS) and polyisoprene (PI), poly(styrene-*b*-isoprene-*b*-styrene)-COOH (PS-PI-PS-COOH, Appendix A.1), is investigated on GaAs in H_2O. The GaAs surface has lateral periodic structures of 120-150 nm width and a depth of about 50 nm. GaAs shows a root-mean square (RMS) roughness (1.2 nm), which is clearly under the dimensions of structured items. Measurements are performed by using the optical image of the AFM setup to align the cantilever over the writefield (WF) region (Figure 4.2 a). Figure 4.2 b indicates the WF design and an AFM image of the indicated WF, having a height of 50 nm. Friction curves for PS-PI-PS-COOH in H_2O illustrate DS, followed by a slip event, once F_x counterbalances F_R. No difference between the structured GaAs areas (Figure 4.2 c) and the unstructured areas (Figure 4.2 d) can be monitored. In particular the slope in the F_z-x graph as well as the height of the final plateau F_z are similar (25-30 pN, Table 4.1).
The data on CH_3-SAM, GaAs, PTFE, diamond and mica (see below) show that the friction force does not depend on the roughness (Table 4.2). So, the friction behavior depends only marginally on surface topography and surface defects. Interlock and asperities (such as spanning over asperities) are unlikely as significant cause for single polymer friction, which contrasts with the common view for macroscopic bodies [5].

4.3 Influence of Solvent on Stick-Slip

The direct solvent related polymer friction is below the detection limit and hence neglected, but the solvent might affect the substrate-polymer friction. PS-PI-PS-COOH

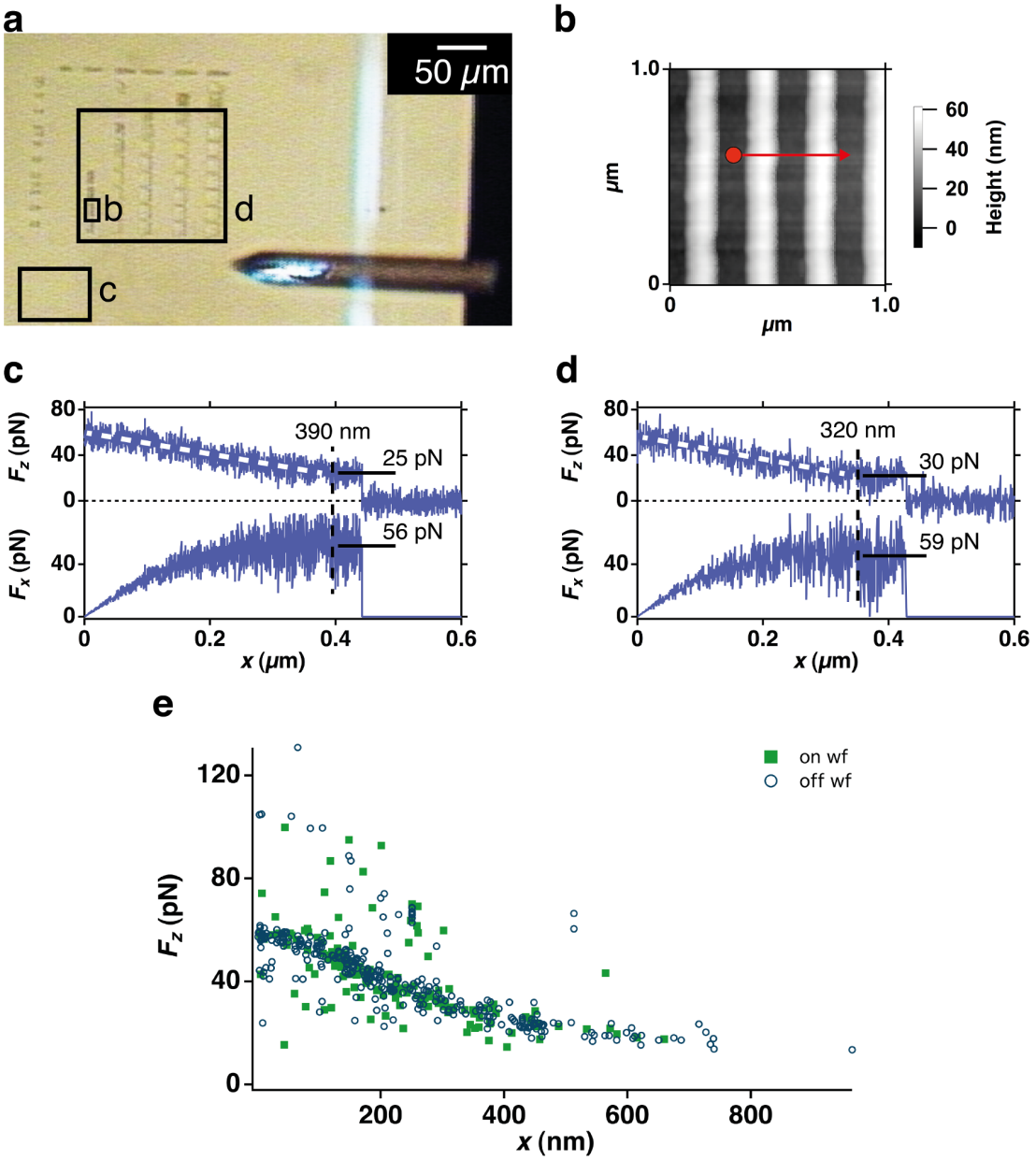

Figure 4.2: Surface topography effect on stick-slip. (a) Optical image of patterned GaAs in the AFM experimental setup. (b) AFM image of patterned GaAs to investigate the effect of surface topography. Lateral pulling is performed along the red line with arrow. (c) Typical F_z- and F_x-x curve of a PS-based polymer across topographically patterned GaAs in H_2O. Dashed white lines indicate the DS event, while dashed black lines indicate the transition from DS to slip. (d) F_z-x traces next to the pattern show the same behavior. (e) Distributions of the point, where the polymer detaches from the substrate - every point represents a F_z-x curve. The curves are all taken at a R_z value of about 160 nm and with v_x varying from 0.03 μm·s^{-1}- 4.17 μm·s^{-1}. Irrespective of the friction experiment location (on or off the WF patterns), each curve reveals decreasing F_z with increasing lateral extension x. Higher forces (up to 120 pN) result from pulling of two or three polymers bound to the cantilever tip in parallel. Here, F_z drops to 0, which means that these polymers detach at the same time. Adapted from [203].

and poly(styrene-*b*-propylene sulfide), PS-PPS, is pulled across the above discussed substrates in good and poor solvent (Section 2.1.3).
Figure 4.3 a shows a DS trace for PS-PPS on PTFE in the poor solvent H_2O, also known as a non-solvent, while in Figure 4.3 b DS is followed by a slip event for the same system. The decrease of F_z with increasing x is shallower than in the previous cases (Figures 4.1 and 4.2), because the polymer detachment length z_{det} is much higher (Table 4.1) and therefore the angle ϕ is changing more slowly. PS-PPS cannot form hydrogen bonds (HBs), but nevertheless a DS behavior is observed.
For PS-PPS on PTFE in H_2O the polymer angle between polymer and normal to the substrate changes with lateral extension up to a point of about 2592 nm, where it remains constant (Figure 4.3 b). Now the geometrical configuration remains constant leading to a steady state sliding. Thus, the polymer angle ϕ can be calculated from $R_x = 2592$ nm and $R_z = 2679$ nm (assumed to be constant during whole lateral pulling event) by Equation 2.44 to be 44.1° and $R = 3728$ nm. The maximum desorption length is $L = 3841$ nm. A detailed overview is given in Table 4.1.
In the discussion of DS it is assumed that the anchor point lies below the cantilever tip and the polymer chain is perpendicularly aligned. Misalignments in vertical and lateral direction might occur, but are much smaller than those discussed in refs. [226, 232, 233]. Nevertheless, two arguments should sustain the rather heuristic assumptions made. Indeed, a misalignment of e.g. $\phi_0 = 1°$ can easily happen. With F_{tan} typically less than 100 pN and according to Equation 2.45, the change in F_z is less than 0.01 pN for an angle of $\phi_0 = 1°$ and therefore undetectable with the presented method. For significant changes in F_z the angle ϕ_0 would have to be more than 10°. A second argument is given by the fit curves shown in Figure 4.3 a,b. Here, a slightly modified version of the Equation 2.45 is used:

$$F_z = F_{tan} \cos\left(\arctan\left(\frac{R_x}{R_z}\right) + \phi_0\right) \tag{4.1}$$

These fits give a value for ϕ_0 of about 6°, which is much smaller than the values obtained for the DS mechanism, ranging up to almost 70° (Table 4.1).
Figure 4.3 c presents PS-PI-PS-COOH on H-terminated diamond (HD) in H_2O with $z = 525$ nm. The adsorbed polymer length is 666 nm (maximum desorption length: 1191 nm). No detachment occurs within about 500 nm of lateral pulling. Still, the corresponding time trace of F_z shows a negative slope on the forward (blue) and positive slope on the backward (black) lateral trace. This indicates that the polymer angle increases up to the point, where the lateral motion is stopped (Figure 4.3 d). Further changes in the polymer angle are not observed during a dwell time of 1 s (grey). On the backward trace, the F_z value increases reaching approximately the initial value.
How does the friction force of the DS behavior, determined by Equation 2.43, depend on velocity and polymer length? Figure 4.3 e,f represents the friction force F_R vs. velocity v_x and adsorbed polymer length L_N or PS-PI-PS-COOH on HD. Surprisingly, the friction force does not significantly depend on the velocity v_x nor on the adsorbed polymer length L_N, rendering the Rouse model with $F_R \propto N$ [19, 128, 125], sub-linear $F_R \propto N^{\frac{3}{4}}$ [234] or super-linear scaling $F_R \propto N^{\frac{3}{2}}$ [235, 78, 125] with N as the number of monomers, inappropriate for DS. This independence on pulling velocity places the measurement range in the boundary friction regime (Section 2.3.2) [103, 8].

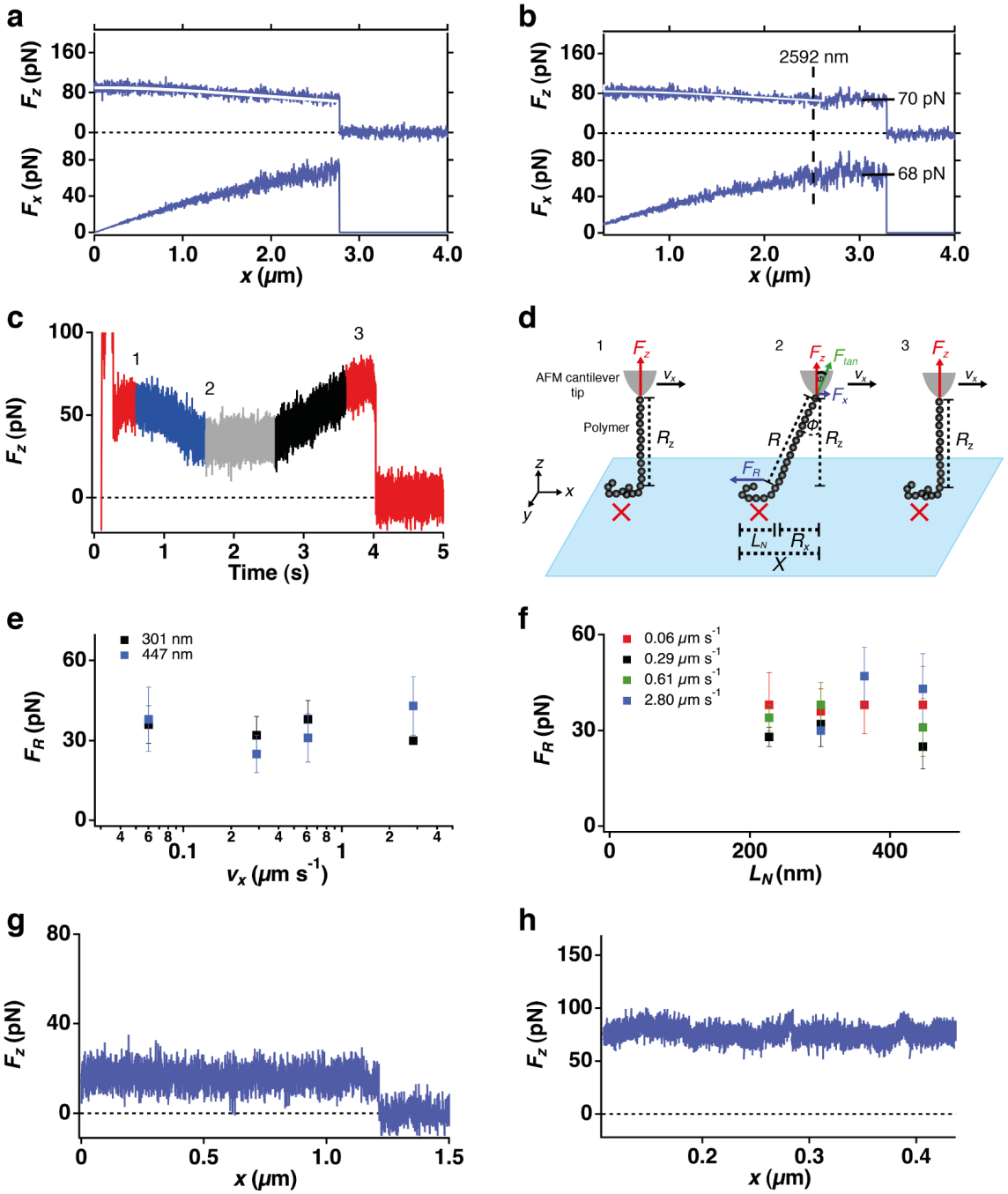

Figure 4.3: Solvent effect on stick-slip. (a) Typical F_z- and F_x-x plots for PS-PPS on PTFE in H_2O with $v_x = 1.05$ μm·s^{-1} showing DS during lateral pulling until detachment at around 2.8 μm lateral extension. The white line indicates a fit to F_z with Equation 4.1. (b) Typical F_z- and F_x-x curves for PS-PPS on PTFE in H_2O with a DS event followed by slip, where F_x balances F_R at around 2.6 μm. The dashed black line indicates the transition from DS to slip. The white line indicates a fit to F_z with Equation 4.1. (c) F_z -time for PS-PI-PS-COOH on HD in H_2O ($z = 525$ nm, $v_x = 0.52$ μm·s^{-1}) showing a decrease of F_z on forward (blue) lateral pulling motion and F_z increase to the initial value after the end of the backward (black) lateral movement ($x = 0.51$ μm). During the dwell time of 1 s F_z remains constant (grey). Further dwell times up to 60 s attest the same behavior. This confirms the DS model. (d) Scheme of the DS event given in (c). Red crosses indicate the fixed position of the polymer globule during lateral pulling. (e) Dependence of friction force F_R on pulling velocity v_x for an adsorbed polymer length of L_N: 301 (black) and 447 (blue) for PS-PI-PS-COOH on HD in H_2O. (f) F_R dependence on adsorbed polymer length L_N for the velocities v_x: 0.06 μm·s^{-1} (red), 0.29 μm·s^{-1} (black), 0.61 μm·s^{-1} (green) and 2.80 μm·s^{-1} (blue) for PS-PI-PS-COOH on HD in H_2O. (g) PS-PI-PS-COOH on PTFE in $CHCl_3$ with $v_x = 0.20$ μm·s^{-1} resulting in slip (undetectable friction force). PS-PI-PS-COOH and PS-PPS show both the same qualitative behavior. Thus, the block structure of the polymer does not seem to be decisive for the frictional behavior. (h) PGA on PTFE in H_2O with $v_x = 0.03$ μm·s^{-1} resembling slip. Adapted from [203].

DS can be explained by a part of the polymer sticking at a constant position with respect to the substrate, but the main body of the polymer continuously desorbing, until it detaches from the substrate. Here, the friction force F_R is higher than the lateral force component F_x and desorption is favored over sliding with negligible internal polymer friction.
HBs can cause DS, but they are not required, as a poor solvent can cause a similar behavior. The solvent causes a DS behavior by lateral confinement for the polymer on the substrate. In order to move the polymer across the surface, a significant amount of solvent has to be displaced simultaneously, resulting in forces of several 10 pN (Table 4.1). Therefore, desorption is favored compared to lateral movement for large parts of the friction experiment.
This interpretation is supported by the measurement of PS-PI-PS-COOH in chloroform, $CHCl_3$, which is a good solvent for PS-based polymers [19, 8]. Here, only negligible friction below the detection limit is observed, enabling immediate sliding and high mobility of the polymer on the PTFE substrate (Figure 4.3 g). This means that the friction forces are at least two orders of magnitude lower than in H_2O, although the viscosity is only reduced by half [236]. Consistently, the same behavior is obtained for PGA on PTFE in H_2O, which is a good solvent for this system (Figure 4.3 h). The data suggest that DS is determined by a combination of solvent and surface chemical properties.

4.4 Stick-Slip Behavior on Hydrophilic Substrates

In order to verify the impact of chemical surface termination in a controlled manner, patterned mono-crystalline diamond is used, fabricated by oxygen (O)- and hydrogen (H)-termination (OHD) by means of electron beam lithography (Figure 4.4 a and Appendix B.8). This pattern is confirmed by FFM (Appendix B.8). The O/H pattern makes it possible to compare friction on hydrophilic and hydrophobic substrate in a single measurement.
In order to position the polymer at a defined spot, a force map is taken prior to every single polymer friction experiment. Figure 4.4 b shows such a force map and indicates the lateral pulling paths of the polymer across the surface for the data depicted in Figure 4.4 c-e. Those exhibit F_z-x curves starting in a H-terminated area and crossing the boundary to the O-terminated part. In the H-terminated section, PGA results in a constant plateau force during lateral pulling, i.e. slip with undetectably low friction force. As soon as the O-termination is reached, the polymer sticks to the substrate.
These traces can be explained by two stick modes: The first, DS, is described above and observed for more than 80 % of the friction plots (e.g. Figure 4.4 c), where F_z decreases linearly until sliding or detachment of the polymer from the substrate occurs. The second comprises cooperative stick (CS). Here, the polymer is stretched up to a point, where the bonds between substrate and polymer break and the polymer detaches (Figure 4.4 d,e). Such traces have been found for vertical pulling before, but not for horizontal pulling. They require the absence of fast internal relaxation of the polymer, as the part of the polymer in between the tip and the substrate is elastically stretched, resembling the well-known WLC increase in force [72, 156, 76, 237, 207, 69] (Section 2.1.7). This appears never on H-terminated diamond and only in about 10 % of the traces on O-terminated di-

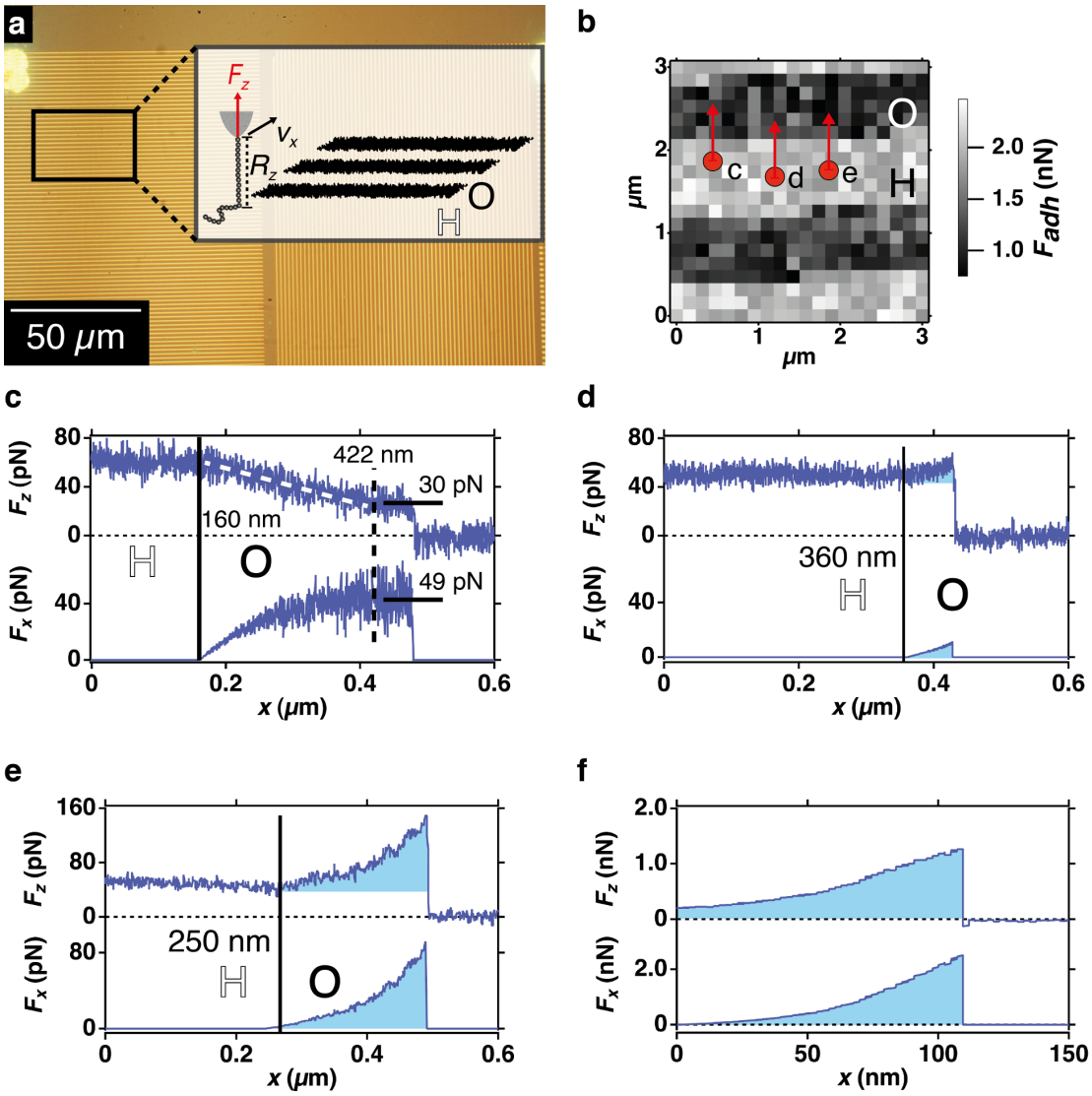

Figure 4.4: Stick-slip on hydrophilic substrates. (a) Optical wide-field image of the e-beam resist pattern used for selective O- and H-termination of the the diamond substrate (OHD). Zoom-in indicates the stripe pattern: 500 nm H/ 500 nm O. Friction curves are taken perpendicular to these stripes. (b) Force map of an OHD surface. The H-terminated region shows higher tip-substrate interaction F_{adh} than the O-terminated. The force maps help to define pathways across the O/H boundary (red lines with arrow). (c) F_z- and F_x-x curve for PGA on OHD in H_2O with R_z = 160 nm, v_x = 0.42 μm·s^{-1} showing DS on O-terminated region. (d) F_z- and F_x-x curve for PGA on OHD in H_2O with R_z = 397 nm with CS on O-terminated region and v_x = 0.36 μm·s^{-1}. (e) F_z- and F_x-x curve for PGA on OHD in H_2O with R_z = 397 nm and v_x = 3.31 μm·s^{-1} with CS on O-terminated region. (f) F_z- and F_x-x curves for PAAm on mica in 5 mM $MgSO_4$ with R_z = 55 nm and v_x = 1.91 μm·s^{-1}. The crossing of the O/H boundary is indicated in the lateral pulling trace by a vertical black line. The CS events are highlighted in light blue. Adapted from [203].

amond. In this case strong directional bonds, in particular HBs, prevent internal relaxation [125, 126, 127].
For strongly adsorbing bodies the following version of Amontons' law (Section 2.3.1), with friction coefficient μ and normal force divided into load F_L and desorption force $F_{plateau}$, applies to single polymer systems as well [8]:

$$F_R = \mu(F_L + F_{plateau}) \tag{4.2}$$

In case of single molecules, the load is negligible leading to a linear dependence on adhesion force. While the adhesion force on these two surface terminations differ less than 10 pN (Table 4.1), the friction force between the H- and O-termination differs by several orders of magnitude. Thus, DS behavior is largely independent of desorption force (i.e. normal force), which contrasts with Amontons' law.

4.5 Cooperative Stick is Dominated by Hydrogen Bonds

HBs can cause DS, but they are not required, as a poor solvent can cause DS as well. On the contrary, CS requires the absence of fast internal relaxation of the polymer. Here, strong directional bonds, in particular HBs, prevent internal relaxation [125, 126, 127]. The breaking and reforming of HBs depends on velocity and can be regarded as an underlying mechanism for CS, as suggested by Serr et al. [125]. Here, the Rouse model can be considered for CS, in contrast to DS.
The energy for bond breakage of PGA on O-terminated diamond can be determined due to the area under the F_x-x curve (Figure 4.4 d-f):
$E_{0.36}$ = 3.12·10^{-19} N·m (Figure 4.4 d) and $E_{3.31}$ = 6.69·10^{-18} N·m (Figure 4.4 e). Assuming an energy of 5 k_BT per HB [125] and having determined that the adsorbed polymer part is at maximum 131 nm (Table 4.1) with a monomer length of 0.37 nm [168], the number of HBs that are broken can be estimated. Thus, 0.04 HBs/monomer (14 HBs/polymer) are obtained for v_x = 0.36 μm·s^{-1} and 0.90 HBs/monomer (323 HBs/polymer) for v_x = 3.31 μm·s^{-1}. The respective monomer friction coefficients determined due to the rupture force in the F_x-x plot and using the Rouse model are $\mu_{0.36}$ = 9.28·10^{-8} kg·s^{-1} and $\mu_{3.31}$ = 7.68·10^{-8} kg·s^{-1}.
For PAAm on mica in 5 mM $MgSO_4$ (Figure 4.4 f, indicated in light blue) a value of E = 8.55·10^{-17} N·m is gained. 13 HBs/monomer are received with a monomer length of 0.25 nm [174]. This exceeds the possible number of HBs by far. The friction coefficient based on the Rouse model results to μ = 1.85·10^{-6} kg·s^{-1}. Thus, the friction coefficient per HB ranges between 10^{-6} to 10^{-8} kg·s^{-1}, which is at least two orders magnitude higher than the friction coefficients discussed in ref. [125].
In Erbas et al. [126, 127] a steady-state friction coefficient is derived from the Fokker-Planck equation in the presence of an external force in a corrugated periodic potential. A cooperativity factor of m = 3, specifying how many HBs are broken collectively, results in a HB friction coefficient of $\mu_{\mathrm{HB}} \approx$ 10^{-8} kg·s^{-1}, while m = 4 leads to $\mu_{\mathrm{HB}} \approx$ 10^{-6} kg·s^{-1}. Thus, a cooperative breakage of HBs is necessary to explain the obtained results. Besides cooperative HB breakage, possible additional contributions might be of electrostatic origin.

Combination	$F_{plateau}$**(pN)**	F_z**(pN)**	F_R**(pN)**	z_{det}**(nm)**	R_z**(nm)**	R_x**(nm)**	R**(nm)**	v_x**(μm·s^{-1})**	ϕ(°)	L_N**(nm)**
PS-PPS/PTFE	96 (±2)	70	68	3662 (±123)	2679	2592	3728	10.15	44	113
PS-PI-PS-COOH/GaAs	60 (±3)	25	56	348 (±189)	175	390	427	2.32	66	135
PS-PI-PS-COOH/GaAs	60 (±3)	30	59	348 (±189)	162	320	359	4.17	63	59
PS-PI-PS-COOH/OHD	61 (±2)	30	41	1074 (±25)	543	746	923	0.80	59	151
PGA/OHD	54 (±3)	30	49	376 (±128)	160	262	307	0.42	54	69
PGA/CH_3-SAM	65 (±2)	40	43	443 (±13)	240	260	354	0.42	47	89
PGA/CH_3-SAM	65 (±2)	55	19	443 (±13)	240	82	254	4.20	19	189

Table 4.1: Quantitative overview of DS experiments. Overview of the friction parameters of different polymer and substrate combinations measured in H_2O revealing DS combined with slip. $F_{plateau}$ and z_{det} result from desorption force by SMFS without lateral pulling (dwell time: 1 s and vertical pulling velocity: 1 μm·s^{-1}, more than 100 F_z-z curves respectively). F_z describes the force, where DS-slip transition occurs. F_R, R_z, R_x, R and ϕ are given by Equation 2.43 and 2.44 and Figure 4.1 a. v_x is the lateral pulling velocity and L_N denotes the adsorbed polymer length. Adapted from [203].

Substrate	Static contact angle (°)	RMS roughness (nm)	Desorption	Friction
CH_3-SAM	96 (±3)	3.3	Plateau	PGA: slip-DS
PTFE	115 (±6)	7.6	Plateau	PS-PI-PS-COOH and PS-PPS: DS-slip PGA: slip
GaAs	33 (±6) 90 (±3) after 18 months storage in air	1.2	Plateau	PS-PI-PS-COOH: DS-slip
OHD	84 (±4)	0.3	Plateau	PS-PI-PS-COOH: DS (O- and H-termination) PGA: DS and CS (O-termination) PGA: Slip (H-termination)
Mica	under detection limit	0.2	Rupture events	PAAm: CS

Table 4.2: Overview of desorption and friction experiments. Static contact angle measurements are taken with H_2O. The RMS roughness of an area of 1 x 1 μm^2 is determined by AFM imaging in air. The last two columns show the type of desorption and friction traces in H_2O. The results are based on more than 100 F_z-x curves respectively, except for PAAm on mica. Adapted from [203].

4.6 Spontaneous Detachment in Lateral and Vertical Pulling

Many of the F_z-x curves show a spontaneous detachment of the polymer when pulled laterally. This happens either in case of slip, DS or CS. While in case of CS the polymer desorbs from the substrate, when directional bonds are broken and contact to the surface is lost, the desorption turns out to be more complicated for slip and DS. In the following PS-PI-PS-COOH on PTFE in H_2O is investigated more in detail. The lateral pulling is started at $R_z = 930$ nm (Figure 4.5 a). After a DS event, a constant force is reached at $x = 336$ nm. Soon after, spontaneous detachment occurs at $x = 444$ nm (Figure 4.5 b).
This spontaneous detachment can be analyzed by waiting-time experiments. To that aim, the cantilever is moved away from the surface up to a z-extension at which the polymer is still adsorbed and a non-zero plateau force is measured (Figure 4.5 c). Keeping the cantilever height fixed, the time is recorded for the polymer to spontaneously detach form the surface. Here, a sudden drop of the plateau force to zero is observed. This protocol is repeated for various distances from the surface. A maximum waiting time of 10 s (cut-off time) is set. Two different scenarios are discovered. The first shows a constant force over the whole waiting time with a fixed height of $R_z = 1.14$ μm (Figure 4.5 d). The second reveals a spontaneous detachment event after little more than 5 s at $R_z = 1.14$ μm (Figure 4.5 e).
Figure 4.5 f comprises a whole set of such curves, where each red point represents a waiting time curve. The black squares point out average values for each 25 consecutive points. The critical time t^* for spontaneous desorption in dependence on the height over substrate can be fitted by a exponential function. An Arrhenius-like behavior, where an exponential dependence of the dwell time on the adsorption free energy is assumed (free energy scales linearly with polymer length), is well accepted for weakly adsorbed polymers. Still, experimental and theoretical investigations have shown that the desorption time should rather obey a polymer length dependent power-law [59, 238, 239, 240]. The whole height range, where t^* falls between the cut-off time of 10 s and 0, is just 50-100 nm. The more the height reaches z_{det}, taken from experiments without lateral pulling or waiting time (Figure 4.5 g), the higher is the probability of spontaneous detachment. Here, the polymer is in a metastable or unstable state. Similarly, spontaneous detachment has to be considered during lateral pulling of adsorbed polymer lengths of about 100 nm or less.
Staple et al. [172] explain the spontaneous detachment behavior: as the pulling height increases, the free energy of the system increases linearly. z_{det} or rather the equilibrium adsorption length is determined by the following condition. The free energy of the adsorbed polymer at fixed cantilever height from the surface equals that of the unperturbed polymer in solution. So, if the pulling height is further increased, the system becomes metastable up to the maximal height, where the polymer is adsorbed on the surface only via a single monomer. During this metastable phase, the polymer can detach from the substrate at a much smaller height than the maximal height or contour length. Here, further investigations are required to determine the exact dependence of desorption height on polymer contour length, adsorption strength and pulling velocity.

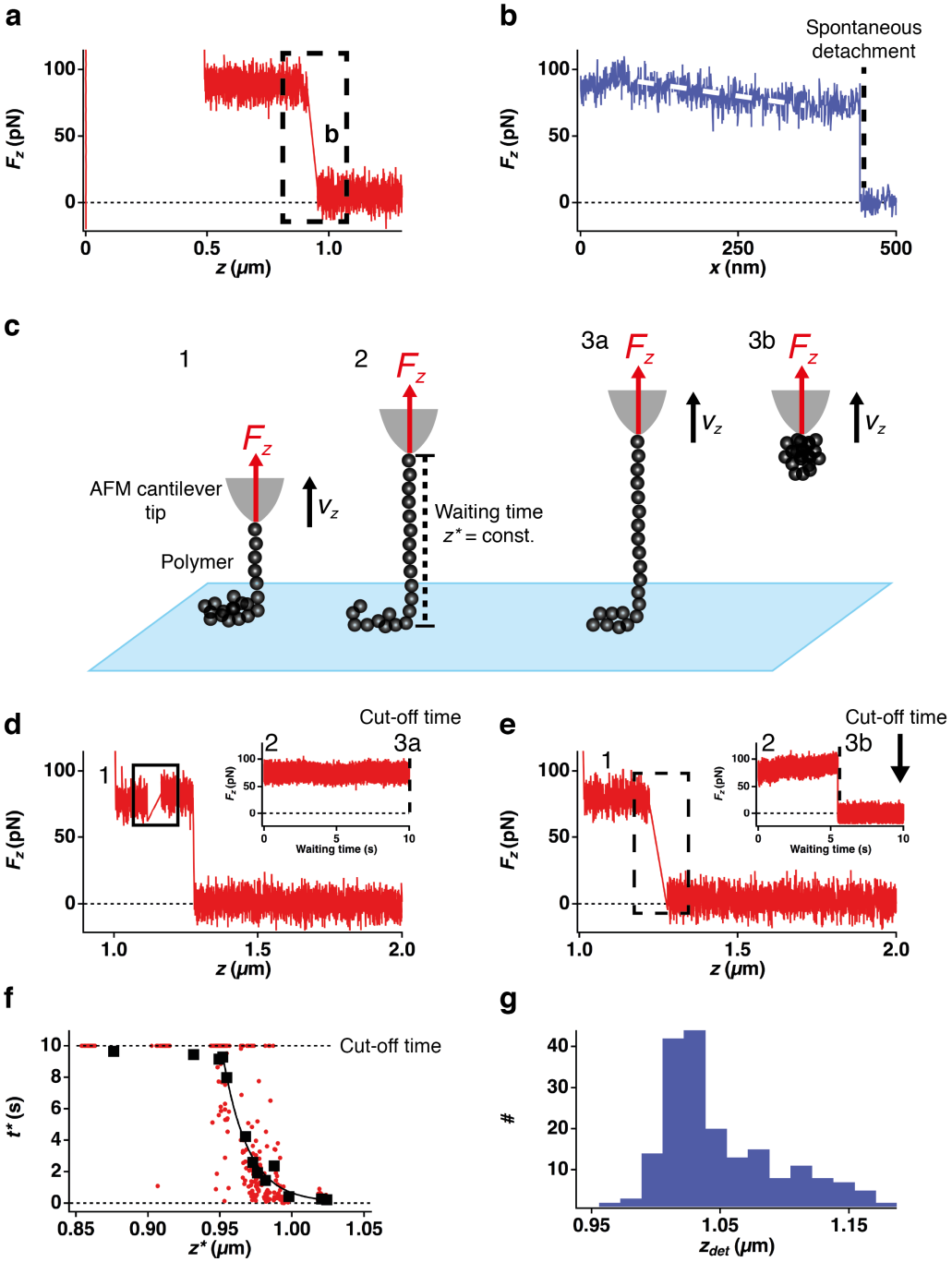

Figure 4.5: Spontaneous detachment for lateral and vertical pulling. Such a behavior is illustrated for PS-PI-PS-COOH on PTFE in H_2O. (a,b) Desorption (F_z-z, red) and lateral pulling (F_z-x, blue) curve. (c) Scheme of waiting time experiment. (d,e) Typical waiting time curves. Desorption is performed up to a certain height z^*, where the motion is stopped and the polymer behavior is observed for a waiting time span of 10 s (inset). Then, the desorption is continued. While (d) shows a constant force for the whole time span, (e) presents spontaneous detachment. (f) Waiting time data, where the polymer is held at a constant height over substrate, until it desorbs by itself at a critical time t^* with a cut-off time of 10 s. The black squares indicate average values for each 25 consecutive points. An exponential function is fit to the data. (g) z_{det} distribution for desorption in z-direction without lateral pulling or waiting time event with a mean value of 1050 ($\pm$ 48) nm.

4.7 Conclusion

In conclusion, any measured friction trace motif can be explained with either CS, DS or slip or a combination of at least two of them. DS is a friction mechanism that is independent of normal force, polymer length and velocity. This contrasts with any theoretical model assuming a linear dependence of the friction force on velocity or normal force such as Amontons' law or the Rouse model. Nevertheless, the observed

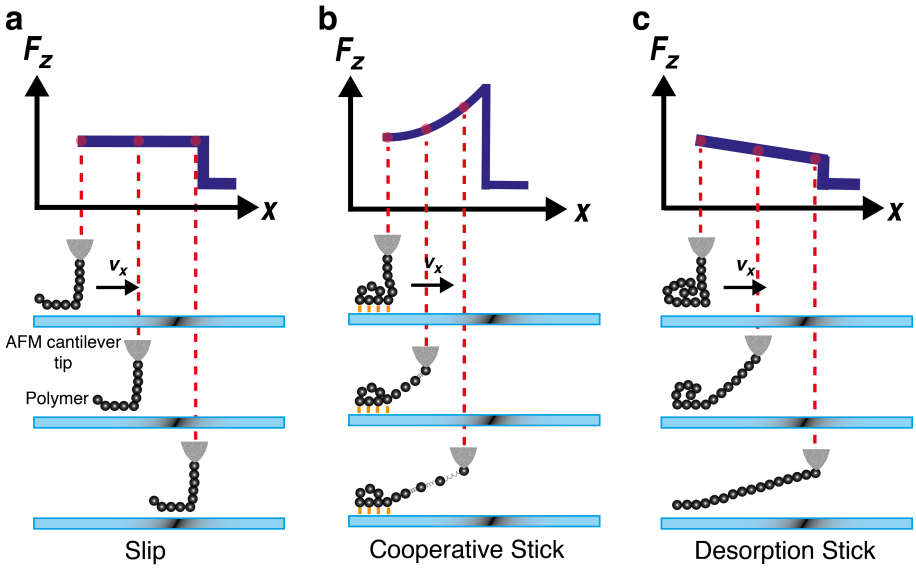

Figure 4.6: Scheme of the nanoscale friction mechanisms. A single polymer at a solid-liquid interface can respond in different ways to a lateral external force, here exerted by an AFM cantilever tip depicted in grey. (a) Slip occurs when the polymer has a very high mobility and responds with undetectably low friction (0.1 pN for the AFM setup). In this case, F_z-x plot shows a plateau of constant force, before the polymer detaches from the surface and F_z becomes zero. (b) In several cases the polymer is stuck to the surface due to strong directional bonds (indicated as orange sticks), i.e. confined in three dimensions (CS). A lateral external force elastically stretches the polymer. (c) The most frequent motif is denoted as DS. The characteristic decrease in F_z with increasing x shows that the static friction coefficient is high enough to favor desorption over slipping. While the polymer does not move laterally, it leaves the surface continuously with very low internal friction, i.e. the polymer is confined in two dimensions. In the images one sphere corresponds to at least 100 monomers. Adapted from [203].

stick-slip resembles macroscopic systems: the stick-slip amplitude and periodicity depend on the velocity similar to macroscopic friction [114, 241]. The details of the stick-slip movement are largely dominated by the collapsed structure of the polymer during adsorption, which depends strongly on the hydrophobicity of the substrate and the solvent, but hardly on the substrate topography. By contrast, CS is mainly caused by directional bonds, such as HBs. The single polymer friction behavior on solid substrates can be summarized by the following four essential insights:

- Good solvent and a homogeneously hydrophobic substrate result in slip without stick events (Figure 4.6 a).
- The strong formation of directional bonds (e.g. HBs) leads to stretching of the polymer and thus to CS (Figure 4.6 b).
- Poor solvents cause DS, irrespective of the substrate (Figure 4.6 c).
- All intermediate cases result in a significant and dominating amount of DS (Figure 4.6 c).

Chapter 5

Adhesion Mechanisms on Polyelectrolyte Multilayers

Polymer coatings are of great interest for surface modification and composite material preparation [242, 243, 97, 244, 245, 246]. As described in Section 2.2.1, adhesion can be of chemical, mechanical or diffusive origin [95, 91]. Adhesive joint failure can be of cohesive manner, either located in the adhesive, the adherent or some boundary layer [95]. Here, interfacial layers and the interphase region (Section 2.2.3) are responsible for the stability of these films and thus have to de understood on the molecular level.
Friction is often tightly linked to adhesion. Therefore, a fundamental understanding of adhesion is required as well. AFM-based SMFS opens new ways to delineate adhesion mechanisms of single polymers on solid substrates, but also on polymer films. Both imaging under varying humidity conditions and SMFS are used to study the interphase properties of thin polymer films, such as polyelectrolyte multilayers (PEMs) on Si. Most parts of this chapter are published in refs. [247, 248].

5.1 Polyelectrolyte Multilayer

PEMs can be prepared from sequential adsorption of oppositely charged PEs onto a charged surface from aqueous solutions (Figure 5.1) [249, 250, 251, 252]. This layer-by-layer (LbL) method falls in the category of template assisted assembly and can be applied to almost any kind and shape of template substrate (planar interfaces, particles). The thickness of PEMs can be tuned with Å precision by the number of PE layers from a total thickness of several Å up to several 100 nm. The stability, the mode of growth (linear or exponential), the structure (extent of interdigitaion of PE layers or roughness) and the physical properties (density, swelling behavior, chain mobility, elasticity) are based on the preparation conditions [252]. Those include the type of PE, the PE charge density, the PE concentration, the PE molecular weight and the adsorption time. PEMs are known to be sensitive to external parameters such as salt concentration [253, 254], type of salt [255, 256, 257, 258], pH [259, 260] and temperature [261], either during preparation as well as during application. Furthermore, atmospheric humidity can determine the PEM thickness [262].
The LbL method enables the construction of ultrathin films with defined thickness, composition and chemical functionalities. Patterned PEMs can be fabricated on chemically patterned surfaces [266] by polymer-on-polymer stamping [267] or by

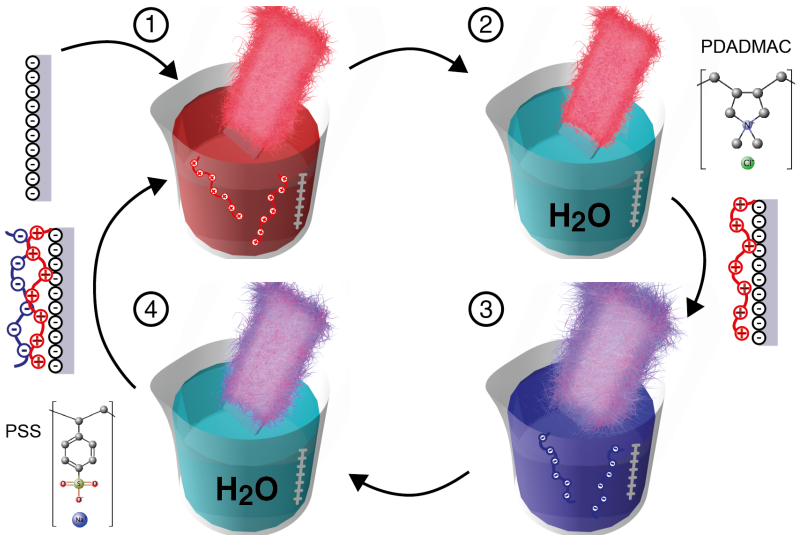

Figure 5.1: Concept of LbL deposition. Schematic representation of adsorption steps starting with a positively charged substrate. Upon polyanion (blue) and polycation (red) adsorption a net charge reversal is observed [263, 264, 265]. Counterions are omitted for clarity.

ink-jet-printing [268]. PEMs have gained a great variety of applications such as pervaporation, nanofiltration [269, 270], biosensing [271], optical devices [272], separation [273, 274], encapsulation [275] and catalysis [276]. A broad overview of PEM properties and applications is given in [53].
The PEM properties are very sensitive to the balance between intrinsic charge compensation (complexation between oppositely charged PEs) and extrinsic charge compensation (interaction between PEs and counter ions in solution), which are both of enthalpic origin. In case of poly(sodium-4 styrene sulfonate)/ poly(diallyl dimethyl ammonium chloride), PSS/PDADMAC, the extrinsic charge compensation is found to be energetically more favorable as shown by MD simulations [277]. Still, the major factor for PEM stability is the release of counter ions from the PEM during built up. In fact, this effect increases the entropy of the total system [252]. Dependent on the PE combination, specific interactions, such as hydrogen bonds, can account for PEM stability as well [53].
A PEM does not show homogenous properties over the whole film. Here, a three zone model (precursor zone, core zone, and outer zone) is suggested [278, 279]. While the precursor zone is influenced by the substrate charges, the core zone lies beyond the range of substrate influence and bears neutral charge. The outer zone provides the excess charges and contacts the respective medium. While precursor and outer zone preserve their thickness, the core zone is responsible for PEM thickness growth. These zones have a gradual transition behavior and reflect the change in chemical composition and structure from the interfacial layer, close to the supporting substrate, to the boundary layers, having bulk-like behavior [97].
Still, the mechanism for PEM stability and the adhesion mechanism for built-up are not fully understood. Here, SMFS is used to detect and distinguish interface, interphase and bulk region.

5.2 Thickness and Swelling Behavior

The hydration and swelling behavior of PEMs is the subject of several recent publications [280, 281, 282, 283, 259, 284, 285, 286, 287]. These estimate the typical amount of H_2O uptake under high humidity or in H_2O between 39 vol. % for a PSS/PAAm system [280] and 300 vol. % in the case of a poly(acrylamide)/ PDADMAC system [259].
Neutron reflectivity has so far served to investigate the effect of ionic strength and type of ion on the swelling water of PEMs. Increasing ionic strength and preparation with anions of increasing size lead to an increasing amount of swelling water and an increasing thickness of the multilayers. Neutron reflectivity revealed two different types of water. First, the void water, which changes the scattering length density, but does not contribute to swelling. Second, the swelling water, which directly contributes to the increase in multilayer thickness and can be determined by the swelling ratio [262].
In the following, the thickness and swelling behavior of PEMs is investigated, either by ellipsometry and by AFM imaging under varying humidity conditions. To that aim, PEMs, consisting of double layers of PSS/PDADMAC, are prepared from aqueous solution of 0.1 M and 0.5 M NaCl. NaCl constitutes the zero point of ion specific effects (Section 2.4.2). The effect of further types of salt according to the Hofmeister series is discussed by Dodoo et al. [262]. The integer numbers correspond to PEMs with PDADMAC as outermost layer.
Ellipsometric measurements (Appendix B.4) are performed in a home-made humidity cell equipped with humidity and temperature sensors (S. Dodoo, TU Berlin). The AFM imaging in air is done in a home-built closed fluid cell, comprising a reservoir underneath the sample. Here, different solutions can be filled in, leading to the required humidity environment (B.N. Balzer, TU München). A humidity sensor records the respective r.h. during the whole experiment (Section 3.1.7). With that setup, measurements between 1 % r.h. and 98 % r.h. are performed. For measurement at 100 % r.h. a closed fluid cell filled with H_2O is used.
The thickness of multilayers with up to 4 double layers is obtained by taking a 20 x 20 μm^2 image in intermittent-contact mode. Then, a 5 x 5 μm^2 image in the center area of the previously scanned 20 x 20 μm^2 image is taken by means of contact mode AFM. Force loads up to 1 μN are used to scratch the surface and to remove the PEM, similar to experiments on the aging of H-terminated diamond [288]. Afterward, a 20 x 20 μm^2 image in intermittent-contact mode reveals the previous indentation due to contact mode imaging. Finally, the thickness can be measured from cross sections along 10 different positions, placing the cursors on the treated and non-treated area and taking the height difference at each position.
The determination of the thickness of multilayers having 14 or more double layers is completed by scratching the multilayer with a scalpel prior to imaging and taking a 20 x 20 μm^2 image in intermittent-contact mode. The thickness is then determined from cross sections at 10 different positions (Figure 5.2).
Figure 5.3 shows the thickness as a function of the r.h. for PSS/PDADMAC multilayers prepared at an ionic strength of 0.1 M and 0.5 M, respectively. While Figure 5.3 a,b represents the ellipsometry results, Figure 5.3 c,d presents the AFM data. The measured thicknesses from both methods are consistent within the experimental error and result in an increase with r.h. and with ionic strength. Figure 5.3 e,f

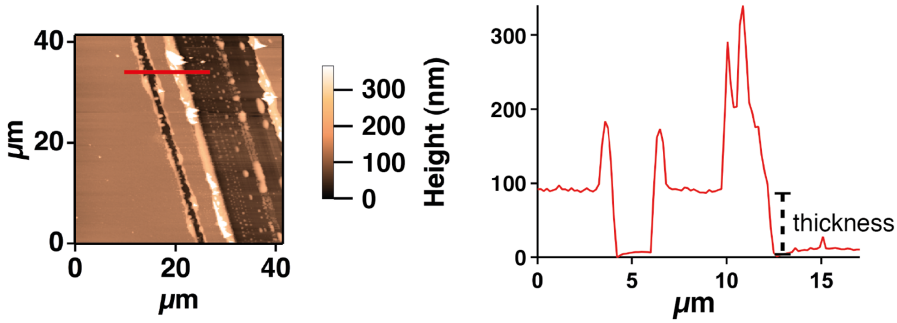

Figure 5.2: AFM-based determination of PEM thickness. AFM intermittent-contact mode height image taken in pure H_2O on $(PSS/PDADMAC)_{14}$, prepared in 0.1 M NaCl and scratched with a scalpel. The cross section of the scratched region is given along the red line. Height values of at least 10 cross sections are taken for the average thickness determination. Adapted from [248].

demonstrates how the amount of swelling water varies with r.h.. The swelling water is calculated using:

$$\phi_{swell}(r.h.) = \frac{d_{swollen}(r.h.) - d_{dry}}{d_{swollen}(r.h.)} \cdot 100 \tag{5.1}$$

ϕ_{swell} represents the swelling water, $d_{swollen}$ the thickness of the swollen PEM at r.h. > 1 % or against liquid H_2O (100 % r.h.), and d_{dry} constitutes the thickness of the dry multilayer at 1 % r.h. .

For PEMs prepared in 0.1 M NaCl, the swelling water increases from four to one double layer of PSS/PDADMAC as given in Figure 5.3 g. Hence, the swelling water decreases with the increasing number of layers for thin PEMs. From 6 to 30 double layers of 0.1 M NaCl, the swelling water increases again. Wong et al. [257] have already reported about decreasing swelling water with increasing number of layers for PSS/PAH up to 6 double layers prepared from 0.25 M NaCl. For low ionic strength (0.1 M NaCl) the first double layers are loosely packed. Adsorbing more layers leads to a densification and strong interdigitation with the former adsorbed double layer (intrinsic charge compensation). Mobility and permeability measurements reveal a higher diffusion coefficient of PE chains in the outer layer, which decreases with increasing number of layers [289, 290]. This model explains the formation of multilayers at least up to a number of 4 double layers, where the swelling water decreases from 1 to 4 double layers. For more than 4 double layers, the attraction between the outer polycation layer and the substrate is screened, leading to both less dense packing and stronger swelling. Thus, PEMs consisting of up to 4 double layers exhibit interphase behavior, where the PEM is still affected by the substrate. The adsorption of more than 4 double layers shows bulk behavior with respect to the amount of swelling water.

By contrast, for PEMs prepared in 0.5 M NaCl, the swelling water shows a monotonous increase with increasing number of PSS/PDAMADC double layers (Figure 5.3 f). High ionic strength (0.5 M NaCl) leads to enhanced screening of the PE charges (extrinsic charge compensation). Two effects arise: the stronger screening of substrate charges results in a less dense packing of the first PE layers close to the substrate. Furthermore, the PE chains are adsorbed in a more loose conformation and the amount of ultrapure H_2O is increased (up to 70 % for $(PSS/PDADMAC)_{30}$ prepared from 0.5 M NaCl). Therefore, taking the electrostatic attraction between

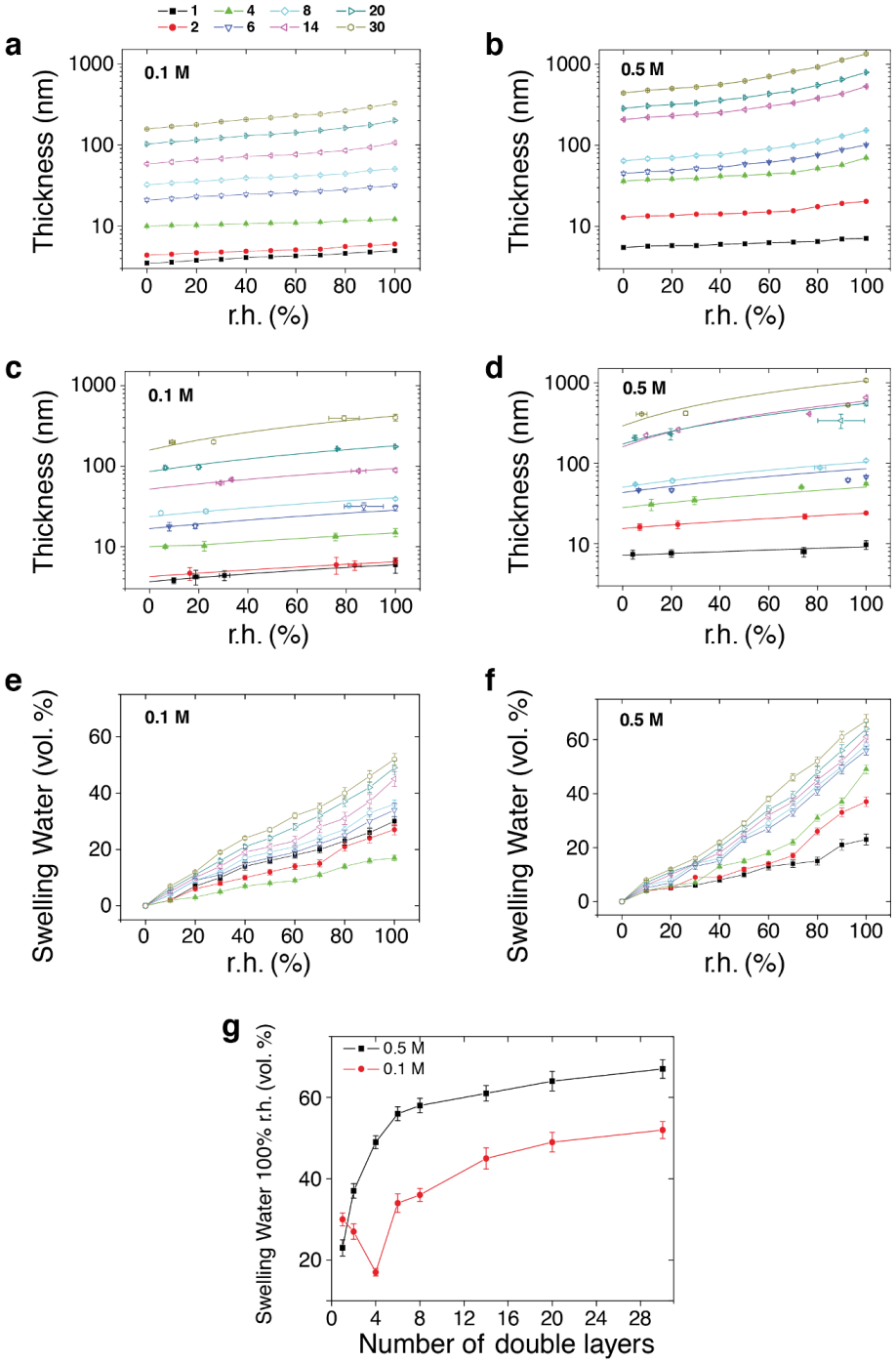

Figure 5.3: Humidity dependent PEM thickness. Thickness of PEMs, prepared in 0.1 M NaCl and 0.5 M NaCl respectively, in dependence on number of PE layers and r.h. (a,b) determined by ellipsometry and (c,d) AFM imaging. (e) Amount of swelling water calculated by Equation 5.1 as a function of r.h. for PEMs prepared from aqueous solutions of 0.1 M NaCl, and (f) 0.5 M NaCl. Solid lines are a guide to the eye. The data points at 100 % r.h. are obtained from measurements against liquid H_2O. The numbers in the legend correspond to the number of PSS/PDADMAC double layers. (g) Amount of swelling water (100 % r.h.) as a function of number of double layers for PEMs prepared from aqueous solutions of 0.1 M NaCl and 0.5 M NaCl. Adapted from [247].

substrate and outermost layer as criteria, PEMs prepared in 0.5 M NaCl already illustrate a bulk behavior at a low number of PE layers.

5.3 Single Molecule Desorption Behavior of PEMs

SMFS measurements are performed in H_2O by pressing the AFM cantilever tip bound polymer onto the PEM layer. Trigger forces of several hundred pN are used in a way that only the top region is touched upon dwell on the PEM, while the underlying Si substrate is not reached. After the polymer adsorbs onto the surface, a dwell time of usually 1 s is used, before retracting the cantilever tip. Now, the polymer successively desorbs from the PEM. Hence, thin polymer film adhesion properties can be detected with high spatial precision.

Layer composition	$\mathbf{c_{salt}}$ **(M NaCl)**	**PEM**		**OEM**	
		d_{dry}(nm)	d_{H_2O}(nm)	d_{dry}(nm)	d_{H_2O}(nm)
Si	-	0.5 (oxide)	-	-	-
Si+PEI	-	2	-	-	-
Si+PEI+(X)	0.1	4	5	-	-
Si+PEI+(X)/PSS	0.1	8	10	3	8
Si+PEI+$(X)_2$	0.1	5	6	-	-
Si+PEI+$(X)_2$/PSS	0.1	10	13	4	10
Si+PEI+$(X)_3$	0.1	-	-	-	-
Si+PEI+$(X)_4$	0.1	11	22	4	9
Si+PEI+$(X)_4$/PSS	0.1	16	20	5	12
Si+PEI+$(X)_{14}$	0.1	69	92	11	22
Si+PEI+$(X)_{14}$/PSS	0.1	66	80	12	24
Si+PEI+(X)	0.5	6	14	-	-
Si+PEI+$(X)_2$	0.5	14	20	-	-
Si+PEI+$(X)_4$	0.5	42	70	8	12
Si+PEI+$(X)_4$/PSS	0.5	-	-	9	14
Si+PEI+$(X)_{14}$	0.5	252	530	45	76
Si+PEI+$(X)_{14}$/PSS	0.5	-	-	57	88

X=PSS/PDADMAC

Table 5.1: Overview of PEM and OEM thickness. PEM and OEM compositions, salt concentration c_{salt} of the NaCl solution for preparation and thickness measured by ellipsometry in air (20 °C and r.h. 40 %) d_{air} and in H_2O d_{H_2O}. The standard deviation of the thickness corresponds to about 10 % of the reported value. Prior to SMFS measurements, the samples are allowed to swell for about 30 minutes in a H_2O filled fluid cell. Adapted from [248].

5.3.1 Effect of Number of Adsorbed PE Layers

PAAm or PLL, both being positively charged at neutral pH, are used as molecular force sensor. The plateau desorption force $F_{plateau}$ is measured for PTFE, CH_3-SAM, HD and Si in the absence of any polymer coating (see Figure 5.4 a). This is consistent with experiments on solid substrates (Section 2.4.2).
The PEM interphase is investigated by adding branched poly(ethylene imine), PEI, and then successive PE layers according to the standard protocols (Appendix B.4).

$F_{plateau}$ decreases continuously from first PSS/PDADMAC double layer on and reaches down to one third of the initial value at four double layers (Figure 5.4 a). In addition, the detachment length z_{det} immediately drops after the first (PSS/PDADMAC) layer (Figure 5.4 b). In summary, $F_{plateau}$ and z_{det} decrease significantly with increasing number of PSS/PDADMAC layers.

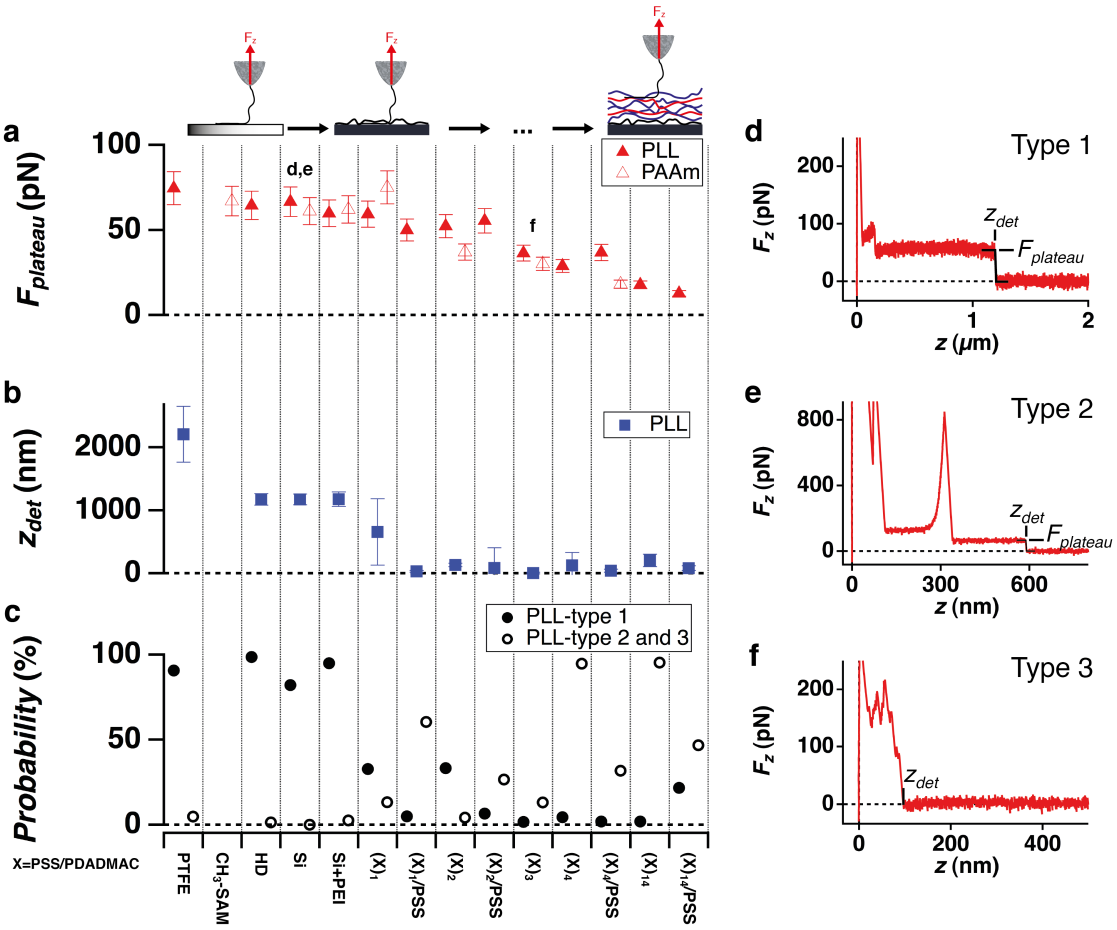

Figure 5.4: Interphase properties of PEM substrates. Single polymer desorption from PTFE, CH_3-SAM, HD, Si, PEI covered Si (Si+PEI), $(PSS/PDADMAC)_1$, $(PSS/PDADMAC)_2$, $(PSS/PDADMAC)_3$, $(PSS/PDADMAC)_4$, $(PSS/PDADMAC)_4$/PSS, $PSS/PDADMAC)_{14}$, $PSS/PDADMAC)_{14}$/PSS in H_2O. These PEMs are prepared in 0.1 M NaCl. (a) $F_{plateau}$ (type 1 and 2) for PAAm and PLL molecular force sensors, (b) z_{det} and (c) probability of curve type occurrence. (d) Typical F_z-z curve for PLL on Si and (e,f) PLL on $(PSS/PDADMAC)_3$, showing type 1 (plateau), type 2 (plateau and stretching) and type 3 (stretching and rupture only). All curves are taken at a pulling velocity of 1 $\mu m \cdot s^{-1}$ and at a dwell time of 1 s. Errors correspond to the standard deviation. For 0.1 to 60 s of dwell time the same dependencies are found. Adapted from [248].

Besides plateaus of constant force (here termed type 1, Figure 5.4 d), representing equilibrium events another type of F_z-z is discovered as well: non-linear structures evidence non-equilibrium stretching and rupture events (termed type 3, Figure 5.4 f). Those resemble the F_z-z curves for the rupture of single covalent bonds [23] or unfolding of secondary structures [75, 150] and can be fitted by a WLC function [51, 291, 292] (Section 2.1.7). Type 2 F_z-z plots comprise more complex curves, including both plateau and non-linear structures (Figure 5.4 e). A forth type of F_z-z curves shows an unspecific adhesion peak only, i.e. no single polymer events. For PEMs with more than one PSS/PDADMAC double layer, a transition from

equilibrium (type 1) to non-equilibrium desorption (type 3) is obtained. At four double layers, most of the traces reveal non-equilibrium events. This is sustained by the ratio of plateau desorption curves (type 1, only equilibrium events) to all curves taken for a polymer-substrate combination (Figure 5.4 c). In general, a qualitative and quantitative change in polymer adhesion can be observed with increasing number of PE layers. A variation of the dwell time in contact with the PEMs between 0.1 s and 60 s shows similar $F_{plateau}$ and probability of plateau occurrence for the respective substrate.
The quality of these observations is confirmed by taking a force map with PLL as molecular force sensor in H_2O on the scratched $(PSS/PDADMAC)_{14}$ (prepared in 0.1 M NaCl) substrate, given in Figure 5.2. Here, plateau desorption curves (type 1) only appear in the scratched region, while the intact PEM layer shows a strongly reduced unspecific adhesion peak Figure 5.5. The PEM layers screen the substrate potential and represent mainly non-equilibrium events. These results are confirmed on selected PEMs with 4 or 14 double layers, probed by PLL and by a polystyrene (PS-PPS) force sensor such as given in Figure 5.6. The occurrence of type 2 and 3 desorption curves for four and more double layers of PSS/PDADMAC is similar for preparation in either 0.1 M NaCl and 0.5 M NaCl.

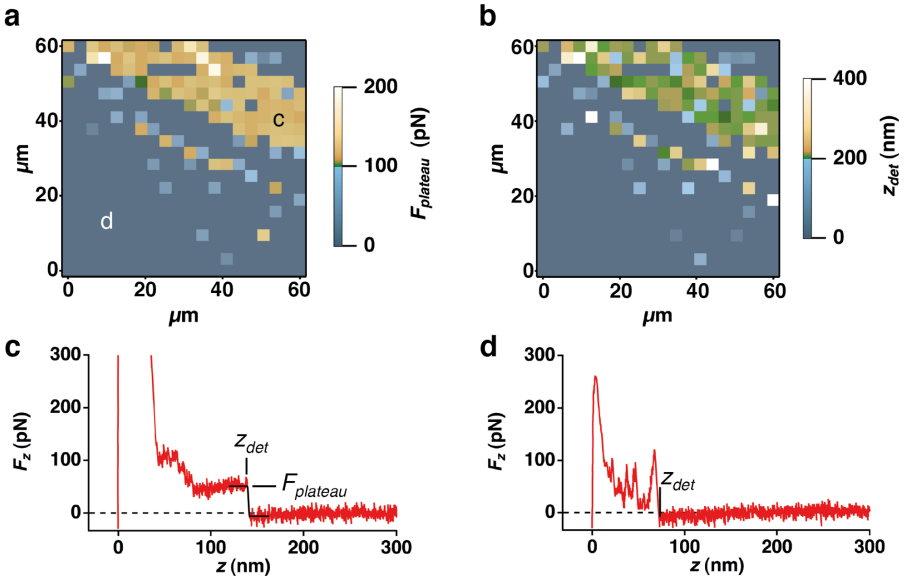

Figure 5.5: Impact of PEM layer on desorption behavior. Force map with PLL as molecular force sensor on an area of $(PSS/PDADMAC)_{14}$ (prepared in 0.1 M NaCl) in H_2O along the same scratch shown in 5.2. (a) $F_{plateau}$, (b) z_{det}. For non-equilibrium events (type 2 and 3), $F_{plateau}$ and z_{det} are set to 0. Consistent with Figure 5.4, the PEM region demonstrates the rare occurrence of equilibrium desorption events. (c) F_z-z curve taken in scratch region showing a plateau of constant force (type 1). (d) F_z-z curve taken on PEM region with sticky behavior in non-equilibrium (type 3). The data are taken at a pulling velocity of 1 $\mu m \cdot s^{-1}$ and at a dwell time of 1 s. Adapted from [248].

Furthermore, PLL is desorbed from oligoelectrolyte multilayers (OEMs). They are made of PDADMAC and PSS with more than 10 times shorter chains than the PEMs and tend to be stiffer and less coiled. This leads to less interdigitation and thinner low-roughness films. The mobility of OEM layers is one order of magnitude higher than for the long chain equivalents, but show similar swelling behavior

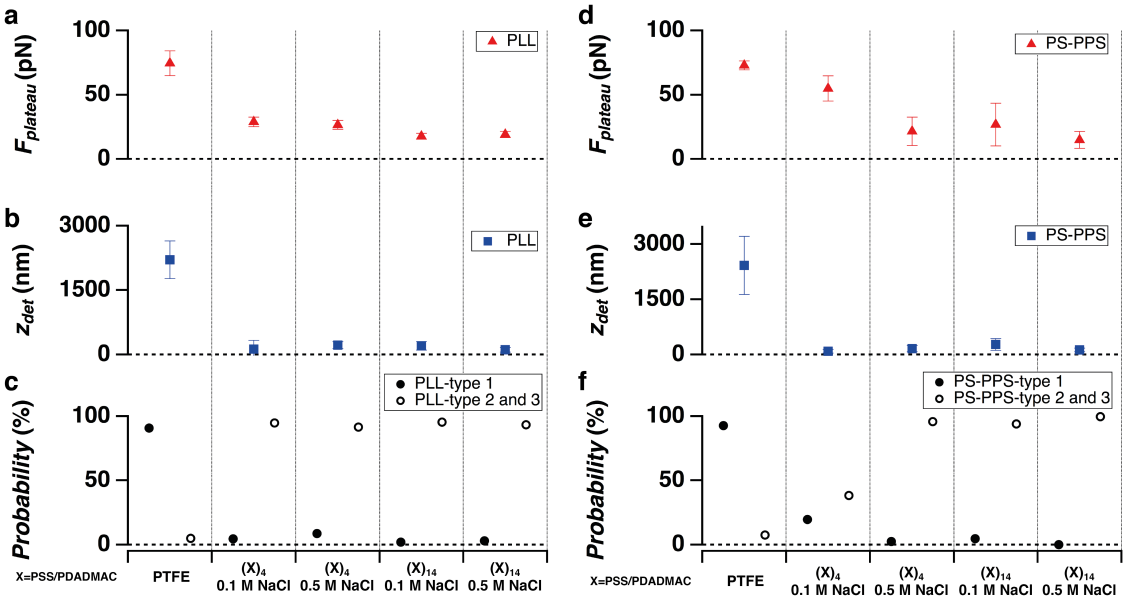

Figure 5.6: Similar desorption behavior of hydrophilic and hydrophobic polymers. Single polymer desorption from PTFE, $(PSS/PDADMAC)_4$ (prepared in 0.1 M NaCl), $(PSS/PDADMAC)_4$ (0.5 M NaCl), $(PSS/PDADMAC)_{14}$ (0.1 M NaCl), $(PSS/PDADMAC)_{14}$ (0.5 M NaCl) in H_2O are presented. PLL in H_2O: (a) $F_{plateau}$ (type 1 and 2), (b) z_{det}, (c) probability of curve type occurrence and PS-PPS in H_2O: (d) $F_{plateau}$ (type 1 and 2), (e) z_{det}, (f) probability of curve type occurrence. The data are taken at a pulling velocity of 1 $\mu m \cdot s^{-1}$ and at a dwell time of 1 s. Errors correspond to the standard deviation. Adapted from [248].

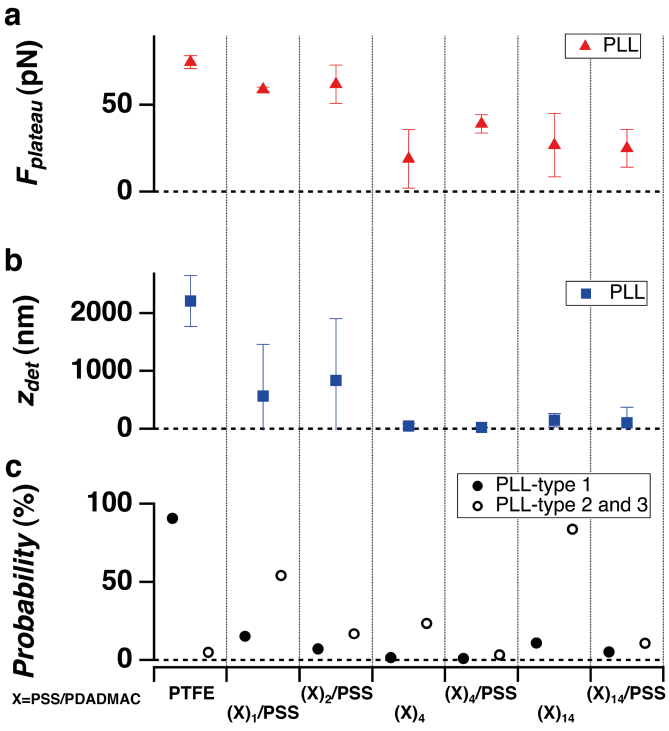

Figure 5.7: Desorption behavior on OEMs. Single polymer desorption of PLL molecular force sensor from PTFE, $(PSS/PDADMAC)_1/PSS$ prepared in 0.1 M NaCl, $(PSS/PDADMAC)_2/PSS$ (0.1 M NaCl), $(PSS/PDADMAC)_4$ (0.1 M NaCl), $(PSS/PDADMAC)_4/PSS$ (0.1 M NaCl), $(PSS/PDADMAC)_{14}$ (0.1 M NaCl), $(PSS/PDADMAC)_{14}/PSS$ (0.1 M NaCl) in H_2O. (a) $F_{plateau}$ (type 1 and 2), (b) z_{det}, (c) probability of curve type occurrence. The data are taken at a pulling velocity of 1 $\mu m \cdot s^{-1}$ and at a dwell time of 1 s. Errors correspond to the standard deviation. Adapted from [248].

[290, 293, 294]. Regarding the single polymer desorption behavior, OEMs exhibit the same tendency (Figure 5.7) as PEMs. With increasing distance from the substrate, $F_{plateau}$, z_{det} and occurrence of desorption plateaus decrease, starting after the second PSS/PDADMAC double layer. While still many type 1 events give the initial z_{det} value, the type 2 and 3 events tend to represent much shorter values. This leads to the broad z_{det} distributions in Figure 5.7 b. The probability of constant force plateaus in the F_z-z curves is quite low from the first double layer on.

5.3.2 Desorption Motif Determines Interphase

For thin PEMs the substrate potential dominates the adhesion, but is already significantly screened after a few PSS/PDADMAC double layers. This is indicated by $F_{plateau}$ decreasing by about a factor of 3 upon addition of the first three double layers. Furthermore, the shortening of z_{det} from the first PSS/PDADMAC layer hints towards a mechanism, where the polymer interacts with the PEM only partly. A second issue refers to the type of single polymer desorption motif. Already at the second double layer, more and more non-equilibrium F_z-z traces are observed. They resemble spikes (type 2 and 3) instead of plateaus (type 1). The plateaus can be interpreted as desorption from the top layer of the PEM or the underlying Si substrate. In that case, the single polymer is either mobile on the PEM or desorbs in a zipper-like fashion [295] (Figure 5.8). By contrast, non-linear F_z-z curves of type 2 and 3 have to be explained in a different manner. Here, sticky connections in between the tip attached polymer and the PEM coated substrate are necessary. As soon as the single tip attached polymer penetrates into the PEM, it is geometrically trapped into the PEM mesh. Most probably, the polymer disentangles from the mesh, when pulled in z-direction under the exerted force F_z. The non-linear F_z-z (sticky) behavior could either be caused by intermolecular (electrostatic) bonds, broken in a shear-like geometry [295], or breakage of geometrical interlocks, as indicated in Figure 5.8. As these interlocks act between polymer chains, they differ significantly from mechanical interlocks between asperities of solid bodies (Section 2.3).

As soon as the PE layer fully screens the substrate potential (around three double layers), qualitatively different F_z-z traces are discovered, rendering the geometrical interlock more important. This decrease in equilibrium plateau desorption force and increase of non-equilibrium desorption curves (in particular type 3) identify the transition from substrate dominated interphase to bulk behavior with polymer-polymer cohesion. This is consistent with the three zone model, with a very small interphase of 2-3 double layers [278].

For the definition of the interphase, the molecular conformation is crucial [98]. While the global averaged conformation has been obtained before by neutron and X-ray reflectometry [296, 280, 297], single molecule methods are able to gain information on the molecular conformation by contacting a polymer film with a single polymer. Previous experiments on amyloids, such as spider silk proteins [298, 150, 299], could determine the folding structure due to F_z-z patterns. As the PEs in the PEM do not have a unique conformation, only qualitative changes can be tracked. While plateaus in the F_z-z trace indicate that the polymer remains on top of the PEM with a high lateral diffusion coefficient, type 2 and 3 curves confirm stronger local interactions. Interlocks that are formed between the molecular force probe and the

PEM are broken due to vertical pulling. As this motif is observed for polymers of varying composition, charge and hydrophobicity, entanglement formation between single polymer and long chain PEs is expected. Furthermore, the preparation conditions (0.1 M NaCl vs. 0.5 M NaCl) do not cause any desorption behavior change. This is in line with the bulk-like conformation from four PSS/PDADMAC double layers on, as discussed above.

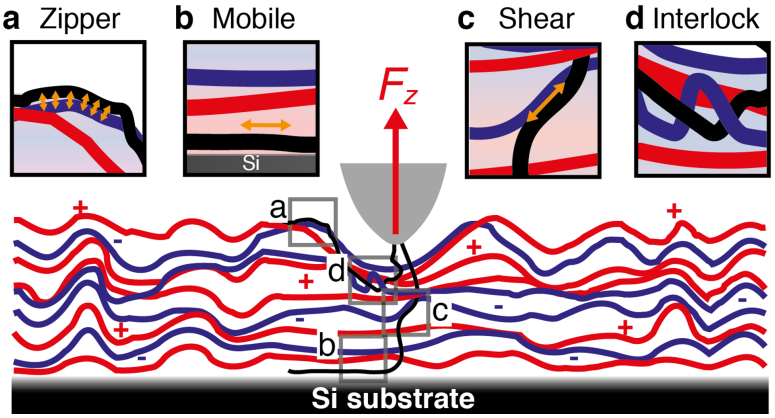

Figure 5.8: Schematic representation of single polymer desorption from PEMs. A molecular force sensor is pressed onto the boundary layer of the PEM. The single polymer (black) is able to entangle, at least partly, into the PEM layer. Upon retraction, the polymer shows four different motifs or combinations of these: (a) The polymer portion not entering the PEM reveals zipper-like detachment. (b) The polymer portion directly contacting the Si substrate indicates equilibrium desorption, with high in-plane mobility. (a) and (b) result in plateaus in the F_z-z curve (type 1). (c) The polymer part within the PEM is subject to shear and/or (d) to geometrical interlock events, both resulting in non-linear F_z-z behavior (type 2 and 3). Adapted from [248].

5.3.3 Role of Charges

The stability of PEMs is known to be due to the release of counter ions, which is an entropic effect [54, 252]. Another reason is the complexation between the oppositely charged PE layers (intrinsic charge compensation), having an enthalpic origin. This interpretation for the type 2 and 3 traces is a formation of complexes between the PEMs and tip bound polymers, which replace intra-PEM complexes between positively and negatively charged PEs. Upon desorption, these newly formed complexes have to be broken, causing the observed rupture peaks in the F_z-z plots, similar to cationic polymers desorbed from grafted anionic PE brushes [300, 301].
Although ζ-potential measurements demonstrate that the net charge of the surface changes after each monolayer adsorption step [263, 264, 265], $F_{plateau}$ and the occurrence of type 2 and 3 curve are similar for e.g. $(PSS/PDADMAC)_4$ and $(PSS/PDADMAC)_4/PSS$. The latter are expected to carry opposite charges at the PEM top layer. The high degree of interpenetration between adjacent layers, which has previously been indicated by neutron reflectometry measurements [296, 280, 297], can serve as explanation for that finding.
This minor role of the charge reversal from layer to layer is confirmed by using hydrophobic PS-PPS force sensors on PEMs with 4 and 14 double layers (Figure 5.6). They show non-equilibrium curves (type 2 and 3) and therefore demonstrate that charges are not necessary to obtain sticky connections, which sustains the idea of geometrical interlock.

5.3.4 Role of Geometrical Interlock

Interlocks of the single polymer with the polymer film, upon contact of the cantilever tip with the PEM, are required to explain the desorption data of type 2 and 3. As soon as the polymer is pulled out of the PEM, it has to find its way through the PE layers in order to be released. Breakage of such interlocks is confirmed by desorption energies E_{des} (area under the F_z-z curve) of the order of 1000 k_BT (Figure 5.9). Such a large value cannot be explained by unspecific interaction only, e.g. screened charge interaction. The formation of interlocks between PE layers has previously been suggested due to X-ray reflectometry (XRR) experiments [302]. Type 2 curves correspond to interlock events, where the polymer portion not entering the PEM is responsible for plateaus of constant force.
Another interesting observation is that z_{det} is largely reduced on PEMs compared to solid substrates irrespective of the type of desorption curve. Here, the cantilever tip attached polymer is only partially incorporated into the PEM upon contact of the cantilever tip. The remaining parts of the polymer stay on top of the PEM. As soon as the incorporated part is pulled off the PEM, the remaining polymer segments are metastable and desorb easily into solution. A detailed description of this spontaneous detachment process on solid substrates is given in Section 4.6. Interlocks can be interpreted as entanglement formation between the long force sensor chain and the PE chains. A detailed discussion with respect to polymer films of different chain length and architecture is given in Chapter 6.

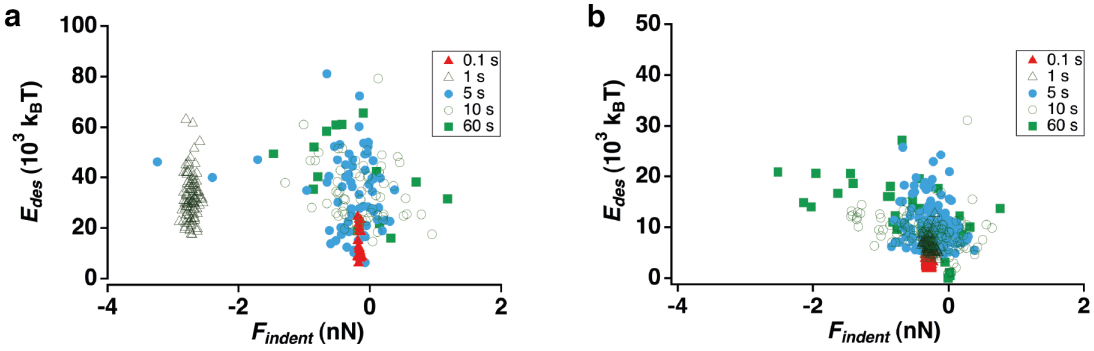

Figure 5.9: Dependence of desorption energy on indentation force and dwell time. Desorption energy E_{des} vs. indentation force F_{indent} for (a) PAH in H_2O on $(PSS/PDADMAC)_1$, prepared in 0.1 M NaCl and (b) PAH in H_2O on $(PSS/PDADMAC)_3$ (0.1 M NaCl). Curves of type 2 and 3 are taken for this evaluation only. All PEMs are prepared in 0.1 M NaCl. Different dwell times between 0.1 s and 60 s are shown. The data has been taken at a pulling velocity of 1 $\mu m \cdot s^{-1}$. The higher E_{des} values for $(PSS/PDADMAC)_1$ results from the higher tip-PEM interaction compared to thicker PEMs. Adapted from [248].

PEMs of more than 3 double layers reveal mostly type 3 curves. The desorption energy E_{des} increases for short dwell times between 0.1 s and 1 s, but is rather constant at higher dwell times up to 60 s. Moreover, the distribution of E_{des} becomes broader with increasing dwell time, which suggests some local conformational changes within the time frame of the dwell process (Figure 5.9 a,b). Increasing the indentation force, i.e. indenting further into the PEM, does not show an increase in total tip desorption energy (Figure 5.9 b). This indicates a rather compact and impenetrable or even glass-state like conformation of the underlying PE layers. This is consistent with the model predicted by Ladam et al. [278] with a dense core zone and a more fluid boundary layer. Fluorescence recovery after photobleaching (FRAP) experiments show that the diffusion coefficient near the film/solution interface is

about one order of magnitude higher than inside the multilayer [290]. Temperature dependent desorption confirms such a fluid boundary layer.

5.3.5 Temperature Impact on Desorption Behavior

$F_{plateau}$, z_{det} and the curve type occurrence are given for $(PSS/PDAMAC)_4$ and $(PSS/PDAMAC)_{14}$ in dependence on temperature (Figure 5.10). With increasing temperature, $F_{plateau}$ and the probability of type 1 curve for $(PSS/PDAMAC)_4$ decrease. While z_{det} reveals a minimum at about 45 °C, type 2 and 3 curves become more frequent with increasing temperature. Additionally, the behavior of $(PSS/PDAMAC)_{14}$ is quite similar, except that the amount of type 1 curve is very low for any temperature.
The glass transition temperature T_g is expected to be little above 50 °C with a in-plane diffusion coefficient of the top layer to increase by an order of magnitude around 55 °C [290]. T_g decreases with decreasing thickness of the PEM [284, 303]. In a more liquefied film state, it becomes easier for the molecular force sensor molecule to entangle into the mesh. The higher probability of interlock causes the non-linear F_z-z motif to occur more often (type 2 and 3). Furthermore, the slightly increasing z_{det} reveals that the PLL molecular force sensor can entangle into the PEM further at higher temperatures. That hints towards some conformational rearrangement in a more liquefied state at high temperature, where no velocity or dwell time dependence is observed.
A step-like change in desorption behavior ($F_{plateau}$ and probability for non-linear F_z-z curves) is not observed for both $(PSS/PDAMAC)_4$ and $(PSS/PDAMAC)_{14}$, but a gradual change. This is rather surprising for the $(PSS/PDAMAC)_{14}$ sample, which is expected to undergo glass transition in the temperature range investigated. A possible explanation can be that only the boundary layer is tested by the single molecule force sensor. Therefore, the underlying PE layers that should undergo glass transition are not reached, as already indicated in Section 5.3.4.

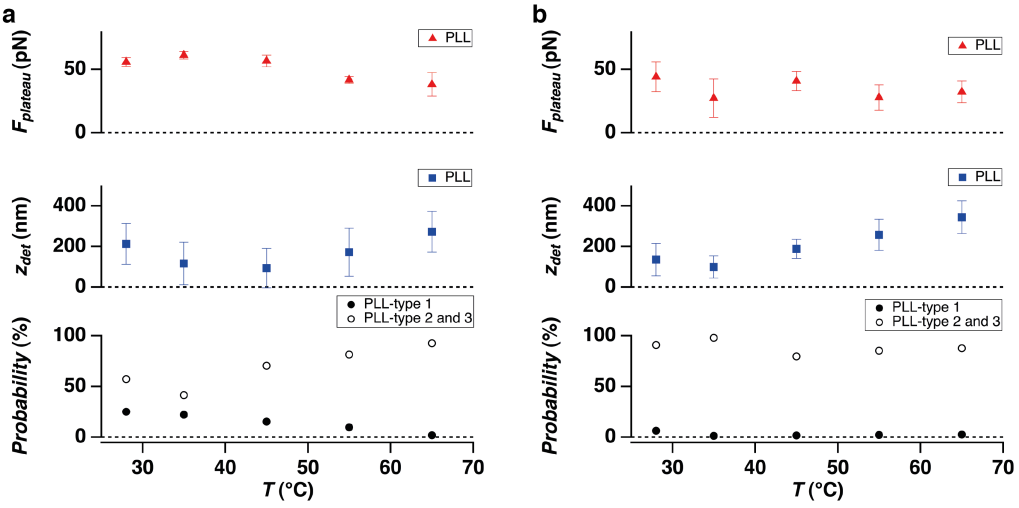

Figure 5.10: Temperature dependent desorption behavior of PEMs. $F_{plateau}$ (type 1 and 2), z_{det} and frequency of curve type occurrence on (a) $(PSS/PDADMAC)_4$ (0.1 M NaCl) and (b) $(PSS/PDADMAC)_{14}$ (0.1 M NaCl). All measurements are performed in H_2O with PLL. The dwell time on substrate is 1 s and the pulling velocity is 1 $\mu m \cdot s^{-1}$. Errors correspond to the standard deviation. The higher $F_{plateau}$ and type 1 occurrence might be explained by degradation effects of the PEM after several months.

Temperature dependent desorption experiments are consistent with a glass-like state for thin PEMs [252], which would reduce the formation of entanglements for very thin layers up to three double layers. As soon as the PEM becomes thicker and the substrate influence decreases, the top layers become more liquefied [290]. This fluid boundary layer model promotes the formation of entanglements and leads to increased interlock probability. With increasing temperature rather thin PEMs, such as $(PSS/PDADMAC)_4$, reach a more liquid state similar to thicker PEMs, such as $(PSS/PDADMAC)_{14}$. This remains valid for hydrophobic polymer films as well, far below T_g, as discussed in Chapter 6. The lateral mobility of single polymers on PEMs is analyzed in Chapter 7.

5.4 Conclusion

Ellipsometry and AFM imaging show that in case of PEM preparation in 0.1 M NaCl, the amount of swelling water in the PEMs decreases with increasing number of adsorbed double layers from one double-layer up to four double-layers of 0.1 M NaCl. Therefore, the PE density increases as a result of the attraction between the positively charged outermost PDADMAC layer and the Si substrate. From 6 double layers to 30 double layers, a much lower PE density and higher swelling water amount is monitored. Here, the attraction is reduced due to a much larger distance between substrate and outermost layer. By contrast, in PEMs prepared from aqueous solution of 0.5 M NaCl, the PE density decreases monotonically with increasing number of PE layers. For this reason, the amount of H_2O constantly increases. The PEM swelling behavior suggests a transition from a more substrate affected interphase behavior to a bulk-like behavior. This transition takes place with increasing number of PE layers. The exact threshold depends on the preparation conditions of the PEM.
AFM-based SMFS determines the adhesion profile in PEMs and short chain PEMs (OEMs) by desorbing single polymers covalently bound to a cantilever tip from PEMs of varying thickness. A decrease in plateau desorption force, detachment length and a transition from equilibrium to non-equilibrium desorption is observed within a few double layers. For thicker films, bulk behavior dominates, which is mainly determined by the way a polymer interlocks with the PEM. Through the interphase, a crossover from substrate influence (equilibrium desorption) to cohesion dominance (non-equilibrium desorption) is revealed. The complexation of PE chains due to charges is not decisive, while geometrical interlock dominates in bulk region.

Chapter 6

Adhesion Mechanisms on Polystyrene Films

Apart from hydrophilic surfaces observed in Chapter 5, thin Si supported polymer films of polystyrene (PS) are investigated by means of SMFS. These presented measurements allow to understand the adhesion mechanisms of a molecular force sensor in contact with the boundary layer of a thin polymer film.
Spin coated PS films (scPSs) [304, 305, 306] are compared to covalently surface-attached polystyrene films (saPSs) that enable to measure under different solvent conditions [61, 62, 307, 308]. The saPSs have been prepared by surface-initiated anionic polymerization, after substrate functionalization with two different types of 1,1-diphenylethylene (DPE)-based initiator precursors. Most parts of this chapter are published in ref. [309].

6.1 Molecular Adhesion on Spin Coated Polystyrene

6.1.1 Desorption Behavior

The desorption of PS has been performed on annealed scPSs on Si with thickness values of 6, 10, 21 and 52 nm (Table 6.1 and Appendix B.5). The RMS surface roughness of these films, determined by intermittent-contact AFM measurements, is below 0.5 nm. As the PS chains are not covalently attached to the Si substrate, they dewet [310, 311, 312, 313, 314], when immersed into polar solvents such as H_2O. Annealing of the scPSs at 90 °C (above the glass transition temperature of such thin films [315]) for 45 minutes leads to a film stability in H_2O within the time frame of the SMFS experiments (Table 6.1). These experiments are performed with PS as molecular force probe in H_2O, which constitutes the limiting case of a poor solvent, also referred to as a non-solvent (Section 2.1.3). Thus, the repulsive PS-PS interaction, such as in good solvents, is expected to be minimal. But how do the polymer chains interact at all?
Analogous to Section 5.3, two typical types of F_z-z curves are obtained. The first type (denoted as type 1) is characterized by plateaus of constant force $F_{plateau}$, with the force dropping to zero as soon as the polymer detaches (Figure 6.1 a, upper curve). In the present experiment, the detached polymer shows a length z_{det} of about 160 nm, corresponding to about 67 kDa. Another typical F_z-z motif (denoted as type 3) represents non-equilibrium stretching and rupture events (Figure 6.1 a,

Substrate	Thickness by XRR (nm)	Contact angle before (°)	Contact angle after SMFS (°)	RMS roughness by AFM (nm)
Si	-	19 (±11)	28 (±6)	-
No.1	6	-	-	-
No.2	10	55 (±28)	23 (±9)	-
No.3	21	74 (±22)	43 (±32)	-
No.4	52	74 (±22)	57 (±32)	-
No.1a	6	91 (±2)	76 (±20)	4.5
No.2a	10	98 (±4)	93 (±4)	0.6
No.3a	21	96 (±2)	95 (±4)	0.4
No.4a	52	97 (±2)	94 (±3)	0.4

Table 6.1: Overview of scPSs. No.1-No.4 denote scPSs and No.1a-No.4a annealed scPSs. Thickness values are determined by XRR, static H_2O contact angles taken before and after SMFS and RMS roughness given by AFM (intermittent-contact mode) images (1 x 1 μm^2) in H_2O at a scan rate of 0.5 Hz. The decrease of static contact angle of scPSs hints towards dewetting, while an increase for Si is assumed to be due to contamination and aging [306]. Adapted from [309].

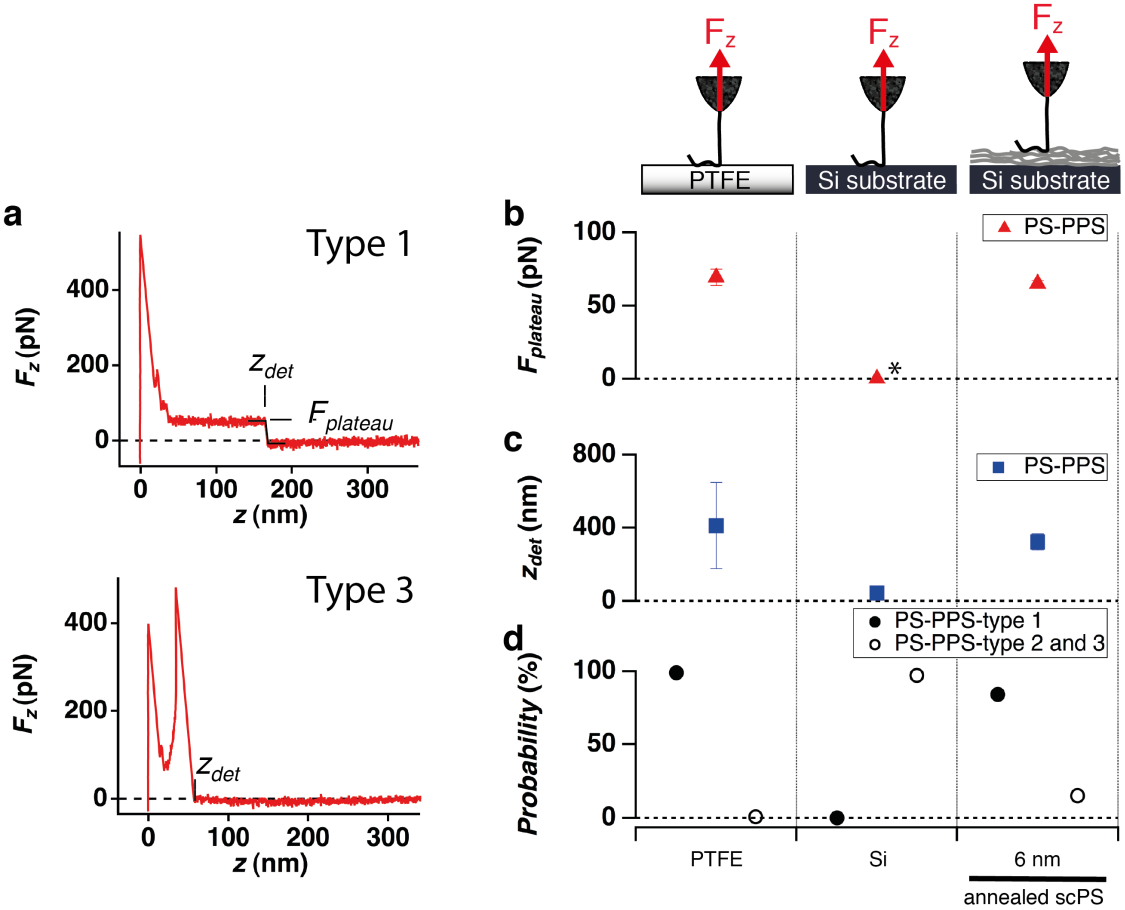

Figure 6.1: Desorption behavior on scPSs. (a) Type 1 F_z-z curves exhibit (equilibrium) plateau desorption, type 3 constitutes a non-linear F_z-z relation, representing non-equilibrium events. (b) $F_{plateau}$, (c) z_{det} and (d) probability of type 1-3 curves for the desorption of PS-PPS from PTFE, Si and annealed scPSs in H_2O. The dwell time and pulling velocity are set to 1 s and 1 $\mu m \cdot s^{-1}$. Errors correspond to the standard deviation. *No plateau events are observed. Adapted from [309].

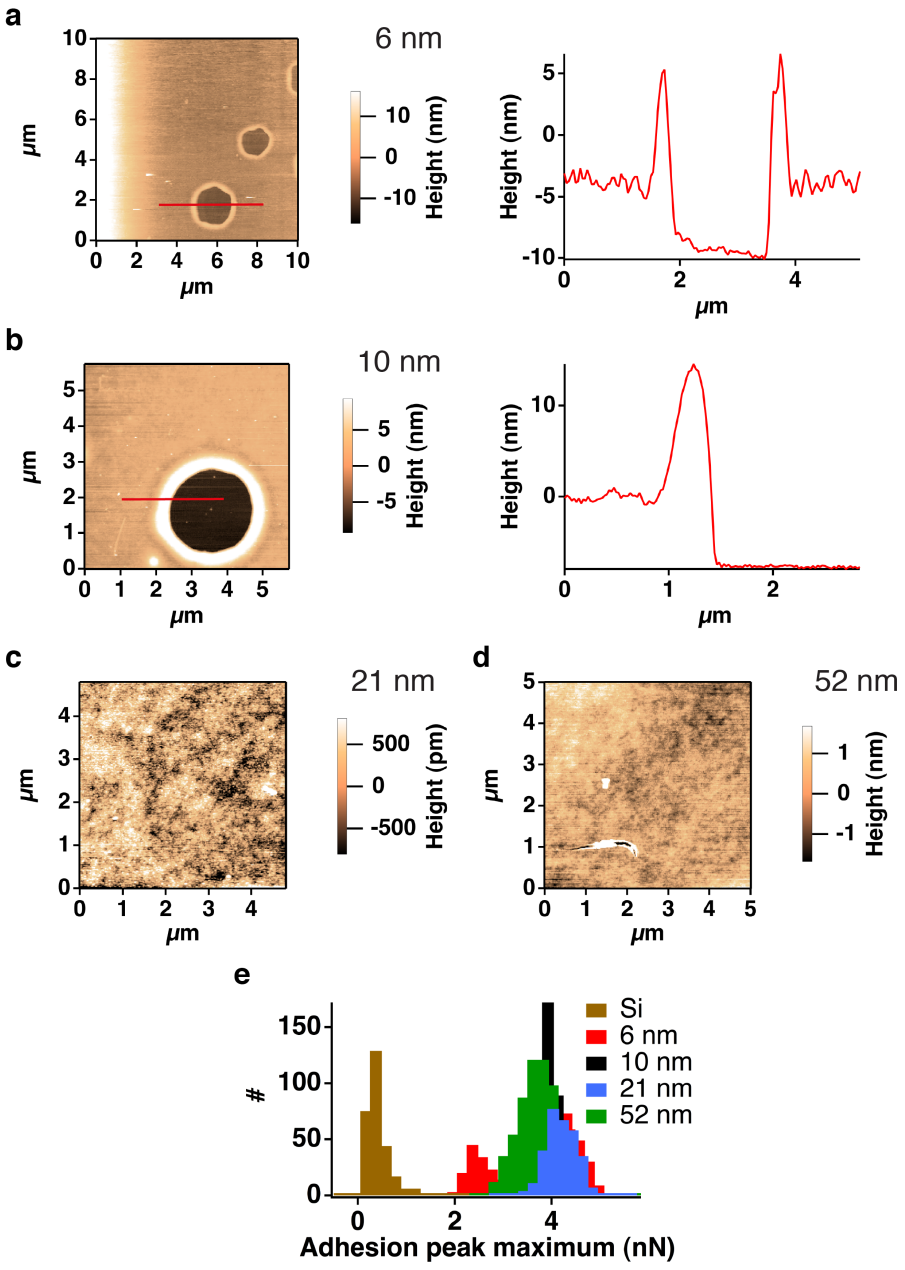

Figure 6.2: Dewetting behavior of scPSs. (a) AFM (intermittent-contact mode) image in H_2O and cross section of 6 nm thick layer shows about 6 nm deep holes due to dewetting. (b) AFM image in H_2O and cross section of 10 nm thick film. The dewetting structures are observed much less than on thinner samples. (c) AFM images in H_2O of 21 nm and 52 nm reveal intact and stable films. (d) Adhesion peak maximum of SMFS measurements with PS-PPS force sensors in H_2O. The partly dewetted 6 nm thick sample shows two distinct peaks. Adapted from [309].

lower curve). The occurrence of both motifs is indicated as type 2.
PS in H_2O on the 6 nm thick annealed scPS reveals a similar $F_{plateau}$ value as on the hydrophobic PTFE substrate (Figure 6.1 b). This results mainly from hydrophobic interaction and water structural effects, as discussion in refs. [171, 181, 147]. The z_{det} values are in a comparable range for PTFE and the annealed scPS sample, except for bare Si (Figure 6.1 c). While type 1 curves dominate on PTFE and on 6 nm annealed scPS, mostly type 3 curves are observed on Si (Figure 6.1 d). Surprisingly, all annealed samples of films thicker than 10 nm do not show any single polymer adhesion events.

6.1.2 Dewetting Behavior

In order to figure out the difference between the scPSs of different thickness, AFM images of the scPSs are taken (Figure 6.2). Similar to non-annealed films, the thin scPS (6 nm) dewets under H_2O exposure (Figure 6.2 a,b), with hole structures surrounded by rims of high roughness. By contrast, thicker annealed scPSs remain stable during many long and repeated measurements (Figure 6.2 c). Figure 6.2 d shows the distribution of the adhesion peak maximum (which accounts for the whole tip-scPS interaction) of several scPSs. The thinnest annealed scPS reveals two peaks, with one resulting from the PS film and the other from the dewetted spots. The thicker scPS samples lead to a monomodal adhesion peak maximum distribution, which means that those scPSs remain intact on the time scale of the presented experiment. The dependence of the characteristic dewetting time τ on the film thickness h leads to the differences in scPS stability. While the time for nucleation and growth scales with h^3, spinodal dewetting time increases with h^5 [316, 317, 318]. The hole structures constitute a highly non-equilibrium state. Yet the rim shape takes a smoother shape with ongoing dewetting [313]. Independent from the exact dewetting type, thin films are prone to dewetting. In fact, this is due to high mobility in the PS film boundary region [319, 320].

6.2 Molecular Adhesion on Surface-Attached Polystyrene

6.2.1 Film Characterization

Dewetting can be prevented by covalent coupling of PS to the Si substrate. Therefore, surface-initiated anionic polymerization is applied as technique of choice to produce well-defined saPSs on Si substrates [62, 307]. In general, "grafting-from" methodologies are able to reach higher grafting densities compared to the "grafting-onto" approach. In particular, this becomes decisive for the modification of flat substrates due to the steric hindrance of surface-attached polymers [321, 322]. Such films enable measurements in different types of solvents.
Here, two different types of DPE-based initiator precursors are synthesized for surface-initiated anionic polymerization of styrene in a similar manner as reported by Advincula et al. [308]: 4-(11'-triethoxysilylundecanyl)diphenylethylene (TEOS-DPE) and 4-(11'-trichlorosilylundecanyl)diphenylethylene (TCS-DPE) (Appendix B.6).
Surface-initiated anionic polymerization for PS has the advantage of avoiding the presence of disturbing reagents, such as transition metals or ligands, which may

influence the intended adhesion experiments. "Free" polymerization, i.e. polymerization of styrene in solution, by adding sacrificial initiator for the determination of PS molar masses [323, 324, 325], has not been possible for the herein described procedure. Still, strong differences between polymers grown on surfaces compared to those in solution are predicted by Wittmer et al. [326]. It can be assumed that all PS chains are formed by initiation of the immobilized initiator. The advantage is that films on the Si substrate are formed exclusively by PS chains and are not influenced by free PS chains. Unfortunately, molar masses of PS cannot be determined by subsequent cleavage [323, 324] due to the lack of material (with a Si substrate area of about 2.3 cm^2) for further analysis [307, 327]. The saPS thickness can be obtained by scratches (Figure 6.3), similar to Dodoo et al. [247].

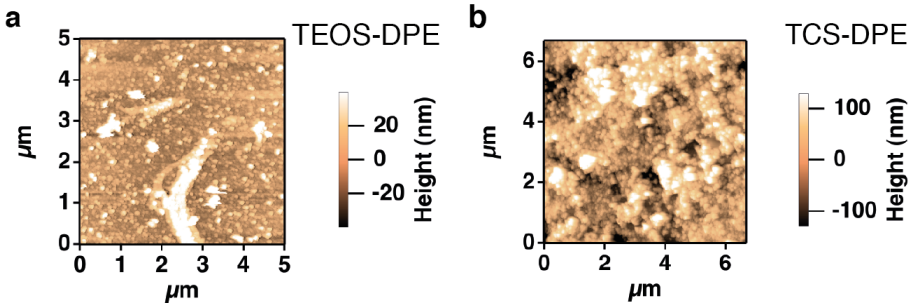

Figure 6.3: Topography of saPSs. AFM (intermittent-contact mode) images in H_2O of saPSs prepared with (a) TEOS-DPE and (b) TCS-DPE. Adapted from [309].

Composition	**Thickness**		**Contact angle**	
	Ellipsometry (nm)	**AFM (nm)**	**before (°)**	**after SMFS (°)**
Si+ TEOS-DPE+ PS	2.5 (oxide layer) 3 (silane) **total:** 17	15(±9)	-	91 (±4)
Si+ TCS-DPE+ PS	2.2 (oxide layer) 0.8–1.1 (silane) **total:** 35.5 (±1.3)	83(±24)	114 (±9)	118 (±8)

Table 6.2: Overview of saPSs. Thickness by ellipsometry and (intermittent-contact mode) AFM imaging in air (20 °C and r.h. 20-30 %), static H_2O contact angles, taken before and after an SMFS experiment for saPSs prepared with TEOS-DPE and TCS-DPE initiator precursors. The different thickness values, observed in particular for the TCS-DPE sample, are due to inhomogeneity of the sample. While AFM imaging detects the local thickness variation, ellipsometry averages over a large film surface area. Furthermore, contact angles are sensitive to the topmost surface composition, which depends on surface morphology and grafting densitiy [308]. Adapted from [309].

Several techniques use the compression of polymer films with an AFM cantilever, having a colloidal probe attached to its end. These experiments are based on the scaling behavior of grafted polymer films, as discussed in Section 2.1.6. In the presented data, a sharp AFM cantilever tip with a tip radius of about 10 nm is used. Knowing the contour length of the grafted polymer chains, the grafting densities can be determined [328, 324, 327]. The so-called equilibrium thickness L_e of the solvent-swollen polymer layer is given as the critical extension from the substrate.

For an extension greater than L_e no repulsive force, originating from steric interaction between the polymer layer and the cantilever tip, can be detected. The true thickness is a sum of the offset thickness L_0 of the film and the constant compliance extension L', beyond which the sample is no more compressible. L_0 is obtained by intermittent-contact AFM imaging of the polymer layer across the boundary of a scratched and an unscratched region (Figure 6.4 a). For L', the onset of repulsive interaction between cantilever tip and polymer film can be analyzed, using the approach curves (Figure 6.4 b). As the contour length N of the PS chains cannot be determined independently, measurements in different environmental conditions lead to a rough estimation of the grafting density Γ and the contour length N [329]. Here, H_2O and chloroform, $CHCl_3$ are used as different solvents:

$$L_e = 12^{\frac{1}{3}} \pi^{-\frac{1}{3}} N \Gamma^{\frac{1}{3}} \omega^{\frac{1}{3}} \nu^{-\frac{1}{3}} \tag{6.1}$$

$$N = 10.74 \cdot L_{e,CHCl_3}^{\frac{3}{2}} L_{e,H_2O}^{-\frac{1}{2}} nm^{-1} \tag{6.2}$$

with the excluded volume parameters $\omega = (2\ \text{Å})^3$ and $\nu = 3a^{-2}$ with $a = 6.7$ Å as the Kuhn length for PS.
Finally, the total equilibrium extension $L_e = L_0 + L'$ results to 14 nm in H_2O and 45 nm in $CHCl_3$ for TEOS-DPE and 76 nm in H_2O and 149 nm in $CHCl_3$ for TCS-DPE. This leads to $N = 867$ and $\Gamma = 0.03$ nm^{-2} for TEOS-DPE and $N = 2241$ and $\Gamma = 0.06$ nm^{-2} for TCS-DPE. The TCS-DPE substrate is more hydrophobic than TEOS-DPE, as macroscopically measured by the static contact angle of H_2O with a value of 114 (±9)° and 91 (±4)° (Table 6.2).

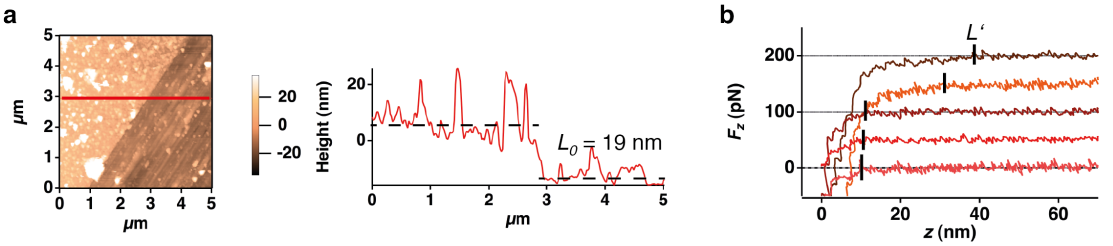

Figure 6.4: Grafting density of saPSs. (a) AFM imaging data of saPSs of a 5 x 5 μm^2 area scratched with a scalpel: TEOS-DPE in $CHCl_3$ and the respective cross section indicated by the red line. The thickness results in L_0. (b) Typical F_z-z approach curves for PS on TEOS-DPE in $CHCl_3$. Here, the constant compliance extension L' can be determined for every single curve. The different L' values result from the local thickness variations. The curves are vertically offset by 50 pN. Adapted from [309].

6.2.2 Desorption Behavior

Desorption experiments on saPSs are performed with hydrophobic PS-PPS and hydrophilic PLL as molecular force sensor in H_2O (Figure 6.5). H_2O is a poor solvent for PS and thus results in a compact and collapsed saPS structure [64]. Most interestingly, both types of molecular force sensors show similar behavior. Hence, the adhesion mechanism is independent of the hydrophobicity of the force sensor molecule.
While the static contact angle underlines that TCS-DPE is more hydrophobic than TEOS-DPE (Table 6.2), they lead to the same qualitative desorption behavior. TCS-DPE reveals a higher $F_{plateau}$ value (type 1 and 2) and a higher probability of plateau occurrence than TEOS-DPE (Figure 6.5 a,c). Yet, many F_z-z curves show

a non-linear force-extension behavior (Figure 6.5 c).
While $F_{plateau}$ values are centered around 50-60 pN on TEOS-DPE and 70-80 pN on TCS-DPE, those taken on TEOS-DPE in $CHCl_3$ (where the saPS is in a more extended conformation due to self-repulsion of the PS chains) are around 10 pN (Figure 6.5 a). This slight decrease in $F_{plateau}$ with surface hydrophobicity and sharp drop of $F_{plateau}$ with solvent quality is similar to that of desorption on hydrophobic solid substrates [181, 147] (Section 2.4.2). Furthermore, the $F_{plateaus}$ behavior correlates with the probability of type 1 curves (Figure 6.5 c). By contrast, the z_{det} distribution is independent of saPS hydrophobicity or solvent quality and takes values around 200-400 nm (84-168 kDa) with a quite broad z_{det} distribution (Figure 6.5 b,e).
While covalent bonds, like the C-C bond, are reported to break at more than 1 nN [23, 25], the force peaks for type 2 and 3 remain below these forces. Still, the work for polymer desorption E_{des}, which is given by the area under the F_z-z curve, is around 10^3 k_BT (Figures 6.6 and 6.8). This strong interaction is observed both in H_2O and in $CHCl_3$.

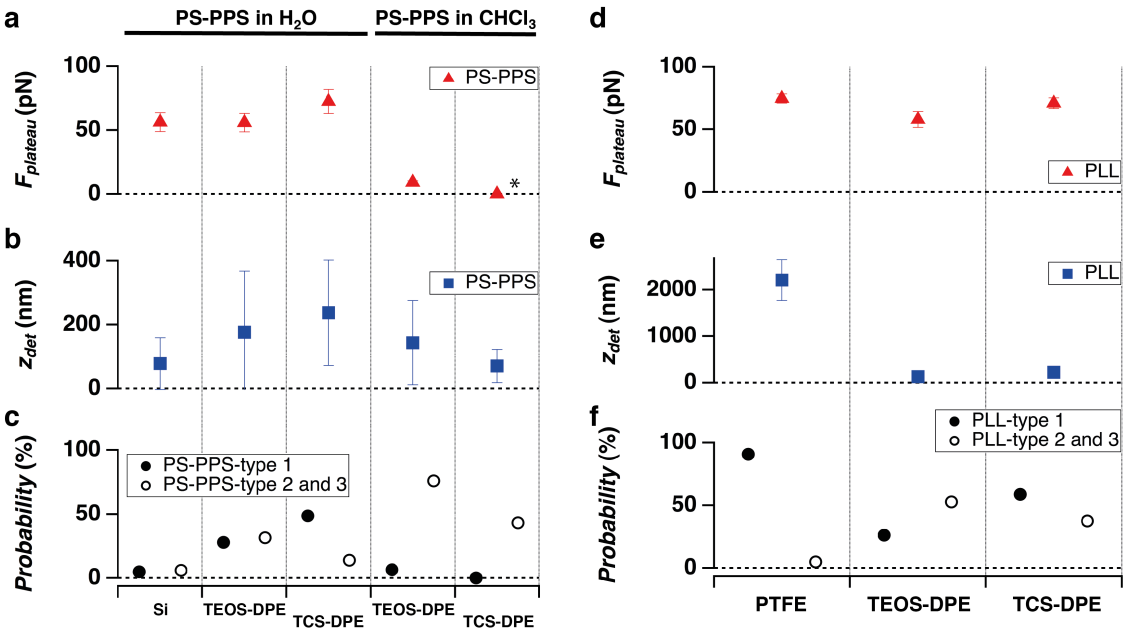

Figure 6.5: Desorption behavior on saPSs. (a) $F_{plateau}$, (b) z_{det} and (c) probability of curve type occurrence for PS-PPS on Si, TEOS-DPE and TCS-DPE in H_2O, and PS-PPS on TEOS-DPE and TCS-DPE in $CHCl_3$. (d) $F_{plateau}$, (e) z_{det} and (f) probability of curve type occurrence for PLL on PTFE, TEOS-DPE and TCS-DPE in H_2O. The dwell time on substrate is 1 s and the pulling velocity is 1 $\mu m \cdot s^{-1}$. *The $F_{plateau}$ value is set to 0, when no plateau events are observed. The errors correspond to the standard deviation. Adapted from [309].

6.3 Geometrical Interlock Dominates Molecular Adhesion

Two different adhesion mechanisms can be detected in desorption experiments. While the first comprises plateau-like F_z-z curves (type 1), the second is described by non-linear events (type 3), representing stretching and rupture events.
Type 1 curves are mainly observed on dewetted scPSs, but to a lesser extent, on

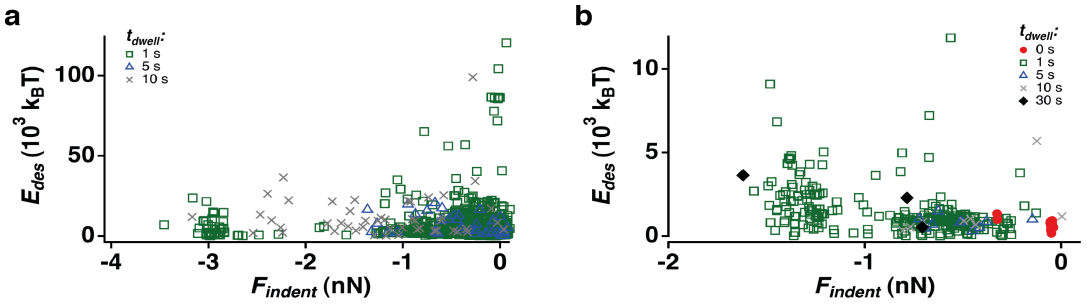

Figure 6.6: Dependence of desorption energy on indentation force and dwell time. Desorption energy E_{des} vs. indentation force F_{indent} for PS-PPS on TEOS-DPE in (a) H_2O (b) in $CHCl_3$. Different dwell times t_{dwell} between 0 s and 30 s are used prior to desorption of PS-PPS molecule. The data are taken at a pulling velocity of 1 μm·s^{-1}. Adapted from [309].

saPSs in H_2O. A constant plateau force during desorption hints towards undetectably low PS-PS or internal friction in the experienced velocity regime. This remains true for both slip or DS in a lateral pulling experiment such as discussed in Chapter 4. Such events can happen even below the glass transition temperature, likely because the glassy saPS exposes a rather fluid boundary layer to the liquid environment.

By contrast, type 3 curves go hand in hand with low in plane polymer mobility. In case of PS-PS, electrostatic interaction cannot explain this behavior, as there are no charges present. In addition, the hydrophilic PLL shows similar results (Figure 6.5 d-f).

As the obtained findings cannot be explained by electrostatic effects, hydrophobic interaction or covalent bonds, another model has to be considered. Similar to Chapter 5, a geometrical interlock model is introduced. While the single polymer is desorbed from the film, it is subject to a constraint. This constraint leads to relaxation times that are much higher than the time scale of the vertical pulling motion. Upon desorption, the polymer is stretched up to a point, where the tip bound polymer is finally released. As expected, vertical pulling seems to shorten the time to overcome the energy barrier, which keeps the molecular force sensor locked in the PS film.

While type 2 and 3 curves occur rarely on dewetted scPSs, they are very frequent on saPSs (Figures 6.1 and 6.5). This finding is consistent with the larger chain length of 91 kDa and 233 kDa compared to scPSs with 7 kDa. The long PS chains enable the formation of entanglements and exhibit much higher relaxation times.

In all cases the z_{det} values are considerably shorter than for PS-PPS and PLL (200-400 nm) on hydrophobic solid substrates like PTFE, i.e. the polymer interacts only partly with the PS film (Figure 6.5).

The molecular force sensor, having a coiled conformation, is pushed into the film boundary layer due to the indentation force F_{indent}. While a part of the force sensor polymer interlocks with the PS film, another part might remain coiled on top of the PS film. Upon retraction, the molecular force sensor is desorbed (type 3 traces) with the non-interlocked tail detaching all in one, similar to the behavior on solid substrates (Section 4.6). While this explains the shortening of z_{det}, variations in local PS conformation in the boundary layer lead to the broad distributions for z_{det}.

Both variation of indentation force F_{indent} and dwell time t_{dwell} do not show any significant change in desorption energy E_{des} and $F_{plateau}$ (Figure 6.6 a and Figure

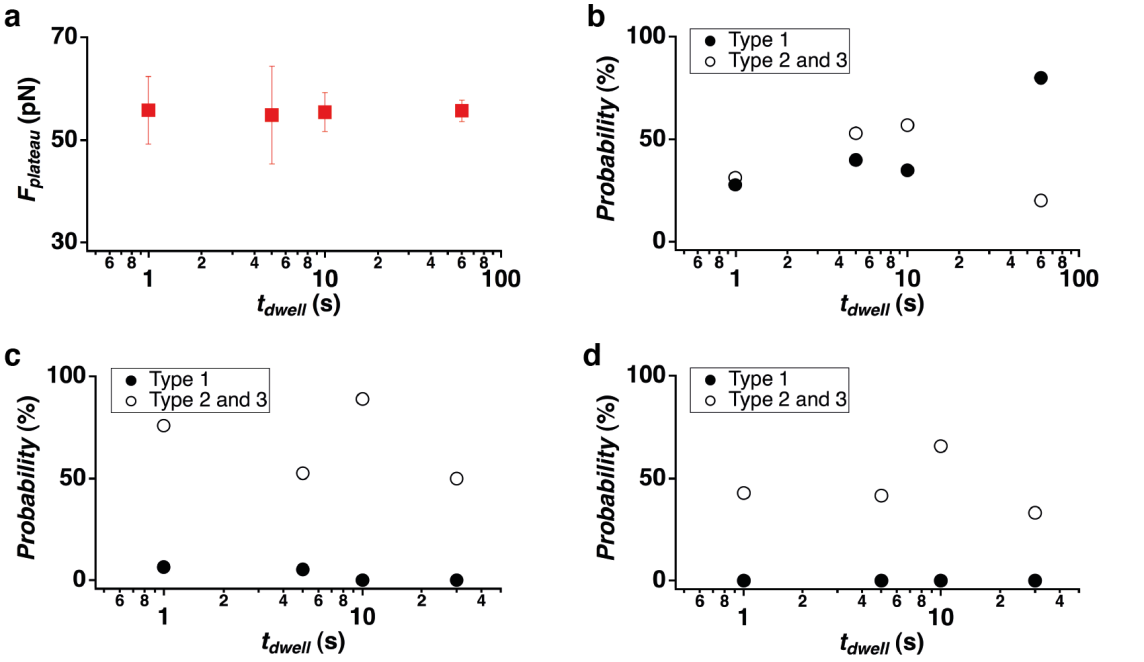

Figure 6.7: Dependence of desorption force and curve type occurrence on dwell time. (a) $F_{plateau}$ vs. dwell time t_{dwell} of PS-PPS on TEOS-DPE in H_2O. (b) Probability of curve type occurrence vs. t_{dwell} of PS-PPS on TEOS-DPE in H_2O. (c) Probability of curve type occurrence vs. t_{dwell} for PS-PPS on TEOS-DPE in $CHCl_3$ and (d) Probability of curve type occurrence vs. t_{dwell} for PS-PPS on TCS-DPE in $CHCl_3$. The pulling velocity is 1 $\mu m \cdot s^{-1}$. The errors correspond to the standard deviation. Adapted from [309].

6.7 a,b). In the usual range of the presented experiments (-0.1 nN to -1 nN), no indentation force dependence is observed (Figure 6.6 a). In fact, even low F_{indent} values lead to penetration of the PS film boundary layer at short contact times ($<$ 1 s). The layer underneath the boundary film region is not penetrated even after long dwell times and strong indentation forces. This finding sustains the assumption that the PS film consists of a rather fluid boundary layer and a rather glassy state underneath the boundary layer (Section 6.4).

Type 2 and 3 curves are much more pronounced in a good solvent such as $CHCl_3$, which is consistent with results by Thormann et al. [330]. Longer dwell times and higher indentation forces even favor those curves (Figure 6.6 b and Figure 6.7 c,d). A slight increase of E_{des} with indentation force F_{indent} is only observed, when using $CHCl_3$ as solvent (Figure 6.6 b). At the same time, the forces during rupture are found to be similar (Figure 6.8). This supports the entanglement hypothesis: a good solvent increases the likelihood of loops and tails and the possibility for entanglement formation, while the force to rupture entanglements once they are formed remains similar.

In summary, a geometrical interlock model (Figure 6.9) is required by several observations: First, similar results for two very different polymers (PS or PLL) are obtained. Therefore, electrostatics, hydrophobic interaction and covalent bonds have been excluded as an specific mechanism. Second, type 2 and 3 curves show that the polymer is pulled under a strong constraint, which leads to stretching of the polymer (Figure 6.9 a,b). The vertical pulling velocity is far higher than the time, which the polymer needs to release itself from the PS film. Third, the increase of type 3 curves for a saPS in $CHCl_3$ can be explained by polymer tails, which are now accessible for the molecular force sensor (Figure 6.9 c).

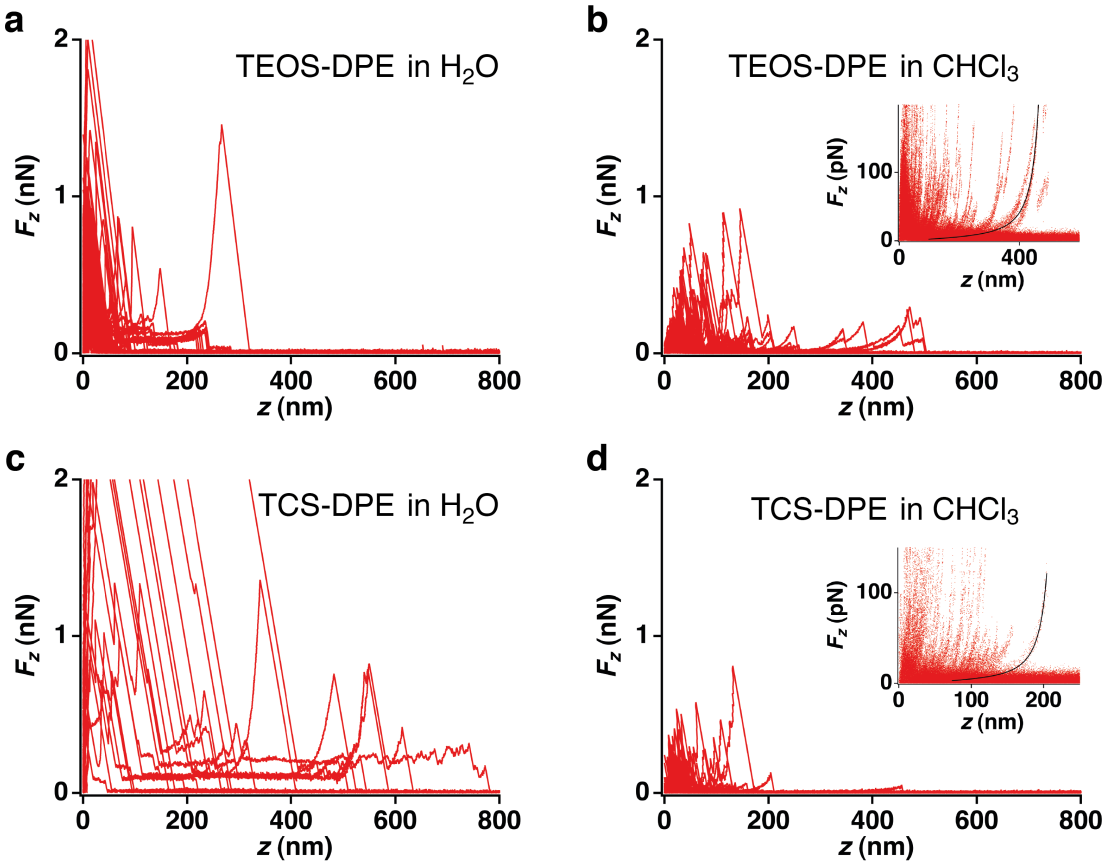

Figure 6.8: Solvent dependence of non-equilibrium events. Overlay of about 100 F_z-z curves of type 2 and 3. PS-PPS on (a) TEOS-DPE in H_2O, (b) TEOS-DPE in $CHCl_3$, (c) TCS-DPE in H_2O and (d) TCS-DPE in $CHCl_3$. Zoom-ins show fits for selected curves using the WLC model (Section 2.1.7). Adapted from [309].

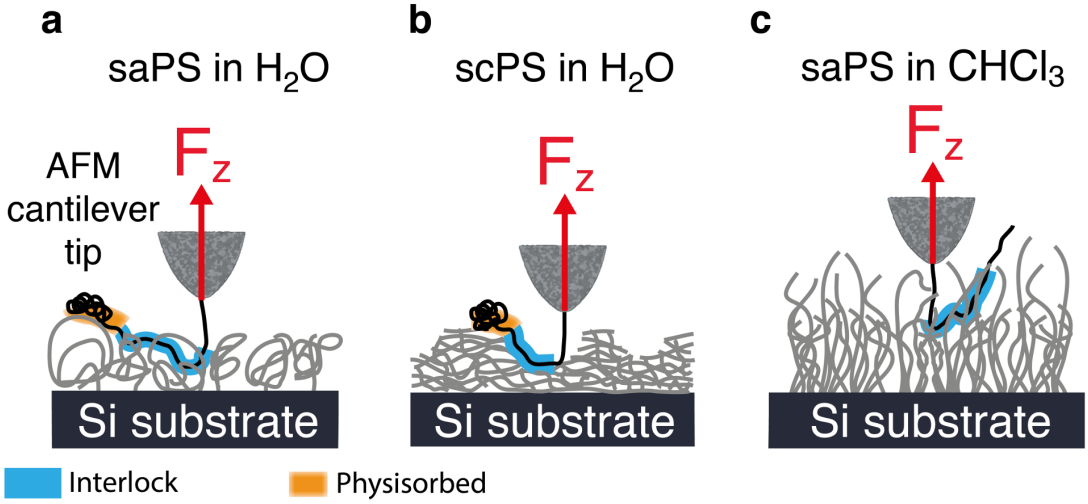

Figure 6.9: Adhesion mechanisms of a molecular PS force sensor on PS films. (a) SaPS in a poor solvent such as H_2O. Boundary layers are in a more liquid state, favoring the molecular force sensor to entangle into the film. Interlocked parts are indicated in blue. (b) Annealed scPS in H_2O. As long as no dewetting takes place, the molecular force sensor cannot entangle into the film. (c) SaPS in $CHCl_3$. Here, the saPS is in a more stretched conformation, which favors the geometrical interlock mechanism in comparison to H_2O. Adapted from [309].

6.4 Boundary Layer Affects the Adhesion Behavior below Glass Transition Temperature

The desorption behavior of PS on saPSs in $CHCl_3$ reveals mostly type 3 events. Interlock is formed, once the PS molecule is pushed into the PS film mesh. Such events are observed in H_2O and with dewetted scPSs as well. So, there is evidence that geometrical interlock is possible in H_2O well below T_g. This is surprising as entanglement formation is not expected in a glassy polymer state.
While the glass transition temperature T_g for bulk PS is about 100 °C [331], the T_g behavior of polymer films has been a contentious issue in the past two decades. A decrease of T_g of thin polymer films compared to bulk has been observed with decreasing thickness for Si (or rather Si oxide), supported and free standing thin polymer films (both spin casted and end grafted) [332] with ellipsometry [242, 333], x-ray reflectivity [334], lifetime analysis of positron annihilating in nanometer voids [335], local thermal analysis [331], dielectric techniques [336] and surface plasmon resonance [337]. This trend is very sensitive to the interfacial energy of the substrate [334] and the mass of the PS [338] but independent of sample preparation (spin-casting, grafting or Langmuir- Blodgett-Kuhn technique) [337]. The T_g of PS on Si oxide decreases by as much as 25 °C below the bulk value for 13 nm thick films [331]. Dynamic wetting of liquid droplets could even show that T_g decreases to 72 °C for ultrathin films of 4.5 nm [339]. T_g values decrease with decreasing film thickness irrespective the atmosphere (ambient, dry nitrogen, and vacuum) [340].
Apart from a change in T_g, a glass forming liquid consists of different regions, which can be described by a layer model with a highly mobile surface layer existing on top of a less mobile bulk layer. While these regions are structurally indistinguishable, they differ in their dynamics [338, 315]. This is in line with single molecule fluorescence microscopy experiments that show a fraction of polymers with a higher mobility close to the polymer-air interface for thin supported PS films below T_g. This leads to a heterogeneous T_g profile perpendicular to the substrate [341, 342].
In order to explain the geometrical interlock model for type 2 and 3 curves on scPSs and saPSs at room temperature, a further aspect has to be considered. Loop formation has been theoretically expected [343] and experimentally investigated by SFA measurements of polymer coated substrates by Maeda et al. [12]. There, the mobility of two cross-linked polymer interfaces being sheared turned out to be orders of magnitude lower than that of uncross-linked polymer interfaces. In the latter case, polymers are free to enter the adjacent polymer film. For a scPS, annealing prevents loop formation, if no dewetting can take place. By contrast, dewetted scPSs or saPSs with a high RMS roughness certainly bear loops in their boundary region. Thus, molecular force sensor chain is free to entangle with the adjacent polymer film (Figure 6.9 a).

6.5 Conclusion

The desorption behavior of single hydrophobic and hydrophilic polymers on either spin coated PS films and surface-attached PS chains on Si substrate in poor and good solvents leads to the following results: on annealed scPSs adhesion of PS-PPS in a poor solvent, such as H_2O, is hardly observed. For dewetted scPSs and saPSs in poor

solvent, equilibrium desorption events comparable to hydrophobic solid substrates are found. This is in line with the glassy state of the scPS below the glass transition temperature and collapsed conformation of the PS film in H_2O. Surprisingly, non-equilibrium stretching and rupture events are obtained as well. This is even more pronounced in good solvents for the PS film, such as in $CHCl_3$. These findings can only be explained by a geometrical interlock mechanism between the molecular force sensor and the polymer chains in the PS film boundary region (Figure 6.9). The constraints between these polymers cannot be released on the time scale of the desorption experiment. For films consisting of long PS chains, such as for the presented saPSs, entanglement formation is the basis for geometrical interlock. The geometrical interlock model is consistent with a heterogeneous T_g profile of thin PS films and loop formation in the boundary region. Hence, the tremendous impact of the boundary region and its conformation on the adhesive behavior of thin polymer films can be probed by single polymer desorption.

Chapter 7

Single Polymer Dynamics on Thin Polymer Films

Energy dissipation due to friction and wear can be reduced by coating substrates with a lubricating polymer layer [12]. Precise understanding of tribological behavior is required for the design of an appropriate coating. Besides technological applications, the friction mechanisms of polymer coatings play a crucial role for biolubrication such as in articular joints [344, 345, 346, 347].
The lateral pulling technique presented in Chapter 4 enables to investigate polymer dynamics at the nanoscale by contacting supported polymer films with single polymers covalently bound to an AFM cantilever tip [248]. Using this single polymer approach, the polymer-polymer interaction can be probed in the boundary region of a polymer film due to low steric repulsion effects. Therefore, friction mechanisms that are investigated for such coatings correspond to the case, where polymer films are sheared under high compression leading to strong interpenetration. As the cantilever is pulled actively, a much faster response is achieved than purely diffusion-based methods [348, 341, 342].
Here, two different model substrates are investigated: first, PEMs on Si, where the lateral mobility of adsorbed chains plays a great role for reaching equilibrium conformation and for the swelling behavior [297], as discussed in Chapter 5. The second type of polymer films comprises saPSs as given in Chapter 6.

7.1 The Role of Polymer Coatings for Lubrication

Polymer coatings have been investigated in detail in the last two decades by means of the pin-on-disk method [349], the SFA [7, 12, 5, 350, 351, 352, 353], surface force balance [354, 355, 356, 357, 358, 359] and AFM colloidal probe technique [360]. A high reduction of friction coefficient is observed due to coatings, in particular using PEs. These reveal extremely low friction coefficients of as low as 0.006-0.0001 [355, 357, 358, 359, 360] and show self-healing [352]. The main reason for this lubrication effect is the steric repulsive interaction between polymers from opposing layers [354, 355, 356, 358, 351, 359]. This effect is even more pronounced with charged polymers. A hydration layer forms between those polymer layers [354, 355, 357, 358, 359, 361]. Though, the compression of the coating layers yields to increased friction forces with stick-slip motion and wear effects due to interpenetration of the opposing polymer films upon compression [7, 107]. The extent

of the interpenetration layer between the opposing charged polymer brushes, in particular the number of sheared polymer segments within the interpenetration region, dominate the energy dissipation [362, 354, 358, 350, 351, 352, 360]. This holds true regardless of the degree of ionization and the presence of added salt [363], and is observed for both charged as well as neutral polymer layers [355, 356]. While interpenetration can be described by the Rouse model (Section 2.1.8) for short chains, large chain dynamics require reptation theory [362] (Section 2.1.8).

7.2 Complex Stick-Slip Motifs

The three friction motifs that are described in Chapter 4, are slip, DS and CS. Here, these motifs appear in combination. These complex motifs have to be distinguished carefully and are then transformed into statistics by counting the number of curves with the respective motive appearing alone or in combination with the other motifs, normalized by the number of overall curves with at least one friction motif. DS events are distinguished from slip events by taking any event as DS, where the force F_z decreases by at least half of the noise (which is about 10 pN). DS events followed by a sudden increase to the initial F_z value or less are interpreted as a DS-slip event. CS events are characterized by increasing F_z in a non-linear way (with a force increase of at least 10 pN). Consecutive CS events are usually accompanied by polymer segment desorption or slip events after each CS event. Overall decrease in F_z with non-linear spikes are counted as DS-CS events. Altogether, the following combinations of friction motifs are observed: slip-DS, slip-CS, DS-CS, slip-DS-CS. Still, the distinction of many motifs might be challenging and can give only approximate values of motif transition points for lateral extension x. This becomes even more complicated, when several polymer segments interact with the polymer film or desorb during lateral pulling. Any F_z-x curve shown are representative for at least 50–100 F_z-x curves.

7.3 Stick-Slip on Polyelectrolyte Multilayers

At first, lateral pulling on PEMs is observed with PLL in H_2O on $(PSS/PDADMAC)_4$ prepared in 0.1 M NaCl. A vertical force F_z vs. lateral extension x plot is given in Figure 7.1 a. The first polymer segment shows DS until it desorbs. Between 15 and 60 nm a slip event is followed by a series of CS-slip events until final desorption of the last polymer segment at 180 nm.
Next, PLL is laterally pulled over coated and scratched areas of $(PSS/PDADMAC)_{14}$ prepared in 0.1 M NaCl. The sample used is analyzed by AFM imaging as shown in Figure 5.2. On both areas stick-slip events are observed (Figure 7.1 b,c). Figure 7.1 b represents a DS event until about 200 nm of lateral extension x with a detachment of a polymer segment. A plateau of constant force F_z with a desorption event at 250 nm follows. Then, a sudden increase in force is observed, which hints towards a stretching event, before the last polymer detaches and the force drops down to 0 at 285 nm. CS events might be due to the interaction of the cantilever tip bound polymer with the Si substrate or some PSS, PDADMAC or PEI (initial layer) residues in the scratch area.

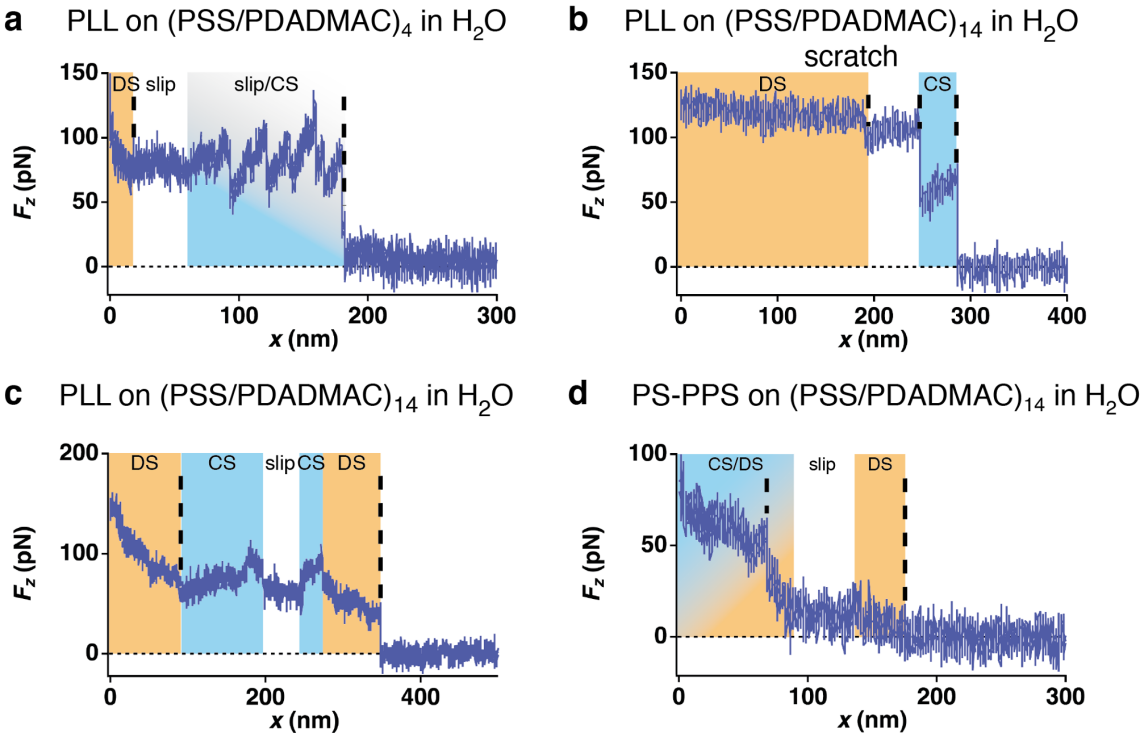

Figure 7.1: Stick-slip behavior on PEMs. Typical F_z-x curves. (a) PLL force sensor on $(PSS/PDADMAC)_4$ prepared in 0.1 M NaCl. (b,c) PLL on $(PSS/PDADMAC)_{14}$ prepared in 0.1 M. NaCl across scratch and PEM region. (d) PS-PPS on $(PSS/PDADMAC)_{14}$ prepared in 0.1 M. DS is indicated in orange, CS in blue. The dashes black lines denote the detachment of a polymer segment.

Figure 7.1 c shows a more complex F_z-x curve taken on an area completely coated by PSS/PDADMAC layers. The first polymer segment exhibits DS until about 80 nm of lateral extension, before desorbing from the PEM layer. Then, the last adsorbed polymer segment shows CS until 180 nm. Afterward, the polymer relaxes and slips over the PEM until 245 nm. After another CS event, a final DS process occurs from 270-350 nm and then detaches from the substrate. Although the F_z-x curves taken on $(PSS/PDADMAC)_{14}$ show many DS (60 % of the friction events), most of the friction motifs are CS events (80 %). The detailed statistics for different PEM substrates are given in Figure 7.3.
Furthermore, PS-PPS as molecular force sensor is laterally pulled over a $(PSS/PDADMAC)_{14}$ sample (Figure 7.1 d). Here, an alternation of CS and DS events, where the first polymer segment desorbs at 68 nm, is followed by a slip event between 90 and 140 nm. A final DS event occurs before desorption of the last segment at 180 nm.

7.4 Stick-Slip on Polystyrene Films

For comparison, hydrophobic saPSs are used. PS films have been frequently used as model systems for fundamental investigations of polymer film stability and film mobility [364, 365, 366, 367, 245]. Due to grafting, a saPS makes measurements under different solvent conditions possible, without risking dewetting.
For PLL on saPS (TEOS-DPE) in H_2O, slip-DS motifs are found (Figure 7.2 a). After a DS event of the PLL segment starts, the polymer slips over 110 nm until

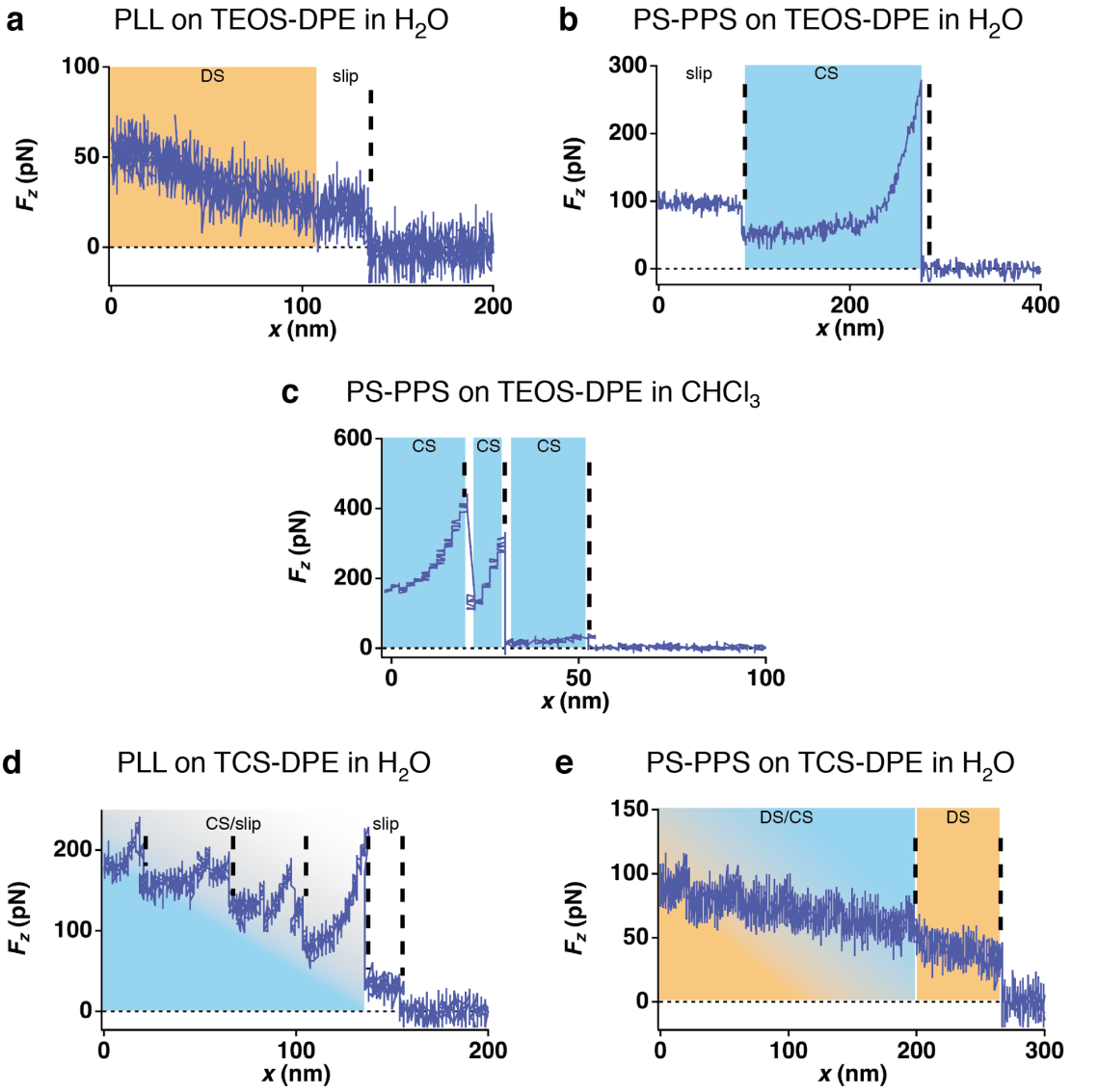

Figure 7.2: Stick-slip behavior on saPSs. Typical F_z-x curves. (a) PLL on TEOS-DPE in H_2O. (b) PS-PPS on TEOS-DPE in H_2O. (c) PS-PPS on TEOS-DPE in $CHCl_3$ (d) PLL on TCS-DPE in H_2O. (e) PS-PPS on TCS-DPE in H_2O. DS is indicated in orange, CS in blue. The dashes black lines denote polymer the detachment of a polymer segment.

detachment from the TEOS-DPE at 135 nm.
Most F_z-x curves resemble Figure 7.2 b. Here, PS-PPS is pulled over TEOS-DPE in H_2O. The upper force plateau is constant until 90 nm of lateral extension, where the first polymer segment detaches from the PS film. The lower force plateau corresponds to a slip event of the last polymer segment. Before final polymer detachment from the saPS at 275 nm, a CS event starts with a high force peak. Figure 7.2 b reveals a typical curve with CS, which is the main motif, such as in case of PEMs. While measurements in H_2O show DS and slip events (Figure 7.2 a,b), those in $CHCl_3$, reveal a more pronounced frequency of CS events (Figure 7.2 c). $CHCl_3$, being a good solvent for PS, causes the TEOS-DPE to swell due to the repulsive interaction of the grafted PS chains. This makes it easier for the cantilever tip bound polymer (several 100 nm length) to entangle with the polymer tails of the PS film. CS events, observed either in H_2O or $CHCl_3$, reveal force peaks with similar magnitude. The same qualitative results are obtained on saPSs with TCS-DPE precursor as well (Figure 7.2 d,e).
Figure 7.3 presents an overview of the frequency of friction events for PEMs with different layer number (4 and 14 layers of PSS/PDADMAC) prepared in either 0.1 M NaCl and 0.5 M NaCl. While all PEMs evidence a high amount of CS events, the slip motif is more pronounced on scratched PEM areas. Furthermore, Figure 7.3 summarizes the saPS behavior. Again, CS events dominate with both PS-PPS and PLL. In $CHCl_3$, these CS events are even more frequent, while slip and DS events vanish. These findings contrast with the results on solid substrates in Chapter 4. There, a solid hydrophobic substrate such as PTFE probed by PS-PPS in H_2O leads to a high amount of DS. A PS-PI block copolymer (PS-PI-PS-COOH) on PTFE in $CHCl_3$ shows mostly slip behavior.

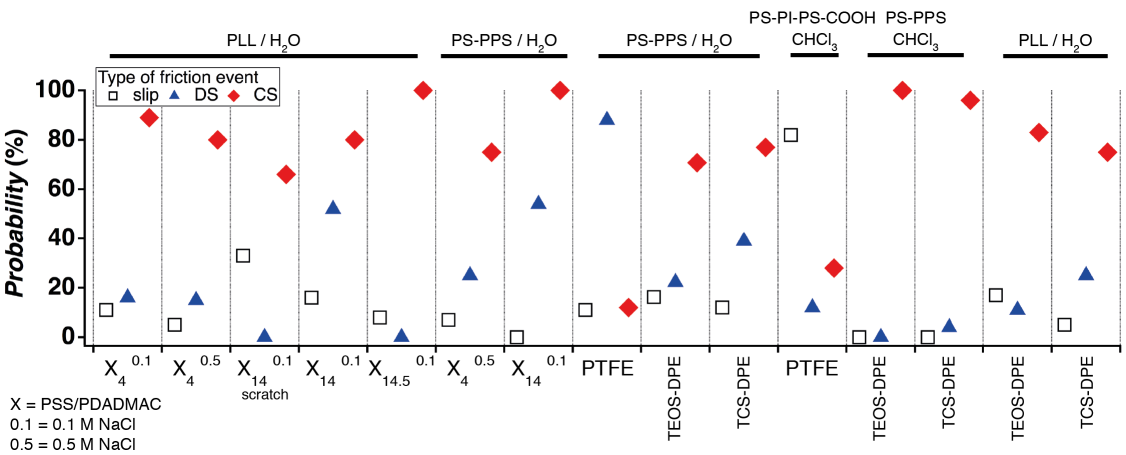

Figure 7.3: Occurrence of friction motifs. Frequency of slip, DS and CS events in lateral pulling F_z-x curves for PS-PPS, PS-PI-PS-COOH and PLL on various PEMs in H_2O and PTFE in H_2O as well as saPSs (with TEOS-DPE or TCS-DPE precursor) in either H_2O and $CHCl_3$. The figure comprises about 1200 curves.

7.5 Geometrical Interlock Dominates Stick-Slip

In fact, every single trace can be explained by a succession of slip, DS and CS. First, slip means that the sensor molecule and the surface attached polymer are able to slip past each other without strong bonds (Figure 7.4 a). Second, for DS the cantilever

tip bound molecule has to be confined at a certain position feeling a lateral constraint that prevents the polymer from slipping over the underlying film. Therefore, desorbing into solution is more favorable. Still, the internal friction is quite low, which is analogous to the behavior on solid substrates. Thus, the film confines the polymer chain attached to the cantilever tip in two dimensions (Figure 7.4 b). In a three dimensional energy landscape, the probability to overcome the vertical barrier is much higher than the lateral. Third, CS requires strong directional bonds or a constraint that prevents the polymer chain from following the cantilever tip motion (Figure 7.4 c). Ionic bonds, salt bridges or hydrogen bonds can be assumed as a source of energy dissipation for CS (Section 4.5).

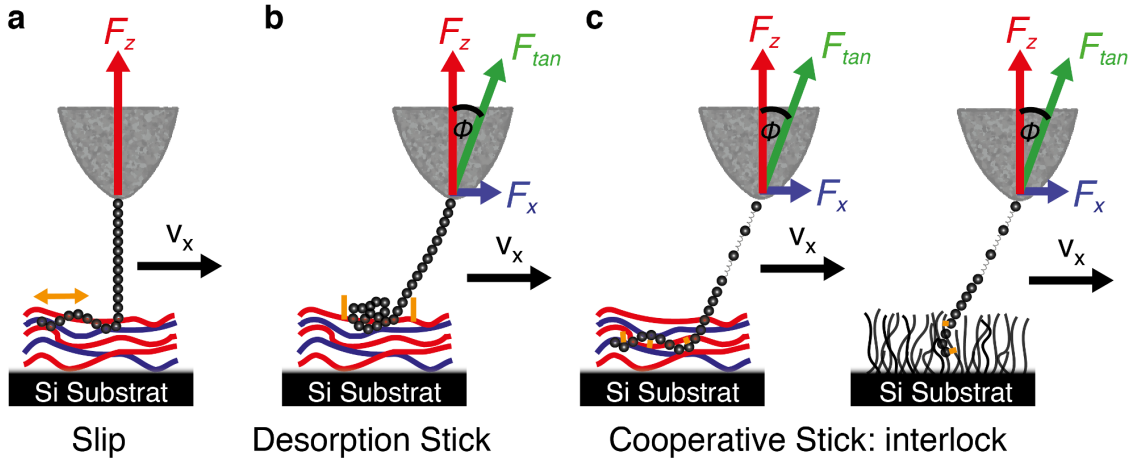

Figure 7.4: Schematic representation of friction motifs. (a) Slip means that the polymer can slip over the film without any confinement or constraint. The orange arrow indicates high mobility. (b) DS is characterized by confinement in two dimensions, indicated by orange sticks. This motif is preferentially observed on PEMs and saPSs under poor solvent conditions (such as H_2O). (c) CS results from confinement in three dimensions, indicated by orange sticks. The formation of entanglements turns out to be the dominating mechanism.

In case of PEMs probed with PLL, a possible mechanism for CS could be the formation and breakage of ionic bonds, while the polymer is pulled laterally. Surprisingly, both hydrophilic and hydrophobic force sensor polymers (PLL, PS-PPS) indicate similar CS behavior (Figure 7.3). Therefore, a model, independent from the chemical interactions (such as ionic bonds), has to be considered. Such a mechanism can be geometrical interlock.

Upon contact of the cantilever tip bound polymer with the boundary layer of the polymer film, entanglements can be formed (Figure 7.4 c). Those are in particular responsible for the cohesion of polymer layers. As already discussed in Chapter 6, high molecular weight polymers (100 nm corresponding to 40 kDa for PLL and 42 kDa for PS-PPS) for molecular force sensors and PEMs as well as saPSs make the formation of entanglements possible. CS-slip events correspond to alternating entanglement and disentanglement events. This mechanism resembles the solid-like (high friction) to liquid-like (low friction) transition obtained for stick-slip behavior of surfactant coated surfaces [7]. Here, a Deborah number of about 1 is assumed, where energy dissipation is maximal [21].

Entanglement formation due to polymers that are free to enter the adjacent polymer film, has been discussed as reason for increased friction and adhesion hysteresis between uncross-linked polymer coatings [12, 359]. This mechanism is even valid for PS films below glass transition temperature T_g [12].

As the results on saPSs show slip and DS events at room temperature (25 °C), where the saPSs are in a glassy state, a liquefied boundary region is required to explain the CS events due to geometrical interlock. This finding is sustained by a heterogeneous T_g profile perpendicular to the substrate with a highly mobile surface layer on top of a less mobile as experienced by Flier et al. [342].
Hence, geometrical interlock is experienced far below T_g. This leads to high energy dissipation, mainly due to CS events. Still, the probability of CS increases even further for PS-PPS on saPSs in $CHCl_3$ (Figure 7.3). In that case the grafted PS chains can swell in solution, providing more free chain tails to entangle with the cantilever tip bound PS-PPS molecule. Therefore, the possibility of entanglement formation correlates well with the probability of CS events.
This is in contrast with the assumption that increased mobility in the boundary polymer film results in low friction. Klein et al. [354, 355] even assume that polymer films with low T_g provide better lubrication. Furthermore, good solvent conditions are known to increase the mobility in the boundary film region, leading to lower friction [368, 353, 360]. This contradiction can be solved: here the AFM cantilever tip bound polymer is pushed into the PS film. This contrasts with bulk experiments, where the repulsion between polymer chains does not allow interpenetration, in particular at low loads or low normal force. Therefore, the presented approach is able to probe the local properties of a single polymer chain with the boundary region of a polymer film under high load conditions.
The velocity for the presented data ranges between 0.03 and 4.52 $\mu m \cdot s^{-1}$. Although low velocities show more slip events, a minor effect is observed, both for PEMs and saPSs. Irrespective of the polymer-substrate-solvent combination, high velocities lead to CS. From the macroscopic point of view, a transition from stick-slip to slip is expected for high velocities [362, 12, 359]. This limit for the critical velocity can be of the order of 1 $mm \cdot s^{-1}$ or even higher depending on the chain length [349]. The range of velocities presented here, is far below any such critical velocities. So, a high occurrence of stick-slip is in line with macroscopic findings.
For entanglement formation on the single molecule scale, a more appropriate quantity with regard to the presented single polymer approach is the time for release of the constraints and the relaxation of the polymer. From the high occurrence of CS events and consecutive CS-slip events, the time scale for release can be estimated to milliseconds. For short polymers, Casoli et al. [349] indicate an upper limit for the relaxation time of 100 ns. The relaxation time is expected to increase with higher interpenetration [355]. In addition, the molecular force sensors have contour lengths of several hundred nanometers. Thus, the longer relaxation times are consistent with the presented lateral pulling data.
The lateral mobility for PEMs has been investigated by TIRF microscopy [289] or fluorescence recovery after photobleaching (FRAP) [290]. There, the diffusion coefficients are of the order of 0.1 $nm^2 s^{-1}$ [290]. For PSS/PDADMAC multilayers, the diffusion coefficient near the film-solution interface is about one order of magnitude higher than inside the multilayer. This proves the assumption that the layers are more loosely packed in the outer layers due to minor interdigitation of polyelectrolyte chains due to extrinsic charge compensation. Therefore, PE charge density and salt concentration affect the polymer mobility in the film. Furthermore, solvent conditions can affect the PE mobility. Finally, Nazaran et al. [290] could show that the mobility in PEMs increases with increasing distance to the supporting substrate

and decreasing distance to the upper interfacial layer.
The transition from equilibrium to non-equilibrium adsorption, as given in Chapter 5, is in line with these findings. SMFS probes the upper interfacial layer. The underlying PE layers cannot be reached and are in a rather glassy state. Temperature increase leads to a solid-liquid transition and thus a high diffusion coefficient (Section 5.3.5). At the same time, the probability of interpenetration increases, which leads to an increase of type 3 curves. In fact, non-equilibrium desorption curves and CS friction motif mean that the boundary layer conformation of the film is in a more loose state.

7.6 Conclusion

The friction behavior of single PLL and PS-PPS polymers on hydrophilic and hydrophobic polymer coated substrates, such as PEMs and saPSs, can be elucidated by lateral pulling in a liquid environment. Any single polymer friction trace can be described by either CS, DS or slip. A high amount of CS is obtained for both PEMs and saPSs. By contrast with the general view that stick-slip consists of slip and CS, the presented data show that a further friction mechanism, DS, does contribute to the stick-slip behavior. Still, the dominating mechanism is obviously CS. The high occurrence of CS can be explained by a geometrical interlock model, based on entanglement formation, and is enhanced under good solvent conditions. This underlines the importance of the dynamic behavior of polymer film boundary layers, even below glass transition temperature.
Furthermore, the dynamic behavior of polymer films, in particular in the boundary layer region, is important for their self-healing ability. Such self-repair mechanisms show a complex time dependent behavior, as indicted by Stukalin et al. [88].

Chapter 8

Outlook

AFM-based single polymer friction experiments allow for the discovery and characterization of friction mechanisms on solid substrates in liquid environment. Apart from slip and cooperative stick (CS), a third and yet unknown friction motif, the desorption stick (DS), is detected and explained. This novel motif is independent of normal force, velocity and adsorbed polymer length, which contrasts with friction models based on Amontons' law and the Rouse model. Furthermore, the succession of slip and desorption stick, similar to macroscopic stick-slip, is discovered. Desorption and friction experiments on thin polymer films reveal that a geometrical interlock mechanism is responsible for non-linear force-extension (non-equilibrium desorption) curves and the high occurrence of CS for lateral pulling.
The high potential of AFM-based single polymer experiments can be extended by an alternative approach, using TIRF microscopy to investigate the adsorption and the lateral mobility of single labeled polymers at the solid-liquid interface (Appendix C).

Future work should investigate the effect of different salts on single polymer friction, in particular for PEMs. Friction and desorption experiments with PS- and PI-based block copolymers should be extended by investigating the role of bulky polymer side chains, such as in case of dendronized polymers [369] or comb-like polymers for friction and adhesion. The friction behavior of single polymers on membranes, embedded in membranes [370, 371] or on specific biological samples such as cartilage would be of high importance [344, 345]. As self-healing coatings have a tremendous potential for many adhesion and friction related applications, such polymer systems, based on non-covalent bonds with the underlying substrate [86, 88], can be probed using the method established in this thesis. Furthermore, a profound understanding of the geometrical interlock mechanism for polymer films is needed. Dynamic polymer chain properties should be studied with systematic variation of the solvent condition, of the temperature and of the molar masses of the polymer film chains as well as of the single molecule force sensors.
An upscaling of the experimental scale is required in order to close the gap between single molecule approaches and macroscopic findings. After investigating single polymers on polymer films, the same systems should be probed using friction force microscopy (FFM). Experiments on a nanotribometer and a macroscopic tribometer could complete those results. Here, cartilage, consisting of a matrix of various proteins such as aggrecan and lubricin, could be a fascinating biologically and medically important system [344, 345, 347, 346, 13].

A similar upscaling approach could be performed in the field of lubricant and surface coating design. To that aim, this thesis has been accompanied by friction force microscopy (FFM) experiments in the context of the PEGASUS project (Project number 0327499A-G, Federal Ministry of Economics and Technology, BMWi) [372]. This project aims to understand and to use the superlubricity effect of diamond-like carbons (DLCs) for future automotive applications. Carbon-based materials, summarized as DLC, have a great potential for industrial applications as they combine high lubricity, anti-adhesive properties, chemical stability and extreme material hardness. DLCs are known to have tremendously low friction coefficients in the range of 0.0001 (superlubricity) [9, 10, 11, 373, 374, 375].

The findings, presented in this thesis, can serve as a basis to understand polymer behavior at the nanoscale. Future experiments and simulations will benefit from these single polymer experiments in order to design novel lubricants and surface terminations.

Appendix A

Molecular Force Sensor Synthesis and Preparation

A.1 Synthesis of Polystyrene-Based Polymers

Markus Gallei and Matthias Rehahn, TU Darmstadt

The following protocols are presented with the kind permission of Markus Gallei. Most of them are published in ref. [203].

Instrumentation

The nuclear magnetic resonance (NMR) spectra are recorded on a Bruker ARX 300 NMR spectrometer, working at 300 MHz (^{1}H-NMR) and 75 MHz (^{13}C-NMR) and on a Bruker DRX 500 NMR spectrometer, working at 500 MHz (^{1}H-NMR) and 125 MHz (^{13}C-NMR). NMR chemical shifts are given relative to tetramethylsilane (TMS).
Standard size exclusion chromatography (SEC) is performed with tetrahydrofuran (THF) as the mobile phase (flow rate 1 ml·min^{-1}) on a SDV column set (SDV 1000, SDV 100000, SDV 1000000, Polymer Standard Service, Germany) at 30 °C. Calibration is carried out using polystyrene standards from Polymer Standard Service (Germany).

Reagents

Chemicals and solvents are purchased from Acros, Aldrich and Strem chemical companies. Isoprene, styrene and propylene sulfide (PPS) are purified by 3-fold distillation over calcium hydride (CaH_2). Prior to use, the monomers are freshly distilled from those solutions. 1,1-diphenylethylene (DPE) is freshly distilled after titration with *n*-butyllithium (*n*-BuLi) from the deeply red solution. Succinic anhydride is sublimated twice under high vacuum and 35 °C prior to use, while tetrahydrofuran (THF) and cyclohexane (CH) are dried and deoxygenated following standard procedures. Deuterated solvents are purchased from Deutero (Germany). All syntheses are carried out under an atmosphere of purified nitrogen or argon, using Schlenk technique or a glovebox equipped with a Coldwell apparatus.

Synthesis of Poly(styrene-*b*-propylene sulfide), PS-PPS

In a glove box 3.6 g neat styrene is dissolved in 150 ml dry CH in an ampoule and 22 μl of a 0.13 M *sec*-butyllithium (BuLi) solution is added quickly via a syringe at room temperature. The mixture is stirred at room temperature for 48 h to ensure complete conversion. A sample is taken for SEC measurements. 110 mg of freshly distilled PPS is added and the solution is stirred for 30 minutes. 50 ml precooled THF (-30 °C) is added and the solution is stirred for further 3 h at 0 °C. After that time, degassed methanol (MeOH) is added to finish the reaction. The polymer is precipitated in MeOH, filtered and dried in vacuum. Finally, the polymer is stored in a fridge at -15 °C under argon atmosphere.

Characterization via NMR:
^{1}H-NMR (CD_2Cl_2): δ = 0.45-2.30 (aliphatic backbone), 2.45-2.61 (CH-S), 2.66-2.93 (CH_2-S), 6.25-7.20 part per million (ppm) (aromatic).

Characterization via SEC:
M_n = 1.26 MDa PDI = 1.06

Synthesis of Poly(styrene-*b*-isoprene-*b*-styrene-*b*-propylene sulfide), PS-PI-PS-PPS

In a glove box 2.31 g neat styrene is dissolved in dry 150 ml CH in an ampoule and 27 μl of a 1.3 M *sec*-BuLi solution is added quickly via a syringe at room temperature. The mixture is stirred at room temperature for 24 hours to ensure complete conversion. A sample is taken for SEC measurements. 2.63 g isoprene is added via a syringe and the mixture is stirred at room temperature for further 24 hours. A sample is taken for SEC measurements. The reaction solution is divided into two parts: one for characterization of the AB block copolymer and one for reaction with styrene and the endcapping reaction.
For further reaction, 15 ml of the living block copolymer precursor (3.5 μmol) is brought into an ampoule with 100 ml cyclohexane and 2.3 g styrene is added. The solution is again stirred for further 24 hours. A sample is taken for SEC measurement. 200 mg freshly distilled PPS is added and the viscous solution is stirred for 3 hours. 50 ml of precooled THF (-30 °C) are added and the solution is stirred for further 3 h at 0 °C. After that time, degassed MeOH is added to finish the reaction. The polymer is precipitated in MeOH and dried in vacuum. The polymer is stored in a fridge at -15 °C under argon atmosphere.

Characterization via SEC:
PI-PS-PPS

polyisoprene	M_n = 178 kDa	5 % 3,4- and 95 % 1,4-structure
poly(styrene-*b*-propylene sulfide)	M_n = 190 kDa	
poly(isoprene-*b*-styrene-*b*-propylene sulfide)	M_n = 368 kDa	PDI = 1.01

PS-PI-PS-PPSa

polystyrene	M_n = 117 kDa	
polyisoprene	M_n = 208 kDa	
poly(styrene-*b*-propylene sulfide)	M_n = 273 kDa	
poly(styrene-*b*-isoprene-*b*-styrene-*b*-propylene sulfide)	M_n = 598 kDa	PDI = 1.02

PS-PI-PS-PPSb

polystyrene	M_n = 65 kDa	
polyisoprene	M_n = 151 kDa	
poly(styrene-*b*-propylene sulfide)	M_n = 642 kDa	
poly(styrene-*b*-isoprene-*b*-styrene-*b*-propylene sulfide)	M_n = 858 kDa	PDI = 1.07

Synthesis and Endcapping of Poly(styrene-*b*-isoprene-*b*-styrene) with COOH, PS-PI-PS-COOH

In a glove box 2.31 g neat styrene is dissolved in dry 150 ml CH in an ampoule and 27 μl of a 1.3 M *sec*-BuLi solution is added quickly via a syringe at room temperature. The mixture is stirred at room temperature for 24 hours to ensure complete conversion. A sample is taken for SEC measurements. 2.63 g isoprene is added via a syringe and the mixture is stirred at room temperature for further 24 hours. A sample is taken for SEC measurements. The reaction solution is divided into two parts: one for characterization of the AB block copolymer and one for reaction with styrene and the endcapping reaction.
For further reaction, 50 ml of the living block copolymer precursor (12 μmol) is brought into an ampoule with 100 ml CH and 2.8 g styrene is added. The solution is again stirred for further 24 hours. A sample is taken for SEC measurements. 4 μl DPE (2 eqiv. concerning the living chain ends) is added and the solution is stirred for further 48 hours. After that time, 12 mg succinic anhydride (10 eqiv.) in 10 ml THF is added and the deep-red color disappears immediately. After 30 minutes MeOH is added to terminate the reaction. The polymer is precipitated in MeOH and dried in vacuum. The polymer is stored in a fridge at -15 °C under argon atmosphere.

Characterization via NMR:
^{1}H-NMR (CD_2Cl_2): δ = 0.90-2.30 (aliphatic backbone), 4.55-4.80 (1.2-and 3.4-PI unsaturated), 4.90-5.20 (1.4-PI unsaturated), 6.25-7.20 ppm (aromatic).

Characterization via SEC:

polystyrene	M_n = 65 kDa	
polyisoprene	M_n = 151 kDa	
poly(styrene-COOH)	M_n = 232 kDa	
poly(styrene-*b*-isoprene-*b*-styrene-COOH)	M_n = 448 kDa	PDI = 1.01

A.2 Molecular Force Sensor Preparation

Reagents

- Vectabond reagent (Axxora, Germany) similar to (3-aminopropyl)triethoxysilane (APTES)
- Dry acetone (< 50 ppm H_2O, Acros organics or VWR, Germany)
- Dry chloroform ($CHCl_3$, > 99.9 %, Sigma-Aldrich or max. 0.003 % H_2O, SeccoSolv, Merck, Germany)
- Triethylamine (TEA, Thermo Fisher Scientific or Sigma Aldrich, Germany)
- Ultrapure water (sterile, suitable for HPLC, Biochrom, Germany)
- Borate buffer (50 mM, pH = 8.0, using di-sodium tetraborate and boric acid, Merck, Germany)
- Monofunctional α-methoxy-ω-NHS PEG, 5kDa (mPEG, Rapp Polymere, Germany)
- Homobifunctional α,ω-bis-NHS PEG, 6 kDa (di-NHS-PEG, Rapp Polymere, Germany)
- Heterobifunctional α-maleinimidohexanoic-ω-NHS PEG, 5 kDa (mal-hex-NHS-PEG, Rapp Polymere, Germany)
- N-Ethyl-N'-(3-dimethylaminopropyl)carbodiimid (EDC, Sigma-Aldrich, Germany)
- N-hydroxysuccinimide (NHS, Sigma-Aldrich, Germany)
- Tris/HCl solution (pH = 8.0) (> 99.9 %, neoLab, Germany)

Vectabond and PEG are hygroscopic and PEG is subject to oxidation in air. For that reason, both chemicals are stored at -20 °C under nitrogen or argon gas. To avoid frequent exposure of the stock to atmospheric oxygen and moisture, smaller aliquots are prepared, e.g. using a glovebox system with a nitrogen atmosphere. Aliquots, which have been warmed up and opened, are discarded after use. Chemicals with low H_2O content, such as dry acetone and dry $CHCl_3$ are taken in this protocol instead of aqueous buffers to minimize hydrolysis on reactive groups. Those are used rapidly and stored dry, but not longer than a week.

Procedure

Cantilever Cleaning and Activation

1. The cantilever chips are stored in dry $CHCl_3$ for 20 minutes after removal from gel pad box in order to dissolve any contaminants.
2. Then, the cantilever chips are placed in the evacuated reaction chamber of a plasma system at 0.05 mbar (TETRA 30 LF PC, Diener electronic, Germany)

or 0.1 mbar (FEMTO, Diener electronic, Germany) for half an hour. Oxygen is added up to a constant pressure of 0.1 mbar (TETRA) or 0.25 mbar (FEMTO). First, the cantilevers are exposed to oxygen plasma for 5 minutes at 600 W, followed by a second exposure for 20 minutes at 420 W (TETRA) or 15 minutes at 20 W (FEMTO).
The plasma process can be controlled by three parameters: electric power at 40 kHz, gas pressure and plasma exposure time. While pressure should be maintained to ensure homogeneity of the surface treatment, the other two parameters have to be adjusted according to the kind of cantilever material used in order to avoid extensive heating. At elevated temperatures above 80 °C the cantilevers will bend irreversibly. Heat dissipation can be enhanced by placing the cantilever chips on a (precooled) metal plate.
The plasma process both cleans the surface and enhances the bonding of Vectabond reagent, as described in the following [376].

3. Amino functionalization using Vectabond reagent:

   (a) The cantilever chips are quickly transferred from the plasma chamber and rinsed in dry acetone.

   (b) Then, they are immediately stored into a solution of 50 μl Vectabond reagent, dissolved in 2.5 ml dry acetone for 10 minutes.

   (c) The Vectabond solution is diluted by adding at least 5 ml dry acetone to the crystallising dish.

   (d) Afterward, the cantilevers are transferred into a new crystallizing dish with 10 ml dry acetone.

   It is essential to perform the transfer from the highly concentrated Vectabond solution into H_2O or dry $CHCl_3$ respectively as quickly as possible. Due to its high vapor pressure, acetone quickly evaporates and leaves behind an undefined multilayer of Vectabond reagent. The formation of air bubbles should be avoided. This treatment ensures the formation of only a monolayer of amino-terminated molecules on the tip surface and avoids possible polymerization when using aminosilanes.

4. The reaction with PEG (PEGylation) can only be performed by the reaction of the N-hydroxsuccinimidyl ester with amines in their deprotonated form. Storage in a buffer solution with pH of about 8-9 ensures that most of the amine groups on the cantilever surface are no longer protonated. This allows for a high yield during the following coupling reaction. Still, this step is not recommended for PEG coupling in $CHCl_3$. Due to immicibility of $CHCl_3$ with H_2O, the risk of still having H_2O adsorbed on a cantilever tip is high, when immersing the chips into $CHCl_3$. In that case, the PEG solution cannot reach the cantilever surface for reaction.

Cantilever PEGylation

1. The cantilevers are extensively rinsed in a crystallizing dish with 10 ml dry $CHCl_3$ to ensure that all remaining acetone has been removed.

2. Two different PEGylation protocols are presented. One for amine- and one for sulfhydryl-terminated polymers.

   (a) 37.5 mg of mPEG (5 kDa) is dissolved in 300 μl dry $CHCl_3$ (25 mM) with 5 vol. % TEA.

   (b) Preparation of bifunctional PEG:

      i. For later coupling of amine-terminated polymers:
      4.5 mg of di-NHS-PEG (6 kDa) is dissolved in 300 μl dry $CHCl_3$ (2.5 mM) 5 vol. % TEA and the di-NHS-PEG solution is further diluted in dry $CHCl_3$ with 5 vol. % TEA to 0.25 mM.

      ii. For later coupling of sulfhydryl-terminated polymers:
      4.5 mg of mal-hex-NHS-PEG (5 kDa) is dissolved in 300 μl dry $CHCl_3$ (2.5 mM) 5 vol. % TEA and the mal-hex-NHS-PEG solution is further diluted in dry $CHCl_3$ with 5 vol. % TEA to 0.25 mM.

   (c) The cantilevers are immersed in a 6:1 mixture (21 mM total PEG concentration) of mPEG and bifunctional PEG in a clean glass perti dish of 500 μl maximal volume for 45 minutes.

The flexible PEG linker not only prevents the free end of the sensor polymer from adsorbing at the tip surface, but also reduces the undesired, unspecific adhesion between tip and substrate material significantly by increasing the distance between the sensor molecule and the surface of the tip apex [168]. The molar ratio of monofunctional and bifunctional PEGs should be adjusted in order to observe a reduced unspecific adhesion peak and a single molecule while desorption.
Alternatively, PEGylation and the following coupling of the polymer can also be done in aqueous buffer solutions at pH 8-9 [179, 180]. However, the use of aqueous solution promotes hydrolysis of the active ester and needs thorough time management and very fast handling. This is difficult to control properly and results in only a moderate amount of functionalized cantilevers [377].

Binding of the Sensor Molecule to the Cantilever Tip

Binding of the sensor polymer can be performed in aqueous buffers or in organic solvents, such as $CHCl_3$, depending on the polymer solubility.

1. Binding poly (amino acids) in aqueous buffers:

   (a) The polymer is dissolved in in 50 mM borate buffer (pH = 8.0) at 1 $mg{\cdot}ml^{-1}$ to approximately 2 μM (max. 10 $mg{\cdot}ml^{-1}$ to 20 μM).

   (b) The cantilevers are thoroughly swayed in crystallizing dishes with 50 mM borate buffer (pH = 8.0).

   (c) The cantilever chips are placed in reaction tubes (at least 20 μl of polymer solution) such that the tips are immersed in the polymer solution for at least 2 hours in a box with high atmospheric humidity.

   Again, the use of aqueous buffer solution for polymer coupling promotes hydrolysis of the PEG active ester. There is the possibility to perform a buffer exchange and to transfer the polymer, which is to be used as sensor molecule, from its initial solvent to the coupling buffer by means of spin columns (Zeba

Spin Desalting Columns, Thermo Scientific) in a centrifuge. At concentrations of 1 mg·ml^{-1} (which equals 20 μM for a 50 kDa polymer) aggregation and precipitation rarely occur on the time scale of hours or even days at room temperature.

2. Binding of PPS-terminated PS- and PI-based polymers in dry $CHCl_3$:
   (a) The polymer used as molecular sensor is dissolved in dry $CHCl_3$ to maximum 2 μM (e.g. 1 mg·ml^{-1} for a 500 kDa polymer).
   (b) Then, the cantilevers are rinsed thoroughly in crystallizing dishes with dry $CHCl_3$.
   (c) The cantilevers are placed in the petri dishes (with 400 μl of polymer solution) such that the tips immerse the polymer solution over night (14 h) .

3. Binding of carboxyl-terminated polymers such as PS-PI-PS-COOH in dry $CHCl_3$:
   For carboxyl-terminated polymers, the PEG linker is not used. So the following steps are performed directly after amino functionalization of the cantilever tip.
   (a) The polymer used as molecular sensor is dissolved in dry $CHCl_3$ to maximum 2 μM (e.g. 1 mg·ml^{-1} for a 500 kDa polymer).
   (b) EDC is dissolved in 1 ml dry $CHCl_3$ with 5 vol. % TEA and diluted to 2.3 mM.
   (c) NHS is dissolved in 1 ml dry $CHCl_3$ 5 vol. % TEA and diluted to 0.23 mM.
   (d) Then, the cantilevers are swayed thoroughly in crystallizing dishes with dry $CHCl_3$.
   (e) The cantilevers are placed for 2 h in a 1:1:10 mixture of EDC, NHS and polymer solution in a clean glass perti dish of 400 μl maximal volume over night.

   Due to the high vapor pressure of $CHCl_3$, the cantilevers need to be stored in a box with $CHCl_3$ atmosphere to prevent drying. Incubation times of up to 14 hours give the amino groups on the polymer the time needed to react with the NHS ester of the PEG linker molecules.

4. After withdrawing the cantilevers carefully from the reaction tubes, unspecifically bound polymers are removed by rinsing the cantilever chips in a crystallizing dish with ultrapure H_2O or $CHCl_3$ respectively.

5. Optionally, the cantilevers are placed in 5 ml of 50 mM aqueous Tris/HCl solution (pH 8.0) for 10 minutes to quench the coupling reaction and to eliminate unreacted NHS groups.

6. Finally, the cantilevers are rinsed in H_2O and proceeded to force spectroscopy measurements immediately.

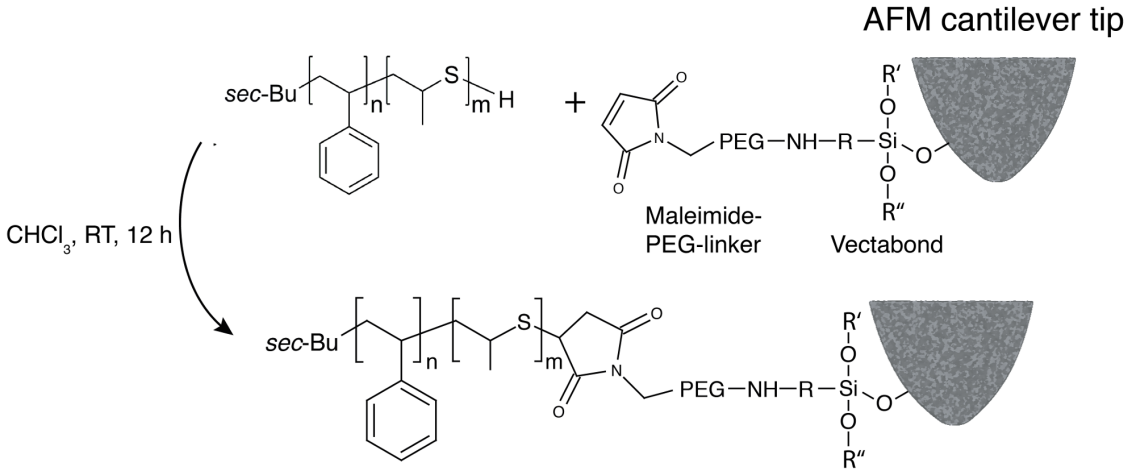

Figure A.1: AFM cantilever tip functionalization. Coupling scheme of PS-PPS to the linker system consisting of heterobifunctional PEG (such as mal-hex-NHS-PEG) after reaction with Vectabond bound to a Si_3N_4 AFM cantilever tip. Apdated from [248].

Appendix B

Substrate Preparation

B.1 PTFE

Samples of 1.5 mm thickness are purchased from GM (Germany).

B.2 Mica

Muscovite mica slides (11 x 11 mm^2, $KAl_2(OH,F)_2AlSi_3O_{10}$, Plano, Germany) are cleaved using a tape to gain an atomically flat and clean substrate. Tape residues are cleaned by immersing in acetone and drying with a gentle nitrogen stream prior to use. Furthermore, mica is inert against many solvents. A detailed description of the mica structure and a broad overview of different mica types are given in ref. [378].

B.3 Self-Assembled Monolayer

Self-Assembled Monolayers (SAMs) are prepared as discussed in refs. [379, 189]. Glass slides are cleaned for 15 minutes in an ultrasonic bath in 2 % Hellmanex solution (Hellma, Germany) and twice with ultrapure water (sterile, suitable for HPLC, Biochrom, Germany). After drying in air, the glass slides are coated by vapor deposition (Edwards, Germany) with a 10 nm layer of chrome and nickel as adhesion promoter, followed by a 100 nm Au layer.
The Au slides are cleaned in a RCA solution (5:1:1 solution of H_2O, 32 % ammonia, NH_3, and 35 % hydrogen peroxide, H_2O_2) at 70 °C for 15 minutes, rinsed with H_2O and dried under a gentle stream of nitrogen. Hydrophobic SAMs of are obtained by immersing the Au coated slides for 12 h in 2 mM 1-dodecanethiol (98+ %, Sigma Aldrich,Germany) in ethanol (absolute for analysis, Merck, Germany). Then, the SAMs are rinsed with ethanol and with H_2O. The slides are dried under a gentle stream of nitrogen and directly used for measurements.
SAMs exhibit a high mechanical stability due to the thiol-Au interaction, with a bond energy of about 120 $kJ \cdot mol^{-1}$ [380], which enables long time stability.

B.4 Polyelectrolyte Multilayer

Samantha Miciulla, Samuel Dodoo, Maximilian Zerball and Regine v. Klitzing, TU Berlin

Details about polyelectrolyte multilayer (PEM) synthesis and characterization are described elsewhere [381, 382]. The procedure given in this thesis refers to refs. [247, 248].
For PEM thickness determination with a polarizer-compensator-sample-analyzer (PCSA) ellipsometer, Multiscope (Optrel, Germany) is used with a wavelength of 632.8 nm and an incident angle of 70° (close to the Brewster angle of the Si/air interface) and 60° (solid/H_2O). A homemade humidity chamber of stainless steel, with rubber sealed windows on the sides for the light guides connected to the laser and detector arms of the ellipsometer, is equipped with a relative humidity (r.h.) sensor. The PEM thickness d and refractive index n are determined from measured Δ and Ψ values by the Elli software (Optrel, Germany) using a least squares fit with a four-layer box model: (i) air ($n = 1$) or H_2O ($n = 1.332$), (ii) multilayer, (iii) Si oxide ($d = 1.5$ nm; $n = 1.4598$) and (iv) Si ($n = 3.8858$, $k = -0.020$). For each PEM, both thickness and refractive index are fitted simultaneously without assuming a fixed refractive index. In case of PEMs with thickness less than 10 nm (1 and 2 double layers in 0.1 M NaCl and 1 double layer in 0.5 M NaCl), the Garnett equation [383] is used to cross check the obtained thickness and refractive index, showing no significant difference from those given by the software.
The linear poly(diallyl dimethyl ammonium chloride), PDADMAC, with 135 kDa (PDI = 1.75) and 5 kDa (PDI = 1.5) is synthesized by free-radical polymerization. Branched poly(ethylene imine), PEI, with 750 kDa and poly(sodium 4-styrene sulfonate), PSS, with 70 kDa (PDI = 2.5) are obtained from Aldrich (Germany). Low molecular weight PSS (6 kDa, PDI < 1.2) is bought from Polymer Standard Service (Germany). NaCl (99.9 %) is purchased from Merck (Germany). PEMs are prepared on Si substrates from AG Siltron (Korea).
First, the substrates are treated with piranha solution (sulfuric acid, H_2SO_4: H_2O_2, 1:1 v/v) in order to remove organic contaminants and to activate the surface for PE adsorption. The LbL technique is used for PEM deposition on Si wafers. While the Si substrates are immersed for 20 minutes in high molecular weight PEs, they are immersed for 5 minutes in low molecular weight PEs (for OEMs built-up) with a monomer concentration of 10^{-2} M in 0.1 or 0.5 M NaCl respectively. The short dipping time for OEMs is experienced to assure stable growth. After each deposition step, the films are rinsed with H_2O. A precursor PEI layer is deposited from salt-free aqueous solution by dipping clean Si substrates for 30 minutes and rinsing with H_2O. The presence of a PEI precursor layer is found to be efficient for a pronounced thickness increment and reduction of heterogeneity [384, 385]. The multilayers are dried with nitrogen after completion of the multilayer assembly process.

B.5 Spin Coated Polystyrene Film

Markus Schindler and Peter Müller-Buschbaum, TU München

X-ray reflectometry (XRR) is performed on a D8 Discovery (Bruker, Germany) and evaluated by using the Parratt algorithm to fit the measured data and to determine the film thickness of scPSs.
A spin coated polystyrene film (scPS) is synthesized using the protocol given in ref. [309]. The Si wafers are cleaned in an acidic bath consisting of deionized H_2O (54 ml), H_2O_2 (84 ml) and H_2SO_4 (198 ml) for 15 minutes at 80 °C [306]. Then, the substrates are rinsed with deionized H_2O and dried in a dry nitrogen flow. Polystyrene (PS, M_w = 7 kDa, M_n = 6.7 kDa, PDI = 1.04, Polymer Standard Service, Germany) is dissolved in toluene (Roth, Germany) to obtain polymer solutions with different concentrations. These solutions are spin coated at a velocity of 2500 rpm for 30 s. Then, the samples are annealed in vacuum at 90 °C for 45 minutes in order to avoid peeling or dewetting of the polymer film from the substrate during SMFS experiments in H_2O. Via XRR thickness values of 5.6 nm, 10.0 nm, 20.7 nm and 50.5 nm are determined, corresponding to concentrations of 1 g·l^{-1}, 2 g·l^{-1}, 4 g·l^{-1} and 10 g·l^{-1} respectively.

B.6 Covalently Surface-Attached Polystyrene Film

Katrin Sondergeld and Matthias Rehahn, TU Darmstadt

The synthesis and characterization of a covalently surface-attached polystyrene film (saPS) is described as given in ref. [309].

Instrumentation

Ellipsometric measurements for saPS thickness determination are done by an imaging ellipsometer (nanofilm EP3), equipped with an incidence beam wavelength of 658 nm. Incident angle variations are performed between 60° and 86°. For analysis the received angles Δ and Ψ are fitted with the ellipsometric analysis EP4 software. The NMR spectra are recorded on a Bruker ARX 300 NMR spectrometer, working at 300 MHz (^{1}H-NMR) and 75 MHz (^{13}C-NMR) and on a Bruker DRX 500 NMR spectrometer, working at 500 MHz (^{1}H-NMR) and 125 MHz (^{13}C-NMR). NMR chemical shifts are given relative to tetramethylsilane (TMS). The signal assignment is carried out according to the numbering of protons and carbons, as specified in the corresponding schemes (Figure B.1).

Reagents

All solvents and reagents are purchased from Alfa Aesar, Sigma Aldrich, Fisher Scientific, ABCR and Merck. Tetrahydrofuran THF, toluene and cyclohexane (CH) are distilled from sodium/benzophenone under reduced pressure (cryo-transfer) prior to the addition of DPE and *n*-BuLi followed by a second cryo-transfer. Styrene and divinylbenzene (DVB) are purified by 3-fold distillation over calcium hydride (CaH_2).

Prior to use, the monomers are freshly distilled from these solutions. Deuterated solvents are purchased from Deutero (Germany). 4-bromo-DPE and 4-(10´-undecenyl)-DPE are synthesized similar to Advincula et al. [308] and Zhou et al. [386]. All syntheses are carried out under an atmosphere of nitrogen, using Schlenk technique or a glovebox, equipped with a Coldwell apparatus.

Synthesis of 4-(11'-triethoxysilylundecanyl)diphenylethylene (TEOS-DPE)

In dry toluene (20 ml) 4-(10´-undecenyl)-DPE (4.41 g, 13.3 mmol, 1 eqiv.) and triethoxysilane (TEOS) (3.67 ml, 19.9 mmol, 1.5 eqiv.) are charged with platinum dioxide (PtO_2, 15 mg, 6.64 10^{-5} mol) and stirred for 18 h at 55 °C. To separate the catalyst, the reaction mixture is filtrated twice with celite. The solvent and the excess of TEOS are removed *in vacuo*. The product is quantitatively obtained as yellow oil. The ^{1}H-NMR and ^{13}C-NMR spectra are given in Figure B.1 a,b:

^{1}H-NMR (300 MHz, $CDCl_3$):
δ = 0.53-0.57 (m, 1H, $H^{11´}$), 1.13-1.40 (m, 20 H, $H^{3´-9´,10´,11´}$), 1.49-1.59 (m, 2H, $H^{2´}$), 1.87-1.98 (m, 1H, $H^{10´}$), 2.52 (t, 2H, $H^{1´}$), 3.73 (q, 4H, OCH_2), 5.33 (d, 2H, H^{14}), 7.06 (m, 2H, $H^{3,5}$), 7.17 (m, 2H, $H^{2,6}$), 7.21-7.27 (m, 5H, H^{8-12}) ppm.

^{13}C-NMR (75 MHz, $CDCl_3$):
δ = 10.62 ($C^{11´}$), 18.56 (-CH_3), 23.01 ($C^{10´}$), 29.48, 29.61, 29.82, 29.70, 29.81, 29.89 ($C^{3´-8´}$), 31.69 ($C^{2´}$), 33.43 ($C^{9´}$), 35.91 ($C^{1´}$), 58.49 (OCH_2), 113.82 (C^{14}), 127.80 (C^{10}), 128.30 ($C^{3,5,8,12}$), 128.37 ($C^{9,11}$), 128.52 ($C^{2,6}$), 138.92 (C^1), 141.95 (C^7), 142.82 (C^4), 150.15 (C^{13}) ppm.

Synthesis of 4-(11'-trichlorosilylundecanyl)diphenylethylene (TCS-DPE)

In a flask 4-(10´-undecenyl)-DPE (2 g, 6.9 mmol, 1 eqiv.) is dissolved in dry toluene (10 ml). Under an atmosphere of nitrogen platinum(0)-1,3-divinyl-1,1,3,3-tetramethyldisiloxane (Karstedt Catalyst, 0.3 ml, 2 wt. % in xylene) is added and the reaction vessel is cooled with liquid nitrogen. Trichlorosilane (TCS, 1.05 ml, 10.4 mmol, 1.5 eqiv.) is added dropwise and the reaction is stirred for 12 h at room temperature. The solvent and the excess of TCS are removed *in vacuo*. The product is quantitatively obtained as green oil. ^{1}H-NMR analysis of aliquots indicates complete consumption of 4 (10´-undecenyl)-DPE. ^{1}H-NMR is given in Figure B.1 c:

^{1}H-NMR (300 MHz, $CDCl_3$):
δ = 0.75-1.67 (m, 18H, $H^{3´-11´}$), 1.85 (m, 2H, $H^{2´}$), 2.30-2.51 (m, 2H, $H^{1´}$), 5.25-5.29 (m, 2H, H^{14}), 6.67-7.18 (m, 9H, $H^{2,3,5,6,8-12}$) ppm.

Preparation of Si Wafers and Initiator Immobilization

For the immobilization of TEOS-DPE on Si wafers, 1 x 1 cm^2 pieces are cut and cleaned by Soxhlet extraction with dry toluene. For the immobilization of TCS-DPE, 1.5 x 6.5 cm^2 pieces of Si wafers are cut and every wafer scratched into 1.5 x 1.5 cm^2 pieces for subsequent breaking after polymerization steps. The wafers are cleaned by Soxhlet extraction, using dry toluene followed by a treatment with Caro´s acid

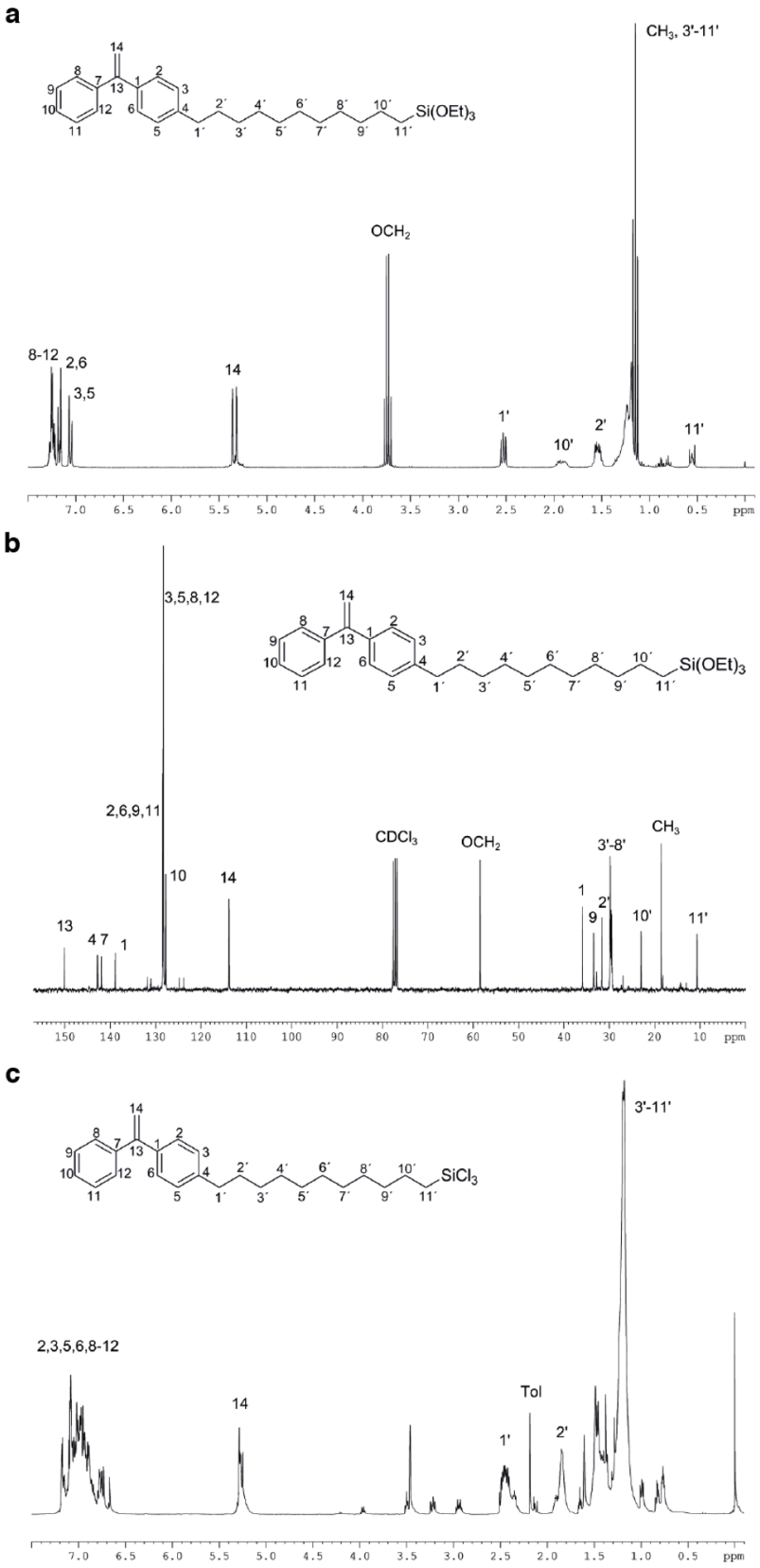

Figure B.1: NMR spectra of saPS initiators. (a) ^{1}H NMR spectrum of TEOS-DPE. (b) ^{13}C-NMR spectrum of TEOS-DPE. (c) ^{1}H-NMR spectrum of TCS-DPE. Apdated from [248].

for 45 minutes and rinsing with distilled H_2O. Wafers are dried *in vacuo*. Under an atmosphere of nitrogen, cleaned wafers are immersed in a 2 mM solution of either TEOS-DPE or TCS-DPE in dry toluene, charged with dry triethylamine (TEA, 0.1 ml). The reaction mixture is stirred for 12 h at room temperature. For purification all wafers are cleaned by Soxhlet extraction with dry toluene for 24 h.

Surface-Initiated Anionic Polymerization of Styrene

In a glovebox both TCS-DPE and TEOS-DPE initiator functionalized Si wafers are immersed in dry CH, containing a large excess of *n*-BuLi (1.6 M) for at least 2 h to initiate the precursor functionalities. Simultaneously, this procedure ensures deactivation of all impurities, which may disturb the anionic polymerization reaction of styrene. Wafers are taken off the vessel and cleaned very carefully by rinsing with dry CH. All wafers are transferred to another vessel containing dry CH and styrene (for TEOS-DPE 3 ml of CH and 0.5 ml of styrene are used; for TCS-DPE 30 ml of CH and 2 ml of styrene are used) and stirred for 12 h at room temperature. The polymerization is terminated by adding MeOH. Wafers with immobilized TCS-DPE are carefully broken at previously scratched positions and all wafers are cleaned by Soxhlet extraction using toluene (Figure B.2).

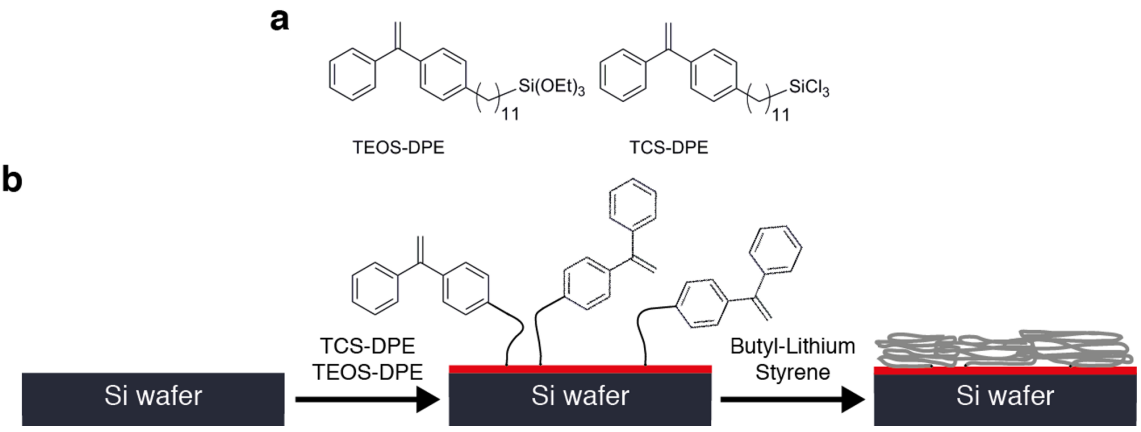

Figure B.2: Preparation of saPS. (a) DPE-based initiator precursors and (b) immobilization on Si wafers for surface-initiated anionic polymerization of styrene. Apdated from [248].

B.7 Structured Gallium Arsenide

Markus Stallhofer and Alexander Holleitner, TU München

The structured gallium arsenide (GaAs) sample is fabricated by a wet etching technique as described in ref. [203]. First, the sample is cleaned thoroughly with acetone and isopropanol. Then, a poly(methyl methacrylate), PMMA, electron beam-resist (500 k) is spin-coated onto the chip (1 s at 800 rpm, 30 s at 5000 rpm). The sample is heated 100 s during a prebake procedure to 170 °C on a hotplate. By electron beam lithography, different areas filled with elongated stripes, as depicted in Figure B.3 b, are exposed with doses ranging from 48 μAs·cm^{-2}- 78 μAs·cm^{-2}. Important geometrical parameters, varied between the different design areas, are the width of the stripes w, the distance between the stripes d and the illumination dose I (Figure B.3 b). After exposure, the sample and resist are heated in a postbake procedure to 120 °C for 4 minutes. Then, they are developed with isopropanol : methyl isobutyl ketone 3:1 for 50 s. To remove residual PMMA and to achieve a perfect etching, the developed regions are exposed to an oxygen plasma (200 W) for 90 s. The etching is consecutively performed by dipping the sample into a diluted Piranha solution for 15 s (mixing ratio H_2SO_4 (98 %):H_2O_2 (30 %):H_2O = 1:3:100) [387]. Afterward, the etchant is washed away in distilled H_2O and the resist is removed with acetone. The approximate etch depth amounts to 50 nm in all structures.
GaAs shows a RMS roughness (1.2 nm), which is clearly under the dimensions of structured items. Measurements are performed by using the optical image of the AFM setup to align the AFM cantilever over the writefield (WF) region (Figure B.3 a). Figure B.3 b illustrates the WF design and an AFM image of the indicated WF having 50 nm height.
Aging and corrosion turn out to be an important issue. While the roughness stays rather constant, the H_2O contact angle shifts from 33 ($\pm$6)° to 90 ($\pm$3)° after 18 months. The contact angle can be reduced to 47 ($\pm$6)° by repeated immersion into 16 % H_2SO_4 for 10 s and rinsing in H_2O [388]. But the initial contact angle cannot not be reached any more. Figure B.3 c,d shows representative F_z-z curves for an old GaAs sample before H_2SO_4 treatment and a new GaAs surface. The transition from plateau curves (about 30-50 % of all F_z-z curves) on hydrophobic GaAs to curves with an unspecific adhesion peak close to the surface (plateau curves occurred in 5-10 % of all F_z-z curves) on hydrophilic GaAs is given by the Berg limit at about 65° of H_2O contact angle [195, 196, 192] (Section 2.4.2). H_2SO_4 treatment leads to similar results with a new GaAs sample, confirming the prediction given by the Berg limit. The friction cycles shown in Chapter 4 are taken after 5 months of storage of the GaAs sample in air. There, the plateau curve occurrence indicates a contact angle above the Berg limit.

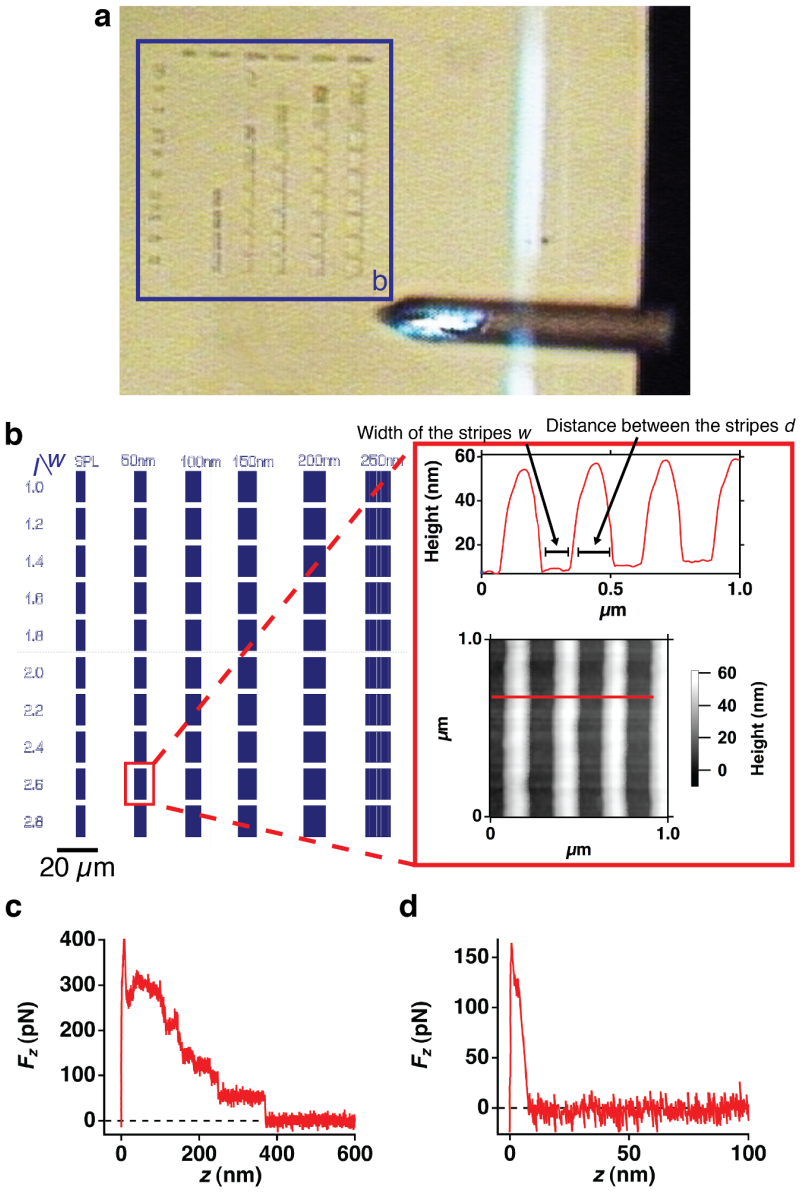

Figure B.3: Characterization of nanostructured GaAs substrates. (a) Optical image of the substrate in the AFM setup. (b) WF scheme with inset showing an intermittent-contact mode AFM image of the microstructure. Typical F_z-z curves on (c) hydrophobic GaAs with a H_2O contact angle of 85 ($\pm$7)° and (d) on hydrophilic GaAs with a H_2O contact angle of 42 ($\pm$8)°. Adapted from [203].

B.8 Diamond

Moritz Hauf and Alexander Holleitner, TU München

Hydrogen-Terminated Diamond

The hydrogen-terminated diamond (HD) sample is fabricated as described in ref. [389]. Diamond samples with [100] orientation and impurity concentrations lower than 1 part per million (ppm) for nitrogen and 50 part per billion (ppb) for boron are purchased from Element Six (U.K.). Diamond surfaces are cleaned in sulfuric acid prior to surface termination. H-termination is performed in a microwave-assisted H-plasma. Contact angle measurements with H_2O show a contact angle of 80°-90°. The HD sample is cleaned as stated below for OHD.

Oxygen/Hydrogen-Terminated Diamond

The synthesis of a oxygen/hydrogen-terminated diamond (OHD) is performed as described in ref. [203]. Here, an undoped single crystalline diamond sample grown by plasma-enhanced chemical vapor deposition (PECVD) is used. Impurity concentrations are specified to be lower than 1 ppm for nitrogen and 50 ppb for boron. The RMS roughness is given as lower than 0.3 nm (Diamond Detectors, UK). Diamond surfaces are cleaned in sulfuric acid prior to surface termination. Ti/Au reference marks are fabricated on the sample by optical lithography and thermal evaporation of 10 nm Ti and 100 nm Au, followed by a lift-off process. H-termination is performed in a microwave-assisted H-plasma. Then, the surface is spin-coated with an e-beam resist (ZEP 520A, ZEON Europe) and patterned with an electron-beam lithography system. The patterned resist serves as a mask during the following oxygen plasma treatment for 300 s to selectively oxidize the surface (Figure B.4 a). This method allows the fabrication of O-terminated lines with a minimum width below 100 nm. Afterward, the resist is removed with N-methyl-2-pyrrolidon (NMP) and mechanically cleaned with acetone and isopropanol and blown dry with nitrogen.
In order to exclude any influence of residues of the lithographic mask or other pollutants, the patterned diamond is cleaned mechanically by rubbing forcefully over the surface several times with a fuzz-free acetone-soaked wipe wrapping a spatula, followed by ultrasonic cleaning in acetone, 2-propanol, and ethanol respectively. Before and after each measurement this procedure is repeated.
The Ti/ Au marks ensure correct orientation. FFM [121] reveals the stripe patterns very well (Figure B.4 b,c). Here, a Si AFM cantilever tip is used to image the OHD sample in contact mode. A clear difference between O- and H-termination is observable. The O-terminated spots shows higher friction force (137 nN) than the H-terminated (86 nN) using:

$$F_R = \mu(F_{setpoint} + F_{adh}) \tag{B.1}$$

where $F_{setpoint}$ denotes the trigger force used for the indentation of the AFM tip and F_{adh} the maximum force of the unspecific adhesion peak from F_z-z curves. The friction coefficient μ (between Si and OHD) can be obtained to $\mu_O = 0.70$ and $\mu_H = 0.35$. The reduction of friction coefficient for H-termination on diamond substrates corresponds to the results of Grierson et al. [11]. The lateral cantilever

sensitivity is determined by diamagnetic levitation spring method [390, 391]. The area of interest is characterized by force mapping (Figure B.4 d). Here, the sample is divided into sectors. Each sector represents a single F_z-z curve. Force mapping gives information about tip-substrate interaction, measured by unspecific adhesion peak maximum F_{adh}. The H-terminated region shows higher tip-substrate interaction than the O-terminated. Force maps help to orient and to find a starting point within H-terminated (hydrophobic) spots for single polymer friction curves as performed in Chapter 4.

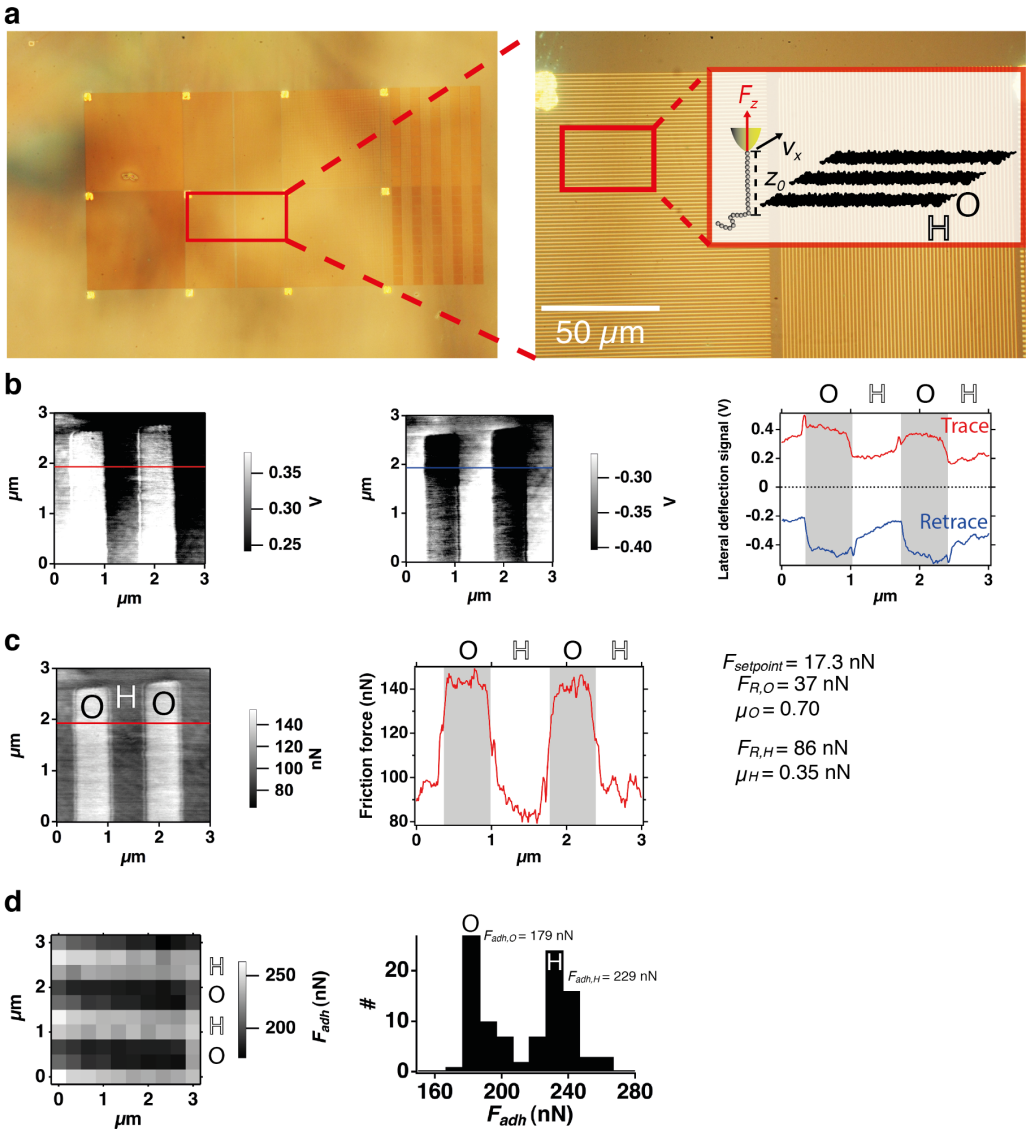

Figure B.4: Characterization of OHD substrates. (a) Optical wide-field image of the e-beam resist pattern used for selective oxygen (O)- and hydrogen (H)-termination of the diamond substrates. Zoom-in indicates the stripe pattern: 500 nm H/ 500 nm O. Friction cycles are performed perpendicular to these stripes. (b) FFM of OHD. Trace (left) and retrace (middle) images taken in contact mode and the respective sections (right) showing the difference in lateral deflection between H- and O-terminated stripes. The images are taken with a scan angle of 90° in order to use the symmetry of the cantilever perpendicular to its long axis. (c) FFM friction loop image (left) and section (right) determining the friction force. (d) Force map of adhesion peak maximum force F_{adh} (left), revealing a bimodal distribution relating to the O- and H-terminated parts of the sample (right). Adapted from [203].

Appendix C

Single Molecule Fluorescence Microscopy: Adhesion and Friction

A complementary approach to AFM-based experiments is the investigation of adhesion and friction by means of total internal reflection fluorescence (TIRF) microscopy. With this method, time resolved adhesion and diffusion behavior of single labeled polymers is investigated nearby a quarz glass substrate. Furthermore, the substrate hydrophobicity can be modified by e.g. silanization, oxygen plasma activation or coating with polymers.

C.1 Preparation and Setup

TIRF is based on the principle of total internal reflection [392]. A laser beam passing the interface between a medium with high refractive index n_1 (glass) and low refractive index n_2 (H_2O) is totally reflected, if the incident angle of light is higher than the critical angle (Figure C.1 a):

$$\alpha_c = arcsin\left(\frac{n_2}{n_1}\right) \tag{C.1}$$

Although the light is totally reflected, an evanescent field propagates parallel to the surface in the plane of incidence and penetrates into the second medium (H_2O). The light intensity of this evanescent field decays exponentially with the perpendicular distance z:

$$I(z) = I_0 \exp\left(-\frac{z}{d}\right) \tag{C.2}$$

The penetration depth d is dependent on the polarization of the incident light and is given by:

$$d = \frac{\lambda_0}{4\pi}\left(n_1^2 \sin^2(\alpha) - n_2^2\right)^{-\frac{1}{2}} \tag{C.3}$$

which can be estimated to about 100 nm. Thus, selective illumination of molecules close to the glass–H_2O interface enables visualization of cellular structures or single molecule studies. Two different TIRF microscopy setups are usually used. The first comprises a prism, directing the illumination light toward the glass-H_2O interface. The fluorescence is collected on the other side by an objective [392]. The second setup type uses a high-numerical-aperture (> 1.4) objective in order to illuminate the sample and to collect the fluorescence [393]. TIRF microscopy is capable of

detecting labeled polymers, which enter and leave the thin evanescent field region in bulk, and to track substrate-bound diffusion of single labeled polymers [394].
For the presented data, polymers are labeled with PromoFluor 555 dyes (PromoCell, Germany) for excitation with a wavelength of $\lambda_0 = 532$ nm or Atto 647N dyes (Atto-Tec, Germany, $\lambda_0 = 635$ nm). The respective dye has to carry a NHS terminal group for coupling to PLL or PAAm. In case of PGA, a dye with an amino terminal group (using EDC and N-hydroxysulfosuccinimide, NHSS, for activation of carboxy groups) can be used. The coupling is done as given by the manufacturer's protocol. Zeba Desalt Spin Columns (0.5 ml, sample size 30-130 μl, Thermo Scientific) are used for purification from unbound fluorescence dyes. Afterward, a SEC is performed to obtain a narrow mass distribution of labeled polymers [225, 395].
Then, polymer solutions are further diluted to concentrations of μM to pM. Starting with the lowest concentration, the samples are introduced into the sample chamber (Figure C.1 a). Both dwell time on substrate and the coverage can be determined from fluorescence images (Figure C.1 b). For long dwell times and high mobility (which is expected in case of a hydrophobic substrate coating), the diffusion of a substrate adsorbed labeled polymer can be analyzed (Figure C.1 c). IGOR Pro (Wavemetrics) is used for data evaluation.
A major challenge is the polymer labeling. While a high labeling ratio is required in order to avoid rapid bleaching, the fluorescence dyes attached to the side chains (PAAm, PLL, PGA) can alter the polymer with regard to hydrophobicity, charging state or persistence length. For the determination of the degree of labeling and the location of the bound fluorophores different methods can be used such as UV-Vis spectroscopy, AFM-based molecular combing [396] or stimulated emission depletion (STED) microscopy [397].
The fluorescence spots that are visible can be likewise due to polymer aggregates instead of a single polymer. This causes a further challenge for data interpretation.

C.2 Adsorption Dynamics and Diffusion

The polymer dwell time (inverse of the off-rate) on substrate and the surface coverage Θ are linked to the equilibrium constant K via the Langmuir isotherm [399] with the polymer concentration c:

$$\Theta = \frac{Kc}{1 + Kc} \tag{C.4}$$

Fluorescence images of 128 x 256 pixel^2 correspond to 50 x 100 μm^2. A single polymer has a radius of gyration of $R_g = b\sqrt{\frac{N}{6}}$ for a θ-solvent or rather $R_g = b\frac{N^{0.588}}{\sqrt{6}}$ for a good solvent [19]. For PAAm (65 kDa), PLL (70-300 kDa) or PGA (50-100 kDa) the R_g values are around 2-6 nm.
The equilibrium constant K is given by an Arrhenius-like equation with the free enthalpy ΔG, the on-rate k_{on} and the off-rate k_{off} (Figure C.1 d):

$$K = \frac{k_{on}}{k_{off}} = \exp\left(\frac{\Delta G}{k_B T}\right) \tag{C.5}$$

Then, k_{off} results from:

$$k_{off} = A \exp\left(\frac{\Delta G^*}{k_B T}\right) \tag{C.6}$$

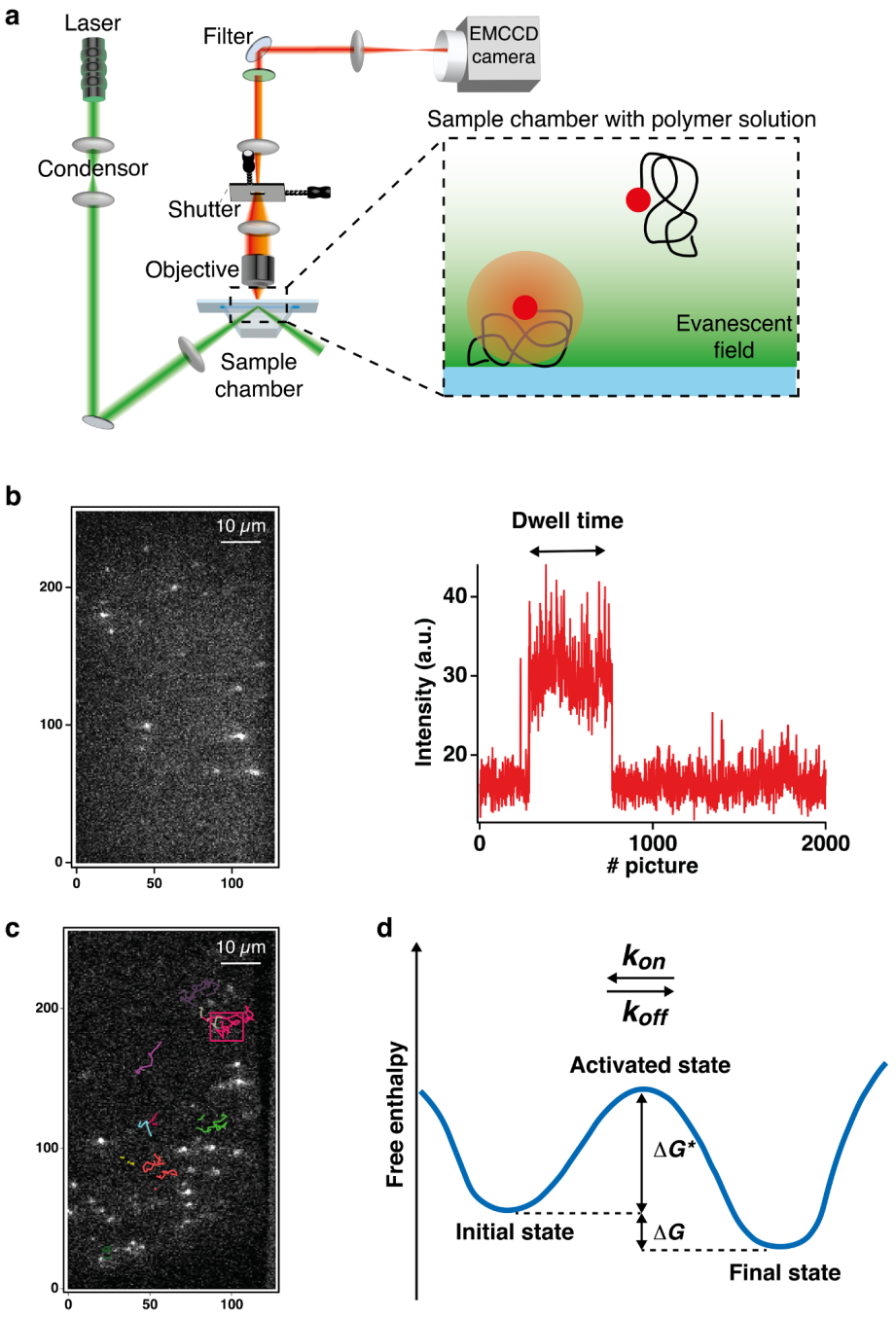

Figure C.1: TIRF microscopy based detection of single polymer adsorption and diffusion. (a) Prism type TIRF setup used for experiments with PromoFluor 555 dyes (adapted from [398]). A Nd:YAG laser (DPSSL-473-50, 50 mW, Roithner, Austria) with a wavelength of $\lambda_0 = 532$ nm, at a critical angle $\alpha = 66°$ is used with a H_2O immersion objective (CFI Plan Apochromat VC 60 x WI, N.A. 1,20, Nikon Instruments Europe). Images are captured with an electron multiplying charge-coupled device (EMCCD) camera (Andor iXon DV 887, Andor, Northern Ireland). The sample chamber is built of sandwiched and sealed quarz glass slides (G. Finkenbeiner, USA). The sample volume is introduced into the chamber by means of a syringe pump (300 μl with 2 ml·min^{-1}). (b) Images are taken with a time resolution of 120 ms (exposure time of 100 ms). Dwell times of single polymer adhesion events (bright spots) can be extracted from intensity vs. time plots, leading to the dwell time distribution and the area covered by polymers in every image frame. (c) Determination of single polymer diffusion constants is done by tracking of single molecule 2D random walks. Each center position of a polymer is localized by a 2D-Gaussian, such as given in [394]. (d) Two state model for adsorption and desorption process, fulfilling an Arrhenius-like equation.

.

with the free enthalpy of the transition state ΔG^* and the attempt frequency A, which in assumed to be of the order of 10^8 s^{-1} [400].
While quarz glass reveals dwell times of 0.7 ($\pm$0.1) s, silanization with Vectabond leads to 8.1 ($\pm$2.2) s [225]. ΔG^* results to about 15 k_BT per polymer. The values from AFM-based measurements with plateau forces are about 5 k_BT per monomer. Thus, the free enthalpy gained by TIRF experiments is about two orders of magnitude smaller than for AFM-based desorption. A reason could be a partial adsorption of the polymer in case of TIRF experiments, where a polymer consists of either loop, tail and train sections. By contrast, in AFM-based desorption, a polymer is peeled off the surface. Furthermore, a low ΔG^* value accounts for a high cooperativity of the desorption process.
Another aspect refers to the depletion layer on hydrophobic substrates (Section 2.1.2). While the TIRF-based desorption occurs from the top of the depletion layer, the AFM cantilever tip indents this layer and deposes a polymer on the substrate. In fact, this leads to a higher activation energy barrier for the following desorption process.
The diffusion coefficients, found by the presented TIRF measurements (Figure C.1 c), are in the range of $D = 0.1$ $\mu m^2 \cdot s^{-1}$. The friction coefficient follows from the Einstein-Smoluchowski relation (Equation 2.23) to $\mu = 10^{-8}$ $kg \cdot s^{-1}$ [395].
Further measurements have to be done to understand the discrepancy between TIRF microscopy and force induced desorption by AFM and to analyze the type of adhesion and diffusion under various solvent conditions.

List of Abbreviations

AFM	atomic force microscope
BuLi	butyllithium
CH	cyclohexane
CH_3-SAM	self-assembled monolayer of CH_3-terminated alkanthiols on Au
CS	cooperative stick
di-NHS-PEG	α,ω-bis-NHS PEG
DLC	diamond-like carbon
DPE	1,1-diphenylethylene
DS	desorption stick
dsDNA	double-stranded DNA
EDC	N-Ethyl-N'-(3-dimethylaminopropyl)carbodiimid
FFM	friction force microscopy
FJC	freely jointed chain
FRAP	fluorescence recovery after photobleaching
GaAs	structured gallium arsenide
HB	hydrogen bond
HD	hydrogen-terminated diamond
HE	hydrophobic effect
LbL	layer-by-layer
mal-hex-NHS-PEG	α-maleinimidohexanoic-ω-NHS PEG
MD	molecular dynamics
MEMS	micro-electro-mechanical systems
MeOH	methanol
mPEG	α-methoxy-ω-NHS PEG
NHS	N-hydroxysuccinimide
NMR	nuclear magnetic resonance
OEM	oligoelectrolyte multilayer
OHD	oxygen/hydrogen-terminated diamond
OLS	optical lever sensitivity
PAAm	poly(allylamine)
PDADMAC	poly(diallyl dimethyl ammonium chloride)
PDI	polydispersity index
PE	polyelectrolyte
PEG	poly(ethylene glycol)
PEI	poly(ethylene imine)

PEM	polyelectrolyte multilayer
PGA	poly-L-(glutamic acid) sodium salt
PI	polyisoprene
PI-PS-PPS	poly(isoprene-*b*-styrene-*b*-propylene sulfide)
PLL	poly-L-lysine hydrobromide
PMMA	poly(methyl methacrylate)
ppb	part per billion
ppm	part per million
PPS	propylene sulfide
PS	polystyrene
PSD	power spectral density
PS-PI-PS-COOH	poly(styrene-*b*-isoprene-*b*-styrene-COOH)
PS-PI-PS-PPS	poly(styrene-*b*-isoprene-*b*-styrene-*b*-propylene sulfide)
PS-PPS	poly(styrene-*b*-propylene sulfide)
PSS	poly(sodium 4-styrene sulfonate)
PT	poly(tyrosine)
PTFE	poly(tetrafluorethylene)
r.h.	relative humidity
RMS	root-mean square
SAM	self-assembled monolayer
saPS	covalently surface-attached polystyrene film
scPS	spin coated polystyrene film
SEC	size exclusion chromatography
SFA	surface force apparatus
SHO	simple harmonic oscillator
Si	silicon
SMFS	single molecule force spectroscopy
ssDNA	single-stranded DNA
TCS	trichlorosilane
TCS-DPE	4-(11'-trichlorosilylundecanyl)diphenylethylene
TEA	triethylamine
TEOS	triethoxysilane
TEOS-DPE	4-(11'-triethoxysilylundecanyl)diphenylethylene
THF	tetrahydrofuran
TIRF	total internal reflection fluorescence
WF	writefield
WLC	worm-like chain
XRR	X-ray reflectometry

Bibliography

[1] B. Bhushan, ed., *Handbook of Micro/Nano Tribology* (CRC Press, 1999), second edn.

[2] N. Canter, *Tribology and Lubrication Technology* **68**, 8 (2011).

[3] J. S. Wong, S. Granick, *Journal of Polymer Science Part B-Polymer Physics* **45**, 3237 (2007).

[4] V. Mittal, ed., *Characterization Techniques for Polymer Nanocomposites* (Wiley-VCH, Weinheim, 2012).

[5] M. Urbakh, J. Klafter, D. Gourdon, J. Israelachvili, *Nature* **430**, 525 (2004).

[6] R. W. Carpick, *Science* **313**, 184 (2006).

[7] H. Yoshizawa, Y. L. Chen, J. Israelachvili, *Journal of Physical Chemistry* **97**, 4128 (1993).

[8] H. J. Butt, M. Kappl, *Surface and Interfacial Forces* (Wiley-VCH Verlag, Weinheim, 2010).

[9] J. Robertson, *Materials Science and Engineering R-Reports* **37**, 129 (2002).

[10] A. Erdemir, C. Donnet, *Journal of Physics D-Applied Physics* **39**, R311 (2006).

[11] D. S. Grierson, R. W. Carpick, *Nano Today* **2**, 12 (2007).

[12] N. Maeda, N. H. Chen, M. Tirrell, J. N. Israelachvili, *Science* **297**, 379 (2002).

[13] D. W. Lee, X. Banquy, J. N. Israelachvili, *Proceedings of the National Academy of Sciences of the United States of America* **110**, E567 (2013).

[14] D. J. Goetz, M. E. Elsabban, B. U. Pauli, D. A. Hammer, *Biophysical Journal* **66**, 2202 (1994).

[15] B. T. Marshall, *et al.*, *Nature* **423**, 190 (2003).

[16] A. Soranno, *et al.*, *Proceedings of the National Academy of Sciences of the United States of America* **109**, 17800 (2012).

[17] V. Bormuth, V. Varga, J. Howard, E. Schaeffer, *Science* **325**, 870 (2009).

[18] R. C. Advincula, W. J. Brittain, K. C. Caster, J. Ruehe, *Polymer Brushes* (Wiley-VCH, Weinheim, 2004).

[19] M. Rubinstein, R. H. Colby, *Polymer Physics* (Oxford University Press, New York, 2003).

[20] P. J. Flory, *Statistical Mechanics of Chain Molecules* (Hanser, München, 1988).

[21] J. N. Israelachvili, *Intermolecular and Surface Forces* (Elsevier, 2011), third edn.

[22] E. M. Lupton, *et al.*, *Chemical Physics Letters* **414**, 132 (2005).

[23] M. Grandbois, M. Beyer, M. Rief, H. Clausen-Schaumann, H. E. Gaub, *Science* **283**, 1727 (1999).

[24] M. K. Beyer, H. Clausen-Schaumann, *Chemical Reviews* **105**, 2921 (2005).

[25] P. Schwaderer, *et al.*, *Langmuir* **24**, 1343 (2008).

[26] S. W. Schmidt, A. Kersch, M. K. Beyer, H. Clausen-Schaumann, *Physical Chemistry Chemical Physics* **13**, 5994 (2011).

[27] H. C. Hamaker, *Physica* **4**, 1058 (1937).

[28] L. Bergstrom, *Advances in Colloid and Interface Science* **70**, 125 (1997).

[29] B. Derjaguin, L. Landau, *Acta Physico Chemica URSS* **14**, 633 (1941).

[30] E. J. W. Verwey, J. T. G. Overbeek:, *Theory of the Stability of Lyophobic Colloids.* (Elsevier, Amsterdam, 1948).

[31] W. Blokzijl, J. B. F. N. Engberts, *Angewandte Chemie-International Edition* **32**, 1545 (1993).

[32] G. Hummer, S. Garde, A. E. Garcia, M. E. Paulaitis, L. R. Pratt, *Journal of Physical Chemistry B* **102**, 10469 (1998).

[33] W. Kauzmann, *Advances in Protein Chemistry* **14**, 1 (1959).

[34] E. E. Meyer, K. J. Rosenberg, J. Israelachvili, *Proceedings of the National Academy of Sciences of the United States of America* **103**, 15739 (2006).

[35] H. S. Frank, M. W. Evans, *The Journal of Chemical Physics* **13**, 507 (1945).

[36] D. M. Huang, D. Chandler, *Proceedings of the National Academy of Sciences* **97**, 8324 (2000).

[37] D. Chandler, *Nature* **417**, 491 (2002).

[38] D. Chandler, *Nature* **437**, 640 (2005).

[39] R. L. Baldwin, *Proceedings of the National Academy of Sciences* **83**, 8069 (1986).

[40] K. Lum, D. Chandler, J. D. Weeks, *Journal of Physical Chemistry B* **103**, 4570 (1999).

[41] R. R. Netz, *Current Opinion in Colloid and Interface Science* **9**, 192 (2004).

[42] F. Sedlmeier, *et al.*, *Biointerphases* **3**, FC23 (2008).

[43] T. M. Raschke, *Current Opinion in Structural Biology* **16**, 152 (2006).

[44] R. D. Mountain, D. Thirumalai, *Proceedings of the National Academy of Sciences of the United States of America* **95**, 8436 (1998).

[45] M. Sotomayor, K. Schulten, *Science* **316**, 1144 (2007).

[46] P. Flory, *Principles of Polymer Chemistry* (Cornell University Press, 1953).

[47] R. R. Netz, D. Andelman, *Physics Reports* **380**, 1 (2003).

[48] P. Debye, E. Huckel, *Physikalische Zeitschrift* **24**, 185 (1923).

[49] T. Odijk, *Journal of Polymer Science Part B-Polymer Physics* **15**, 477 (1977).

[50] J. Skolnick, M. Fixman, *Macromolecules* **10**, 944 (1977).

[51] T. Hugel, *et al.*, *Macromolecules* **34**, 1039 (2001).

[52] R. R. Netz, *Macromolecules* **34**, 7522 (2001).

[53] G. Decher, J. B. Schlenoff, eds., *Multilayer Thin Films* (Wiley VCH Verlag, 2003).

[54] J. F. Joanny, M. Castelnovo, R. Netz, *Journal of Physics-Condensed Matter* **12**, A1 (2000).

[55] R. R. Netz, J. F. Joanny, *Macromolecules* **31**, 5123 (1998).

[56] R. R. Netz, *Journal of Physics-Condensed Matter* **15**, S239 (2003).

[57] S. Alexander, *Journal de Physique* **38**, 977 (1977).

[58] P. G. Degennes, *Macromolecules* **13**, 1069 (1980).

[59] P. G. Degennes, *Advances in Colloid and Interface Science* **27**, 189 (1987).

[60] S. T. Milner, T. A. Witten, M. E. Cates, *Europhysics Letters* **5**, 413 (1988).

[61] S. T. Milner, T. A. Witten, M. E. Cates, *Macromolecules* **21**, 2610 (1988).

[62] S. T. Milner, *Science* **251**, 905 (1991).

[63] P. Auroy, L. Auvray, L. Leger, *Physical Review Letters* **66**, 719 (1991).

[64] A. Halperin, *Journal de Physique* **49**, 547 (1988).

[65] H. J. Kreuzer, S. H. Payne, L. Livadaru, *Biophysical Journal* **80**, 2505 (2001).

[66] O. Kratky, G. Porod, *Recueil des Travaux Chimiques des Pays-Bas-Journal of the Royal Netherlands Chemical Society* **68**, 1106 (1949).

[67] M. Doi, S. F. Edwards, *The Theory of Polymer Dynamics* (Oxford University Press, Oxford, 1998).

[68] T. Hugel, M. Seitz, *Macromolecular Rapid Communications* **22**, 989 (2001).

[69] B. N. Balzer, T. Hugel, *Single-Molecule Detection and Manipulation* (Elsevier BV, Amsterdam, 2012), pp. 629–645.

[70] M. Fixman, J. Kovac, *Journal of Chemical Physics* **61**, 4939 (1974).

[71] J. F. Marko, E. D. Siggia, *Macromolecules* **28**, 8759 (1995).

[72] C. Bustamante, J. F. Marko, E. D. Siggia, S. Smith, *Science* **265**, 1599 (1994).

[73] C. Bouchiat, *et al.*, *Biophysical Journal* **76**, 409 (1999).

[74] T. Odijk, *Macromolecules* **28**, 7016 (1995).

[75] M. Rief, M. Gautel, F. Oesterhelt, J. M. Fernandez, H. E. Gaub, *Science* **276**, 1109 (1997).

[76] M. Rief, F. Oesterhelt, B. Heymann, H. E. Gaub, *Science* **275**, 1295 (1997).

[77] P. E. Rouse, *Journal of Chemical Physics* **21**, 1272 (1953).

[78] D. Mukherji, G. Bartels, M. H. Müser, *Physical Review Letters* **100**, 1 (2008).

[79] S. F. Edwards, *Proceedings of the Physical Society* **92**, 9 (1967).

[80] M. Doi, S. F. Edwards, *The Theory of Polymer Dynamics* (Oxford University Press, Oxford, 1986).

[81] P. G. Degennes, *Journal of Chemical Physics* **55**, 572 (1971).

[82] N. Fatkullin, E. Fischer, C. Mattea, U. Beginn, R. Kimmich, *ChemPhysChem* **5**, 884 (2004).

[83] E. Fischer, U. Beginn, N. Fatkullin, R. Kimmich, *Macromolecules* **37**, 3277 (2004).

[84] E. Helfand, D. S. Pearson, *The Journal of Chemical Physics* **79**, 2054 (1983).

[85] C. M. Roland, L. A. Archer, P. H. Mott, J. Sanchez-Reyes, *Journal of Rheology* **48**, 395 (2004).

[86] M. D. Hager, P. Greil, C. Leyens, S. van der Zwaag, U. S. Schubert, *Advanced Materials* **22**, 5424 (2010).

[87] X. Luo, P. T. Mather, *ACS Macro Letters* **2**, 152 (2013).

[88] E. B. Stukalin, L.-H. Cai, N. A. Kumar, L. Leibler, M. Rubinstein, *Macromolecules* **46**, 7525 (2013).

[89] H. Lee, B. P. Lee, P. B. Messersmith, *Nature* **448**, 338 (2007).

[90] A. Y. Stark, *et al.*, *Proceedings of the National Academy of Sciences* **110**, 6340 (2013).

[91] A. Baldan, *International Journal of Adhesion and Adhesives* **38**, 95 (2012).

[92] H. Hertz, *Journal für die Reine und Angewandte Mathematik* **1882**, 156 (1882).

[93] K. L. Johnson, K. Kendall, A. D. Roberts, *Proceedings of The Royal Society of London Series A-Mathematical and Physical Sciences* **324**, 301 (1971).

[94] B. V. Derjaguin, V. M. Muller, Y. P. Toporov, *Journal of Colloid and Interface Science* **53**, 314 (1975).

[95] L. H. Sharpe, *Journal of Adhesion* **4**, 51 (1972).

[96] S. Voyutski, *Autohesion and Adhesion of High Polymers.* (Wiley-Interscience, New York, 1963).

[97] B. Pukanszky, *European Polymer Journal* **41**, 645 (2005).

[98] A. Hartwig, *et al.*, *Journal of Adhesion* **89**, 77 (2013).

[99] J. J. Bikerman, *The Science of Adhesive Joints* (Academic Press, New York, 1968), second edn.

[100] W. Possart, ed., *Adhesion: Current Research and Applications* (Wiley VCH Verlag, 2005).

[101] W. Possart, *et al.*, *The Journal of Adhesion* **57**, 227 (1996).

[102] S. N. G. Matthias Scherge, *Biological Micro- and Nanotribology* (Springer Verlag, Heidelberg-Berlin, 2001).

[103] B. Bhushan, *Introduction to Tribology* (John Wiley and Sons, New York, 2002).

[104] F. P. B. Tabor, D, *The Friction and Lubrication of Solids* (Oxford University Press, 1954).

[105] W. F. Brace, J. D. Byerlee, *Science* **153**, 990 (1966).

[106] P. A. Thompson, M. O. Robbins, *Science* **250**, 792 (1990).

[107] H. Yoshizawa, J. Israelachvili, *Journal of Physical Chemistry* **97**, 11300 (1993).

[108] Q. Li, T. E. Tullis, D. Goldsby, R. W. Carpick, *Nature* **480**, 233 (2011).

[109] T. Strunz, F. J. Elmer, *Physical Review E* **58**, 1601 (1998).

[110] T. Strunz, F. J. Elmer, *Physical Review E* **58**, 1612 (1998).

[111] A. Serr, Dynamics of Single Polymers at Surfaces, Ph.D. thesis, TU München, München (2007).

[112] M. Weiss, F. J. Elmer, *Physical Review B* **53**, 7539 (1996).

[113] M. G. Rozman, M. Urbakh, J. Klafter, *Physical Review Letters* **77**, 683 (1996).

[114] M. G. Rozman, M. Urbakh, J. Klafter, F. J. Elmer, *Journal of Physical Chemistry B* **102**, 7924 (1998).

[115] M. Urbakh, E. Meyer, *Nature Materials* **9**, 8 (2010).

[116] R. J. Cannara, *et al.*, *Science* **318**, 780 (2007).

[117] B. N. J. Persson, A. I. Volokitin, *Journal of Chemical Physics* **103**, 8679 (1995).

[118] A. Socoliuc, *et al.*, *Science* **313**, 207 (2006).

[119] J. Israelachvili, *et al.*, *Reports on Progress in Physics* **73**, 1 (2010).

[120] J. Krim, *Nano Today* **2**, 38 (2007).

[121] C. M. Mate, G. M. McClelland, R. Erlandsson, S. Chiang, *Physical Review Letters* **59**, 1942 (1987).

[122] Y. Mo, K. T. Turner, I. Szlufarska, *Nature* **457**, 1116 (2009).

[123] J. S. Choi, *et al.*, *Science* **333**, 607 (2011).

[124] T. D. B. Jacobs, R. W. Carpick, *Nature Nanotechnology* **8**, 108 (2013).

[125] A. Serr, D. Horinek, R. R. Netz, *Journal of the American Chemical Society* **130**, 12408 (2008).

[126] A. Erbas, D. Horinek, R. R. Netz, *Journal of the American Chemical Society* **134**, 623 (2012).

[127] A. Erbas, R. R. Netz, *Biophysical Journal* **104**, 1285 (2013).

[128] F. Kühner, *et al.*, *Langmuir* **22**, 11180 (2006).

[129] V. Lulevich, S. Kim, C. P. Grigoropoulos, A. Noy, *Nano Letters* **11**, 1171 (2011).

[130] D. Tabor, R. Winterton, *Proceedings of the Royal Society of London Series A-Mathematical and Physical Sciences* **312**, 435 (1969).

[131] J. N. Israelachvili, G. E. Adams, *Journal of the Chemical Society-Faraday Transactions I* **74**, 975 (1978).

[132] A. Ashkin, J. M. Dziedzic, J. E. Bjorkholm, S. Chu, *Optics Letters* **11**, 288 (1986).

[133] C. Gosse, V. Croquette, *Biophysical Journal* **82**, 3314 (2002).

[134] K. C. Neuman, S. M. Block, *Review of Scientific Instruments* **75**, 2787 (2004).

[135] K. C. Neuman, T. Lionnet, J. F. Allemand, *Annual Review of Materials Research* **37**, 33 (2007).

[136] K. C. Neuman, A. Nagy, *Nature Methods* **5**, 491 (2008).

[137] E. Meyer, H. J. Hug, R. Bennewitz, *Scanning Probe Microscopy* (Springer Verlag, Berlin, 2004).

[138] T. Ando, *et al.*, *ChemPhysChem* **4**, 1196 (2003).

[139] Y. Martin, H. K. Wickramasinghe, *Applied Physics Letters* **50**, 1455 (1987).

[140] M. Nonnenmacher, M. P. Oboyle, H. K. Wickramasinghe, *Applied Physics Letters* **58**, 2921 (1991).

[141] C. D. Frisbie, L. F. Rozsnyai, A. Noy, M. S. Wrighton, C. M. Lieber, *Science* **265**, 2071 (1994).

[142] R. W. Carpick, M. Salmeron, *Chemical Reviews* **97**, 1163 (1997).

[143] D. J. Muller, A. Engel, *Nature Protocols* **2**, 2191 (2007).

[144] X. Chatellier, T. J. Senden, J. F. Joanny, J. M. di Meglio, *Europhysics Letters* **41**, 303 (1998).

[145] T. J. Senden, J. M. di Meglio, P. Auroy, *European Physical Journal B* **3**, 211 (1998).

[146] I. T. S. Li, G. C. Walker, *Journal of the American Chemical Society* **132**, 6530 (2010).

[147] I. T. S. Li, G. C. Walker, *Proceedings of the National Academy of Sciences of the United States of America* **108**, 16527 (2011).

[148] H. Dietz, M. Rief, *Proceedings of the National Academy of Sciences* **101**, 16192 (2004).

[149] M. Geisler, R. R. Netz, T. Hugel, *Angewandte Chemie-International Edition* **49**, 4730 (2010).

[150] M. Geisler, S. B. Xiao, E. M. Puchner, F. Grater, T. Hugel, *Journal of the American Chemical Society* **132**, 17277 (2010).

[151] S. Kienle, S. Liese, N. Schwierz, R. R. Netz, T. Hugel, *ChemPhysChem* **13**, 982 (2012).

[152] S. K. Kufer, E. M. Puchner, H. Gumpp, T. Liedl, H. E. Gaub, *Science* **319**, 594 (2008).

[153] E. M. Puchner, S. K. Kufer, M. Strackharn, S. W. Stahl, H. E. Gaub, *Nano Letters* **8**, 3692 (2008).

[154] S. K. Kufer, *et al.*, *Nature Nanotechnology* **4**, 45 (2009).

[155] T. Hugel, *et al.*, *Science* **296**, 1103 (2002).

[156] S. B. Smith, Y. J. Cui, C. Bustamante, *Science* **271**, 795 (1996).

[157] A. Ahsan, J. Rudnick, R. Bruinsma, *Biophysical Journal* **74**, 132 (1998).

[158] H. Clausen-Schaumann, M. Rief, C. Tolksdorf, H. E. Gaub, *Biophysical Journal* **78**, 1997 (2000).

[159] J. van Mameren, *et al.*, *Proceedings of the National Academy of Sciences* **106**, 18231 (2009).

[160] M. Rief, H. Clausen-Schaumann, H. E. Gaub, *Nature Structural & Molecular Biology* **6**, 346 (1999).

[161] H. Clausen-Schaumann, M. Seitz, R. Krautbauer, H. E. Gaub, *Current Opinion in Chemical Biology* **4**, 524 (2000).

[162] F. Oesterhelt, M. Rief, H. E. Gaub, *New Journal of Physics* **1**, 6.1 (1999).

[163] M. Mickler, *et al.*, *Proceedings of the National Academy of Sciences* **104**, 20268 (2007).

[164] G. I. Bell, *Science* **200**, 618 (1978).

[165] M. Schlierf, M. Rief, *Biophysical Journal* **90**, L33 (2006).

[166] O. K. Dudko, G. Hummer, A. Szabo, *Proceedings of the National Academy of Sciences of the United States of America* **105**, 15755 (2008).

[167] X. Chatellier, J. F. Joanny, *Physical Review E* **57**, 6923 (1998).

[168] M. Geisler, *et al.*, *Langmuir* **24**, 1350 (2008).

[169] M. Geisler, B. N. Balzer, T. Hugel, *Small* **5**, 2864 (2009).

[170] M. Geisler, D. Horinek, T. Hugel, *Macromolecules* **42**, 9338 (2009).

[171] D. Horinek, *et al.*, *Proceedings of the National Academy of Sciences* **105**, 2842 (2008).

[172] D. B. Staple, M. Geisler, T. Hugel, L. Kreplak, H. J. Kreuzer, *New Journal of Physics* **13**, 013025/1 (2011).

[173] S. Kienle, T. Pirzer, S. Krysiak, M. Geisler, T. Hugel, *Faraday Discussions* **160**, 329 (2013).

[174] C. Friedsam, H. E. Gaub, R. R. Netz, *Europhysics Letters* **72**, 844 (2005).

[175] M. Seitz, C. Friedsam, W. Jostl, T. Hugel, H. E. Gaub, *ChemPhysChem* **4**, 986 (2003).

[176] C. Friedsam, M. Seitz, H. E. Gaub, *Journal of Physics-Condensed Matter* **16**, S2369 (2004).

[177] C. Friedsam, A. D. Becares, U. Jonas, H. F. Gaub, M. Seitz, *ChemPhysChem* **5**, 388 (2004).

[178] C. Friedsam, H. E. Gaub, R. R. Netz, *Biointerphases* **1**, MR1 (2006).

[179] M. Geisler, Single Molecule Sensors to Study Hydrophobic Phenomena, Ph.D. thesis, TU München (2009).

[180] T. Pirzer, Zur Lehre von Grenzflächen und von der Wirkung der Salze, Ph.D. thesis, TU München (2010).

[181] T. Pirzer, T. Hugel, *ChemPhysChem* **10**, 2795 (2009).

[182] F. Hofmeister, *Archiv für Experimentelle Pathologie und Pharmakologie* **24**, 247 (1888).

[183] K. D. Collins, *Methods* **34**, 300 (2004).

[184] W. Melander, C. Horváth, *Archives of Biochemistry and Biophysics* **183**, 200 (1977).

[185] P. H. V. Hippel, K.-Y. Wong, *Science* **145**, 577 (1964).

[186] R. L. Baldwin, *Biophysical Journal* **71**, 2056 (1996).

[187] N. Schwierz, D. Horinek, R. R. Netz, *Langmuir* **26**, 7370 (2010).

[188] N. Schwierz, D. Horinek, R. R. Netz, *Langmuir* **29**, 2602 (2013).

[189] T. Pirzer, M. Geisler, T. Scheibel, T. Hugel, *Physical Biology* **6**, 025004/1 (2009).

[190] D. Horinek, *et al.*, *Langmuir* **24**, 1271 (2008).

[191] A. Scherer, C. Zhou, J. Michaelis, C. Brauchle, A. Zumbusch, *Macromolecules* **38**, 9821 (2005).

[192] N. Schwierz, *et al.*, *Journal of the American Chemical Society* **134**, 19628 (2012).

[193] E. Ostuni, R. G. Chapman, R. E. Holmlin, S. Takayama, G. M. Whitesides, *Langmuir* **17**, 5605 (2001).

[194] J. Janecek, R. R. Netz, *Langmuir* **23**, 8417 (2007).

[195] J. M. Berg, L. G. T. Eriksson, P. M. Claesson, K. G. N. Borve, *Langmuir* **10**, 1225 (1994).

[196] E. A. Vogler, *Advances in Colloid and Interface Science* **74**, 69 (1998).

[197] A. Serr, R. R. Netz, *Europhysics Letters* **73**, 292 (2006).

[198] G. Binnig, C. F. Quate, C. Gerber, *Physical Review Letters* **56**, 930 (1986).

[199] T. R. Albrecht, S. Akamine, T. E. Carver, C. F. Quate, *Journal of Vacuum Science and Technology A* **8**, 3386 (1990).

[200] G. Meyer, N. M. Amer, *Applied Physics Letters* **53**, 1045 (1988).

[201] M. B. Viani, *et al.*, *Journal of Applied Physics* **86**, 2258 (1999).

[202] B. N. Balzer, M. Gallei, *GIT Labor-Fachzeitschrift* **11** (2013).

[203] B. N. Balzer, *et al.*, *Angewandte Chemie-International Edition* **52**, 6541 (2013).

[204] G. T. Hermanson, *Bioconjugate Techniques* (Elsevier, 2008), second edn.

[205] A. Ebner, *et al.*, *STM and AFM Studies on (Bio)Molecular Systems: Unravelling the Nanoworld* **285**, 29 (2008).

[206] J. E. Sader, *Calibration of Atomic Force Microscope Cantilevers* (Marcel Dekker, New York, 2003), pp. 846–856.

[207] H. J. Butt, B. Cappella, M. Kappl, *Surface Science Reports* **59**, 1 (2005).

[208] J. P. Cleveland, S. Manne, D. Bocek, P. K. Hansma, *Review of Scientific Instruments* **64**, 403 (1993).

[209] C. T. Gibson, D. A. Smith, C. J. Roberts, *Nanotechnology* **16**, 234 (2005).

[210] J. E. Sader, J. W. M. Chon, P. Mulvaney, *Review of Scientific Instruments* **70**, 3967 (1999).

[211] J. L. Hutter, J. Bechhoefer, *Review of Scientific Instruments* **64**, 1868 (1993).

[212] H. J. Butt, M. Jaschke, *Nanotechnology* **6**, 1 (1995).

[213] T. Pirzer, T. Hugel, *Review of Scientific Instruments* **80**, 035110/1 (2009).

[214] C. Bergaud, L. Nicu, *Review of Scientific Instruments* **71**, 2487 (2000).

[215] E. L. Florin, *et al.*, *Biosensors and Bioelectronics* **10**, 895 (1995).

[216] R. W. Stark, T. Drobek, W. M. Heckl, *Ultramicroscopy* **86**, 207 (2001).

[217] R. Lévy, M. Maaloum, *Nanotechnology* **13**, 33 (2002).

[218] R. Proksch, T. E. Schaffer, J. P. Cleveland, R. C. Callahan, M. B. Viani, *Nanotechnology* **15**, 1344 (2004).

[219] T. E. Schäffer, *Nanotechnology* **16**, 664 (2005).

[220] C. P. Green, *et al.*, *Review of Scientific Instruments* **75**, 1988 (2004).

[221] J. M. Neumeister, W. A. Ducker, *Review of Scientific Instruments* **65**, 2527 (1994).

[222] J. E. Sader, *Review of Scientific Instruments* **66**, 4583 (1995).

[223] J. Alcaraz, *et al.*, *Langmuir* **18**, 716 (2002).

[224] H. Janovjak, J. Struckmeier, D. J. Muller, *European Biophysics Journal with Biophysics Letters* **34**, 91 (2005).

[225] B. N. Balzer, Haftung und Reibung von Einzelpolymeren auf Festkörperoberflächen in Wässrigem Medium, Master's thesis, TU München (2008).

[226] F. Kühner, M. Erdmann, H. E. Gaub, *Physical Review Letters* **97**, 218301 (2006).

[227] A. F. Stalder, G. Kulik, D. Sage, L. Barbieri, P. Hoffmann, *Colloids and Surfaces A-Physicochemical and Engineering Aspects* **286**, 92 (2006).

[228] A. F. Stalder, *et al.*, *Colloids and Surfaces A-Physicochemical and Engineering Aspects* **364**, 72 (2010).

[229] B. Maier, J. O. Radler, *Physical Review Letters* **82**, 1911 (1999).

[230] T. Cellmer, E. R. Henry, J. Hofrichter, W. A. Eaton, *Proceedings of the National Academy of Sciences of the United States of America* **105**, 18320 (2008).

[231] A. Borgia, *et al.*, *Nature Communications* **3**, 1195 (2012).

[232] C. Ke, Y. Jiang, M. Rivera, R. L. Clark, P. E. Marszalek, *Biophysical Journal* **92**, L76 (2007).

[233] M. Rivera, *et al.*, *Biophysical Journal* **95**, 3991 (2008).

[234] T. G. Desai, P. Keblinski, S. K. Kumar, S. Granick, *Physical Review Letters* **98**, 218301/1 (2007).

[235] S. A. Sukhishvili, *et al.*, *Nature* **406**, 146 (2000).

[236] J. A. Dean, *Lange's Handbook of Chemistry* (Mcgraw-Hill, 1999), 15th edn.

[237] M. S. Z. Kellermayer, S. B. Smith, H. L. Granzier, C. Bustamante, *Science* **276**, 1112 (1997).

[238] H. E. Johnson, J. F. Douglas, S. Granick, *Physical Review Letters* **70**, 3267 (1993).

[239] J. F. Douglas, H. E. Johnson, S. Granick, *Science* **262**, 2010 (1993).

[240] Y. M. Wang, R. Rajagopalan, W. L. Mattice, *Physical Review Letters* **74**, 2503 (1995).

[241] D. Gourdon, J. N. Israelachvili, *Physical Review E* **68**, 1 (2003).

[242] J. L. Keddie, R. A. L. Jones, R. A. Cory, *Europhysics Letters* **27**, 59 (1994).

[243] O. Prucker, J. Ruhe, *Langmuir* **14**, 6893 (1998).

[244] K. Viswanathan, T. E. Long, T. C. Ward, *Journal of Polymer Science, Part A: Polymer Chemistry* **43**, 3655 (2005).

[245] M. Tress, *et al.*, *Macromolecules* **43**, 9937 (2010).

[246] Z. Yang, Y. Fujii, F. K. Lee, C.-H. Lam, O. K. C. Tsui, *Science* **328**, 1676 (2010).

[247] S. Dodoo, B. N. Balzer, T. Hugel, A. Laschewsky, R. v. Klitzing, *Soft Materials* **11**, 157 (2011).

[248] B. N. Balzer, *et al.*, *ACS Applied Materials and Interfaces* **5**, 6300 (2013).

[249] G. Decher, J. D. Hong, J. Schmitt, *Thin Solid Films* **210**, 831 (1992).

[250] G. Decher, *Science* **277**, 1232 (1997).

[251] P. T. Hammond, *Current Opinion in Colloid and Interface Science* **4**, 430 (1999).

[252] R. von Klitzing, *Physical Chemistry Chemical Physics* **8**, 5012 (2006).

[253] H. A. Vanderschee, J. Lyklema, *Journal of Physical Chemistry* **88**, 6661 (1984).

[254] M. R. Bohmer, O. A. Evers, J. Scheutjens, *Macromolecules* **23**, 2288 (1990).

[255] G. Ahn-Ercan, H. Krienke, W. Kunz, *Current Opinion in Colloid and Interface Science* **9**, 92 (2004).

[256] V. Vlachy, B. Hribar-Lee, Y. V. Kalyuzhnyi, K. A. Dill, *Current Opinion in Colloid and Interface Science* **9**, 128 (2004).

[257] R. von Klitzing, J. E. Wong, W. Jaeger, R. Steitz, *Current Opinion in Colloid and Interface Science* **9**, 158 (2004).

[258] M. Salomaki, P. Tervasmaki, S. Areva, J. Kankare, *Langmuir* **20**, 3679 (2004).

[259] S. T. Dubas, J. B. Schlenoff, *Langmuir* **17**, 7725 (2001).

[260] A. A. Antipov, G. B. Sukhorukov, H. Mohwald, *Langmuir* **19**, 2444 (2003).

[261] R. Steitz, V. Leiner, K. Tauer, V. Khrenov, R. von Klitzing, *Applied Physics A-Materials Science and Processing* **74**, S519 (2002).

[262] S. Dodoo, R. Steitz, A. Laschewsky, R. von Klitzing, *Physical Chemistry Chemical Physics* **13**, 10318 (2011).

[263] F. Caruso, H. Lichtenfeld, E. Donath, H. Mohwald, *Macromolecules* **32**, 2317 (1999).

[264] M. Adusumilli, M. L. Bruening, *Langmuir* **25**, 7478 (2009).

[265] S. Enrique Moya, J. J. Iturri Ramos, I. Llarena, *Macromolecular Rapid Communications* **33**, 1022 (2012).

[266] S. L. Clark, P. T. Hammond, *Langmuir* **16**, 10206 (2000).

[267] X. Jiang, H. Zheng, S. Gourdin, P. T. Hammond, *Langmuir* **18**, 2607 (2002).

[268] S. Y. Yang, M. F. Rubner, *Journal of the American Chemical Society* **124**, 2100 (2002).

[269] R. H. Lajimi, A. Ben Abdallah, E. Ferjani, M. S. Roudesli, A. Deratani, *Desalination* **163**, 193 (2004).

[270] D. M. Sullivan, M. L. Bruening, *Journal of Membrane Science* **248**, 161 (2005).

[271] F. Caruso, D. N. Furlong, K. Ariga, I. Ichinose, T. Kunitake, *Langmuir* **14**, 4559 (1998).

[272] A. Wu, D. Yoo, J. K. Lee, M. F. Rubner, *Journal of the American Chemical Society* **121**, 4883 (1999).

[273] J. J. Harris, M. L. Bruening, *Langmuir* **16**, 2006 (2000).

[274] S. T. Dubas, T. R. Farhat, J. B. Schlenoff, *Journal of the American Chemical Society* **123**, 5368 (2001).

[275] E. Donath, G. B. Sukhorukov, F. Caruso, S. A. Davis, H. Mohwald, *Angewandte Chemie-International Edition* **37**, 2202 (1998).

[276] Y. Lvov, K. Ariga, M. Onda, I. Ichinose, T. Kunitake, *Colloids and Surfaces A-Physicochemical and Engineering Aspects* **146**, 337 (1999).

[277] B. F. Qiao, J. J. Cerda, C. Holm, *Macromolecules* **43**, 7828 (2010).

[278] G. Ladam, *et al.*, *Langmuir* **16**, 1249 (2000).

[279] J. B. Schlenoff, S. T. Dubas, *Macromolecules* **34**, 592 (2001).

[280] M. Losche, J. Schmitt, G. Decher, W. G. Bouwman, K. Kjaer, *Macromolecules* **31**, 8893 (1998).

[281] S. T. Dubas, J. B. Schlenoff, *Macromolecules* **32**, 8153 (1999).

[282] T. Farhat, G. Yassin, S. T. Dubas, J. B. Schlenoff, *Langmuir* **15**, 6621 (1999).

[283] R. Steitz, V. Leiner, R. Siebrecht, R. von Klitzing, *Colloids and Surfaces A-Physicochemical and Engineering Aspects* **163**, 63 (2000).

[284] R. Kugler, W. Knoll, *Macromolecular Chemistry and Physics* **203**, 923 (2002).

[285] B. Schwarz, M. Schonhoff, *Langmuir* **18**, 2964 (2002).

[286] M. McCormick, *et al.*, *Macromolecules* **36**, 3616 (2003).

[287] R. N. Smith, L. Reven, C. J. Barrett, *Macromolecules* **36**, 1876 (2003).

[288] M. Geisler, T. Hugel, *Advanced Materials* **22**, 398 (2010).

[289] R. VonKlitzing, H. Möhwald, *Macromolecules* **29**, 6901 (1996).

[290] P. Nazaran, V. Bosio, W. Jaeger, D. F. Anghel, R. von Klitzing, *Journal of Physical Chemistry B* **111**, 8572 (2007).

[291] E. M. Puchner, H. E. Gaub, *Current Opinion in Structural Biology* **19**, 605 (2009).

[292] H. B. Li, Y. Cao, *Accounts of Chemical Research* **43**, 1331 (2010).

[293] S. Micciulla, A Study on The Effect of Salt Concentration on Self-Assembly and Surface Properties of Oligoelectrolyte Multilayers, Master's thesis, TU Berlin (2011).

[294] S. Dodoo, Structure and Swelling Behavior of Polyelectrolyte Multilayer, Ph.D. thesis, TU Berlin (2011).

[295] T. Strunz, K. Oroszlan, R. Schafer, H. J. Guntherodt, *Proceedings of the National Academy of Sciences of the United States of America* **96**, 11277 (1999).

[296] J. Schmitt, *et al.*, *Macromolecules* **26**, 7058 (1993).

[297] H. W. Jomaa, J. B. Schlenoff, *Macromolecules* **38**, 8473 (2005).

[298] Á. Karsai, *et al.*, *Journal of Structural Biology* **155**, 316 (2006).

[299] D. Alsteens, C. B. Ramsook, P. N. Lipke, Y. F. Dufrene, *Acs Nano* **6**, 7703 (2012).

[300] E. Spruijt, M. A. Cohen Stuart, J. van der Gucht, *Macromolecules* **43**, 1543 (2010).

[301] E. Spruijt, S. A. van den Berg, M. A. Cohen Stuart, J. van der Gucht, *Acs Nano* **6**, 5297 (2012).

[302] Y. Lvov, G. Decher, H. Mohwald, *Langmuir* **9**, 481 (1993).

[303] R. Mueller, K. Kohler, R. Weinkamer, G. Sukhorukov, A. Fery, *Macromolecules* **38**, 9766 (2005).

[304] C. J. Lawrence, *Physics of Fluids* **31**, 2786 (1988).

[305] D. W. Schubert, *Polymer Bulletin* **38**, 177 (1997).

[306] P. Müller-Buschbaum, *European Physical Journal E* **12**, 443 (2003).

[307] B. Zhao, W. J. Brittain, *Progress in Polymer Science* **25**, 677 (2000).

[308] R. Advincula, *et al.*, *Langmuir* **18**, 8672 (2002).

[309] B. N. Balzer, *et al.*, *Macromolecules* **46**, 7406 (2013).

[310] N. Rehse, *et al.*, *European Physical Journal E* **4**, 69 (2001).

[311] G. Reiter, *Physical Review Letters* **87**, 186101/1 (2001).

[312] R. Seemann, S. Herminghaus, K. Jacobs, *Physical Review Letters* **86**, 5534 (2001).

[313] P. Müller-Buschbaum, *Journal of Physics- Condensed Matter* **15**, R1549 (2003).

[314] P. Müller-Buschbaum, E. Bauer, O. Wunnicke, M. Stamm, *Journal of Physics-Condensed Matter* **17**, S363 (2005).

[315] J. A. Forrest, K. Dalnoki-Veress, *Advances in Colloid and Interface Science* **94**, 167 (2001).

[316] A. Vrij, J. T. Overbeek, *Journal of the American Chemical Society* **90**, 3074 (1968).

[317] F. Brochardwyart, C. Redon, C. Sykes, *Comptes Rendus de l'Académie des Sciences Série II* **314**, 19 (1992).

[318] R. Xie, A. Karim, J. F. Douglas, C. C. Han, R. A. Weiss, *Physical Review Letters* **81**, 1251 (1998).

[319] J. Kraus, P. Müller-Buschbaum, T. Kuhlmann, D. W. Schubert, M. Stamm, *Europhysics Letters* **49**, 210 (2000).

[320] S. Ok, *et al.*, *Macromolecules* **43**, 4429 (2010).

[321] R. C. Advincula, *Journal of Dispersion Science and Technology* **24**, 343 (2003).

[322] V. Mittal, N. B. Matsko, A. Butte, M. Morbidelli, *Polymer* **48**, 2806 (2007).

[323] M. Ejaz, S. Yamamoto, K. Ohno, Y. Tsujii, T. Fukuda, *Macromolecules* **31**, 5934 (1998).

[324] S. Yamamoto, M. Ejaz, Y. Tsujii, M. Matsumoto, T. Fukuda, *Macromolecules* **33**, 5602 (2000).

[325] C. Kim, *et al.*, *Colloid and Polymer Science* **291**, 2087 (2013).

[326] J. P. Wittmer, M. E. Cates, A. Johner, M. S. Turner, *Europhysics Letters* **33**, 397 (1996).

[327] S. Yamamoto, M. Ejaz, Y. Tsujii, T. Fukuda, *Macromolecules* **33**, 5608 (2000).

[328] S. Yamamoto, Y. Tsujii, T. Fukuda, *Macromolecules* **33**, 5995 (2000).

[329] R. Jordan, A. Ulman, J. F. Kang, M. H. Rafailovich, J. Sokolov, *Journal of the American Chemical Society* **121**, 1016 (1999).

[330] E. Thormann, A. C. Simonsen, P. L. Hansen, O. G. Mouritsen, *Langmuir* **24**, 7278 (2008).

[331] D. S. Fryer, P. F. Nealey, J. J. de Pablo, *Macromolecules* **33**, 6439 (2000).

[332] R. A. L. Jones, *Current Opinion in Colloid and Interface Science* **4**, 153 (1999).

[333] J. L. Keddie, R. A. L. Jones, R. A. Cory, *Faraday Discussions* **98**, 219 (1994).

[334] D. S. Fryer, *et al.*, *Macromolecules* **34**, 5627 (2001).

[335] G. B. DeMaggio, *et al.*, *Physical Review Letters* **78**, 1524 (1997).

[336] K. Fukao, Y. Miyamoto, *Europhysics Letters* **46**, 649 (1999).

[337] O. Prucker, *et al.*, *Macromolecular Chemistry and Physics* **199**, 1435 (1998).

[338] Y. M. Boiko, R. E. Prud'homme, *Journal of Polymer Science Part B- Polymer Physics* **36**, 567 (1998).

[339] B. Zuo, *et al.*, *Macromolecules* **46**, 1875 (2013).

[340] A. N. Raegen, M. V. Massa, J. A. Forrest, K. Dalnoki-Veress, *European Physical Journal E* **27**, 375 (2008).

[341] B. M. I. Flier, *et al.*, *Physical Chemistry Chemical Physics* **13**, 1770 (2011).

[342] B. M. I. Flier, *et al.*, *Journal of the American Chemical Society* **134**, 480 (2012).

[343] P. G. de Gennes, *European Physical Journal E* **2**, 201 (2000).

[344] L. Han, D. Dean, P. Mao, C. Ortiz, A. J. Grodzinsky, *Biophysical Journal* **93**, L23 (2007).

[345] L. Han, D. Dean, L. A. Daher, A. J. Grodzinsky, C. Ortiz, *Biophysical Journal* **95**, 4862 (2008).

[346] G. W. Greene, *et al.*, *Proceedings of the National Academy of Sciences of the United States of America* **108**, 5255 (2011).

[347] L. Han, A. J. Grodzinsky, C. Ortiz, *Annual Review of Materials Research* **41**, 133 (2011).

[348] B. Frank, A. P. Gast, T. P. Russell, H. R. Brown, C. J. Hawker, *Macromolecules* **29**, 6531 (1996).

[349] A. Casoli, M. Brendle, J. Schultz, P. Auroy, G. Reiter, *Langmuir* **17**, 388 (2001).

[350] S. Yamada, *Langmuir* **24**, 1469 (2008).

[351] B. Liberelle, S. Giasson, *Langmuir* **24**, 1550 (2008).

[352] T. Drobek, N. D. Spencer, *Langmuir* **24**, 1484 (2008).

[353] C. Drummond, G. Marinov, P. Richetti, *Langmuir* **24**, 1560 (2008).

[354] J. Klein, *et al.*, *Macromolecules* **26**, 5552 (1993).

[355] J. Klein, E. Kumacheva, D. Mahalu, D. Perahia, L. J. Fetters, *Nature* **370**, 634 (1994).

[356] U. Raviv, *et al.*, *Langmuir* **18**, 7482 (2002).

[357] U. Raviv, J. Klein, *Science* **297**, 1540 (2002).

[358] U. Raviv, *et al.*, *Nature* **425**, 163 (2003).

[359] M. Chen, W. H. Briscoe, S. P. Armes, J. Klein, *Science* **323**, 1698 (2009).

[360] A. Nomura, K. Okayasu, K. Ohno, T. Fukuda, Y. Tsujii, *Macromolecules* **44**, 5013 (2011).

[361] W. Zhang, *et al.*, *Biomacromolecules* **14**, 394 (2013).

[362] J. F. Joanny, *Langmuir* **8**, 989 (1992).

[363] M. Sirchabesan, S. Giasson, *Langmuir* **23**, 9713 (2007).

[364] M. Ruths, D. Johannsmann, J. Ruhe, W. Knoll, *Macromolecules* **33**, 3860 (2000).

[365] V. Lupascu, H. Huth, C. Schick, M. Wubbenhorst, *Thermochimica Acta* **432**, 222 (2005).

[366] A. Serghei, F. Kremer, *Macromolecular Chemistry and Physics* **209**, 810 (2008).

[367] K. Viswanathan, T. E. Long, T. C. Ward, *Langmuir* **25**, 6808 (2009).

[368] J. Klein, E. Kumacheva, D. Perahia, D. Mahalu, S. Warburg, *Faraday Discussions* **98**, 173 (1994).

[369] L. Grebikova, *et al.*, *Macromolecules* **46**, 3603 (2013).

[370] M. Tanaka, J. Hermann, I. Haase, M. Fischer, S. G. Boxer, *Langmuir* **23**, 5638 (2007).

[371] F. Stetter, Zur Nanomechanischen Charakterisierung von Oberflächengestützten Biomembranmodellen, Ph.D. thesis, TU München (2013).

[372] F. Meyer, Superlubricity in Vehicles - New Carbon-Based Materials Reduce Fuel Consumption and Wear, *Tech. rep.*, Bine Information Service, Energy Research for Practical Applications, a Service from FIZ Karlsruhe (2012).

[373] M. Kano, *et al.*, *Tribology Letters* **18**, 245 (2005).

[374] M. I. D. Bouchet, *et al.*, *International Conference on Science of Friction* **89**, 12003 (2007).

[375] C. Matta, *et al.*, *Lubrication Science* **20**, 137 (2008).

[376] E. M. Liston, *Journal of Adhesion* **30**, 199 (1989).

[377] Y. Nojima, K. Iguchi, Y. Suzuki, A. Sato, *Biological and Pharmaceutical Bulletin* **32**, 523 (2009).

[378] M. Rieder, *et al.*, *Canadian Mineralogist* **36**, 905 (1998).

[379] C. D. Bain, *et al.*, *Journal of the American Chemical Society* **111**, 321 (1989).

[380] G. Nelles, *et al.*, *Langmuir* **14**, 808 (1998).

[381] D. Ruppelt, J. Kotz, W. Jaeger, S. E. Friberg, R. A. Mackay, *Langmuir* **13**, 3316 (1997).

[382] H. Dautzenberg, E. Gornitz, W. Jaeger, *Macromolecular Chemistry and Physics* **199**, 1561 (1998).

[383] J. E. Wong, F. Rehfeldt, P. Hanni, M. Tanaka, R. V. Klitzing, *Macromolecules* **37**, 7285 (2004).

[384] V. Bosio, F. Dubreuil, G. Bogdanovic, A. Fery, *Colloids and Surfaces A-Physicochemical and Engineering Aspects* **243**, 147 (2004).

[385] M. Kolasinska, R. Krastev, P. Warszynski, *Journal of Colloid and Interface Science* **305**, 46 (2007).

[386] Q. Zhou, S. Wang, X. Fan, R. Advincula, J. Mays, *Langmuir* **18**, 3324 (2002).

[387] K.-D. Hof, *et al.*, *Nano Letters* **10**, 3836 (2010).

[388] K. C. Nowack, Electrical Manipulation and Detection of Single Electron Spins in Quantum Dots, Ph.D. thesis, TU Delft (2009).

[389] A. Hartl, *et al.*, *Journal of the American Chemical Society* **129**, 1287 (2007).

[390] Q. Li, K. S. Kim, A. Rydberg, *Review of Scientific Instruments* **77**, 065105/1 (2006).

[391] L. Wiegleb, Kalibration eines Rasterkraftmikroskops für Reibungsmessungen, Bachelor Thesis, TU München (2011).

[392] D. Axelrod, T. P. Burghardt, N. L. Thompson, *Annual Review of Biophysics and Bioengineering* **13**, 247 (1984).

[393] D. Axelrod, *Biophysical Journal* **78**, 796 (2000).

[394] T. Schubert, Influence of Molecular Structure on Ordering and Dynamics of Lipids and Proteins in Biological Membrane Models, Ph.D. thesis, Universität Heidelberg (2009).

[395] S. Asbeck, Optimierung von Fluoreszenzmarkierungsmethoden zur Fluoreszenzmikroskopie basierten Diffusionsmessung von Einzelpolymeren, Bachelor thesis, TU München (2012).

[396] J. F. Allemand, D. Bensimon, L. Jullien, A. Bensimon, V. Croquette, *Biophysical Journal* **73**, 2064 (1997).

[397] S. W. Hell, J. Wichmann, *Optics Letters* **19**, 780 (1994).

[398] M. Mickler, Kinetik des ATPase-Zyklus von Hsp90 in Einzelmolekulexperimenten, Ph.D. thesis, TU München (2008).

[399] P. Atkins, J. de Paula, *Atkins' Physical Chemistry* (Oxford University Press, Oxford, 2006), 8th edn.

[400] L. Cohen-Tannoudji, *et al.*, *Physical Review Letters* **94**, 038301/1 (2005).

List of Publications

Parts of this thesis have been published in or submitted to peer-reviewed journals. A part of this thesis is published in a book chapter. Further manuscripts are in preparation for submission.
These contributions include:

1. M. Geisler, B. N. Balzer and T. Hugel, *Polymer Adhesion at the Solid-Liquid Interface Probed by a Single-Molecule Force Sensor.* small, 5(24), 2864-2869, 2009.

2. S. Dodoo, B. N. Balzer, T. Hugel, A. Laschewsky and R. von Klitzing, *Effect of Ionic Strength and Layer Number on Swelling of Polyelectrolyte Multilayers in Water Vapour.* Soft Materials, 11(2), 157-164, 2011.

3. B. N. Balzer and T. Hugel, *Single-Molecule Detection and Manipulation.* Polymer Science: A Comprehensive Reference. K. Matyjaszewski and M. Möller. Amsterdam, Elsevier BV, 2, 629–645, 2012.

4. N. Schwierz, D. Horinek, S. Liese, T. Pirzer, B. N. Balzer, T. Hugel and R. R. Netz, *On the Relationship between Peptide Adsorption Resistance and Surface Contact Angle: A Combined Experimental and Simulation Single-Molecule Study.* Journal of the American Chemical Society, 134(48), 19628-19638, 2012.

5. B. N. Balzer, M. Gallei, M.V. Hauf, M. Stallhofer, L. Wiegleb, A. Holleitner, M. Rehahn and T. Hugel, *Nanoscale Friction Mechanisms at Solid–Liquid Interfaces.* Angewandte Chemie International Edition, 52(25), 6541-6544, 2013.

6. B. N. Balzer, S. Micciulla, S. Dodoo, M. Zerball, M. Gallei, M. Rehahn, R. von Klitzing and T. Hugel, *Adhesion Property Profiles of Supported Thin Polymer Films.* ACS Applied Materials and Interfaces, 5(13), 6300-6306, 2013.

7. B. N. Balzer, M. Gallei, K. Sondergeld, M. Schindler, P. Müller-Buschbaum, M. Rehahn and T. Hugel, *Cohesion Mechanisms of Polystyrene-Based Thin Polymer Films.* Macromolecules, 46(18), 7406-7414, 2013.

8. B. N. Balzer and M. Gallei, *Das Reibt Sich Gut-Rasterkraftmikroskopie am Einzelmolekül.* GIT Labor-Fachzeitschrift, 11, 2013.

9. B. N. Balzer, S. Kienle, M. Gallei, M. Rehahn and T. Hugel, *Stick-Slip Mechanisms of Nanoscale Friction.* submitted.

10. S. Kienle, M. Gallei, H. Yu, B. Zhang, S. Krysiak, B.N. Balzer, M. Rehahn, D. Schlüter and T. Hugel, *Effect of Molecular Architecture on Single Polymer Adhesion and Friction.* submitted.

11. B. N. Balzer and T. Hugel, *Stick-Slip on Polymer Coated Substrates.* in preparation.

12. B. N. Balzer et al., *AFM-Based Single Polymer Adhesion and Friction Sensors.* in preparation.

Further publication, which is not directly related to this thesis:

J. Elbert, F. Krohm, C. Rüttiger, S. Kienle, H. Didzoleit, B. N. Balzer, T. Hugel, B. Stühn, M. Gallei and Annette Brunsen, *Polymer-Modified Mesoporous Silica Thin Films and First Steps Towards Redox-Mediated Membrane Gating.* Advanced Functional Materials, 2013, DOI: 10.1002/adfm.201302304.

Industrial cooperations corresponding to this thesis:

PEGASUS project (Project number 0327499A-G, Federal Ministry of Economics and Technology, BMWi) led by Bayerische Motoren Werke (BMW)

Acknowledgements/Danksagung

Coming together is a beginning;
keeping together is progress;
working together is success.
Henry Ford (1863-1947)

Die Anfertigung dieser Arbeit gelang nur mithilfe vieler Menschen, denen ich zu Dank verpflichtet bin.

Mein Dank gilt zu allererst meinem Doktorvater, Thorsten Hugel, der die letzten Jahre stets Geduld mit mir bewiesen hat. Er hatte immer für Sorgen und Nöte ein offenes Ohr, kam stets mit neuen Ideen und Herausforderungen und ließ gleichzeitig viel Freiraum für eigene Ideen und Gestaltung. Auch möchte ich mich für die vielen Reisen, die mich u.a. ganz Deutschland und die schönsten Ecken Frankreichs und der USA kennen lernen ließen, bedanken.

Besonderer Dank gilt zwei Kollegen, die in den vergangenen Jahren zu guten Freunden geworden sind: Tobias Pirzer, von dem ich tatsächlich „viel gelernt“ habe und für dessen WaveGuide Serie ich jeden Tag dankbar war, und Frank Stetter, in dessen „Wohnzimmer“ wir immer eine gute Zeit verbracht haben. Des Weiteren sei der gesamten Gruppe E22a für die gute wissenschaftliche Zusammenarbeit und die tolle Arbeitsatmosphäre gedankt, insbesondere Sandra Kienle, Stefanie Krysiak, Bettina Kracke, Sonja Schmid (danke für die TIRF Experimente), meinen ehemaligen Studenten Lorenz Wiegleb und Stefan Asbeck, den ehemaligen Kollegen: Michael Geisler, Moritz Mickler, Michael Gruber, Kristina Ganzinger, Matthias Stahl, Alessandro Sepe und unseren Grazien Martina Dzharova, Christin Sasse und Katharina Lachmann.
Dem IMETUM mit seiner hervorragenden Ausstattung sei stellvertretend Axel Haase, Bernhard Gleich, Josef Hintermair, Susanne Schnell-Witteczek und Christine Rümenapp (danke für den Gelegießen Crashkurs) gedankt.
Auch unserer homebase, der Physik, vertreten durch die Lehrstühle von Matthias Rief (E22) und Andreas Bausch (E27), bin ich dankbar für Hilfe und wertvolle Diskussionen. Hierbei sei Michael Schlierf in Sachen cantilever Funktionalisierung und Thomas Schubert sowie Heinrich Grabmayr für die Unterstützung in Sachen Fluoreszenz gedankt.
Wertvolle Anregungen und Ideen haben wir immer in einer sehr offenen Art von Herrmann Gaub, Martin Benoit und Matthias Erdmann von der Physik Fakultät der LMU erhalten. Danke vielmals!

Ein wichtiger Teil dieser Arbeit umfasst Kooperationen innerhalb und über die Grenzen der TUM und Münchens hinaus. Hierbei sind zu nennen:
Peter Müller-Buschbaum, Markus Schindler und Tilo Hoppe vom Lehrstuhl E13 der TUM Physik für die Polystyroloberflächen und die Grundlagen der Ellipsometrie, Matthias Rehahn, Markus Gallei, Katrin Sondergeld von der TU Darmstadt, für die unzähligen Polymere, Regine v. Klitzing, Samuel Dodoo, Samantha Micciulla von der TU Berlin für die vielen PEM Oberflächen, Alexander Holleitner, Moritz Hauf und Markus Stallhofer vom WSI für die „gestreiften“ Oberflächen, Roland Netz, Nadine Schwierz und Aykut Erbas von der TUM/ FU Berlin, Dominik Horinek von der Universität Regensburg, Robijn Bruinsma von der University of California in Los Angeles und Christian Holm von der Universität Stuttgart für die vielen erhellenden Diskussionen, die uns erst erahnen ließen, was unsere Experimente bedeuteten, Johann Schnagl und Lisa Krell von der BMW AG für die Synthese von molekularen Experimenten mit der „Freude am Fahren“, und der Mann, der mit seinen goldenen Händen jedes noch so zerstörte MFP3D wieder zum Laufen bekommt, Friedhelm Freiss von Asylum Research.

Graduiertenschulen kommen auch in unseren Breitengraden immer stärker in Mode. Ganz spannend war es, eine solche Entwicklung von Anfang an beim Exzellenzcluster Nanosystems Initiative Munich (NIM) mitzuerleben und zu gestalten. Hierbei möchte ich danken für die schöne Zeit im ersten Student Board mit Susanne Braunmüller, Katja Falter, Stephan Heucke und Alexander Mehlich sowie für die Unterstützung durch Peter Sonntag, Birgit Gebauer und Christoph Hohmann (danke für den AE Crashkurs) von der NIM Geschäftsstelle.

Ich danke Markus Gallei, Tobias Pirzer, Kate Robinson, Daniel Soujon und Sandra Meister für das kritische Lesen!
Ganz besonders danke ich der „unbekannten“ Dame. Schließlich möchte ich meinen Eltern für jede erdenkliche Hilfe in den vergangenen 30 Jahren danken. Ohne Euch wäre ich nicht hier. Bei meiner Mutter darf ich mich für die Liebe, die Unterstützung, die Sorge um mein leibliches Wohl und die vielen gebügelten Hemden bedanken!